The University of Nottingham

UNITED KINGDOM · CHINA · MALAYSIA

The effect of nitriding on the fretting wear of a high strength steel at ambient and elevated temperatures

STEPHEN R. PEARSON, MEng.

Thesis submitted to The University of Nottingham
for the degree of Doctor of Philosophy

December 2013

IMAGING SERVICES NORTH
Boston Spa, Wetherby
West Yorkshire, LS23 7BQ
www.bl.uk

ALL MISSING PAGES ARE BLANK IN THE ORIGINAL

Abstract

This work is an experimental evaluation of the wear and friction of a high strength alloy steel (super-CMV (SCMV)) in its as heat treated and plasma nitrided states under fretting conditions in air, at both ambient and elevated temperatures.

In order to conduct the experimental programme, a new test rig and associated data processing and assessment capability was developed. Wearing couples in homogeneous and heterogeneous arrangements were tested to assess the effectiveness of the nitriding process as a fretting palliative—the heterogeneous mating is particularly representative of configurations found in aerospace transmission assemblies. A range of test conditions were examined with a line contact, including normal loads from 25 to 65 $N\,mm^{-1}$, displacement amplitudes from 10 to 100 μm and temperatures from 24 to 450 °C.

At ambient temperatures, the wear behaviour was assessed using an energy-wear analysis, whereupon it was demonstrated that the wear volume was a linear function of the dissipated frictional energy (over the range of loading conditions) with a significant energy threshold before the onset of wear. Accordingly, the fretting wear over the full range of loading conditions could be described by a single wear *rate* and threshold value. The wear rate for homogeneous couples of nitrided super-CMV (SCMVN) was found to be 12 % lower than that for comparable SCMV pairings, although the lower threshold energy for the SCMVN case would lead to them suffering greater wear at < 2.5 kJ of dissipated energy (in the configuration examined). In heterogeneous couples, the harder SCMVN specimen was found to wear preferentially; while the SCMV specimen suffered severe plastic damage of the the surface, a protective oxide debris bed was seen to form, which protected the underlying SCMV from wear and abraded the SCMVN specimen.

At elevated temperatures, the tribology (of both SCMV and SCMVN) was dominated by the formation of a *glaze-layer*. The progressive formation of the glaze, with increasing temperature, led to a critical transition temperature (TT) above which a significant reduction in both the wear and friction of the materials was observed. For SCMV, after only a modest increase in temperature to 85 °C, the overall loss of material from the contact had become negative. At temperatures greater than 85 °C, negative wear was maintained, with the coefficient of friction dropping monotonically until a slight minimum at 300 °C. The behaviour for the SCMVN couples was very similar; the

transition to negative wear occurred at a higher temperature of 150 °C but the friction minimum was also found at 300 °C. It is proposed that the changes in wear rate and friction coefficient were due to changes in the way that the oxide particles sintered to form a protective debris bed, with sintering of the oxide debris particles at these low temperatures being promoted by the nano-scale at which the oxide debris is formed.

Acknowledgements

I would like to thank Prof. Philip Shipway for all of his support and invaluable guidance over the years as my supervisor and also Dr Graham Johnson for many hours of conversation and practical experimental direction. The many university technicians, without whom little research would be done, should of course not go unacknowledged. Most importantly though, I must thank my parents for their continuous support and encouragement throughout the course of my PhD.

I also wish to express my gratitude to Rolls-Royce Holdings plc, Aerospace Group, for their financial support of the research, which was carried out at the University Technology Centre in Gas Turbine Transmission Systems at The University of Nottingham.

Contents

Nomenclature

2D	two dimensional
3D	three dimensional
ASIC	application specific integrated circuit
BSE	back scattered electron
COF	coefficient of friction
CPU	central processing unit
cRIO	compactRIO
DDS	direct digital synthesis
DLC	diamond like carbon
DMA	direct memory access
EDX	energy dispersive X-ray spectroscopy
EMV	electromagnetic vibrator
EP	extreme pressure
FED	force energy displacement diagram
FPGA	field programmable gate array
GUI	graphical user interface
HDF5	hierarchical data format 5
HP	high pressure
IMS	industrial methylated spirit
IP	intermediate pressure
JKR	Johnson-Kendall-Roberts
LP	low pressure
LSMB	lower specimen mounting block
LV	LabVIEW™

LVDT	linear variable differential transformer
MFR	mixed fretting regime
MGC	machinable glass ceramic
MRFM	material response fretting map
NI	National Instruments
PC	personal computer
PCI	peripheral component interconnect
PID	proportional integral derivative
PTFE	polytetrafluoroethylene
PVD	physical vapour deposition
RCFM	running condition fretting map
RH	relative humidity
RT	real-time
RTOS	real-time operating system
SCADA	supervisory control and data acquisition
SCMV	super-CMV
SCMVN	nitrided super-CMV
SE	secondary electron
SEM	scanning electron microscopy
SFTC	system free transition criterion
SMP	specimen mounting plate
TDMS	technical data management streaming
TT	transition temperature
TTS	tribologically transformed structure
USMB	upper specimen mounting block
WL	white layer
XRD	X-ray diffraction
ZDDP	zinc dialkyldithiophosphate

Chapter 1

Introduction

Fretting is a tribological mechanism of surface degradation, occurring between mated surfaces as the result of cyclic loading causing reciprocating slip (typically of tens of microns) between the components [1, 2]. Such mating contacts are often assumed to be static by the designer; consequently, attributed failures may only be found after months or years in service. The damage resulting from fretting can be detrimental in a number of ways: generation of debris may be sufficient to cause seizure; alternatively, enough material may be lost to inhibit the component function through loss of fit, or catastrophic premature fatigue failure may result from accelerated crack nucleation [3].

Both mechanical and chemical processes are demonstrably key to fretting [4]; accordingly, any instance of fretting damage is dependent on a great number of variables [5]. This complexity has frustrated researchers since the early twentieth century; even today, despite over a hundred years of research, there is still no agreed fretting *mechanism* nor universal palliative. Moreover, strategies from the engineers toolbox—such as lubrication, coatings and design modifications—have been successfully applied to particular instances of fretting, only to find that under different conditions the same method is detrimental [1, 6].

Fretting is common across many industries and reported cases may be found in the automotive, aerospace, nuclear and conventional energy sectors [1, 7–9]. At the University of Nottingham, there has been active fretting research for over forty years. In recent times effort has been primarily focussed on fretting problems in aeroengines, particularly the main-shaft spline couplings—through work conducted within the Rolls-Royce transmissions UTC [10–12]. Starting with the RB211 family, Rolls-Royce engines have featured a triple spool arrangement, allowing independent pressure stages and consequently greater efficiency. Each of the mainshafts has a splined coupling between the compressor and turbine sections to facilitate assembly and disassembly for maintenance and inspection. In flight, gyroscopic loads from the fan assembly and misalignment inevitably result in slip within the coupling and hence fretting. The significant pressures on engine manufacturers to increase

performance, while simultaneously reducing fuel burn and weight, has led to higher bypass ratios and reduced core size and consequently significantly greater demands of the mainshafts and couplings. For example, the current Trent series—compared to the previous RB211 generation of engines—doubled the torque density of the low pressure (LP) shaft [13]. This performance gain was delivered by the development of a new steel (super-CMV (SCMV)) and optimisation of the spline design; similar gains in future designs will only be met with increased understanding of the materials and life limiting tribological mechanisms at work.

Recent efforts at the Nottingham transmissions UTC have focused on using finite element methods to predict the fretting related failures of the mainshaft splines [14–16]. The models simulate the complex spline geometries to identify the local contact conditions; experimentally derived *damage parameters* are then used to calculate the fretting damage at each mesh node. The damage parameters, incorporating the fundamental friction and tribology of the contact, are identified using simplified laboratory scale tests; the methodology has been termed *the representative specimen concept*. Such an approach is highly attractive: it offers the ability to life new designs while avoiding the significant costs (financial and time) of full scale testing.

It is well known that a large number of mechanical and environmental factors affect fretting [1, 5]. Therefore, for any modelling approach to be useful, well controlled experiments—spanning the full range of parameters known to exert the most significant influence—must be conducted, eventually providing a multi-dimensional look up table for the FE user. In the current Trent series of Rolls-Royce engines, the mainshafts and splines are manufactured from SCMV (a high strength steel). Typically, the male splines are nitrided while the female are left in the as heat treated condition. The operating temperature of the splines can exceed 200 °C and along a tooth, a range of displacements and contact pressures are encountered (resulting from barrelling of the spline and the involute profile of the teeth) [11].

A review of the literature (Chapter 2, Page 3) has identified surprisingly little information on the fretting wear of nitrided steels and none (as far as the author is aware) on the elevated temperature fretting of such nitrided steels. More generally, there is limited data on the elevated temperature fretting of steels, particularly high strength steels. Consequently, this work aims to develop an experimental facility and subsequently conduct tests on the ambient and high temperature fretting wear of SCMV and nitrided super-CMV (SCMVN). From these, measurements of wear rates of these materials as a function of test condition will be made, and this along with characterization of damage, will allow the mechanisms of wear to be elucidated.

Chapter 2

Literature Review

2.1 Introduction

In 1911, Eden et al. [17] reported that while conducting fatigue tests

> "A good deal of trouble was caused by corrosion where the test-specimen fits into its holders ... it was often difficult to remove the broken specimen from the holder ..."

Although not described as such, this was the first reported case of fretting. The initial formal investigation of the phenomena did not occur until sixteen years later when Tomlinson [18] published his paper "The rusting of steel surfaces in contact". While Eden et al. suggested that the wear they observed may be due to varying stresses between the specimen and holder, it was Tomlinson who identified the cause of fretting: small amplitude oscillatory motion between contacting surfaces, *slip*. In fact, Tomlinson reported that slip as small as "a few millionths of an inch" was sufficient to cause damage to the surfaces [18].

Incidences of fretting are often identified by the production of oxide debris [1]. It was such red iron oxide debris which Tomlinson observed that led him to term the process "fretting corrosion". Godfrey [19] later showed that the process was not one of a purely corrosive nature by demonstrating fretting between non-metallic and non-oxidising materials. The term, however, has persisted and is still seen in current literature and while it may not be completely accurate, it does indicate that fretting is not purely a mechanical process but is in fact a complex tribo-chemical interaction.

Fretting is distinguished from reciprocating sliding and other forms of wear by the small displacement amplitudes at which it occurs and the correspondingly low sliding velocities [1]. For example, two contacting bodies experiencing a relative sinusoidal tangential displacement of 25 μm at 50 Hz will experience a peak sliding velocity of only 7.9 mm s^{-1}. The exact displacement amplitude at which the transition to sliding wear occurs is debated in the literature and figures from 25 to 300 μm have been suggested [1, 20]. As a consequence of the small displacements, most of a fretting scar

will remain unexposed during a displacement cycle; Fouvry et al. [21] have suggested that this should be the differentiator between fretting and reciprocating sliding wear. Importantly, such contact conditions entrap wear particles within the wear scar and can limit the access of oxygen to it, leading to the complex tribo-chemical nature of fretting.

Fretting is not limited to laboratory tests; serious failures (in the extremis, aircraft crashes) have been caused by damage resulting from fretting [7]. Fretting has been widely reported in mechanical structures ranging from nuclear reactors [8] to wire ropes and even aluminium saucepans in a cyclist's saddlebags [1]. In fact, any contacting surfaces subject to vibrational stressing are susceptible to fretting. Certain examples of fretting can be particularly pernicious as they often occur at interfaces which are considered static by the designer and consequently not engineered for inspection or service; examples include: bolted and riveted joints, press fits between shafts and hubs and bearing races in their housings [9]. The resultant surface degradation may lead to a loss of fit or seizure due to material removal and subsequent retention or ejection of the wear debris—fretting wear; or it may cause premature failure due to crack initiation—fretting fatigue. The predominance of each mode of degradation is governed by the nature of the contact and loading [3].

2.2 Fretting in aeroengines: spline couplings

As discussed in the introduction (Section 2.1, Page 3), any surfaces under a clamping load and subjected to an oscillating tangential force may be susceptible to fretting. Many instances can be found throughout a gas turbine engine; for example dovetail joints, fan-blade snubbers and numerous bolted connections. The main-shaft spline coupling has been the particular focus of fretting research at the University of Nottingham for over a decade.

A spline is a mechanical torque-transmitting coupling, found at the interface between a shaft and power transferring element such as a gear [22]; such couplings are usually adopted in applications where radial compactness and disassembly are also required. The spline tooth profile may be straight sided or involute depending on the design requirements [23] and the axial geometry of the splines may be straight, or helical where an axial load must be carried [24, 25]. Additionally, the width of the tooth can be modified along its length in a process called barrelling to limit the end of engagement stresses [14].

The Rolls-Royce Trent family of engines utilises a triple spool arrangement where the fan (LP), intermediate (IP) and high pressure (HP) compressor stages are driven independently by the LP, IP and HP turbine stages respectively. This enables the blade velocities to be better optimised for their respective operating conditions and allows a shorter and lighter engine than a similar two spool arrangement [26]. The shafts linking the turbine to the compressor in a rotor set are termed "mainshafts"; they run

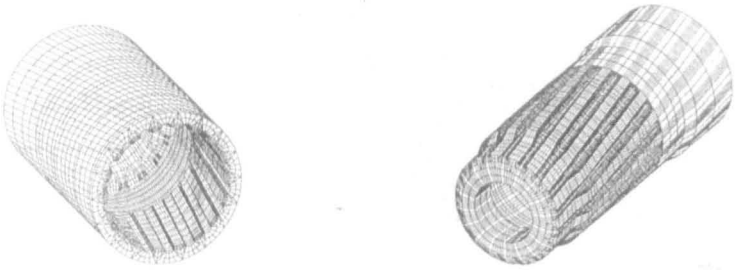

(a) Female spline (b) Male spline

Figure 2.1: Scale model of the helical spline coupling, with involute profile teeth, found on the RR Trent series engine low pressure shaft.

concentrically inside one another, with the LP shaft at the centre. In a high-bypass ratio engine, the majority of the thrust is developed by the fan resulting in the LP shaft being the most highly stressed shaft in the engine, running at approximately 3000 rpm and carrying a torque of up to 135 kN m [13, 15].

To allow assembly and to accommodate any axial misalignment or thermal expansion, the turbine and compressor ends of the shafts are joined by a helical and involute profile spline (Figure 2.1). In service, misalignment, vibration and barrelling of the teeth lead to slip between the coupled shafts and hence to fretting within the coupling [11]. Additionally, thrust induced deformation of the engine carcass and gyroscopic loads from the fan during aircraft manoeuvring lead to further slip.

The relentless pressure to increase engine efficiencies and reduce size and weight places considerable demands on the design of critical engine components such as the mainshafts. Between the Trent series of engine and its predecessor, the RB211 family, the torque density of the LP shaft was doubled, while the weight per unit of torque was reduced by twenty five percent [13]. To continue to deliver such gains in performance will require the development of new, high performance, materials and advances in understanding of tribology at critical interfaces such as the spline couplings.

2.3 Analysis of a fretting contact

2.3.1 Contact mechanics

In order to understand the wear mechanisms operating within a fretting contact, it is necessary to understand the contact conditions: the stresses and surface tractions.

It was Hertz [27] who first studied the mutual compression of contacting bodies loaded against each other; in two papers published in 1949 and 1953, Mindlin [28] and Mindlin and Deresiewicz [29] expanded those theories to the fretting contact i.e., a reciprocating tangential force causing slip at the contact.

In order to study the contact mechanics, it is convenient to generalise mechanical contacts to a simplified situation such as a point or line contact. In this case the

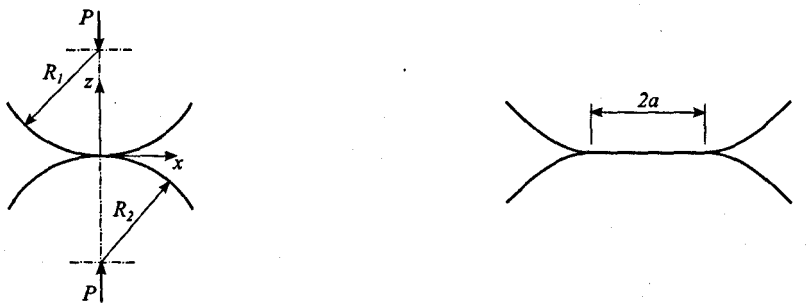

(a) (b)

Figure 2.2: Hertzian contact between two cylinders of radius R_1 and R_2 with a contact load of $P\,\mathrm{N\,m^{-1}}$. (a) showing the contact, loads and coordinate system (b) showing a close up of the contact and the contact width, a.

two-dimensional line contact between two cylinders is considered (the specific case of a cylinder on flat contact is obtained by defining the radius of one cylinder as infinite).

If the two cylindrical bodies, with their axes parallel, of radius R_1 and R_2, are pressed into contact by a force, P per unit length, then they will generate a line contact of width $2a$ (Figure 2.2), given by Hertz theory and detailed by Johnson [30] as

$$a = \left(\frac{4PR}{\pi E^*}\right)^{\frac{1}{2}} \tag{2.1}$$

where E^* is the composite modulus of the contacting bodies given by Equation (2.2) and $1/R$ is the relative curvature given by Equation (2.3), where E and ν have the usual meanings of Young's modulus and Poisson's ratio respectively (with the subscripts referring to the two bodies in contact).

$$\frac{1}{E^*} \equiv \frac{1-\nu_1^2}{E_1} + \frac{1-\nu_2^2}{E_2} \tag{2.2}$$

$$\frac{1}{R} \equiv \frac{1}{R_1} + \frac{1}{R_2} \tag{2.3}$$

The normal pressure distribution, $p(x)$, over the contact is then found to be

$$p(x) = \frac{2P}{\pi a}\left(1 - \frac{x^2}{a^2}\right)^{\frac{1}{2}} \tag{2.4}$$

It can be seen that the contact pressure reaches a maximum at the centre of the contact ($x = 0$) and falls to zero at the edge of the contact ($x = a$). The maximum pressure, p_0, is then

$$p_0 = \frac{2P}{\pi a} = \left(\frac{PE^*}{\pi R}\right)^{\frac{1}{2}} \tag{2.5}$$

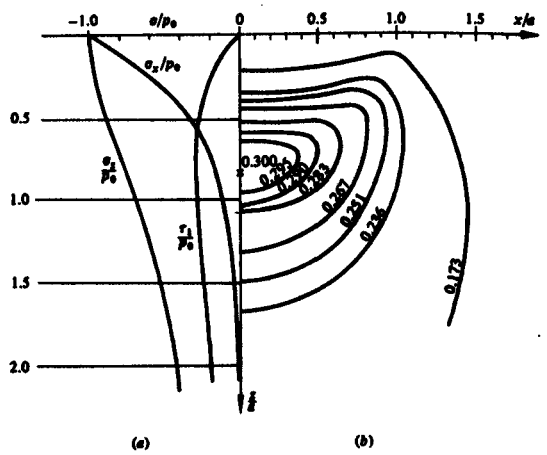

Figure 2.3: (a) subsurface stresses along the axis of symmetry and (b) contours of the principal shear stress, τ_1, for the contact of cylinders [30].

the stress distribution within the bodies can be found to be

$$\sigma_x = -\frac{p_0}{a}\left\{\left(a^2+2z^2\right)\left(a^2+z^2\right)^{-\frac{1}{2}} - 2z\right\} \tag{2.6}$$

$$\sigma_z = -p_0 a\left(a^2+z^2\right)^{-\frac{1}{2}} \tag{2.7}$$

and since these are principal stresses, the principal shear stress, which governs the onset of yield (using the Tresca criterion), is

$$\tau_1 = \frac{p_0}{a}\left\{z - z^2\left(a^2+z^2\right)^{-\frac{1}{2}}\right\} \tag{2.8}$$

from which it can be found that the maximum shear stress is $\tau_1^* = 0.30 p_0$, located at $z = 0.78a$ (Figure 2.3).

If the situation is expanded to one where a tangential force Q per unit length is applied, where $Q < \mu P$ such that there is no gross slip, then there will be a distribution of tangential surface tractions

$$q(x) = \frac{Q}{\pi\left(a^2-x^2\right)^{\frac{1}{2}}} \tag{2.9}$$

It is important to note that this solution requires an infinite surface traction at the edge of the contact ($x = a$). In reality, this stress must be relieved; Mindlin [28] assumed that the shear traction must be limited by friction i.e., $q(x) \leq \mu p(x)$ where μ is the coefficient of friction and $p(x)$ is the normal pressure distribution as defined in Equation (2.4). In order to satisfy this condition, the surfaces must slip relative to each other in a zone starting at the edge of the contact (where otherwise infinite tractions are required) and penetrating toward the centre of the contact until $x = \pm c$,

where c is given by

$$\frac{c}{a} = \left(1 - \frac{Q}{\mu P}\right)^{\frac{1}{2}} \tag{2.10}$$

The tangential surface tractions, $q(x)$, within the central stick region and bounding slip regions are given by

$$q(x) = \begin{cases} \mu p_0 \left(1 - \dfrac{x^2}{a^2}\right)^{\frac{1}{2}} & \text{for } c \le |x| \le a \\ \mu p_0 \left\{ \left(1 - \dfrac{x^2}{a^2}\right)^{\frac{1}{2}} - \dfrac{c}{a}\left(1 - \dfrac{x^2}{c^2}\right)^{\frac{1}{2}} \right\} & \text{for } -c \le x \le c \end{cases} \tag{2.11}$$

As Q is increased, the central stick zone ($-c \le x \le c$) will diminish as the bounding regions of slip penetrate deeper into the contact. When Q approaches the critical magnitude of $Q^* = \mu P$, then $c \to 0$ and the contact will be in a state of incipient slip, no longer one of partial slip. At this point, the tangential traction is simply

$$q(x) = \pm \mu p_0 \left(1 - \frac{x^2}{a^2}\right)^{\frac{1}{2}} \tag{2.12}$$

and the resultant surface stresses, $\bar{\sigma}_x, \bar{\sigma}_z$ and $\bar{\tau}_{xz}$, due to the combined pressure and frictional tractions are given by

$$\bar{\sigma}_x = -p_0 \left\{ \left(1 - \frac{x^2}{a^2}\right)^{\frac{1}{2}} + \frac{2\mu x}{a} \right\} \tag{2.13}$$

$$\bar{\sigma}_z = -p_0 \left\{ \left(1 - \frac{x^2}{a^2}\right)^{\frac{1}{2}} \right\} \tag{2.14}$$

$$\bar{\tau}_{xz} = -\mu p_0 \left\{ \left(1 - \frac{x^2}{a^2}\right)^{\frac{1}{2}} + \frac{2\mu x}{a} \right\} \tag{2.15}$$

The resultant principal shear stress, τ_1, under the action of the contact pressure and surface traction is plotted in Figure 2.4. Compared to the simple Hertzian case, it can be seen that the maximum principal shear stress is closer to the surface. Yield may also occur at the surface if the coefficient of friction is high enough; it is found that for $\mu < 0.25$, sub-surface yield occurs first (by application of the Tresca criterion) [30].

Mindlin and Deresiewicz [29] published a second paper in 1953, "Elastic Spheres in Contact under Oblique Forces", considering the application of an alternating tangential force (a fretting contact). It was shown that if Q alternates between $\pm Q^* \le \mu P$ such that incipient gross sliding does not occur, then the case is similar to the partial slip situation examined above: there will first be slip in a region penetrating to $x = c$ in the positive direction and then again in the negative direction. If Q is plotted against δ, where δ is the displacement of the centre of the cylinder relative to some remote point in the flat body, a symmetrical hysteresis loop will be described as in Figure 2.5; the

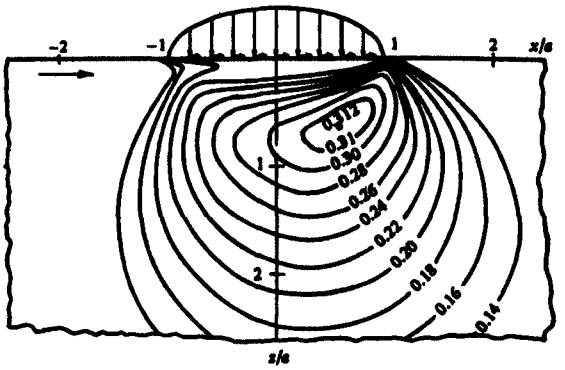

Figure 2.4: Principal shear stress contours, τ_1, under a sliding contact with $\mu = 0.2$ [30].

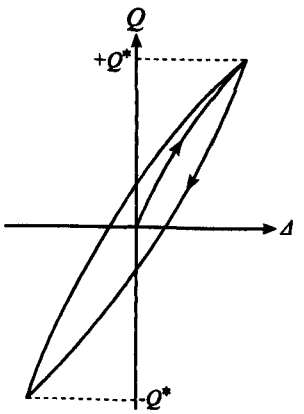

Figure 2.5: Partial-slip hysteresis loop resulting from the application of an alternating tangential load of amplitude Q^* to a Hertzian contact after Mindlin and Deresiewicz [29].

area enclosed by the loop is the energy loss per cycle and is found to be proportional to $(Q^*)^3$.

Johnson [31] conducted an experimental investigation of a point contact (hard steel against steel) under a reciprocating tangential load. He found good quantitative agreement with Mindlin's theoretical analysis of the elastic contact. However, measurements of the energy loss per fretting cycle were found to be larger than predicted. It was suggested that this was due to additional energy being lost in plastic deformation of the asperity junctions that exist between any real contacting surfaces.

2.3.2 Fretting maps

Perhaps one of the more significant developments in the study of fretting has been the development of fretting maps. It is impossible to understand a fretting map without understanding the contact mechanics as first described by Mindlin and Deresiewicz [29], reviewed earlier (Section 2.3.1, Page 5): the central concept is that when a normally loaded, non-conforming contact experiences a tangential load, there will be an outer region of the contact experiencing slip and a central zone which is stuck (together, these are termed a partial slip condition). The stuck zone will decrease in

size until the tangential force is equal to the product of the coefficient of friction (COF) and the normal load, whereby incipient slip will occur over the whole contact; this condition is known as gross sliding.

In 1988, Vingsbo and Söderberg [20] introduced the concept of fretting maps. By comparing force-displacement plots (fretting loops) recorded during fretting experiments (using a ball-on-flat geometry) and subsequent metallographic examination of the wear scars, they were able to identify three distinct fretting regimes characterized by the stick-slip behaviour of the contact:

1. *Stick:* Characteristic of very low displacement amplitudes. The wear scar shows no visible damage beyond limited plastic shearing of individual asperities with no indication of material damage in between.

2. *Stick-slip:* At higher displacement amplitudes, a central stick area and surrounding slip-annulus is seen as would be expected from the Mindlin model. There is evidence of plastic shearing of the asperities in the central stick region as in the stick case, but in the slip annulus, there is considerable crack formation.

3. *Gross sliding:* The entire wear scar shows extensive plastic shear with visible sliding marks.

Examples of the wear scars and fretting loops observed under these fretting regimes are presented in Figure 2.6. It is interesting to note that Mindlin's theory [29] predicts some micro-slip under any tangential load; this implies that the apparently closed fretting loop characteristic of the stick regime only *appears* to be closed due to the resolution of the measuring equipment. From the scanning electron microscopy (SEM) images, it is apparent that micro-slip is occurring but is mainly being accommodated in the local asperity-asperity contacts by elastic-plastic deformation.

Over a series of experiments, it is possible to map the fretting regime transitions in terms of two variables. Typically, normal load and displacement amplitude are selected, although it is also feasible to produce similar maps for frequency or any other variable which may influence the contact sliding condition; examples of these fretting maps are given in Figure 2.7.

In 1992, Zhou et al. [32] expanded the concept of fretting maps. They termed the type of map introduced by Vingsbo and Söderberg a running condition fretting map (RCFM), which plots the fretting regime against the fretting conditions (e.g., load and displacement amplitude). Additionally, they plotted the mechanism of surface degradation against the same axes. The resultant map was termed a material response fretting map (MRFM)—such a map can only be plotted after subsequent examination of the wear scars. It was found that three types of material response could be identified: no degradation, cracking and particle detachment (Figure 2.8b). Although it was found that MRFMs cannot be directly superimposed on RCFMs, a correlation between the fretting regime and surface degradation was observed. While cracking and particle

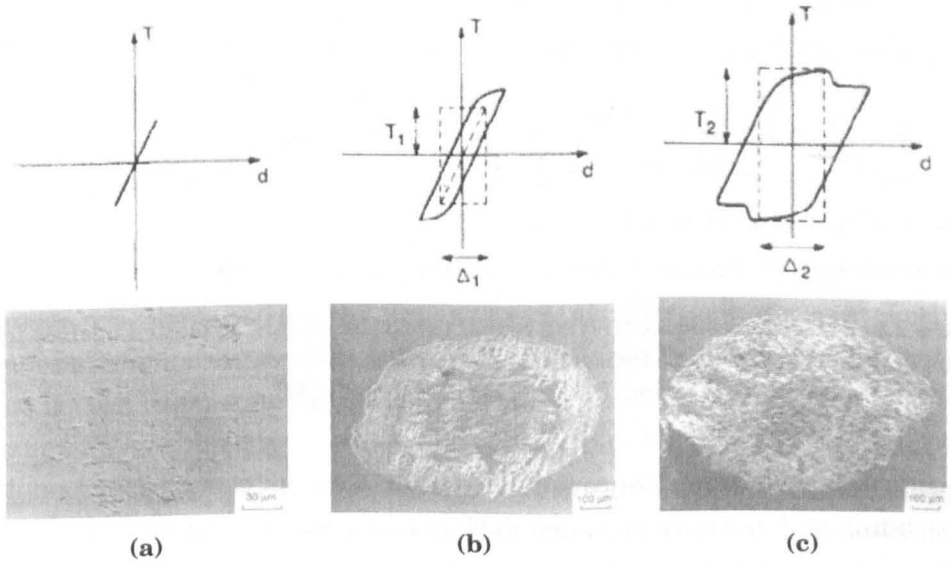

Figure 2.6: Examples of characteristic fretting loops (plotted in terms of tangential force, T, and displacement, d) and wear scars under: (a) stick, (b) stick-slip and (c) gross sliding fretting regimes. Δ_1, T_1 is the displacement amplitude and tangential force at the transition to stick-slip. Δ_2, T_2 are the critical displacement and tangential force values corresponding to the transition to gross sliding [20].

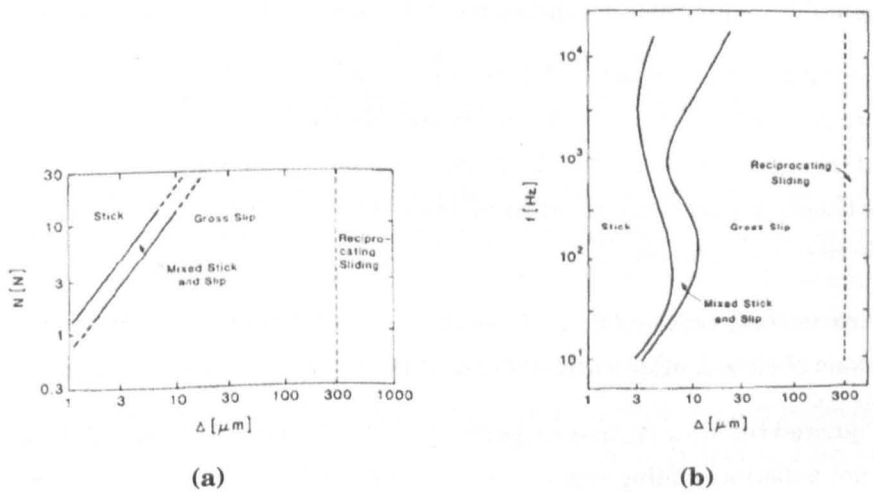

Figure 2.7: Fretting maps, known as running condition fretting maps (RCFMs), in terms of: (a) normal force-displacement and (b) frequency-displacement [20].

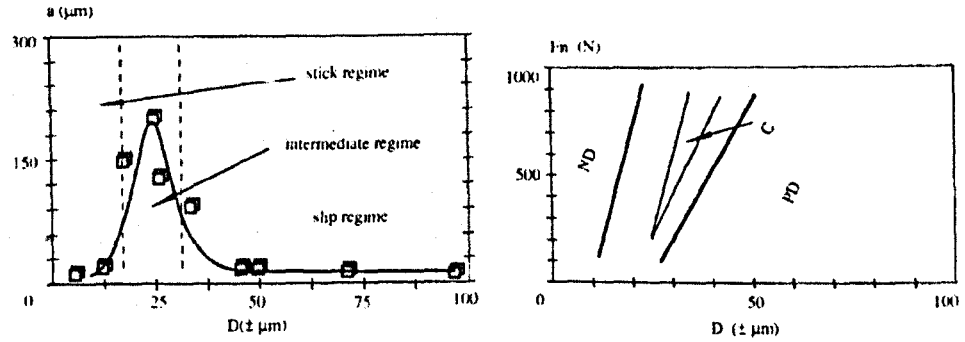

Figure 2.8: Material response fretting maps: (a) Crack length, a, plotted against fretting stroke, D, with the slip regime indicated (b) Map indicating the different degradation domains: ND, no degradation; C, cracking; PD, particle detachment [32].

detachment occurred simultaneously, particle detachment was predominant during gross-sliding and cracking prevailed during a new regime they termed the mixed fretting regime (MFR). This is illustrated in Figure 2.8a.

Up to this point in the discussion, the fretting regimes have been described in terms of the Mindlin model and as presented by Vingsbo and Söderberg [20]. These regimes, possibly naively, had been assumed to be stable i.e., not a function of slid distance. However, Zhou et al. [32] did not find the evolution to be so simple and described a slip regime termed the mixed fretting regime (MFR), which often occurs before gross-sliding, where the fretting loop is unstable with periods where an elliptical fretting loop is observed (similar to Figure 2.6b) and periods where an open fretting loop is observed (similar to Figure 2.6c). In a subsequent paper, Zhou and Vincent [33] described the regimes (as a function of increasing displacement amplitude) which occur at smaller displacement amplitudes than gross-sliding as follows:

1. *Sticking regime:* Associated with a nominally closed fretting loop where the contact is behaving as described by the Mindlin contact mechanics i.e., some central region of the contact is stuck while micro-slip occurs in the outer zones. The chosen terminology of "sticking" is somewhat confusing since this is normally referred to as "partial slip".

2. *Mixed fretting regime (MFR):* Characterised by an unstable fretting loop with periods of closed, elliptically-shaped loops and periods of fully open loops.

They ignored the *stick* regime suggested by Vingsbo and Söderberg [20], suggesting that it is not a distinct sliding regime i.e., in agreement with Mindlin, they argued that there is *always* some outer region of the contact experiencing slip, and therefore no *stick* regime exists in reality. It was suggested that the unstable behaviour observed in the MFR is due to the evolution of the wearing surfaces and generation of loose debris within the contact: initially, the contact may be in gross-sliding due to the lubricating

effect of the surface oxide and contaminant films; however, these will rapidly disperse and as a result, the tangential force will increase as regions of metallic (adhesive) contact form; due to accumulated damage, wear debris will be released, a layer of which can provide a low shear interface, relieving the tangential force and allowing a period of gross sliding. This proposed mechanism was supported by observations made during the testing of 9005 Al-Li where it was found that a MFR could not be established due to the rapid generation of debris [33].

Later work by Hager et al. [34] on Ti6Al4V produced further evidence which supported the overall mechanism, suggesting that either the adhesive junctions which are formed will fatigue and rupture forming debris particles, or that a layer of material with a tribologically transformed structure (TTS) (see Section 2.5.3, Page 23) will form and breakdown to generate the debris.

To quantify the damage processes operating within the MFR, Heredia and Fouvry [35] assessed the proportion of gross-sliding cycles occurring. They termed this parameter $\%GS$ (it should be noted that this is a fraction, *not* a percentage), and showed that it increases monotonically, and smoothly, with increasing applied displacement (Figure 2.9). As such, they demonstrated that while the sliding condition in the MFR is unstable, the transition through the regime is smooth and continuous, thus allowing characterisation of the damage occurring in relation to any regime governing parameter (e.g., load or applied displacement). By varying the applied displacement, at a constant load, it was found that wear was activated only when $\%GS \geq 0.95$. It was suggested that for smaller values of $\%GS$—while energy was being dissipated in the interface and generating wear particles—there was insufficient relative displacement to enable the debris to escape and hence facilitate a continuous wear process. In contrast, cracking within the contact was found to reach a significant maximum at $\%GS \approx 0.7$ (see Figure 2.9). The reported crack length (as a function of displacement amplitude) is in good agreement with the generally accepted reduction in fatigue life associated with applied displacement and slip regime as shown in Figure 2.12 (discussed in Section 2.4, Page 17).

The potential usefulness of fretting maps is clear: they allow tests by different workers to be quantitatively compared since the operative fretting regime can be clearly identified [36]. In fact, as has been shown by the correlation between the mode of surface degradation and the fretting regime [32], it may be impossible to make any meaningful comparison without knowing the location of the test with respect to the regime boundaries. Ultimately, fretting maps can be a practical aid to designers and may be expanded to more dimensions rather than just those of load and stroke [36, 37].

Description of a fretting loop

Before progressing further, it is useful to define the terminology employed in descriptions of fretting, and in particular, the terminology used to describe fretting loops

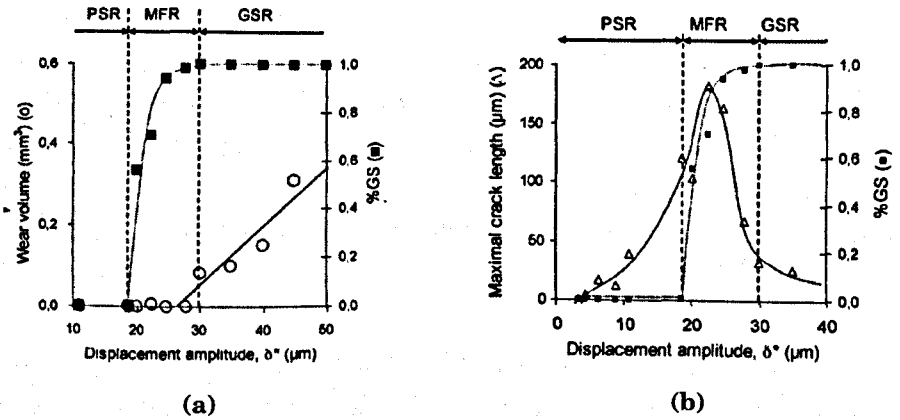

Figure 2.9: Evolution of the *%GS* parameter, with (a) wear volume and (b) maximum crack length, as a function of displacement amplitude [35].

(Figure 2.10). Throughout the literature, a number of terms are used to describe the displacement imposed between fretting specimens; in this work, the applied reciprocating displacement at any point in the cycle is given the symbol Δ, with Δ^* referring to its amplitude.

It is important to recognize that Δ is measured at some point remote from the contact and includes any compliance in the system between the points at which it is measured e.g., that of the specimen bulk itself and any fixturing. The sliding amplitude between the specimens, δ^*, is not easily measured (although it may be possible with modern optical techniques), and is commonly determined by post-processing of the force and displacement data. Depending on the loading conditions and design of the test apparatus, the slid distance per cycle ($4 \times \delta^*$) may be much less than the distance moved by a remote measuring point per cycle ($4 \times \Delta^*$). Additionally, for a given applied displacement, the resultant slid distance (even with the same COF) will be less for higher normal loads due to a greater proportion of Δ being accommodated by the system compliance.

The area enclosed within the loop is the energy dissipated in the contact (E_d) due to micro-slip and gross sliding of the contact. The total energy input into the system is described by the outer box and given by $E_t = 4Q^*\Delta^*$. Of the total energy put into the system, only a proportion is dissipated in the contact (E_d); the rest (E_e) is stored elastically by the system compliance.

2.3.3 Sliding regime transition criteria

Partial slip to gross sliding

The transitions from partial slip to gross sliding and gross sliding to reciprocating sliding are key to the fretting mapping concept, and consequently to the understanding and prediction of the sliding regimes and associated damage mechanisms (Section 2.3.2, Page 9).

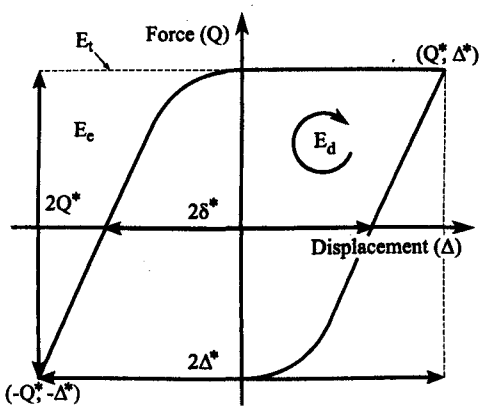

Figure 2.10: Diagram of a fretting loop highlighting the key parameters: applied displacement amplitude (Δ^*), tangential force amplitude (Q^*), sliding amplitude (δ^*) and the dissipated energy (E_d).

Whilst the principles of fretting mapping are relatively simple, experimentally the regime boundaries are harder to determine. Typically, a qualitative approach using characteristic loop shapes or changes in the force trace to identify the regime of operation is used [20, 32, 38, 39]. Nonetheless, Vingsbo and Schön [40] developed force energy displacement diagrams (FEDs) and found that the gross slip transition was always associated with a change in the energy dissipated per cycle. Fouvry et al. [21, 41] also considered the partial slip to gross sliding transition and developed three further non dimensional parameters:

1. *The energy ratio, A:* defined as the ratio between the energy dissipated in the contact and the total energy input: $A = E_d/E_t$. A critical value, $A_t = 0.2$, was found such that for $A < A_t$, the displacement condition is one of partial slip.

2. *The sliding ratio, D:* the ratio between the cycle aperture δ^* and the displacement amplitude, Δ^*: $D = \delta^*/\Delta^*$. A critical value of $D_t \approx 0.26$ is found at the gross-sliding transition.

3. *The system free transition criterion (SFTC), B:* defined as $B = E_d/4Q^*\delta^*$. The gross slip transition is found occur when $B = B_t \approx 0.77$.

Fouvry et al. [41] compared the criteria and whilst the SFTC is independent of the compliance of the system, it was found to be a less sensitive discriminator as it relied on both the variables δ^* and E_d. In addition, criteria based on differentiating $Q^* = f(\delta^*)$ and $E_d = f(\delta^*)$ were investigated. It was found that it was possible to locate the expected discontinuities at the gross sliding transition; however, in order to do so required significant smoothing of the data to avoid the natural amplification of noise by the differentiation.

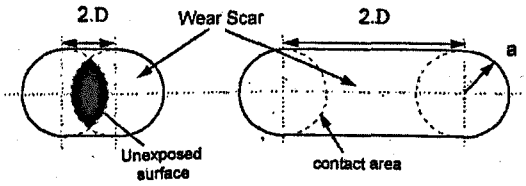

Figure 2.11: Showing the case of fretting, where $\delta^*/a < 1$, and the case of reciprocating sliding, where $\delta^*/a \geq 1$. Where the sliding amplitude (δ^*) is D and the Hertzian contact radius is a [21].

Gross sliding to reciprocating sliding

The transition from gross-sliding-fretting to reciprocating-sliding-wear is of particular interest, since it serves to define the phenomena of fretting. A qualitative difference between the wear modes may be that reciprocating sliding is a multi-pass system—and debris may be reincorporated into the wear track; in contrast, in fretting, due to the small displacements, once debris is ejected from the contact it has no further interaction with the system.

A typical definition of fretting is simply "damage occurring from *small* amplitude reciprocating (relative) motion between two surfaces". The term "small" is clearly unsatisfactory and the use of a dimensional parameter makes it strongly dependent on the system (compliance, scale, load, materials etc.); consequently many displacement amplitudes, ranging from 25 to 300 μm, have been cited in the literature [1, 20, 42–44]. In experimental work, the displacement amplitude at the transition is often defined by considering the wear rate: in fretting, it is generally accepted that the wear rate increases in severity with increasing stroke [3, 20, 43, 45, 46]; this is in contrast to behaviour observed in reciprocating sliding, where the wear rate is constant with displacement amplitude [20, 44] (Figure 2.12).

Some workers in the field have attempted to better define a fretting contact. For example, Fouvry et al. [21] suggested that the "closed" nature of a fretting contact is the differentiator between it and a sliding couple. They proposed that the ratio between the slip amplitude, δ^*, and the Hertzian contact radius, a, could be used as a criterion, such that for $\delta^*/a < 1$, some area of the scar is never exposed and the contact is described as fretting; conversely, for $\delta^*/a \geq 1$, all areas of the scar are exposed at some point during a cycle and the contact is described as being in reciprocating sliding (Figure 2.11). This is a useful parameter since it is non dimensional and can offer a comparison between any experimental set up.

However, in fretting tests on steel (using a $\varnothing$ 60 mm ball on flat configuration), Chen and Zhou [44] found the fretting to reciprocating sliding transition to occur at $\delta = 100$ μm (by identifying the slip amplitude at which the wear wear rate became constant); this value is significantly lower than the 388 μm predicted using the method of Fouvry et al. [21]. Unfortunately, it is not clear if Chen and Zhou [44] used the actual sliding amplitude (δ^*), as indicated by Fouvry et al. [21] or the applied displacement

amplitude (Δ^*). Moreover, the initial Hertzian contact area, used in the determination of the parameter will be immediately modified by any wear.

Later work by Varenberg et al. [47, 48] also considered the transition between reciprocating sliding wear and fretting wear. By dimensional analysis they found that the sliding ratio, s (which Fouvry et al. [21] termed D):

$$s = \frac{\delta^*}{\Delta^*} \tag{2.16}$$

is a function of the dimensionless similarity criterion, α:

$$\alpha = \frac{\Delta^* S_c}{P} \tag{2.17}$$

where S_c is the elastic compliance of the system (i.e., the elastic slope of the fretting loop) and Δ^* and P take their normal meanings of applied displacement amplitude and normal load respectively. Empirically, by considering two systems of very different scales, they found the relationship between s and and α to be

$$s = 1 - \frac{1}{2\alpha} \quad \text{for } \alpha \geq 0.5 \tag{2.18}$$

Using this method, Varenberg et al. [47] found that partial slip existed when $0.5 \leq \alpha < 0.6$, gross slip when $\alpha > 0.8$ and reciprocating sliding when $\alpha > 11$. Additionally, Varenberg et al. [47] proposed a new definition of fretting, suggesting "fretting is a relative cyclic motion between surfaces, having a non uniform distribution of local relative displacement at their contact". While this is a somewhat more precise definition than "small" and also is essentially the same as Fouvry's ratio of sliding amplitude to contact radius, it does not account for a flat on flat contact where there is no partial slip and hence relative displacement distribution.

2.4 Fretting damage: wear and fatigue

It has long been recognised that fretting may manifest itself as fretting fatigue or fretting wear [1, 49]. However, identification of which of these modes is operative is not simply a distinction between material loss or crack formation, as cracking is often observed under "wear" conditions [32]. Fretting damage is typically termed fretting wear when the failure is one of loss of fit or seizure due to the entrapment of debris; alternatively, it is termed fretting fatigue when the fretting action is associated with a reduction in the expected fatigue life of a component.

The similarities between fretting fatigue and fretting wear were discussed by Bill [3]. He showed that changes in parameters (such as temperature, slip amplitude and frequency) which promoted wear also promoted fatigue. However, a more complex relationship between the fretting wear and fretting fatigue processes was highlighted by Vingsbo and Söderberg [20]. After conducting a survey of the literature, they

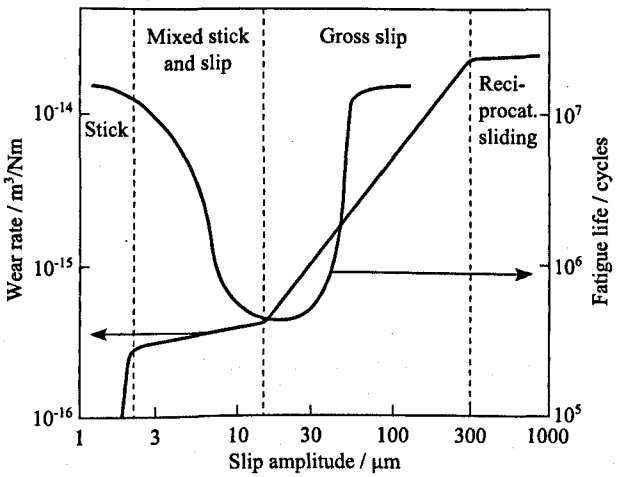

Figure 2.12: Illustration of the relationship between fatigue life, fretting wear rate and the applied displacement amplitude and resulting slip regime [20].

produced a plot of fatigue life and wear rate against fretting stroke (and slip regime) as shown in Figure 2.12. From this figure, it can be seen that the region of the transition between the mixed-slip regime and gross sliding is of particular concern in terms of fatigue life, with the fatigue life recovering both at low slip amplitudes (corresponding to full stick conditions) and at high slip amplitudes (corresponding to gross sliding). From subsequent work (see Section 2.3.2, Page 9), it is known that the transition from partial slip to gross sliding is unstable and is termed the MFR. However, for the following discussion, it is adequate to assume that the transition from partial-slip to gross-sliding is sequential.

Considering the contact mechanics of a fretting contact (Section 2.3.1, Page 5), it is not surprising that within the partial slip regime, cracking is promoted as the slip amplitude increases (and hence fatigue life reduced): it is clearly seen from the Mindlin model that the tangential force amplitude, which governs the stresses, increases directly with the applied stroke. This situation continues until the transition to gross sliding when the tangential force is limited by friction (μP).

The subsequent recovery of the fatigue life, with further increase of the applied displacement amplitude (through the gross sliding regime), has typically been attributed to the growing predominance of material removal (Section 2.3.2, Page 9) i.e., researchers have suggested that any cracks which are nucleated will be quickly eliminated by the increased wear rate [20, 50]. However, modelling work by Ding et al. [51] and Madge et al. [52] has shown that the promotion of wear during gross sliding may have a greater influence through stress re-distribution rather than directly eliminating cracks. Ding et al. [51] showed that for a non-conforming contact (common in both practical applications and laboratory tests associated with fretting), a high wear rate results in the contact-patch rapidly expanding, enveloping material previously at the contact edges and leaving it in a state of compression which is prohibitive to crack nucleation or growth. Moreover, tensile stresses outside the contact patch are reduced

in magnitude as the contact patch increases in size.

2.5 Fretting mechanisms

Whilst there is no commonly defined "fretting wear mechanism", three broad sequential stages have been identified [2, 53–55]:

1. *Initial stage:* characterized by adhesion and resultant metal transfer and significant roughening of the surface. This results in a high COF, but little debris is generated during this phase.

2. *Intermediate stage:* beds of compacted oxide begin to form, which, depending on the hardness of the oxide, may start to cause abrasive wear. The beds act to separate the fretting surfaces, reducing metal-metal contact and adhesion, and hence the COF.

3. *Steady state:* the COF is steady, and lower than in the earlier stages. The oxide beds which began to form in the intermediate stage become dynamically stable, and the wear process can be considered to be one of continuous formation and ejection of debris.

2.5.1 Initial stage

Metallic surfaces are inevitably covered by surface films of oxide, absorbed gas and contaminants [56]; these films are disrupted as the initial asperity contacts plastically deform under load [1]. This has been demonstrated by electrical resistance measurements across the contact where the initial resistance was observed to fall rapidly as the specimens "bed in" [57].

In the initial stages of fretting, the mechanisms of adhesion and ploughing are reasonably well agreed upon in the literature and are supported by experimental observations [55]. Godfrey and Bailey [58, 59] observed wear scars indicative of significant adhesion in the early stages of fretting for several materials including steel, iron, copper and glass combinations. Halliday and Hirst [45] measured the coefficient of friction between mild steel specimens at several load and stroke combinations. In all cases, they observed the characteristic peak in COF during the initial stages of fretting, indicative of the occurrence of adhesive wear. Berthier et al. [60] produced more detailed measurements of the development of the COF with time, clearly showing the transition from interaction of the surface films to first body contact and then to a situation with an increasing influence of the accumulated debris.

2.5.2 Intermediate stage

The mechanisms of production, and then action, of the oxide debris in the intermediate and steady state phases are less well agreed upon. Under normal laboratory conditions,

the debris resulting from the fretting of steel surfaces is a finely divided red-brown iron oxide, identified as α-Fe_2O_3, along with traces of metallic debris [19, 45, 55]. Similarly, the debris produced for other oxidising materials is found to be an oxide, usually that associated with the final oxidation state for the material [59]. For example, the fretting of aluminium was found to produce a black debris containing Al_2O_3, and up to 23 % metallic aluminium [61]. When fretting copper, Godfrey and Bailey [58] found the initial debris produced to be metallic with an increasing proportion of CuO as the test progressed.

The particle size of fretting debris has been reported over a range of values. Feng and Rightmire [55] found metallic iron particles of about 20 μm, while the oxide particles were on average 0.25 μm. Halliday and Hirst [45] reported the metallic debris to range from 50 to 0.3 μm, with the initial oxide debris being from 1 to 0.1 μm in diameter; as the test progressed, they found that the oxide debris became finer and suggested it may be as small as 0.01 μm in diameter. Observations by Bill [62] of debris produced by the fretting of iron in dry air confirmed that the debris can be extremely small, typically being less than 0.005 μm in diameter. When examining the fretting debris from ammunition crates in a ship's hold, Andrew et al. [61] found the average particle size to be 0.15 μm and the median size to be 0.10 μm.

The importance of both the mechanical, and chemical (oxidational) aspect of fretting has been recognised since the early studies by Feng and Uhlig [63], Uhlig [4], and Halliday and Hirst [45]. The influence of the oxidational aspect is highlighted by the significant change in damage observed during fretting in a non-oxidising environment, either under an inert atmosphere or vacuum [4, 63]. One of the first fretting mechanisms proposed to account for the production of oxide was that of Tomlinson [18]; in his 1927 paper, he suggested that the fretting action resulted in the plucking of metallic particles from the fretting surfaces, due to "molecular cohesion", which then oxidised spontaneously. However, the first model to attempt to capture the tribo-chemical nature of the process was advanced by Uhlig [4] and has an explicit "chemical factor" and "mechanical factor". The model is described by Equation (2.19), where: W is the specimen weight loss, L is the load, f is the frequency, C is the number of cycles, l is the slip and k_0, k_1 and k_2 are constants.

$$W = \underbrace{(k_0 L^{\frac{1}{2}} - k_1 L)\frac{C}{f}}_{\text{chemical}} + \underbrace{k_2 l L C}_{\text{mechanical}} \tag{2.19}$$

The model is based on asperity interactions; it is supposed that as an asperity moves across a counterface, it will leave a clean track of metal. This track will then immediately begin to oxidise and the oxide will be removed by the next passing asperity—the chemical factor. The asperity can, additionally, interact with the underlying virgin metal, producing metallic wear particles by adhesion and ploughing—the mechanical factor. It is then proposed that the metallic particles would progressively be conver-

ted to iron oxide by a "secondary fretting action", resulting from the attrition of the particles against both themselves and the primary surfaces [4].

The concept that the oxide is produced by metallic debris (itself produced by mechanical deformation of a large number of asperity interactions) being oxidised under the action of fretting is supported by many authors [19, 55, 58, 59, 64, 65]. However, experimental evidence was lacking until Pendlebury [66] fretted iron particles between inert surfaces to produce fine oxide debris; the high observed oxidation rate (compared to oxidation of similar particles with no fretting action) was attributed to the large surface area on which the oxide grows and from which it is repeatedly detached (due to normal wear mechanisms) rather than any grossly abnormal activation energy for oxidation under fretting action.

The relative importance ascribed to the chemical and mechanical aspects has varied between researchers. The work of Quinn [67] places much greater emphasis on the formation of surface oxide films. In contrast, other workers believe that the process can be explained by adhesion, similar to that in uni-directional sliding wear [68]. Suh [69, 70] proposed a wear model based on subsurface dislocation pileups leading to void formations and propagation of sub-surface cracks. It was proposed that cracks grow until a critical length is reached, resulting in the release of a thin flake of metal. Sproles and Duquette [71] and Waterhouse and Taylor [65] both found supporting evidence for Suh's delamination theory of wear. These workers suggested that the traditional (adhesive and abrasive) wear mechanisms often proposed cannot account for the flake-like morphology of metallic fretting debris.

An alternative theory was presented by Zhang et al. [46]. They found that the contact interface is not easily described as a homogeneous metallic substrate with a surface oxide film; in fact, three characteristic layers were observed: *Zone I*, a surface layer of compacted oxide; *Zone II*, a region of severe deformation in which the grains are "comminuted" and orientated in the fretting direction and, *Zone III*, a region of plastic deformation.

Similar microstructural changes to those observed by Zhang et al. [46] have subsequently been found in the fretting of many alloys, such as: steels and cast iron, titanium alloys, aluminium alloys and nickel-alloys. The characteristic zone of modified microstructure is termed the tribologically transformed structure (TTS) [72–74] (a schematic diagram indicating the distribution of the TTS in a fretting scar is shown in Figure 2.13).

The TTS is found to be of the same chemical composition as the underlying bulk material. However, the grains are "ultra-fine" (only of a few tens of nanometres in size) and the hardness is found to be significantly higher than that of the bulk alloy (typically some two to three times higher) [72–75]. Sauger et al. [74] observed significant cracking within the TTS, to such a degree in steels that they described it as appearing to "burst". Investigations by X-ray diffraction [74] have shown that the TTS is formed of the more stable crystallographic phase; in the case of steels, ferrite

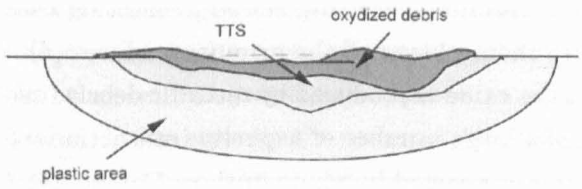

Figure 2.13: Schematic diagram of a cross-section of a fretting scar showing distribution of regions where various damage types predominate [74].

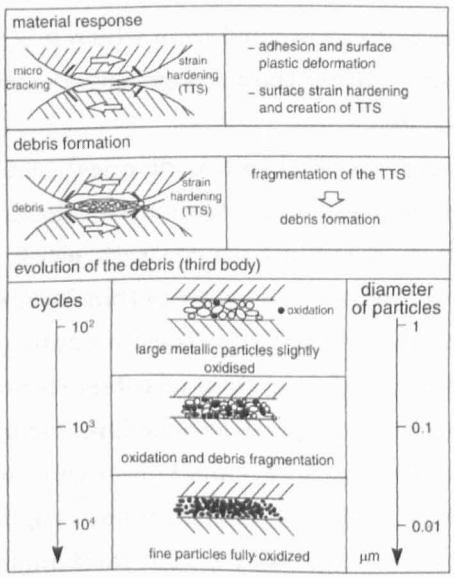

Figure 2.14: Creation and evolution of the third body from the tribologically transformed structure (TTS) [74].

is typically formed regardless of the initial microstructure. While the mechanism of formation of the TTS is not fully understood, it is not believed that the temperature rise within a fretting contact is sufficient to drive the re-crystallization and formation of the TTS. Rather, the mechanism is thought to be driven by repeated high-strain deformation [74–76].

The mechanism of fretting, accounting for the formation of the TTS, is thought to follow several stages (Figure 2.14) [74, 76]. First, the TTS forms rapidly due to the high surface deformation leading to strain hardening. Then, due to its brittle nature, the TTS begins to fragment, forming metallic debris which further fragments and oxidises under the fretting action. The formation and entrapment of the debris leads to a significant reduction in shear stress at the surface due to the third-body effect (discussed in Section 2.5.3, Page 23). Consequently, the TTS formed in the initial stages will be completely consumed after a large number of cycles (explaining why it is rarely reported in an industrial context) and the fretting contact may be considered to be in the steady state.

The observation of high temperature oxides such as α-Fe_2O_3 and recrystallization of surface layers (TTS) in fretting scars has been cited as evidence for high *flash*

temperatures being generated at the fretting surfaces, with values up to 773 K being suggested for fretting conducted under ambient conditions [1, 77–79]. However, doubt has been cast on this hypothesis in light of experiments conducted at low temperatures (133 K) where α-Fe_2O_3 was still produced [63]. Moreover, subsequent experimental work by Sproles and Duquette [80] showed that average asperity temperatures would not exceed 20 K above ambient. More recent work using an infra-red microscope (with a transparent sapphire specimen) similarly found relatively low surface temperature rises, the maximum reported being 130 to 140 K [81].

However, a significant problem with any experimental effort to measure the temperature rise at asperity junctions is resolution. Kennedy [82] found that over 90 % of frictional energy is dissipated within 5 μm of the surface and in experimental work, Vodopivec et al. [83] found small areas of phase transformed material of approximately 5 μm × 1 μm in size. Considering the scale of the expected asperity contacts and the reported experimental evidence, attempts to measure the surface temperature using thermocouples and other methods will at best yield an average value. In a review of the influence of flash temperatures on tribology at low sliding speeds, Kalin [84] concluded that there is evidence that asperity contact temperatures may be significantly higher than the temperature of the apparent contact area. Similarly, modelling of flash temperatures is inconclusive: in a comparison of a number of flash temperature models [85], it was found that the predicted flash temperatures varied dramatically between the models. A high sensitivity to parameters used for the real contact area and thermal conductivity was found, showing a variation of more than 1300 °C.

It is clear that many researchers do not consider that there is strong evidence for high flash temperatures either existing or being the explanation for observed effects; despite this, it is not possible to definitively conclude that high flash-temperatures do not occur at the interface and are the mechanism by which recrystallization (formation of the TTS) occurs.

2.5.3 Steady state: the effect of debris

The accumulation of debris within the fretting contact and subsequent build up of dense oxide beds has been widely reported in the literature [54, 55, 58, 64, 86]. When this occurs, the subsequent tribological behaviour becomes dominated by the presence of trapped wear debris. Experimental work indicates that at this stage, the electrical resistance across the contact is generally high [57], and the coefficient of friction has stabilised [53] (Figure 2.15). Warburton [42] summarised the situation by stating that "in fretting, wear is being thwarted by the products of its own making".

Godet [87, 88] proposed a theory of wear (the third-body approach), analogous to thick-film lubrication theory, where the interposed debris between wearing faces is considered to be critical to the ensuing wear. In this theory, a contact is defined as two "first-bodies" separated by an intermediate film or "third-body". The third-body

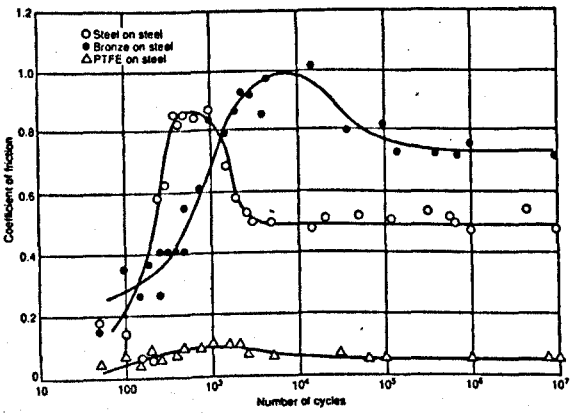

Figure 2.15: Development of coefficient of friction with fretting cycles for three material contact pair types [53].

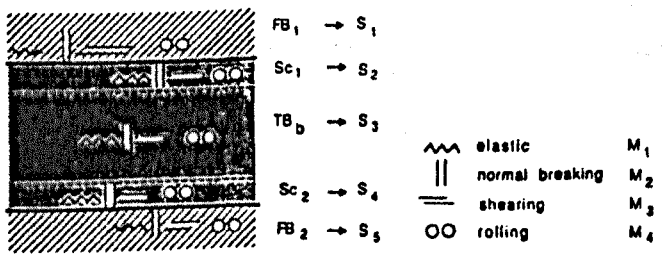

Figure 2.16: Velocity accommodation mechanisms in a three-body contact: FB, first body; TB_b, third-body; S_c, screen; accommodation sites, S_1 to S_5; accommodation modes, M_1 to M_4 [89].

may provide full separation of the first-bodies or only form local struts. However, in either case, the third-body is able to respond kinematically to the velocity difference between the first-bodies. Subsequently, less damage ensues than would result from the asperity-asperity interaction of first-bodies [87].

Figure 2.16 shows a diagram of such a three-body contact. In this definition of a contact, there are five zones where the relative velocity between the first-bodies may be accommodated: within the two first-bodies; at the two interfaces between the two first-bodies and the third-body (termed the screen), and within the third-body itself. At each of these sites: elastic shear, plastic shear, fracture, or rolling may be the mechanisms by which the velocity between the two first-bodies is accommodated [88, 89]. In this third-body approach, the classical wear mechanisms of adhesion, abrasion, fatigue etc. are not considered to be wear, but only particle detachment methods. In order for wear to occur, debris is first detached from a first-body ("source") *and* then ejected from the contact ("sink"). Thus, wear is governed not only by particle detachment but also by the rheology of the third body [88]. This is significantly different to the classical asperity interaction approach and provides a description of the process where the opportunity for wear can be controlled by modifying either (i) the production of particles, (ii) the interaction between the particles and first-bodies or (iii) the ejection

of particulate debris from the contact.

Experimentally, this approach is substantiated by the work of Colombie et al. [64], who introduced artificial oxides and chalk powder into fretting contacts. They demonstrated that the formation of the third-body beds was the governing factor in the determination of first body wear, concluding that the mechanical effect of the debris bed was of more significance than its chemical composition. It was proposed that the third-body was acting as thick film lubricant and wear was found to be governed by the abrasiveness of the third-body. Corresponding results were obtained by Halliday and Hirst [45] where they showed that the initially high COF could be restored by removing debris from the contact in open-and-shut tests. However, they concluded that whilst the debris may be carrying some of the load, the metal-metal (first body) interaction may not be completely eliminated by the existence of the debris bed [45].

Wear still occurs once the debris-beds are formed. It has been proposed that debris bed delamination will continue [65, 90], and that abrasion due to the presence of the debris will occur [55]. When Pendlebury [57] measured the electrical contact resistance throughout long duration fretting tests, he found evidence of continued metal-metal contact and concluded that the primary wear mechanism continued to be one of adhesion. Kayaba and Iwabuchi [90] determined that debris can both be beneficial, and protect the first bodies from wear, or it can enhance wear due to increased abrasion: when fretting a hard specimen against a softer one, they found that hard oxide debris could become compacted on the softer surface and abrade the opposing surface. After further work (involving the artificial supply of oxide to a fretting contact), Iwabuchi [91] concluded that whether the presence of oxide debris is advantageous or not depends on the tendency to form compacted beds, and it was shown that the combination of load and stroke in fretting would govern the formation of such protective beds (Figure 2.17). Where the supply of oxide into the fretting contact was found to be detrimental, it was attributed to increased abrasion during the initial and intermediate stages of fretting. Similar concepts were used to explain the behaviour observed by Varenberg et al. [92] who fretted specimens prepared with micro-pores (which facilitated the removal of debris from the contact); when the dominant wear mechanism was adhesion, then the retained oxide debris was found to reduce wear (by acting as a solid lubricant); conversely when abrasion was dominant, the retained oxide debris enhanced the rate of wear.

However, similar findings were not apparent in studies conducted on a unidirectional sliding interface: the supply of oxide particles was found to universally reduce the running-in period and promote the transition to mild wear [93, 94]. This was attributed to the increased ability of the debris to escape from the fretting contact zone (cylinder-on-flat as opposed to a flat-on-flat contact) [91]. These findings are in agreement with those of Berthier et al. [60], who found that fretting was primarily controlled by the escape of debris from the contact and hence could be considered a "sink" rather than "source" problem.

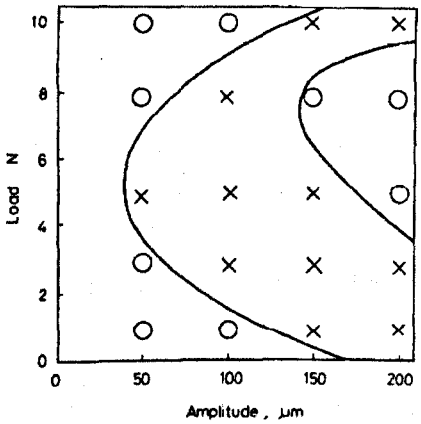

Figure 2.17: Map of the effectiveness of fretting wear reduction by the external supply of oxide particles: ○ beneficial effect, ×, detrimental effect [91].

2.6 Parameters affecting fretting

As many as fifty parameters have been cited as influencing the fretting process; however, normal load, displacement amplitude and the coefficient of friction are generally accepted as the primary mechanical variables [5]. The severity and mechanism of fretting will depend additionally on the environment, materials and contact conditions and the interaction between these and the primary variables [62].

2.6.1 Contact conditions

Load

It is difficult to discuss the effects of load and displacement on fretting behaviour separately, as combined they will determine the sliding regime and hence, to a large extent, the damage mechanism (Section 2.3.2, Page 9 and Section 2.3.3, Page 14). Additionally, increasing the load leads to a greater amount of the applied displacement being accommodated by elastic deformation of the test fixtures etc. and hence leads to less sliding at the contact (Section 2.3.2, Page 13). Such factors led to ambiguity in early studies on the effect of load on fretting wear, with some published results showing an increase in wear with increasing load [2, 95], others finding no effect [96], and others finding a decrease in wear with increasing load [97]. However, later work found common agreement that fretting wear was directly proportional to load [1, 62, 63, 95, 98]. Waterhouse [53] summarised the results with the observation that, as fretting only occurs at the contacting points and the real contact area is proportional to the load, then it would be expected that the fretting wear is also proportional to the load. However, recent work by Mary et al. [99] indicates that the relationship between normal load and fretting wear may not be simple; they found a discontinuity in the wear behaviour between a Ti17 punch and a CuNiIn coated Ti6242 plane at a critical contact pressure. They reported that a predominantly abrasive wear mechanism

operated below the critical pressure threshold, whilst above this threshold, a more severe, adhesive mechanism was activated.

Displacement amplitude

As already discussed (Section 2.3.2, Page 9 and Section 2.3.3, Page 14), the sliding regime and consequently the damage mechanism are governed by the combination of the normal load and applied displacement. However, it is generally accepted that the severity (i.e., rate) of fretting wear is found to increase with stroke [20, 43, 44, 46]; this is in contrast to reciprocating sliding (where the wear rate is independent of sliding amplitude) (Figure 2.12, Page 18).

A common result of many of the early studies was a critical transition in the wear rate between a low rate at small slip amplitudes and a higher rate above some critical value. In the context of the subsequent development of fretting mapping, it is now clear that in many cases, this was in fact the transition between sliding regimes (Section 2.3.2, Page 9 and Section 2.3.3, Page 14). In other cases, all of the applied displacement may have been accommodated by elastic deformation of the test machine i.e., an important distinction should be drawn between the displacement amplitude, measured at some necessarily distant point from the contact (termed Δ^* in this work), and the *actual* sliding amplitude at the contact (δ^* in this work).

A second critical transition, dependent on the sliding amplitude, is the change to reciprocating sliding. Many values, ranging from 25 to 300 μm, have been cited in the literature for this transition [1, 20, 43, 44, 46]. In general, these researchers have used a change to a constant wear coefficient (with displacement amplitude) as the transition criterion.

Frequency

From the work of Feng and Uhlig [63] and Uhlig et al. [95], it appears that at low frequencies (<16 Hz), fretting shows some frequency dependency, with higher wear at a lower frequency. By conducting fretting experiments on steel surfaces in a nitrogen atmosphere (where no frequency dependency was found), it was shown that the observed effects were of a chemical nature and hence time dependent [63, 95]. Uhlig [4] later developed a model to account for the effect; he proposed a mechanism where an oxide film would grow on the surface (of a thickness proportional to the period of the cycle) and be scraped off by the return stroke of the counter face (see Section 2.5.2, Page 19).

At very low frequencies (0.1, 1 and 5 Hz), Berthier et al. [100] found that there was a material dependent frequency effect. Subsurface damage and unstable friction logs were found at frequencies higher than 0.1 Hz. They postulated that this was due to the kinematics of the debris generated (which they proposed was more likely to be ejected

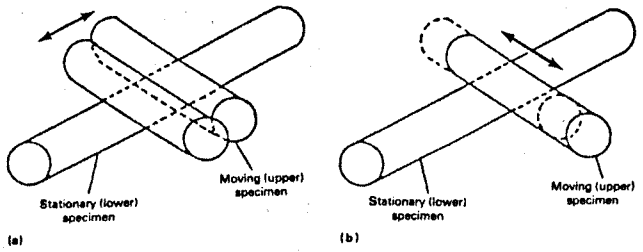

Figure 2.18: Configuration for testing the effect of fretting direction in a crossed cylinder arrangement: (a) Perpendicular to moving specimen; (b) Parallel to moving specimen [104].

at higher frequency) which explained the observation of more debris being formed at the higher frequency.

In complementary pieces of work, Söderberg et al. [101, 102] and Bryggman and Söderberg [103] investigated the effects of displacement frequency into the ultrasonic range (20 kHz). They found that in the gross sliding regime, there was little dependency of either the wear rate or the mechanism of material removal on frequency. Similarly, for a contact experiencing partial slip, increasing frequency was not found to affect the wear. However, both fatigue and corrosion were accelerated due to increases in the interfacial strain rate and temperature, associated with increasing the frequency [101]. In the related work by Bryggman and Söderberg [103], it was found that increasing the frequency could modify the critical amplitude at which gross sliding would occur (with higher frequencies leading to an increase in the critical amplitude); the effect was attributed to the competing effects of strain rate hardening and thermal softening.

Contact geometry

Relatively little work has investigated the effect of contact geometry on fretting wear, despite the large variety of contact geometries found in the literature (Chapter 3, Page 41). Kuno and Waterhouse [104] used a crossed cylinder arrangement and found a difference in wear depending on if the direction of fretting was perpendicular or parallel to the axis of the moving specimen (Figure 2.18). When the motion was parallel, the wear was found to be higher; this was thought to be due to the increased ease of debris escape in this arrangement.

More recently, Fouvry et al. [105] and Merhej and Fouvry [106] investigated the effect of contact size using a conforming (cylindrical punch on flat) and non-conforming (ball on flat) contact geometries respectively. In both cases, it was found that wear was significantly lower for a larger contact and that the wear dropped asymptotically with contact size (Figure 2.19). Similarly to Kuno and Waterhouse [104], both studies attributed the change in wear response to the increased entrapment of debris when a more conformal contact was employed. An important conclusion from this work is that a laboratory test, utilising a simplified non-conforming geometry (e.g., a point or line

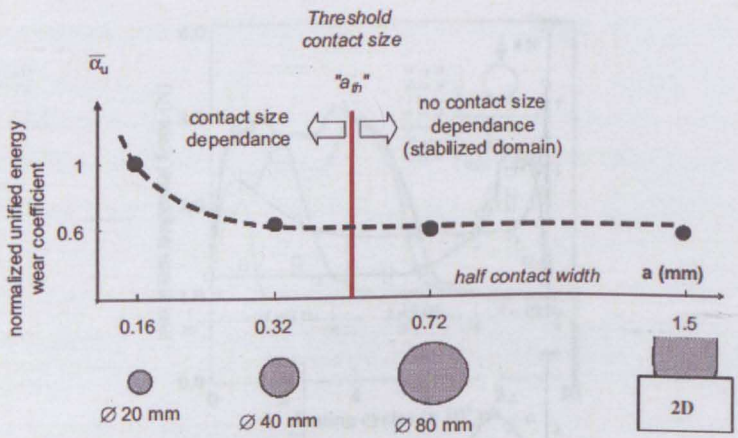

Figure 2.19: Relationship between energy wear rate and contact size [105].

contact), can be used to infer the wear of a larger, fully conforming contact and will tend to produce conservative estimates of wear.

2.6.2 Environmental conditions

Variations in environmental factors such as atmospheric gas content, temperature and humidity have been considered to influence fretting, primarily by affecting the coefficient of friction and hence stress distribution at the contact [5]. This is probably true for small variations in those factors about the values expected in normal laboratory conditions. However, under extremes of environmental conditions, there may be significant changes to the operative fretting mechanism.

As the characteristic debris produced by fretting is an oxide and it is well known how important the production of the oxide is to the fretting process (see Section 2.5, Page 19), then changes in many environmental factors may act through this path to affect the mechanism of fretting. For example, at elevated temperatures (usually $> 200\,°C$ for steels), a significant change in the fretting behaviour has been observed to occur. Above a transition temperature, the COF is generally seen to drop significantly (by up to 30 %) and similarly, the associated wear rate may reduce by over an order of magnitude [90, 107, 108]. These changes are accompanied by a significant change in the scar morphology, an almost complete suppression of loose debris, and in some cases the formation of a smooth, wear resistant "glaze-layer". The mechanisms and effect of temperature is discussed in detail in (Chapter 6, Page 131).

It has long been observed that during shipment, the fretting of automobile bearings is more severe in the winter (when the humidity is lower) than in other seasons. Some of the early fretting work quantified the effect. Feng and Uhlig [63], Uhlig et al. [95], found the fretting wear of mild steel to decrease monotonically with increasing humidity. Subsequent work on pure metals [109, 110] found a slightly more complex relationship. For pure iron, copper, silver, chromium and titanium, fretting wear was found to increase as the humidity was increased from 0 % relative humidity (RH) up

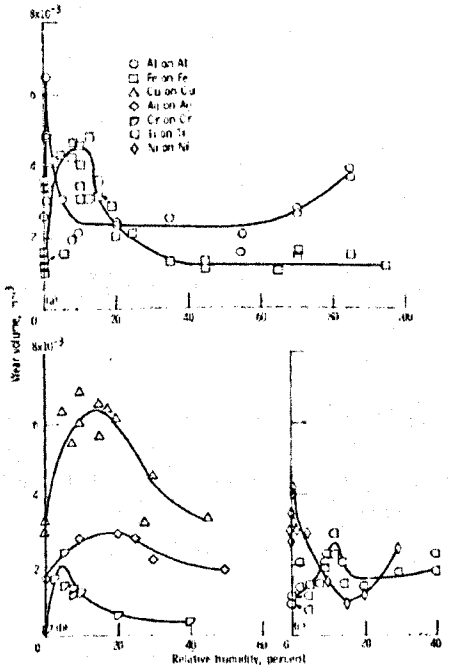

Figure 2.20: Fretting wear volume as a function of humidity at 5.04×10^5 cycles; frequency 60 Hz; applied displacement 80 µm and normal load 2.94 N [110].

to a maximum value, typically in the region 0 to 20 % RH and then drop with further increases in humidity. Iron was found to be insensitive to increases in humidity beyond approximately 40 % RH (Figure 2.20). Observations by Bill [62] of the debris produced from fretting of high purity iron showed that at high humidity, the debris is flat and plate-like with a diameter of approximately 0.02 µm; this is in contrast to the debris produced in dry air, where it was formed of fine particles with a diameter of approximately 0.005 µm (in both cases the debris was α-Fe_2O_3). Bill [62] postulated that adsorbed moisture would permit easy shear of the debris at high humidity and may also affect the mobility of the debris within the contact. Similarly, Waterhouse [1] suggested that in a high humidity atmosphere, a lubricious, hydrated oxide may form.

In work on TiN coatings, Mohrbacher et al. [111] found the COF, and time evolution of the COF, to be significantly influenced by the relative humidity. At low humidity (<10 % RH), the COF rose to ≈ 1 over a period of 2000 cycles. In contrast, at humidity levels greater than 50 % RH, the coefficient reached a lower peak over a similar period but then dropped rapidly to around 0.2. Mohrbacher et al. related the period of high friction at the higher humidity conditions to exposure time (and hence to a tribo-chemical effect) by conducting tests at different frequencies (see Figure 2.21). They suggested that the presence of moisture promoted the formation of layers of low friction TiO_{2-x} debris.

In inert gas environments, such as helium and nitrogen, where oxidation is prevented, fretting results in a continuous process of metal transfer between the surfaces and almost no production of oxide debris [55, 63, 112]. This results in severe roughening

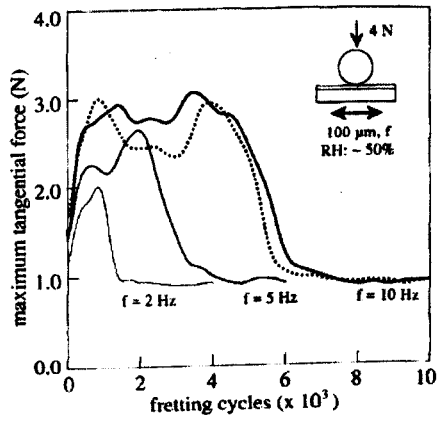

Figure 2.21: The effect of frequency on the maximum tangential force evolution at 50 % RH; normal load 4 N for a TiN coated flat specimen and round corundum specimen [111].

and plastic deformation of the surface and almost no weight loss (wear). The small amounts of wear that were observed were attributed to the dispersal of the initial surface oxide films [55]. When the humidity was varied in an inert (nitrogen) environment, very little influence was found, further supporting the theories that humidity affects the rheology of the debris [63].

2.7 Mitigation of fretting damage

Any premature component failure results in increased maintenance costs, associated warranty costs and loss of reputation; in more extreme cases, injury and loss of life may occur [113]. Fretting is increasingly recognised as a significant failure mode of mechanical systems. It is of particular concern in fixed wing aircraft connections, rotary wing gearboxes, clutches, bearings, bushings, lugs and engines of all types in the aviation industry [114]. Consequently, there is a great need to mitigate fretting damage. However, fretting is not a material property nor a unique tribological mechanism; rather it is a system response resulting from the interaction between the physical structure (material, interface and joint design) and the imposed operating variables (e.g., environment, loading etc.) [114–116].

Strategies used to mitigate fretting damage are varied (even contradictory) and depend strongly on the service application [1]. In general, they may be grouped into methods which modify the design, introduce lubrication or modify the contacting surfaces (surface engineering) [117].

2.7.1 Design

The designer is able to influence the fretting response through both the structure and the operating variables. While the operating variables of the system are mainly prescribed by the purpose of the system, that does not prevent the designer modifying the

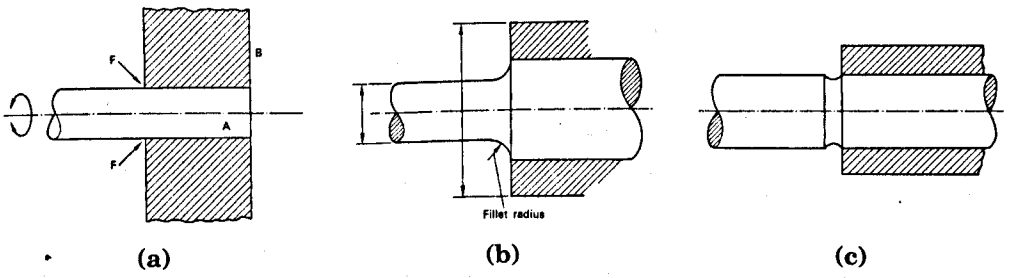

Figure 2.22: Design of a press fit to reduce fretting by reducing the stress concentration: (a) original shaft hub configuration, (b) with stress relieving fillet radius and (c) with stress relieving groove [1].

local stresses and environment at the fretting contact by changing dimensions, improving tolerances or reducing sources of vibration by balancing of rotating elements. More general options available to the designer may include: (i) changing the base material, (ii) reducing the relative slip, (iii) lowering the contact pressure, and (iv) lowering the coefficient of friction. However, choice of the base material of a component is likely to be governed by broader design considerations such as strength or cost. Additionally, changes in items (ii) to (iv) are mutually dependent. For example, lowering the contact pressure or the COF may increase the slip [118]. The problem is alleviated by recognising that many fretting contacts are either displacement-controlled or stress-controlled [115]. In a displacement-controlled system, the slip is independent of the load carried; for example, slip in a splined coupling may be driven by misalignment of the shafts rather than the torque load. In the case of a displacement-controlled contact, where some movement *must* be accommodated, it is desirable to reduce the surface tractions by reducing the contact pressure and COF. Alternatively, it may be possible to accommodate the relative motion within a compliant shim material such as lead, rubber or silver [113, 119]. In contrast, in stress-controlled contacts, it is advantageous to increase the contact pressure and the COF since slip can only occur if $q > \mu p$, where p is the contact pressure and q is the shear stress. The fretting interface may also be designed to reduce the stresses driving the slip. For example, introducing a fillet on the shaft at the interface of a shaft/hub press fit can reduce the stress sufficiently to prevent fretting (Figure 2.22) [1]. Similarly, arranging the bearings on a radially loaded shaft to reduce the bending moment at the point where a press-fitted bearing race or hub is located will reduce the stresses and hence slip and fretting at that interface [1]. For a bolted flange, both the bolt pattern and the flange design can be modified to alter the clamping forces to reduce fretting damage [113].

2.7.2 Lubrication

Due to the low slip amplitudes and sliding velocities, no hydrodynamic or elastohydrodynamic lift can generally be generated in a fretting contact. Consequently, the effectiveness of a lubricant may be expected to depend strongly on its properties as

a boundary lubricant and additionally on its viscosity and ability to penetrate the fretting contact.

Research indicates that, under fretting conditions, lubricants influence both the mechanical and chemical components of fretting by reducing the coefficient of friction (and hence surface tractions) and restricting oxygen access. In general, this reduces fretting wear, but under certain conditions may promote sustained metal-metal contact by suppressing the formation of oxide debris and actually enhance wear [6, 120].

The role of viscosity is also not as clear as may be initially assumed. Neyman [121] conducted fretting tests on mild steel, at a relatively large displacement amplitude of 60 μm, using a variety of oils. In all cases, the introduction of a lubricant was effective in reducing the wear (by more than a factor of 30). The effectiveness of a lubricant was found to be directly proportional to its boundary lubrication properties; no direct correlation between the viscosity of the oil and the resultant fretting wear was found.

Shima et al. [122] similarly conducted a series of tests with a range of oils with varying viscosity, but additionally varied the applied displacement. Their results indicated that viscosity of the lubricant *did* influence the wear but as a function of the displacement: it was found that at low displacement, with higher viscosity lubricants, the oil was unable to penetrate the contact and the COF was higher even than under "dry" conditions. In these cases the oil excluded oxygen from the contact, suppressing oxide formation, consequently promoting metal-metal contact, welding and hence a high COF. Their conclusions were supported by Zhou et al. [123] who observed a similar phenomenon with a grease-lubricated contact: at low slip amplitudes (<50 μm), greater wear and metal-metal contact was observed in grease-lubricated conditions than under un-lubricated conditions. In contrast, at higher slip amplitudes, grease was found to be an effective palliative as it was able to penetrate the contact.

The use of extreme pressure (EP) additives such as zinc dialkyldithiophosphate (ZDDP) has been found to be particularly effective in reducing the COF and wear under fretting conditions. Sato et al. [124] found that a mineral oil reduced the fretting wear of a steel by approximately a factor of 10; the addition of 2 % ZDDP reduced the wear volume by a further 50 % compared to the base oil alone. Later work by Grahn et al. [125] showed similar results but also highlighted the importance of understanding the chemistry of the oil as it was found that other molecules may compete with ZDDP at the surface.

2.7.3 Surface engineering

Surface engineering is the local modification of a material for improved performance; it is commonly employed to enhance resistance to corrosion, wear or fatigue. Hutchings [115] suggests that the most common tribological objectives of surface engineering are to increase the wear resistance of the surface of a component, and to modify its frictional behaviour. The methods available for surface engineering can be broadly

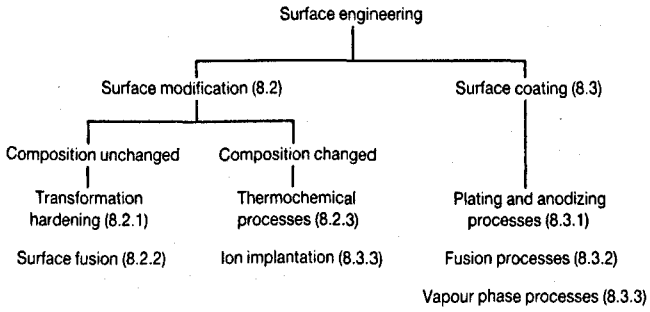

Figure 2.23: A summary of surface engineering techniques [115].

grouped into surface modification techniques (which modify the existing surface structure and/or composition) and surface coating techniques, where a new material is deposited onto the surface of the pre-existing component (Figure 2.23). Of the myriad of possible surface engineering techniques, some examples relevant to amelioration of fretting issues are given in the following sections.

Surface Coating

A large number of coatings have been applied to fretting contacts [117]. Bonded, soft, solid lubricant coatings are a relatively low-cost method and have been found to be effective in reducing fretting wear. For example, MoS_2, graphite and polytetrafluoroethylene (PTFE) films can significantly reduce the COF under fretting conditions: PTFE coatings can result in a COF as low as 0.04 and, in comparative tests between these coatings, have proved to be the most durable [126, 127].

Other low friction coatings (not necessarily considered to be solid lubricants) have found similar application as fretting palliatives. For example, several researchers have investigated diamond like carbon (DLC) coatings [128–131]. DLC is an amorphous form of carbon, deposited to form thin films (typically 2 to 10 μm in thickness) by a vapour deposition process; such material generally exhibits extreme hardness (2400 kg mm^{-2}) and a low COF (0.2 to 0.3) against many metals. Under sliding conditions, the application of a DLC coating has been seen to reduce the wear by a factor > 200 [132]. It is not thought that the increased surface hardness is the only beneficial factor but the debris produced by a DLC coating is composed of graphitic forms of carbon, themselves lubricious in nature [129, 133]. Similarly, DLC coatings have been found to be effective under both fretting fatigue and fretting wear conditions. Kalin and Vižintin [130] found that the fretting wear of DLC/DLC and steel/DLC contacts was as much as 10 times lower than similar steel/steel contacts and the COF was reduced by more than a factor of two. Golden et al. [129] reported an 11 to 26 % increase in fretting fatigue life of a Ti-6Al-4V dovetail joint specimen by the application of a DLC coating.

A common problem with all coatings is that, unlike oils and greases, there is no way to easily replenish the coating at the interface (except for the expensive process of stripping and reapplication of the coating). Hence, the effectiveness of such methods

is entirely governed by their durability, or more importantly the ability to reliably predict their durability.

Surface modification

Surface modification may alter the structure, or the structure *and* composition of the substrate material. For example, shot peening is a purely mechanical method which introduces compressive residual surface stresses. In addition, it increases the surface roughness, which may affect the COF; the surface is work hardened, which may also affect the COF and distortion of the surface grains reduces the propensity for crack nucleation [134]. Shot peening has been applied to fretting problems, primarily fretting fatigue due to the introduction of compressive residual stresses: in work on both titanium and steels, significant increases in the the fretting fatigue life have been observed (in some cases by more than an order of magnitude) [134, 135].

Conversely, under a range of test conditions which resulted in fretting wear, no beneficial effect of shot peening Ti-6Al-4V was observed [136]. The only effect noted was a reduction in the initial coefficient of friction which lasted for less than 500 cycles. This finding is fully supported by the work of Kubiak et al. [137] which found shot peening of a steel had "no impact on [fretting] wear resistance". Moreover, the work of Kubiak et al. [137] highlights an important consideration in surface engineering of components, namely that in many cases, only one component can be treated (due to practical reasons, such as access to the surfaces) and that treatment of only one surface may reduce the wear of the treated component, but be detrimental to the overall system wear by increasing wear on the untreated component. Kubiak et al. [137] fretted a steel couple (cylinder-flat) in which only the flat body had been treated. When the component was shot peened, the *total* wear of the system did not change but it actually increased the wear of the shot peened specimen by approximately 20 %. Similarly, the application of a hard chromium coating reduced the total system wear by approximately 50 %; however, the wear of the untreated surface was approximately the same when fretted against either the coated or un-coated counter-body

Nitriding is an example of a widely used surface engineering technique to relieve both fatigue and wear problems, and is widely used on steels (although can be used on other metals). It is a method which modifies the structure and composition of the substrate through the diffusion of nitrogen atoms into the lattice and the formation of nitrides. It is of significance due to its current use on the Trent series engine main-shaft splines and consequently a detailed review of the process is given in Section 2.7.4.

2.7.4 Nitriding

The nitriding process

Nitriding is a thermochemical surface engineering process for diffusing nascent nitrogen into the surface of ferritic steels. Nitriding is a low distortion process as it involves

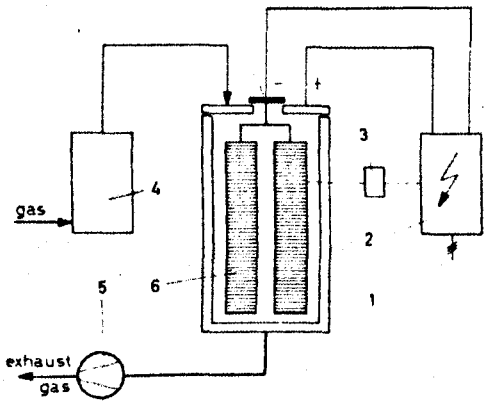

Figure 2.24: Diagram of plasma nitriding equipment: (1) vacuum furnace, (2) power supply, (3) regulating device, (4) gas distribution, (5) vacuum pump, (6) work-piece [140].

no phase change or rapid cooling; there is some small volumetric growth due to the uptake of nitrogen and consequent lattice distortion [138, 139].

A variety of nitrogen providing media have been used, giving rise to the nitriding process names via the relevant state of matter: solid nitriding (or salt bath nitriding, using nitrogen containing salts e.g., cyanide salts—CN^-); gas nitriding (usually using ammonia—NH_3) and plasma nitriding (also known as ion-nitriding, glow discharge nitriding or Ionitriding[†]) [138, 140]. When compared to other techniques, plasma nitriding produces faster nitrogen diffusion, at a lower temperatures (around 500 °C), with lower gas consumption, no harmful waste products and facilitates significantly better control over the surface microstructure; these attributes make it commercially very attractive [138, 139].

The main elements of a plasma nitriding system are a vacuum furnace, a gas distribution system and a high voltage DC electrical power supply (Figure 2.24). The chamber is initially evacuated to remove any contaminating gasses, and then filled with appropriate treatment gasses (typically nitrogen and an inert gas) to a pressure typically from 133 to 1333 Pa. An electrical potential (typically 100 to 1500 V) is is applied between the work pieces (cathode) and the chamber wall (anode) [140].

Under the action of the electric field, naturally occurring ions and electrons are accelerated toward the anode and cathode respectively and collide with gas molecules causing further ionisation and hence current flow. The cathode attracts an accumulation of the large ions which causes a significant number of collisions between the free electrons being accelerated from the cathode and other neutrally charged gas molecules, resulting in further ionisation (plasma formation) [139, 140]. As a result of the frequency of collisions, there is a high electrical impedance in this region and hence a high voltage drop, termed "cathode fall"; consequently, most of the supply power is dissipated in this region (Figure 2.25). Similarly, at the anode there is an

[†]Ionitriding is a trademark of Klöckner group who originally exploited the process commercially.

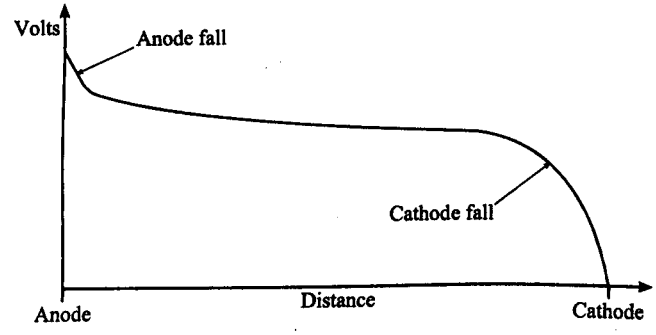

Figure 2.25: Typical voltage gradient between electrodes under glow discharge [139].

accumulation of electrons, but due to their small size, there are far fewer collisions and, as a result, a much smaller voltage drop and thus a smaller power dissipation.

In the highly energetic region around the cathode, the collisions result in the emission of photons, some of which are in the visible spectrum, leading to it being termed the "glow seam". The glow seam closely follows the contours of the work piece, meaning that even complex geometries receive an even surface treatment in the plasma. Increasing the gas pressure moves the glow seam closer to the work piece surface, making it possible to drive the nitriding process through holes and small inlets. Conversely, lower pressures can cause the glow seam to jump over holes etc., thus allowing some control over the nitriding of surfaces. More detailed control of which areas are nitrided is achieved by mechanical masking with metal plates, bolts or stainless steel foil [139, 140].

Collisions between the ions and the cathode (work piece) surface causes heating (no external source is required) and may also liberate metal atoms in a process known as "sputtering". If the gas in the chamber is an inert gas, sputtering can be used to effectively clean the surface, removing oxides and other surface contamination. In a nitrogen containing environment, the liberated iron atoms can combine with the highly reactive nitrogen ions to form FeN. The FeN produced is adsorbed onto the surface where it decomposes to ϵ–$Fe_{2\text{-}3}N$ and γ'–Fe_4N, liberating nitrogen which will diffuse into the work piece. The adsorbed layer of iron-nitrides provides a high concentration of nitrogen on the surface of the steel which is the primary reason for the higher diffusion rate which occurs with plasma nitriding [140]. The resulting surface layer of iron nitrides is termed the compound layer (or white layer (WL), due to its etch resistance in metallographic examination).

In general, the thickness of the compound layer (of the order of microns) is found to increase with increasing treatment time, temperature and nitrogen content of the treatment gas [141]. When the nitrogen content is below a critical value (approximately $< 5\,\%$), then no compound layer is formed [139, 142]. As the proportion of nitrogen in the treatment gas is increased, the compound layer of γ' and ϵ iron nitrides is formed. With increasing temperature and proportion of nitrogen in the treatment gas, the proportion of the ϵ nitride decreases while that of the γ' nitride increases

[141]. The compound layer formed by plasma nitriding may be significantly harder (several hundred HV) than diffusion zone [143]; this is in contrast to the compound layer formed by gas nitriding which is softer due to its more porous nature [144]. It has been suggested that under fatigue loading, the compound layer may be detrimental as its brittle nature may lead to crack initiation [139]. However, experimental work has found that plasma nitriding increased the fatigue strength of a low alloy steel (by 25 to 45 %) and that the fatigue strength was independent of the compound layer thickness [145].

Below the compound layer is the diffusion zone; in the diffusion zone the nitrogen exists in solid solution as single, interstitial, atoms. When the solubility limit is reached, fine nitride precipitates are formed with alloying elements (particularly Al, Cr, V and Mo). The hardness is not significantly changed by the dissolved nitrogen (although the lattice distortion results in a compressive surface stress). However, the hardness is increased significantly by the nitride precipitates [140, 143]. For example, Berg et al. [143] plasma nitrided steels of varying alloy content: stainless steel, tool steel, nitriding steel and low carbon steel (in decreasing alloy content); they found the near-surface hardness of the diffusion layers to be 1300 to 1500 HV, 1200 to 1400 HV, 1000 to 1200 HV and approximately 500 HV respectively. Furthermore, the diffusion coefficient, and hence depth of nitrogen penetration, was found to be reduced by increasing the alloy content as the alloying elements "trapped" the diffusing nitrogen as nitride precipitates [143].

As may be expected, being diffusion controlled, the case depth increases with temperature and time. Furthermore, the surface hardness is strongly dependent on temperature due to interactions between precipitate growth, density and tempering of the matrix at higher temperatures [141, 143].

Wear of nitrided steels

Sliding wear of nitrided steels has been relatively well studied and nitriding is in general found to significantly reduce the severity of wear and delay the onset of severe wear [144, 146, 147]. In contrast there are very few published reports on the fretting wear of nitrided steels; the work that is available is reviewed in detail in Section 5.1 (Page 77).

2.8 Summary

The literature indicates that fretting induced damage is a difficult and pernicious problem. It is ubiquitous across industry—any mechanical joint may be vulnerable to fretting—and often only apparent after a period of time in service. The relentless drive to improve the efficiency of engineered systems and concurrently reduce maintenance costs requires a greater understanding of the tribology of a fretting contact.

Over the past 86 years, a large body of literature has addressed the subject of fretting. The resultant damage, originally termed "fretting corrosion", is now typically classified as fretting fatigue and fretting wear, although this is more a division by failure mode resulting from a common process. Advances in understanding of the contact mechanics, and subsequent experimental work, has led to the concept of slip regimes and fretting mapping; in turn these have greatly improved the interpretation of fretting experiments.

It is apparent that there is no single fretting mechanism and that a large number of variables affect the fretting of a contact. It is also apparent that a great number of experimental methodologies with widely varying parameters, and widely varying control over those parameters, have been used. As a result, it is difficult, if not impossible, to conclusively predict the fretting response of even common engineering materials. However, it is possible to identify a set of primary mechanical variables, namely normal load and displacement amplitude. Additionally, due to the strongly tribo-chemical nature of fretting, it is sensitive to environmental variables such as temperature, humidity and atmospheric gas content—although these are often considered to be secondary to the mechanical variables.

As a consequence of the ubiquitous nature of fretting problems in industry, there is a body of work concerned with its palliatives. However, due to the complex nature of fretting and its sensitivity to basic mechanical and environmental parameters, a set of robust selection criteria does not exist. Moreover, a method may be found to effectively reduce fretting under certain conditions, which, under other conditions, exacerbates the problem.

It is apparent that, for an engineer to improve the design of a component suffering fretting damage that a large, consistent, and systematic body of material specific data is required. In the case of SCMV, or other similar high strength steels used in aeroengine transmission components, this is unavailable—particularly regarding the elevated temperature fretting performance. Furthermore, there is very little work concerning the behaviour of nitrided steels and, as far as the author is aware, none considering the elevated temperature performance of high strength steels. Consequently, this work will explore the tribology of SCMV and SCMVN, at ambient and elevated temperatures.

Chapter 3

Fretting Test Rig: Design and Construction

3.1 Literature review

Throughout the long history of fretting, a variety of ingenious experimental rigs have been devised to explore the underlying mechanisms, and the compound effect of many variables. In its most basic form, a fretting rig must be able to:

1. apply a known normal force to generate a contact between two specimens;
2. generate a reciprocating applied displacement between the specimens—in the order of tens of microns.

Many rigs have been more ambitious and allowed variation, and real-time (RT) control, of the normal load and displacement. Additionally, experiments have been conducted at elevated temperatures, in controlled atmospheres and over a wide frequency range. In the following sections a review of these experimental apparatus is presented. In addition to the fundamental mechanical requirements, to be useful, a rig must measure and record (at a minimum) the variables of:

1. applied displacement,
2. tangential friction force.

The following survey concentrates on the mechanical aspects of fretting wear rigs—while reviewing techniques of instrumentation and data acquisition is interesting, it inevitably leads to a history of the development the microchip and silicon industries, and hence is avoided.

3.1.1 Specimen geometry and alignment

In the course of fretting research, a large variety of contact geometries have been studied; these may, in general, be divided into three basic types: point contacts, line

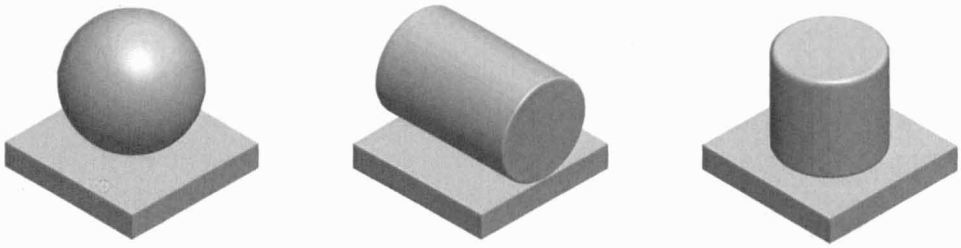

Figure 3.1: Diagram of the three main types of specimen contact: (a) point contact, either ball on flat or crossed cylinders; (b) line contact developed between a cylinder and flat; (c) a complete contact between a punch and flat.

contacts and complete contacts (Figure 3.1). A brief summary of advantages and disadvantages of these geometries is outlined in the following paragraphs.

A point contact (Figure 3.1a) may be developed between a ball (or any section of a spherical body) and flat or with crossed cylinders; examples of this contact geometry, particularly ball on flat, are numerous throughout the literature [3, 18, 31, 96, 101, 148–151]. The popularity of this geometry probably arises from the inherent *self-alignment* of a point contact which greatly simplifies test-system design and enhances test repeatability. Moreover, the stresses and behaviour of the contact are well defined (at least initially) by the contact mechanics of Hertz/Mindlin (Section 2.3.1, Page 5). Additionally, under torsional fretting, the geometry has rotational symmetry but when experiencing linear slip the contact becomes inherently three dimensional (3D), consequently increasing the difficulty of modelling the contact.

A line contact (Figure 3.1b) may be developed between a cylinder and a flat; although not utilised as widely as point contact geometry, there are many examples in the literature [45, 91, 152, 153]. The inherent two dimensional (2D) nature of this type of contact lends itself to computational modelling [51, 153, 154]; moreover, the larger wear scar (and 2D nature) simplifies measurement of wear using tactile profilometry and similar methods. As with a ball on flat geometry, the initial contact stresses can be analytically determined (Section 2.3.1, Page 5). However, the geometry retains the self-alignment of a point contact only about one axis, significantly increasing the complexity of any rig design.

A complete contact (Figure 3.1c) can be developed between two flat surfaces; whilst this may be considered more representative of many real engineering contacts, it presents significant challenges in aligning the specimens. Nonetheless, many researchers have utilised this geometry [43, 54, 92, 95, 96]. To address alignment between the specimens, workers have variously: polished the specimens to each other in situ [95]; allowed the specimens to self-conform and then locked them in place (Figure 3.2a) [54]; or provided a gimbal type arrangement to allow the specimens to take the necessary attitude (Figure 3.2b) [92, 155].

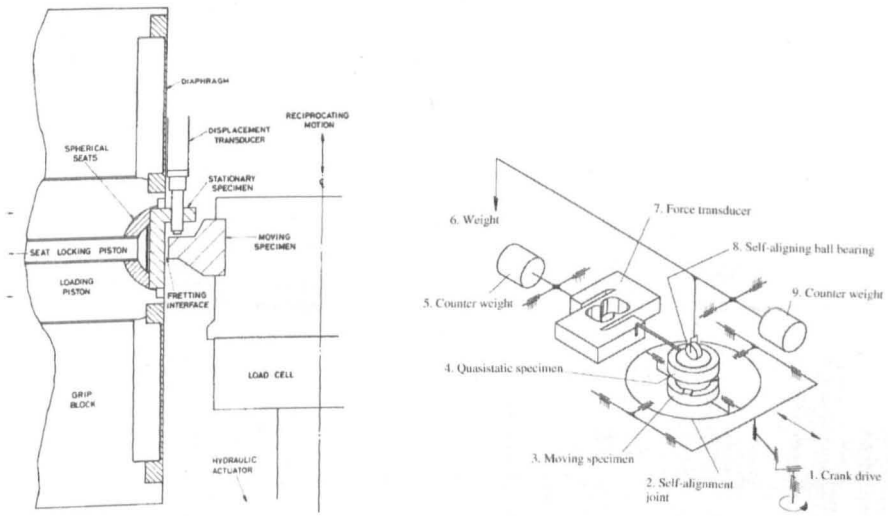

(a) (b)

Figure 3.2: Examples of specimen alignment mechanisms used in fretting test rigs: (a) locking mechanism using a spherical seat [54] and (b) full gimbal arrangement [92].

3.1.2 Types of displacement and motion constraint

The oscillatory slip used in the study of fretting (by the vast majority) is either linear or rotational in nature: linear slip may be generated directly or, as an approximation, via tangential motion some distance from an axis of rotation.

Rotational (torsional) type rigs are common, particularly amongst the earlier experimentalists such as Tomlinson et al. [18, 96] and Uhlig et al. [95]. The predominant advantage of this type of rig is that once an axis of rotation is defined, a lever arm can provide a simple method of reducing the input amplitude of motion to fretting levels; a similar approach can be used to mechanically amplify the motion for measurement (Figure 3.3) [96].

A notable shortcoming of torsional type rigs is that the displacement experienced at the contact is, inherently, a function of the radial distance from the centre of the contact (the axis of rotation)—although this has been claimed to be an advantage as it allows the investigation of a range of slip amplitudes simultaneously [1]. A further complication (apparent in Figure 3.3) is that the centre of the contact will experience zero angular displacement. However, both of these problems can be alleviated, to some degree, by the use of flat circular specimens which develop only a contact annulus (Figure 3.4), although this approach does necessitate the use of a full (flat-flat) contact and consequently has all of the associated alignment challenges.

An example of approximating linear motion by a tangent to some centre of rotation is illustrated by Johnson [31], who used three point-contacts at an equal radial distance from the axis of rotation (Figure 3.5). Another interesting form of fretting might be termed rotational sliding. An example of this is found in the rig used by Halliday [152] and Halliday and Hirst [45]: they loaded a cylindrical specimen, oscillating

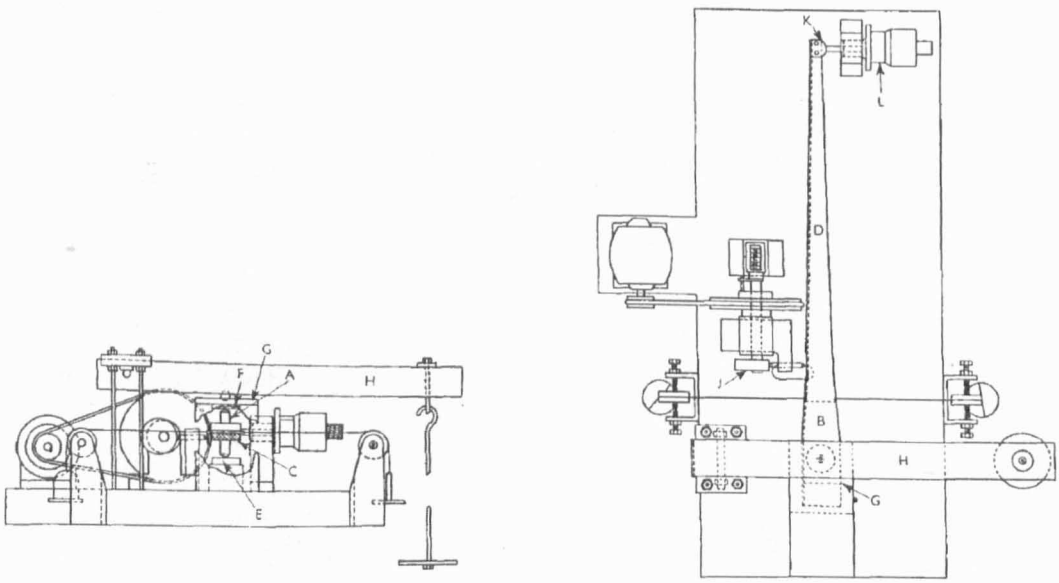

(a) Front view (b) Plan view

Figure 3.3: Diagram of of a test rig utilising rotational fretting with a lever arm to reduce the applied motion and amplify it for measurement. Displacement is generated by an eccentric at (J) and applied to the lever arm (B-D); specimens are at (G) and the displacement is measured at (K); normal load is applied by a dead-weight though arm (H) [96].

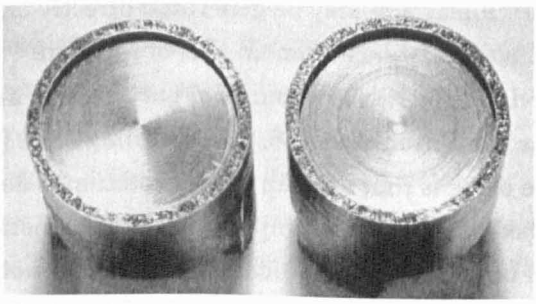

Figure 3.4: A torsional fretting specimen with the centre relieved to create a contact annulus [55].

about its axis, in a V-block producing two line contacts simultaneously as illustrated in Figure 3.6.

In experimental apparatus utilising direct, linear, reciprocating-motion, either the *prime-mover* is a linear actuator, or the motion is generated by another method and conditioned through a linear guide of some sort. Similarly, in rotational fretting, the axis of rotation must be constrained by some sort of bearing (unless the specimen arrangement achieves this as in Figure 3.6). Therefore, in both torsional and linear rigs, there is often a necessity for a bearing arrangement, or at least a joint, which itself will be vulnerable to fretting damage. Additionally, any backlash in mechanical joints may easily be of a similar magnitude as the fretting displacements which need to be generated. Despite these potential problems, there are examples of rigs which have used traditional rolling-element bearings, although no indication is given of

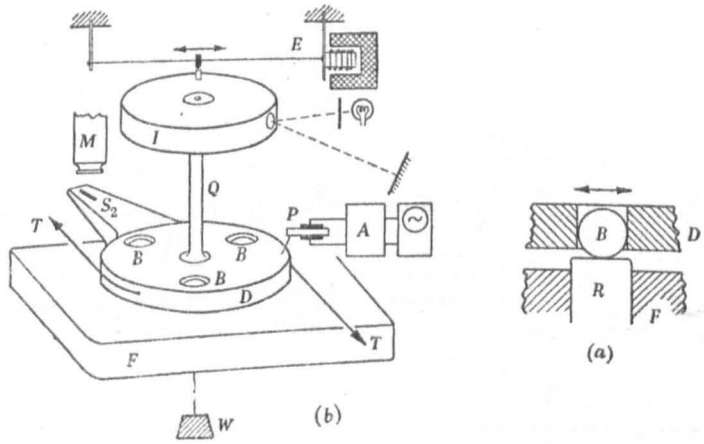

Figure 3.5: Diagram of a rig approximating linear motion by a tangent some radial distance from the axis of rotation: (A) amplifier, (B) steel ball, (D) moving disk, (F) baseplate, (I) vibrating disk applies torsional oscillating shear force, (M) microscope to measure static displacement, (P) displacement pick-up (T) strings apply static shear, (W) normal load [31].

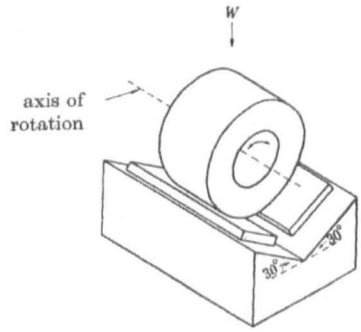

Figure 3.6: Diagram of the contact generated in the rig developed by Halliday [152]. Two line contacts are created between the oscillating cylinder and V-block.

their longevity [155, 156]; others have used non-contacting hydrostatic-bearings to eliminate the problem of wear at the joint [157]. A more widely adopted and robust approach is the use of flexible *vanes* (leaf-springs) to construct flexural bearings and linear guides capable of sustaining small-amplitude reciprocating motion (examples of a rotary and a linear configuration are shown in Figure 3.7 and Figure 3.8 respectively). While eliminating fretting and backlash within the joint, the vanes are unavoidably compliant in directions other than the primary direction of flexure; consequently, they can easily introduce unexpected, and undesirable, degrees of freedom to a test rig [100].

3.1.3 Prime movers: methods of generating displacement

A number of methods of generating the oscillating displacement required for fretting are found in the literature: an eccentric or cam, in conjunction with an electric motor is probably the most commonly used [64, 92, 95, 155, 159, 160]. The popularity of the method is likely due to the relative ease with which a range of displacements can be

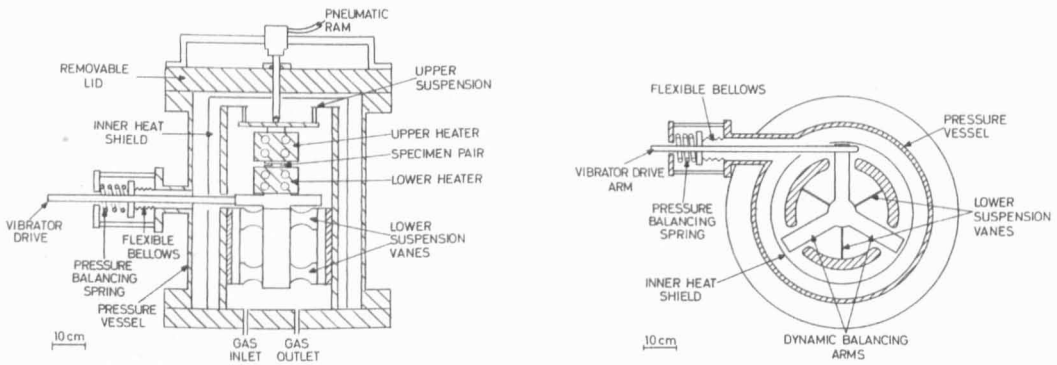

(a) Front view **(b)** Plan view

Figure 3.7: Diagram of a fretting rig using flexible vanes (labelled *lower suspension vanes*) to constrain rotational motion [9].

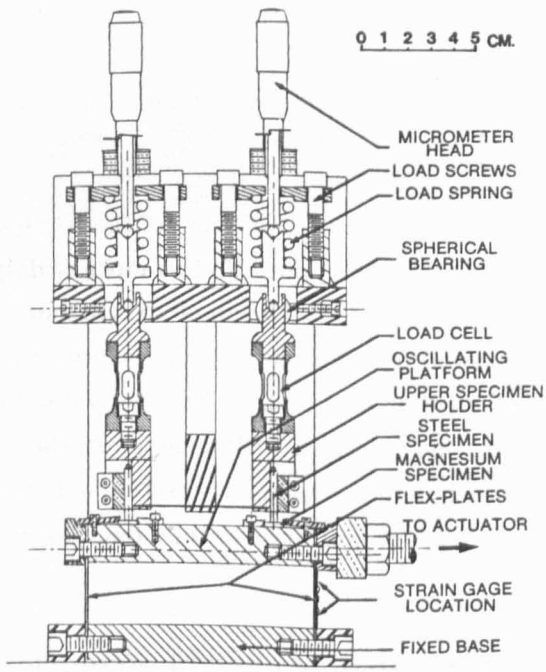

Figure 3.8: Diagram of a fretting rig using flexible vanes (labelled *flex-plates*) as a linear guide [158].

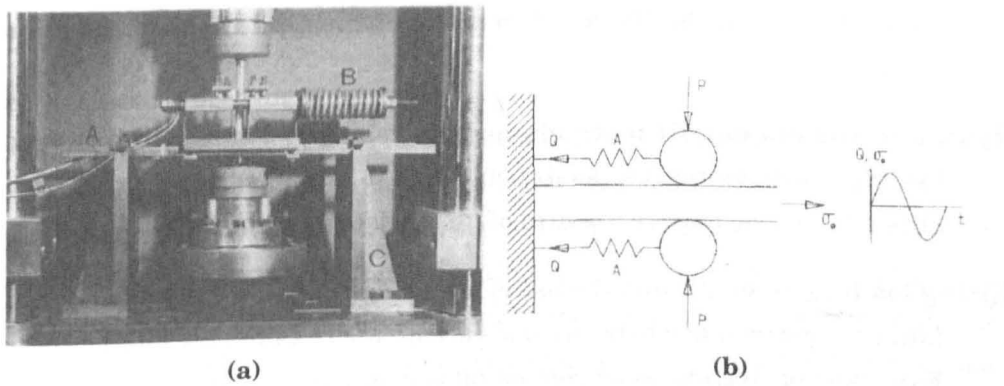

(a) (b)

Figure 3.9: Photograph and schematic diagram of a strain based fretting fatigue rig: (A) flexible beam, (B) compliant springs, (C) support pillars. Changing the length of (A)—by moving the support pillars (C)—changes the pad to ground stiffness [162].

generated by adjusting the eccentric. However, an eccentric or cam does not readily allow the displacement amplitude to be changed during a test. The ability to alter the far-field applied displacement amplitude is desirable as the sliding amplitude at the contact is a function of the drive-train stiffness and friction force. Consequently, the local sliding amplitude at the contact will vary as the COF evolves during a test (or as the applied load is changed if this load is not constant).

Direct sources of linear motion offer obvious advantages: they limit the number of linkages required for conditioning of the motion and are more amenable to active control of the displacement. Methods found in the literature include: electromagnetic vibrators (EMVs) [91, 148, 152], magnetostrictive vibrators [161], hydraulic rams [54, 158], oscillating lead screws [59, 156] and piezoelectric stacks [102, 150]. However, the difficulty of directly generating motion in the order of tens of microns often requires the "gearing down" of a primary source of motion through a lever-arm, usually constrained with a flexural bearing (see Section 3.1.1, Page 41).

Strain derived displacement is more commonly found in fretting fatigue rigs. Typically, this method involves straining one specimen and holding the other specimen(s) (fretting pads) at a changeable stiffness with respect to "mechanical ground", therefore generating a shear force, and fretting, across the contact (a diagram of this type of rig is shown in Figure 3.9). The alternate, and more common, method is to use a *fretting-bridge* loaded against the fatigue specimen to generate the slip.

3.1.4 Application of normal load

Application of the normal load is typically accomplished using one of three methods:

Dead-weight loading is the simplest mechanism of applying the normal load; however, it does not allow for variation or active control of the load during the test, other than crude on/off mechanisms [57]. Examples of dead-weight loading are

found throughout the literature, from the earliest rigs to current equipment [18, 92].

Hydraulic and pneumatic methods are also relatively common in the literature [54, 95]. Such approaches lend themselves to active control and higher loads, although they do require a source of pressurised working fluid.

Spring loading is simple and the use of a *proving-ring* is very common in fretting fatigue experiments where two pads are pressed against the fatigue specimen. Examples of fretting wear rigs using spring loading can similarly be found [96, 158]. A potential problem with spring loading is that the contact may experience a change in load as wear progresses: in some cases, material removal by wear may result in a decrease in load; in other cases (assuming either a Pilling-Bedworth ratio > 1 or a non-uniform build up of debris), there may be an increase in load. However, both situations may be compensated for by selecting a relatively compliant spring.

Although the author is not aware of any reports in the literature, a potential problem using dead-weight loading or hydraulic loading is that they are dynamically *stiff* (in the case of dead-weight loading, this *stiffness* is associated with the high inertia of the loading system). In a fretting motion, as the specimen traverses across the scar each cycle (unless the scar is perfectly flat), it will have a vertical displacement which is a function of its horizontal position; if the normal-loading system is stiff, the applied normal load would consequently vary throughout the displacement cycle. In the case of dead-weight loading, since the variation of load is due to the inertial forces required to accelerate the dead-weight in the vertical direction, the effect would become more significant as the fretting frequency increased. Moreover, in a dead-weight system, these forces could lead to significant, unwanted, excitation and vibration of the the loading mechanism.

3.1.5 Conclusions

It is apparent that there has been a large variety of specimen geometries and types of reciprocating motion employed to study fretting. It is surprising that there is almost no literature comparing the various methodologies: in fact, at the time of writing, the author is aware of only one paper which offers a very basic comparison of fretting modes (with a ball on flat specimen arrangement), insufficient to draw significant conclusions [163].

Similarly, a large variation exists in the design and mechanism of fretting rigs. Although there is no clear *best* design, the use of a direct-drive mechanism to limit the number of linkages and flexures and a prime-mover which is adaptable to closed loop control of the fretting displacement seem to be desirable features.

3.2 Assessment of the existing experimental capability

There has been a fretting wear (and fatigue) capability at the University of Nottingham for several decades. Its last incarnation was based on 2000 V A Derritron electromagnetic vibrator (EMV), driven by a Derritron amplifier, with an integrated signal generator providing the control signal for the oscillatory motion. The output displacement was scaled through a lever arm to produce relative motion between the upper specimen mounting block (USMB) and the lower specimen mounting block (LSMB) of a suitable amplitude for fretting tests. The lever arm made use of a flexural linkage to eliminate fretting damage at the pivot. Normal load was applied to the USMB via a 4.9:1 load arm with dead weights and a pin-jointed linkage. The specimen geometry employed was a crossed cylinder and flat, generating a line contact. The flat specimen was static and the cylindrical specimen was moved relative to it to produce fretting. Typically, normal loads up to 2 kN had been used with applied displacement amplitudes in the range of 50 to 100 µm. In this format, the rig relied on manual (open loop) control of the displacement amplitude. While it had been used successfully to investigate long duration, steady state, gross-sliding fretting where the COF could be considered constant, it struggled with any significant variations in COF and low displacement amplitudes were not readily achievable.

The author was involved in the development of a closed-loop displacement control and integrated data acquisition system for this rig. This system significantly improved the behaviour of the rig, allowing unattended running and smaller displacement amplitudes to be investigated. However, the rig was not originally designed with small displacement amplitude investigations in mind and several issues were observed during the course of the work:

1. while the closed loop controller was a significant improvement, the lack of RT hardware limited its performance and reliability;

2. the rig was designed with large displacement amplitudes, high loads and accompanying wear rates in mind. For a variety of reasons, small displacement and low loads were difficult to achieve;

3. the use of a lever arm resulted in an approximation of linear motion which was thought to be less than ideal;

4. the instrumentation was ranged for high loads and displacements and was not suited for work at lower ranges;

5. the integrated heaters were unsatisfactory, with significant heat loss to the frame of the rig and a limited temperature range;

6. alignment of the specimen pair (the line contact) was complex and unreliable, leading to a high fraction of tests being considered void.

3.3 Requirements for a new test rig

After evaluating the existing rig, the need for an upgraded capability to enable a wider range of fretting tests was clear. The broad aim of the enhanced apparatus was to provide an incremental improvement on the existing capability, enhancing existing features and expanding functionality to meet the demands of the current project. The functionality required for the the current project was identified as:

1. closed-loop control of the applied displacement amplitude, with the future option to control the displacement profile;
2. continuous (high data-rate) recording of the displacement and friction force to enable derivation of any required parameters off-line;
3. an elevated temperature capability;
4. unattended operation for long duration tests.

Similarly, a number of features from the existing set-up were identified as desirable to keep:

1. the specimen geometry to maintain continuity with previous experimental and modelling work at the University of Nottingham;
2. dead weight loading, since it had proven to be simple and reliable;
3. an EMV as the prime mover as it had proven to be an effective method of generating fretting over a range of displacements and frequencies.

Areas where improvement was required were identified as:

1. specimen alignment—to reduce the number of tests being declared as void;
2. data storage—retrieval of data needed to be simplified and an effective method of mining historical data introduced;
3. heater arrangement for elevated temperature work;
4. the control strategy for the slip amplitude.

3.4 Development of a new test rig

In order to provide the required capability for the current project, a significant development programme was undertaken and an entirely new test rig was built. All the design, assembly and installation was completed by the author; the machining was conducted by the Faculty of Engineering workshops at the University of Nottingham.

The following sections give an overview of the design, split into the mechanical and supervisory control and data acquisition (SCADA) sub-systems (Section 3.4.1, Page 51 and Section 3.4.2, Page 58 respectively).

3.4.1 Mechanical design overview

Figure 3.10 is a simplified render of the rig with the main components labelled. The following sections provide a description of these components and refer to more detailed figures where required.

Drive line

The existing rig utilised a lever arm to reduce the amplitude of motion produced at the vibrator face-plate. In a system utilising a cam or eccentric producing a fixed displacement, this is often desirable. However, the EMV produces a force, rather than displacement, proportional to the control voltage supplied to the amplifier. Given the maximum force of the EMV, the friction forces encountered and the reduction ratio of the lever arm, this meant that the EMV was continually operating over a small part of its range. Additionally, the lever arm produced motion along a tangent to its pivot, resulting in an angular offset between the direction of motion and the axis of the specimen.

Considering these issues, the new rig was designed with a linear drive-line. To define the direction of motion for the rig, a linear guide (using flexible vanes) was developed (Figure 3.11). The vanes were sized for an infinite fatigue life, at the maximum design displacement amplitude of $\pm 250\,\mu m$. To prevent damage to the flexible vanes in the event of over travel, the guide also includes hard-stops which limit the maximum displacement to $\pm 1\,mm$. Due to rig-build tolerance stack-up, there will inevitably be some (small) misalignment between the linear guide assembly and the EMV axis; this is accommodated by a flexible *stinger*, internal to the guide assembly. The stinger was sized for both flexibility and also avoidance of buckling and fatigue failure.

A primary concern in the design of the new rig was to enhance the ease of specimen alignment to ensure a uniform load per unit length along the line contact. To improve this, the new design features an *alignment-coupling* which allows the USMB assembly to be disconnected from the load cell. Additionally, the coupling achieves in plane location using a central spigot but allows the USMB assembly to rotate and hence the cylindrical specimen to align to the flat specimen before the coupling bolts are tightened. A small degree of vertical *float* (to accommodate for wear of the specimen and machining tolerances) is allowed by the drive linkage between the load cell and USMB.

Load cell

Integral to the drive line is a purpose built load-cell, enabling a resolution of $< 0.1\,N$ to be achieved up to the maximum design load of $2\,kN$ (Figure 3.12). The sensing

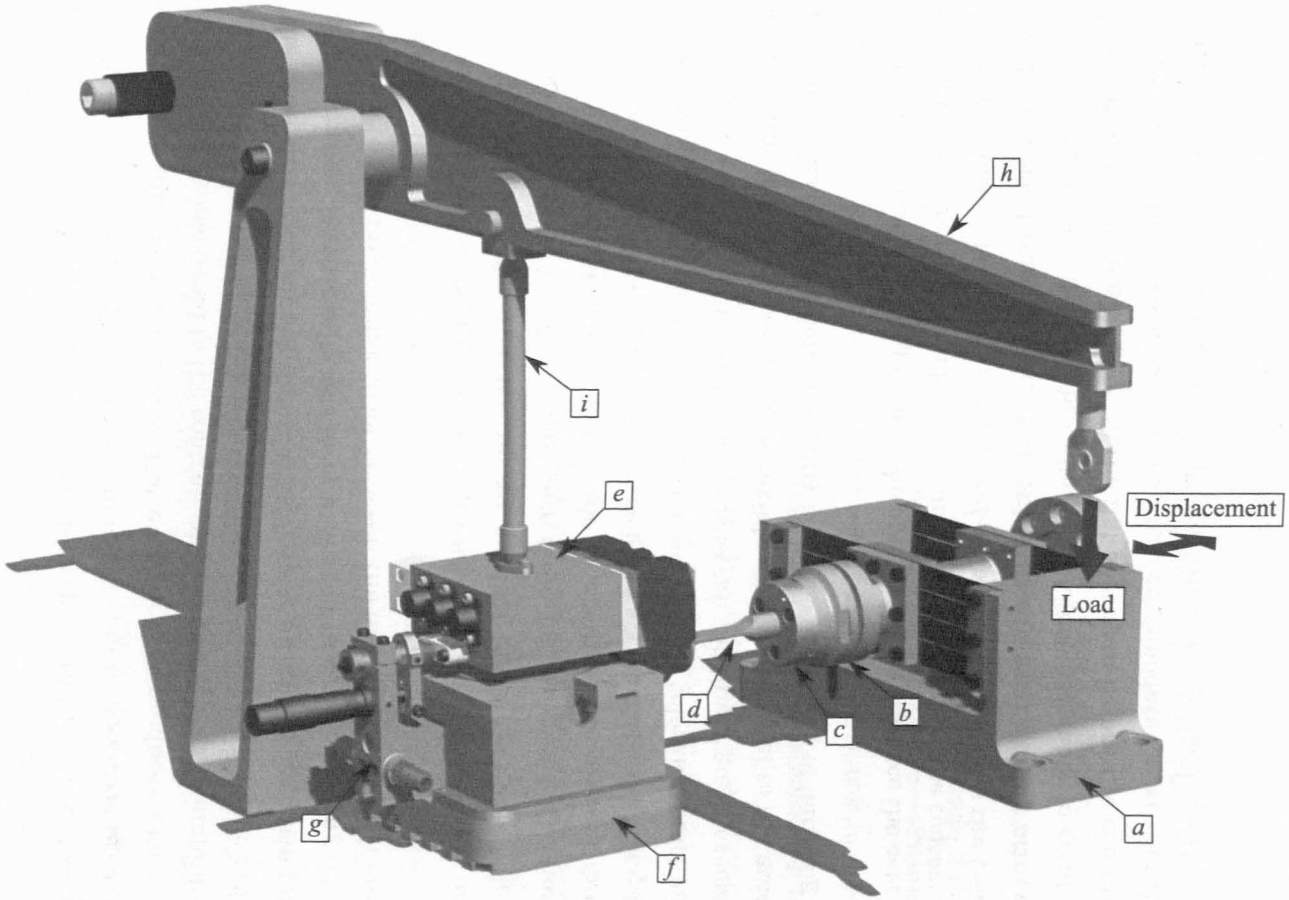

Figure 3.10: Diagram of the drive line for the new test rig: (a) linear guide, (b) load cell, (c) alignment coupling, (d) drive linkage, (e) upper specimen mounting block (USMB), (f) lower specimen mounting block (LSMB), (g) water cooled linear variable differential transformer (LVDT) mount, (h) load arm, (i) load bar; *Displacement* is provided by an EMV and *Load* is from a mass hanger and dead weights.

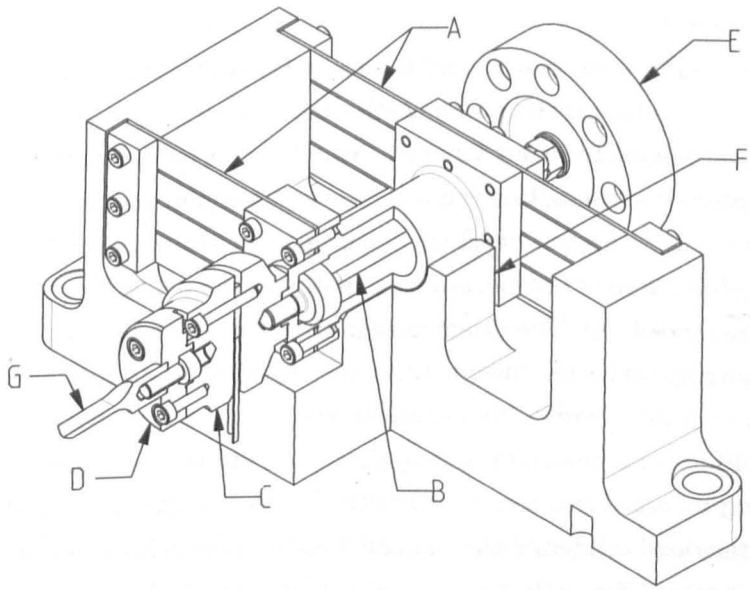

Figure 3.11: Detail view of the linear guide assembly showing: (A) flexible vanes, (B) stinger, (C) load cell, (D) alignment coupling, (E) flange coupling to the EMV, (F) hard stop, (G) drive linkage.

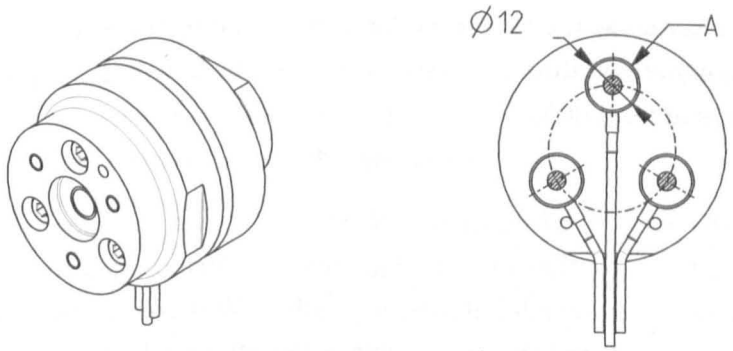

Figure 3.12: Diagram of the custom made load cell: (a) isometric view of the assembly and (b) internal view showing the piezoelectric force sensing elements (labelled (A)).

elements of the load cell are three piezoelectric load washers[†] equispaced on a 28 mm pitch circle diameter. The charge from each sensor is summed before amplification: consequently, by equilibrium consideration, it can be shown that the load cell is insensitive to bending moments.

Each load washer has a measuring range of 0 to 7 kN; to measure both tensile and compressive forces, the load washers are each preloaded to 3.5 kN by individual bolts, resulting in a theoretical range of ±10.5 kN and a maximum bending moment of 59 N m. The load washers have a quoted threshold of < 0.01 N and a stiffness of 1.8 kN μm^{-1}. The high stiffness results in $< 10\%$ of the load being shunted through the pre-loading bolts; therefore, a theoretical sensitivity much greater than the specified

[†]Kistler, model number 9132BA sensor with a Kistler type 5073A charge amplifier

0.1 N may be expected.

Piezoelectric force sensors are ideal for use in fretting applications, offering many advantages over traditional (strain based) sensor technology—the design of which requires an unavoidable trade-off between stiffness and load capacity against sensitivity. For piezoelectric sensors, this is not the case: depending on how the piezoelectric material is cut, the charge produced may be proportional only to the force applied i.e., independent of the area of the piezoelectric material and hence the load capacity and stiffness of the transducer. The disadvantage of piezoelectric sensors is that they can not achieve a truly static measurement, since imperfect insulating materials make charge loss inevitable, leading to a decay in the sensor output with time. However, modern amplifiers can have a very long time constant ($\tau = 10^6$ s for the model used here), making piezoelectric sensors suitable for quasi-static measurements—tests with the custom load cell found the indicated load (under a constant applied load) to reduce at less than $1\,\%\,h^{-1}$. In the case of fretting (where there is no constant force component), this is of no detriment, making piezoelectric force sensors an ideal choice.

As can be seen in Figure 3.10 the load cell is positioned in the moving side of the drive line. This may be considered to be a suboptimal (although not unusual [54, 99, 164]) location as the tangential force measured by the load cell (Q_m) load cell will consequently see additional forces due to acceleration of the mass (m_c) of all of the components in front of it:

$$Q_m = Q + m_c a \tag{3.1}$$

However, at the operating frequency of 20 Hz, assuming a displacement amplitude of 100 µm and knowing that $m_c = 2.5$ kg, this corresponds to a maximum inertial force of < 4 N, which is considered to be negligible. Moreover, as the displacement is continuously recorded (and thus the acceleration can be calculated), it is possible to correct for the inertial forces as a post-processing task.

The advantage of the current location of the load cell (and the main driver for this position being selected) is that of distance from the USMB which is desirable when the USMB is being used at elevated temperature. The long distance, together with the small cross sectional area of the drive linkage results in a poor thermal path between the load cell and the heated USMB meaning that no active cooling of the system is required; consequently, the thermal losses from the specimen mounting blocks are minimised.

Specimen mounting blocks

The LSMB (Figure 3.13b) is stationary and carries the flat specimen while the USMB (Figure 3.13a) carries the cylindrical specimen, moving relative to the LSMB. The specimens are not mounted directly to the specimen mounting blocks; instead there are intermediate specimen mounting plates (SMPs), allowing the rig to adapt to future specimen geometries with minimal changes.

The normal load is applied using a balanced lever-arm with dead weights (Figure 3.10h), with a ratio between the load on the USMB and the load on the mass hanger of 5:1. The interface between the load bar (Figure 3.10i) and the USMB (and also the load bar and load arm) is through a ceramic ball located in a shallow socket. This creates a small, low friction, point contact in order to reduce the heat loss through the load bar and to approximate to a pin-joint (a detail view is given in Figure 3.14).

For heating, the USMB and the LSMB each incorporate three 200 W cartridge heaters. The temperature of the specimen mounting blocks is independently controlled; feedback thermocouples are located 3 mm above/below the specimen, at the centre of the SMPs (the bore for a thermocouple can be seen in Figure 3.13a). In order to reduce thermal losses from the specimen mounting blocks, a number of *thermal bulkheads* (fabricated from Macor machinable glass ceramic (MGC)[‡]) have been included. To further reduce losses, the thermal bulkheads are machined such that they have a 50 % reduced contact area with adjacent components. The main thermal conduction path for the USMB is through the drive linkage which has a cross sectional area of only 31.25 mm^2. In comparison, the LSMB is rigidly bolted to the base plate. In order to reduce the conduction path between the LSMB and the rig frame, the LSMB sits on four MGC *feet* and the base plate has a 50 % reduced contact area with the rig frame, achieved through a machined profile. Furthermore, to reduce radiative and convection losses, the LSMB is enclosed in an insulated box—the voids between the outer box and LSMB are filled with a high temperature fibre insulation.

Finally, the LSMB has an integral oil bath with both inlet and outlet ports to enable lubricant to be flushed through the contact. The lip for the oil bath additionally encloses the specimens leading to an isothermal state when operating at elevated temperatures.

Displacement measurement

The applied displacement is measured by a high accuracy LVDT[§]; the LVDT body is rigidly mounted to the LSMB and the armature is spring loaded against the moving USMB (Figure 3.15). Since the components between the measuring points are unstressed, the LVDT consequently measures a displacement almost identical to the applied relative displacement (between the lower surface of the flat specimen and the upper surface of the cylindrical specimen); any observed elasticity is therefore due to the elasticity of the specimens. To *zero* the LVDT at the beginning of a test and also to allow it to be moved clear of the USMB for mounting and removal of specimens, a micrometer head is integrated into the mount; during a test, the LVDT is clamped in position.

[‡]MGC has a thermal conductivity of 1.46 $W\,m^{-1}\,K^{-1}$ compared to 15.9 $W\,m^{-1}\,K^{-1}$ for 316 stainless steel (both at 25 °C). Additionally, the coefficient of thermal expansion is not very dissimilar to 316 stainless steel: $11.4 \times 10^{-6}\,°C^{-1}$ compared to $17.5 \times 10^{-6}\,°C^{-1}$.

[§]RDP Electronics, model: GT500Z, range: ±0.5 mm

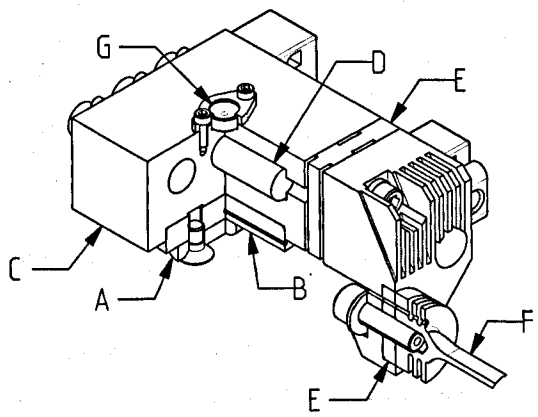

(a) USMB

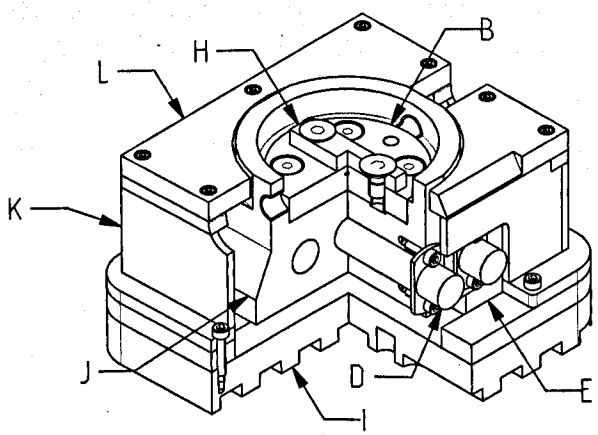

(b) LSMB

Figure 3.13: Cut away views of the specimen mounting blocks, labelled components are: (A) cylindrical specimen, (B) SMP, (C) USMB, (D) cartridge heater, (E) thermal bulkhead, (F) drive linkage, (G) load-bar locating socket, (H) flat specimen, (I) base plate, (J) LSMB (K) thermal box, (L) thermal lid.

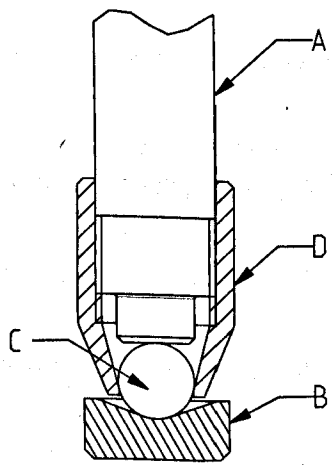

Figure 3.14: Diagram showing the detail of the load-bar contact points: (A) load bar, (B) locating socket, (C) ceramic ball, (D) retaining cap.

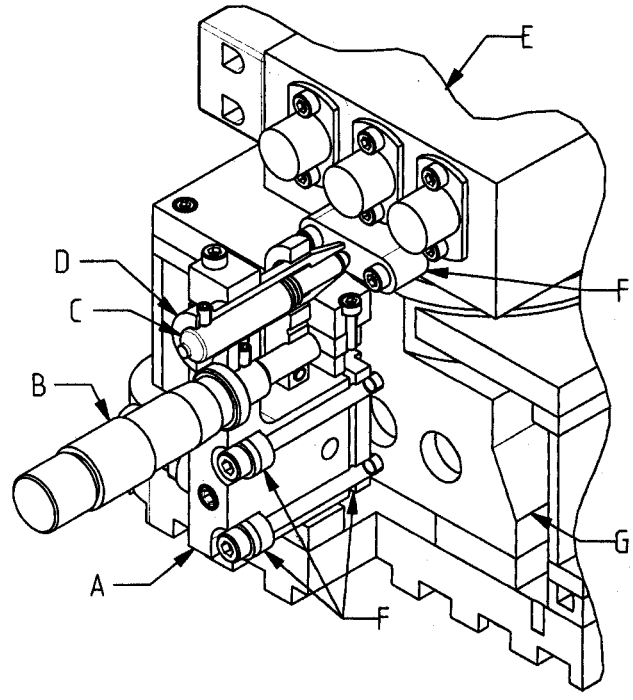

Figure 3.15: Detailed diagram of the LVDT mounting: (A) water-cooled mount, (B) micrometer head, (C) LVDT, (D) copper sleeve, (E) USMB, (F) thermal bulkhead(s), (G) LSMB.

As the LVDT mount is in intimate contact with the heated specimen mounting blocks, it must be actively cooled to maintain the LVDT within its operational limits (−40 to 100 °C). Water ports are integrated into the mount and thermal bulkheads are used to reduce the heat flux into the mount. The LVDT has a point contact with an MGC plate attached to the USMB (minimising heat transfer). The LVDT is housed within a copper sleeve which cools the LVDT by conduction. Additionally, the LVDT has a 15 mm stainless steel extension which significantly reduces the heat transmitted to the armature.

The additional mass of the armature extension may raise concerns that the LVDT could *lift-off* (i.e., lose contact) at the test frequency due to its increased inertia. However, it can be shown, assuming a sinusoidal displacement profile, that the LVDT will remain in contact with the USMB until a critical frequency of:

$$\omega \geq \sqrt{\frac{F_s + k\Delta^*}{m\Delta^*}} \tag{3.2}$$

where $k = 1.7 \times 10^{-2}\,\mathrm{N\,m^{-1}}$ is the spring stiffness of the internal spring, $\Delta^* = 100\,\mu\mathrm{m}$ is the amplitude of motion, $m = 3.5 \times 10^{-3}\,\mathrm{kg}$ is the mass of the armature and $F_s = 1\,\mathrm{N}$ is the pre-load force of the spring at the *zero* position; this gives a maximum frequency of $\omega = 270\,\mathrm{Hz}$—far in excess of the range of interest and above the electrical bandwidth of the signal conditioning (250 Hz).

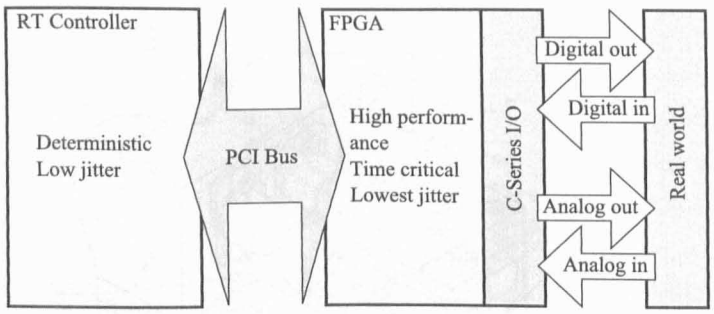

Figure 3.16: Diagram illustrating the hardware architecture of a cRIO.

3.4.2 Supervisory control and data acquisition system overview

Technologies and hardware

The supervisory control and data acquisition (SCADA) system has been programmed in LabVIEW™ (LV), a proprietary language developed by National Instruments (NI). LV is a multi-platform, data flow, graphical programming language where a program is represented as a directed graph rather than text. Data flow languages offer inherent parallelism enabling efficient programming of modern multicore CPU architectures. LV is increasingly adopted for "big science" projects such as the CERN LHC, Lowell Discovery Channel Telescope and others [165, 166].

The target hardware used for the SCADA system is an NI compactRIO (cRIO), communicating via a network with a PC (Figure 3.16 shows a breakdown of the system architecture). A cRIO is a dedicated programmable automation controller, designed for high performance embedded control and data acquisition tasks.

Input and output is via c-series modules; these are plug-in modules incorporating digital to analogue converters, analogue to digital converters and any signal conditioning as required, in an integrated package. All data is then routed through the field programmable gate array (FPGA); an FPGA may be thought of as a user configurable application specific integrated circuit (ASIC), offering all of the associated performance and reliability benefits of without the cost or inflexibility. Code running on an FPGA is essentially "software in hardware".

The next layer of the architecture of the cRIO is the real-time (RT) controller. This is essentially an embedded PC, connected to the FPGA via a dedicated PCI bus. The controller runs a real-time operating system (RTOS), in this case VxWorks™. An RTOS prioritises determinism ahead of performance by implementing pre-emptive multitasking (rather than cooperative multitasking as in a desktop operating system) to allow higher priority tasks to pre-empt lower priority tasks. This allows high priority (control) tasks to run in a deterministic manner while sharing the CPU with lower priority tasks, such as communicating over the network.

The final layer of the system architecture is the PC which runs non-critical tasks such as the graphical user interface (GUI). The PC communicates with the cRIO via

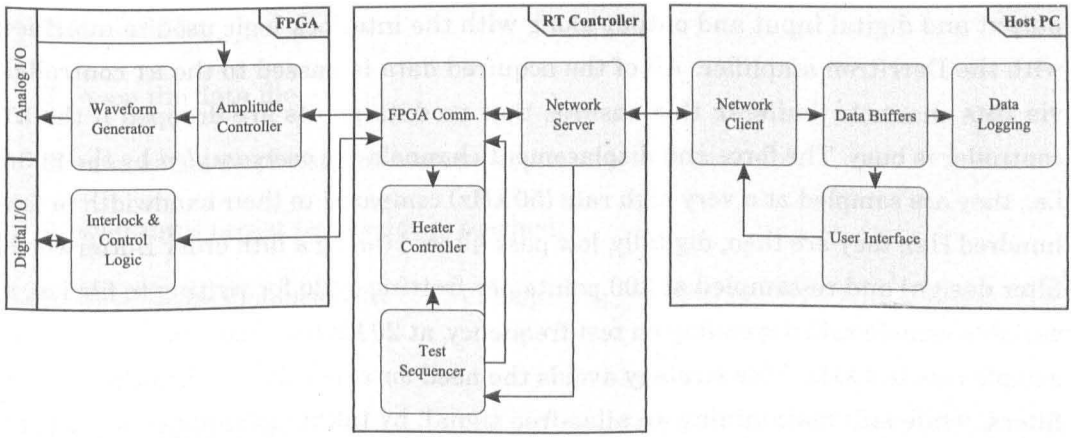

Figure 3.17: Diagram showing the main processes in the SCADA system software and how they correspond to the hardware architecture.

a standard 100 Mbit s^{-1} Ethernet connection using a custom written communication protocol.

An important consideration in the system design was the choice of file format. Data produced by the rig is expected to be used in future projects and as such should be archived in a suitable format, defined by meeting the following requirements: (a) readable in any language for post processing (i.e., an open format); (b) inherent meta-data linking data to test parameters (also implying that the files are searchable by this meta-data); (c) high performance, for streaming data to disk. Very few formats can satisfy these parameters and, after reviewing the possibilities, the author is only aware of two: HDF5 [167] and TDMS [168]. Both formats have a similar underlying hierarchical data model, which is ideal for representing time-series channel based test data. Of the two formats, HDF5 is technically more extensible, and consequently may be considered the *better* format, but as TDMS is natively supported by LV it was selected as the file format for the test rig.

Software

The SCADA system performs several parallel, independent tasks, the most important of which are outlined below in the following paragraphs; Figure 3.17 gives a diagram illustrating these and where they are executed on the hardware.

Each task maps to a software *component* [169]; a component is a discrete software module with a clearly defined set of responsibilities and interface. This approach enables the code to be granular in nature (loose coupling between components), significantly easing testing and debugging of a complex system. In LV, each component is realised as an independent loop, typically itself a state machine, which communicates in an asynchronous manner with other components via a message queue.

Highly deterministic, critical tasks are delegated to the FPGA, these are: data acquisition, displacement signal generator, displacement amplitude control, control

output and digital input and output along with the interlock logic used to interface with the Derritron amplifier. All of the acquired data is passed to the RT controller via DMA channels (buffers); this ensures that no data points are dropped if the RT controller is busy. The force and displacement channels are *oversampled* by the FPGA i.e., they are sampled at a very high rate (50 kHz) compared to their bandwidth (a few hundred Hz); they are then, digitally, low pass filtered (using a fifth order Butterworth filter design) and re-sampled at 200 points per fretting cycle for writing to file i.e., a variable sample rate depending on test frequency, at 20 Hz test frequency the default sample rate is 4 kHz. This strategy avoids the need for expensive analogue anti-alias filters, while still maintaining an alias-free signal, by taking advantage of the very high throughput of the FPGA.

The current control strategy controls the displacement amplitude, rather than the full displacement profile. To do this, a custom signal generator (utilising direct digital synthesis (DDS)) was implemented; this generates a high accuracy sinusoid which is output to the power amplifier driving the EMV. Running in parallel to this is an amplitude detector which analyses the preceding cycle to determine the *actual* displacement amplitude. Another parallel process takes the desired displacement amplitude and the actual displacement amplitude and uses a proportional integral derivative (PID) algorithm to reduce the error between the two by modulating the amplitude of the sinusoid generated by the signal generator.

The RT controller runs four parallel processes: FPGA communication, heater control, data logging, network communication and test control. These are prioritised such that more critical (i.e., control tasks) pre-empt lower priority tasks, allowing the control tasks to run in a deterministic manner.

The test control component is a *sequencer*; it receives an array of *steps* and executes them in order. These *steps* are small tasks such as: setting the set point for the heaters; waiting for the specimen mounting blocks to reach the required temperature; setting the displacement amplitude; wait for x milliseconds; waiting for n displacement cycles to be completed etc. Which particular tasks are executed and their order of execution is completely flexible and configurable at run-time; a full test sequence is generated by concatenating several of these steps. This approach gives the test rig a significant degree of flexibility and allows new (and potentially very different) tests to be defined in the future. Currently a test generally consists of the following steps:

1. set USMB and LSMB heater set-points,
2. enable the heaters,
3. set the displacement amplitude set-point,
4. set the target number of test cycles,
5. wait for the heaters to reach their target temperature,

6. wait 300 s,
7. open the data file,
8. enable the displacement control loop,
9. wait until target test cycles is reached,
10. disable the displacement control loop,
11. disable the heaters,
12. close the data file.

The GUI runs completely independently (asynchronously) on a PC; a screenshot is shown in Figure 3.18. The GUI communicates with the cRIO via a custom written messaging protocol over an Ethernet connection. The GUIs primary tasks are to allow the user to easily configure a test and monitor its progress. To facilitate this, there are live plots of the displacement, tangential force, displacement amplitude and COF. The plots of the displacement and tangential force are *triggered* (similar to an oscilloscope) such that the user views a quasi-static waveform.

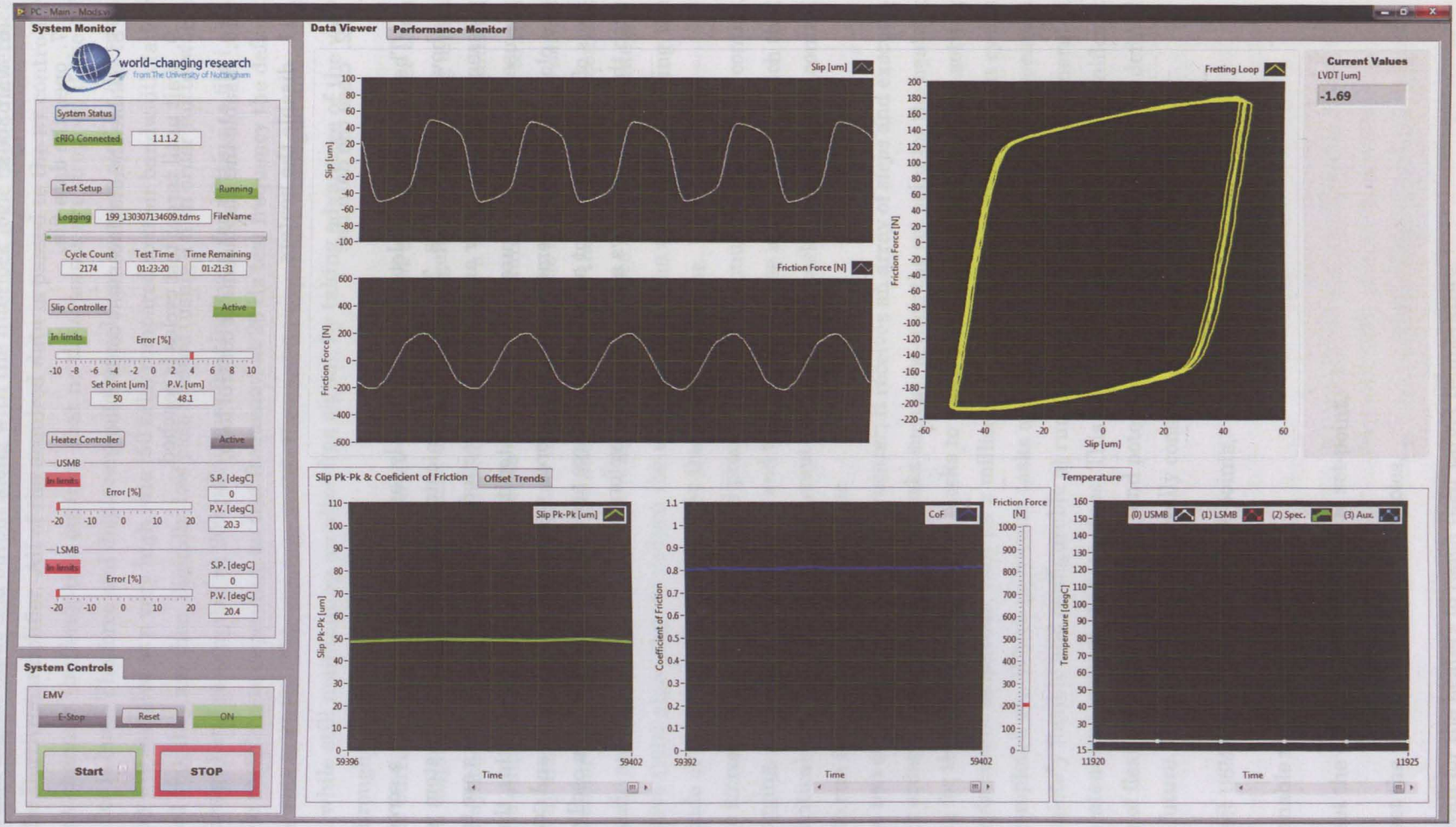

Figure 3.18: A screenshot of the GUI for the new fretting test rig.

Chapter 4

Experimental Method

4.1 Materials and specimens

All specimens were manufactured from SCMV, a high strength alloy steel derived from BS 3S 132:197 (a chromium-molybdenum-vanadium alloy steel) [13]. SCMV was developed by Rolls-Royce to meet the requirements of the Trent series of engines; it allowed the torque density per unit shaft diameter of the LP shaft to be doubled while reducing the weight per unit torque by 25 %. Compared to the parent steel, the chemistry was adjusted to improve the hardenability and a triple vacuum melt process improved the cleanliness of the steel and consequently its fatigue life [13]. The chemical composition of SCMV is given in Table 4.1; Leen et al. [11] previously reported SCMV to have an elastic modulus of 206.8 GPa and a Poisson's ratio of 0.28.

The test material was firstly cut into blanks, with a machining allowance on all dimensions. The blanks were heated (in an air atmosphere) to 940 °C and held for 45 min, after which they were oil quenched; subsequently, they were tempered at 570 °C for 120 min and finally air cooled.

To achieve the final specimen dimensions (Figure 4.2), a minimum of 0.5 mm was ground from the top and sides of the flat specimen and similarly from the curved surface of the cylindrical specimen. Post machining, the Vickers (HV20) surface hardness of seven flat and seven cylindrical specimens was measured (6 readings were taken for each specimen); additionally, a random flat and cylindrical sample was selected, sectioned and core hardness (HV20) and micro-hardness (HV0.5) (as a function of depth from the surface) measurements were made—the relevant results are given in Table 4.2 and the profiles are presented in Figure 4.3. It is apparent that the surface hardness values are consistent with the bulk value, confirming that the softer decarburised

Table 4.1: Composition of SCMV (wt. %) [153].

C	Si	Mn	P	S	Cr	Mo	Ni	V	Fe
0.35–0.43	0.1–0.35	0.4–0.7	< 0.007	< 0.002	3.0–3.5	0.8–1.1	< 0.3	0.15–0.25	Balance

Table 4.2: Core and surface hardness of the plain specimens (uncertainties are the standard error).

	Hardness / GPa	
Specimen	Surface	Core
Flat	4.80 ± 0.02	4.800 ± 0.003
Cylinder	4.90 ± 0.02	4.816 ± 0.002

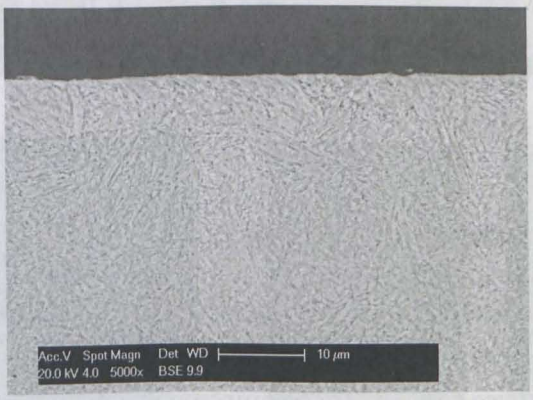

Figure 4.1: SEM micrograph showing the microstructure of a plain SCMV specimen.

layer was removed. A slightly higher hardness is reported for the cylindrical specimen; this is thought to be an inaccuracy resulting from making an indentation in a curved surface. Figure 4.1 is a micrograph of a sectioned SCMV specimen, etched to highlight the microstructure. Engineering drawings for the specimen blanks and specimens are available in Appendix A, Figure A.1 and Figure A.2.

4.1.1 Nitriding

A number of specimens were nitrided by Electroplus[†] using a pulsed plasma nitriding process (for an overview of the nitriding process see Section 2.7.4, Page 35), these

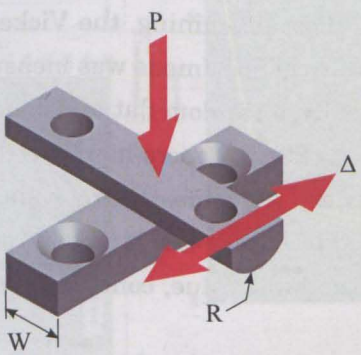

Figure 4.2: Diagram of the specimens and their arrangement in the fretting test: $W = 10\,\text{mm}$, $R = 6\,\text{mm}$, P = normal load, Δ = applied displacement.

[†]ELECTRO GB Ltd., Unit B4 Armstrong Mall, Southwood Business Park, Farnborough, Hampshire, GU14 0NR. Tel: (+44)1252 523 000

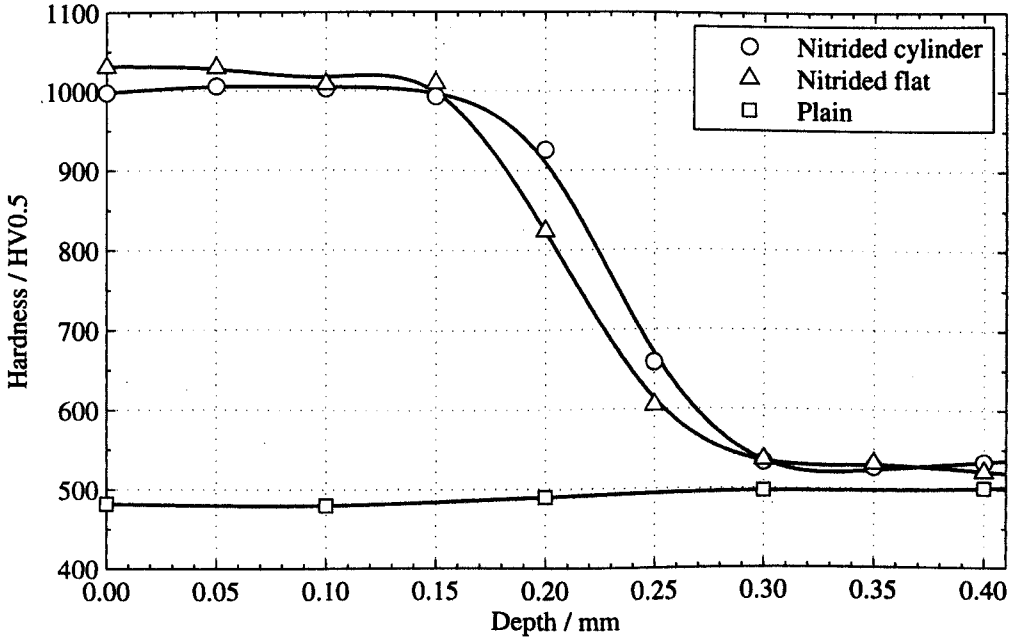

Figure 4.3: Hardness profiles through the specimens for both the SCMV and SCMVN materials.

are referred to as SCMVN specimens. Subsequent sectioning and micro-hardness testing of one randomly selected flat and one randomly selected cylindrical specimen revealed the case depth to be 0.25 mm and 0.28 mm (where the case is defined as core-hardness+0.98 GPa) and the average surface hardness to be 10.1 GPa and 9.8 GPa respectively (corresponding micro-hardness profiles are shown in Figure 4.3).

Figure 4.4a shows an SEM micrograph top view, and Figure 4.4b a cross-section, of a SCMVN (flat) specimen. The WL, clearly seen in the cross section, is approximately 10 μm thick and appears to have a dense structure with finger like protrusions extending up to 20 μm into the diffusion layer; X-ray diffraction (XRD) analysis (Figure 4.5) concluded that the WL is composed, predominately, of $Fe_{2-3}N$ and Fe_4N. Many cracks can be seen in Figure 4.4c, illustrating the brittle nature of the WL. From micro-hardness profiles (Figure 4.3), it is evident that the diffusion layer extends up to 150 μm and transitions to the substrate from 150 to 300 μm below the surface. Figure 4.4a shows that the surface finish of the WL has a micro-granular appearance; some slight vertical striations are visible which are thought to be associated with the lay from the grinding operation.

4.2 Calibration of the test rig

Fixtures were designed and manufactured in order to calibrate the load cell which was built for the fretting test rig, under both tension and compression, using an Instron tensile test machine and a reference load cell (Figure 4.6).

As the sensing elements of the load cell are piezoelectric, they are not suited to

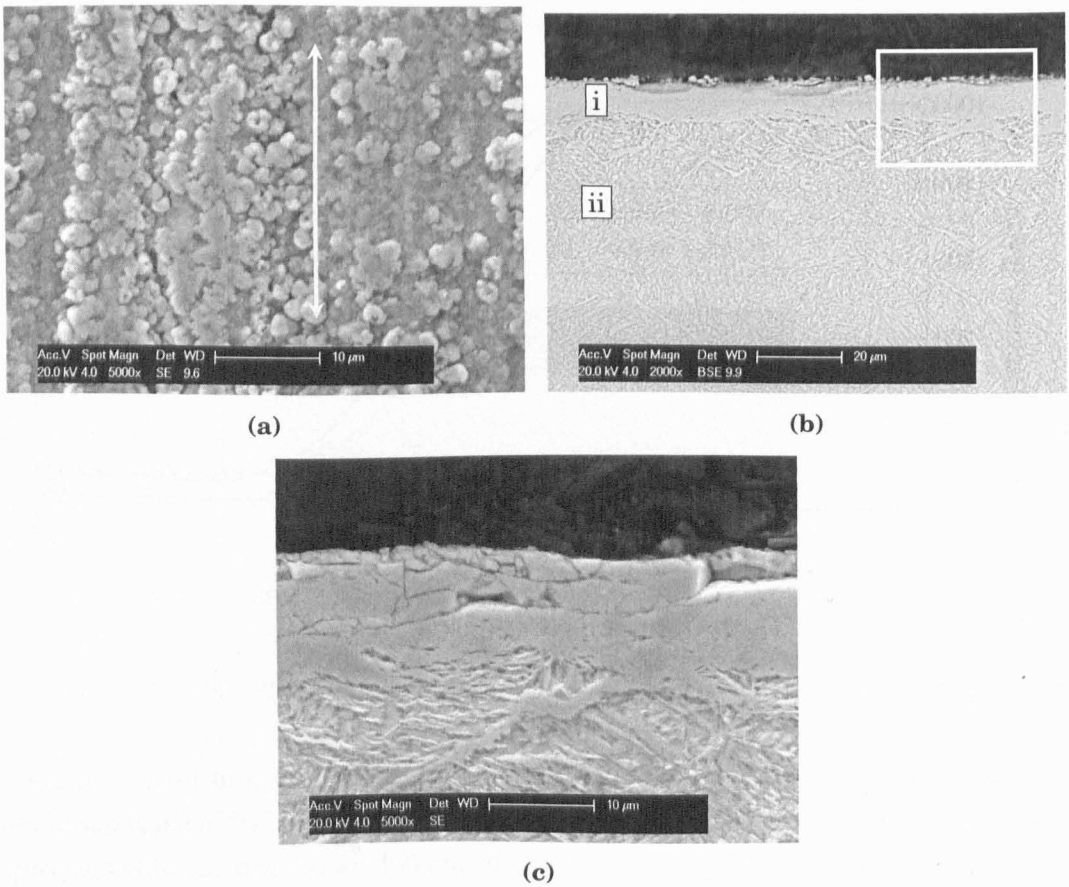

Figure 4.4: SEM micrographs showing microstructure of the nitrided specimens and the thickness of the WL: (a) SE top view, white arrow indicates surface grinding direction; (b) BSE cross-section, (i) white layer, (ii) diffusion zone; (c) high magnification SE view of the highlighted area in b showing the brittle nature of the WL.

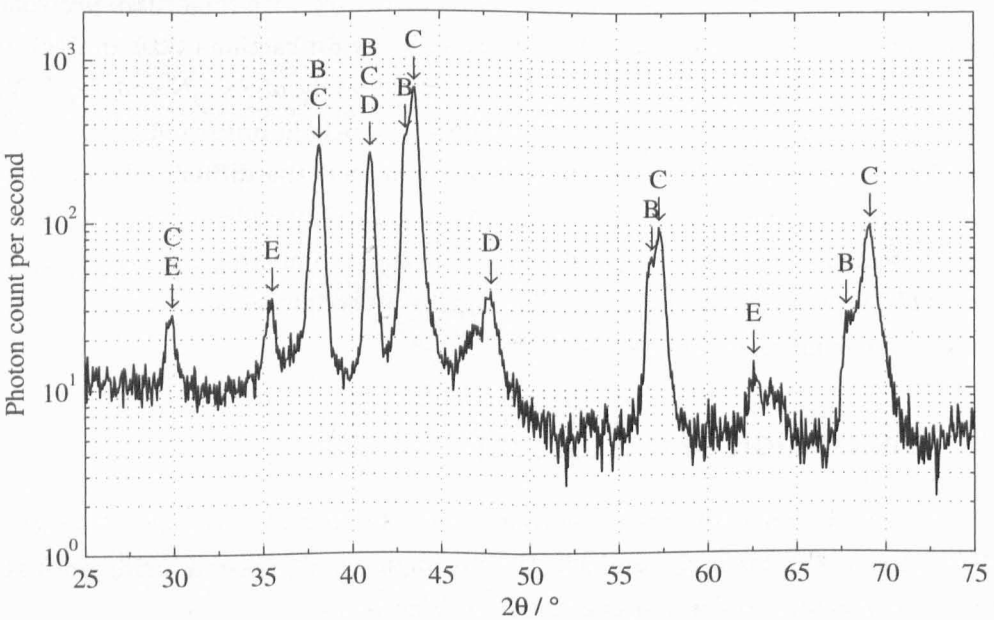

Figure 4.5: XRD spectrum of the nitride WL: (B) Fe_2N, (C) Fe_3N, (D) Fe_4N, (E) Fe_3O_4.

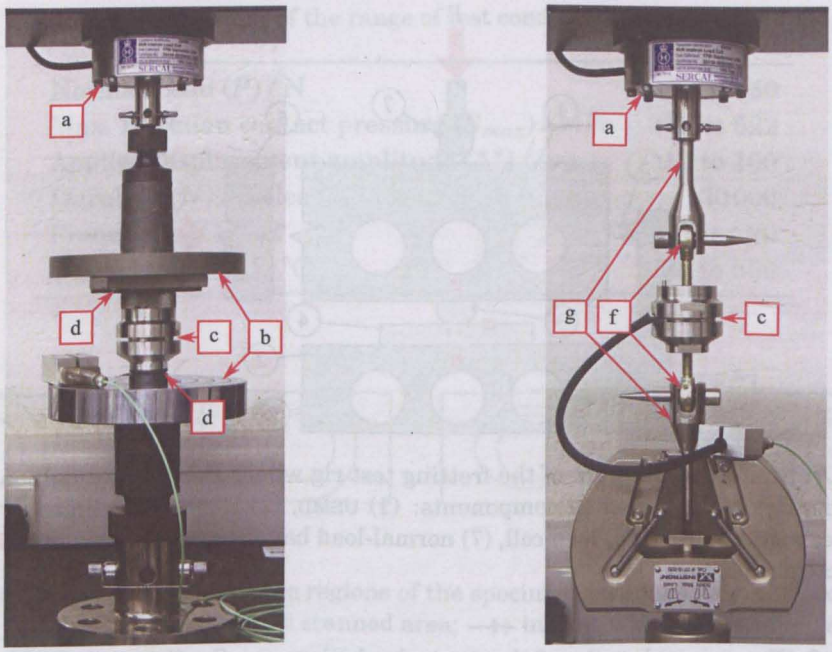

(a) Compression (b) Tension

Figure 4.6: Photographs of the load cell calibration fixtures with labelled components: (a) reference load cell, (b) parallel loading plates, (c) load cell under calibration, (d) spherical alignment washer, (e) 4 mm rubber pad, (f) rod ends and (g) calibration jaws.

measuring static loads due to charge leakage. To account for this, the charge amplifier was initially reset and then the reference load was applied in a single step. The load was then held for constant for a period of 2 s, after which the amplifier was reset and the load was removed allowing a "mirror" reading to be taken. This was later found to be unnecessary as the drop-off during the load hold was found to be negligible ($< 1\,\%\,h^{-1}$). The readings from the load cell and the reference load cell were continuously logged to file (at 1 kHz). To create a calibration point, the data points from each load step 'hold' were averaged to give a single reading from the load cell under calibration and the reference load cell. This procedure was repeated three times, for eight load steps, in tension and compression for both loading and unloading over the range ±2 kN. The results provided a single gain factor (in $V\,N^{-1}$) for the load cell and indicated that it was linear over the region of interest and displayed no measurable hysteresis.

The LVDT was similarly calibrated using a reference drum micrometer over a range of ±250 µm to give a gain factor in $V\,\mu m^{-1}$. The calibration showed (as may be expected) that the LVDT was linear over the full range.

4.3 Test methodology

The tests were all conducted using a crossed cylinder-on-flat arrangement, generating a 10 mm line contact (Figure 4.2). A schematic diagram of the test rig is given in

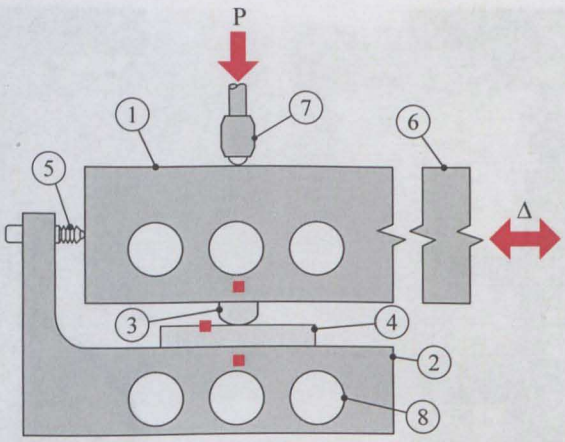

Figure 4.7: Simplified diagram of the fretting test rig where P is the normal load, Δ is the applied displacement. Labelled components: (1) USMB, (2) LSMB, (3) cylindrical specimen, (4) flat specimen, (5) LVDT, (6) load cell, (7) normal-load bar, (8) cartridge heaters; ■ indicates a thermocouple location.

Figure 4.7 (For more details of the test rig design see Section 3.4, Page 50). The flat specimen was attached to the stationary LSMB and the cylindrical specimen to the moving USMB. Before tightening the coupling between the USMB and the load cell, a small load (50 N) was put on the mass hanger, ensuring that the surfaces of the specimens were parallel. Prior to testing, the specimens were demagnetised, thoroughly degreased using detergent, rinsed with industrial methylated spirit (IMS) and finally dried using a hot air dryer.

An oscillatory displacement, Δ (of amplitude Δ^*), and a fixed frequency of 20 Hz was applied to the USMB by an EMV. The relative displacement between the USMB and LSMB was measured by an LVDT. A constant normal load, P, was applied to the USMB via a dead weight and a balanced lever arm (with a 5:1 ratio). The tangential traction forces were measured using a piezoelectric load cell between the EMV and the USMB.

For conducting elevated temperature tests, cartridge heaters are integrated into both the USMB and LSMB with thermocouples (type K, ⌀ 1 mm) located above and below the specimens (embedded 3 mm below the mounting face). Independent temperature control loops are implemented for the USMB and LSMB, ensuring that no thermal gradient exists across the specimen pair. An additional thermocouple was spot welded onto the top surface of the flat specimen (approximately 8 mm from the contact) in order to monitor the temperature in the region of the contact; in all tests, the deviation between the surface temperature and the temperature reported by the embedded thermocouples was relatively small (less than 1.5 °C at 85 °C and less than 3.5 °C at 450 °C).

Fretting tests were conducted across a range of normal loads, applied displacement amplitudes and temperatures; a summary is given in Table 4.3, and more details are given in the relevant results chapters. All tests were conducted in a normal laboratory atmosphere.

Table 4.3: A summary of the range of test conditions used in this work.

Normal Load (P) / N	250 to 650
Max. Hertzian contact pressure (S_{max}) / MPa	386 to 622
Applied displacement amplitude (Δ^*) / μm	10 to 100
Duration (N) / cycles	100000
Frequency (f) / Hz	20
Temperature (T) / °C	24 to 650

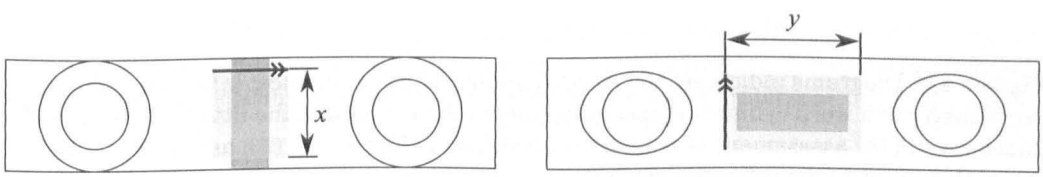

(a) Flat (b) Cylinder

Figure 4.8: Diagram indicating the regions of the specimens scanned with the profilometer: $x = 8$ mm, $y = 13$ mm; ■ wear scar; ▒ scanned area; ⟶ indicates profile direction, all profiles taken at a 250 μm spacing.

4.4 Assessment of worn surfaces

Following a fretting test, quantitative assessment of the wear was conducted using tactile profilometry. Qualitative assessment, to aid identification of the operative wear mechanisms, was achieved using optical microscopy and SEM, with additional examination of cross-sectioned specimens as required. Further chemical characterization was made, as necessary, using energy dispersive X-ray spectroscopy (EDX). Details of the methods and equipment used are given in Sections 4.4.1 to 4.4.3.

4.4.1 Profilometry

A contact profilometer (Taylor-Hobson Talysurf CLI 1000) with a fine diamond stylus (90°, 2 μm radius) was used to measure the surface profile of the worn specimens. Prior to scanning, the specimens were rinsed with IMS to remove any debris not adhered to the surface. As the wear scar extends the full width of the flat specimens, profiles were taken over only the central 8 mm of the scars, with a 0.25 mm spacing between profiles; measurements were taken at 1 μm intervals along each profile. For the cylindrical specimen, similarly spaced profiles were taken over an area completely spanning the wear scar (Figure 4.8).

This process gives a mesh with a very high aspect ratio; however, the contact is a line contact and, consequently, predominantly 2D. The orientation of the mesh is such that the densest grid spacing is in the same direction as the highest information density i.e., across the scar. Moreover, the scan time is essentially proportional to the number of profiles (not the number of points per profile), so to achieve a uniform mesh would increase the scan time by a factor of 250.

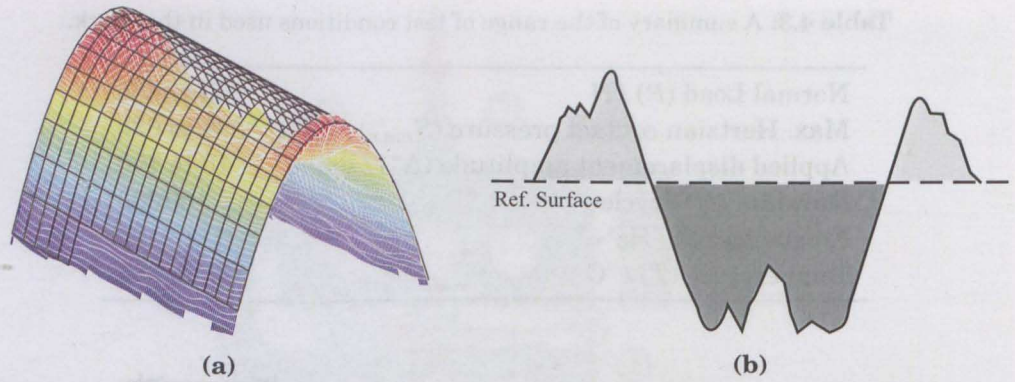

Figure 4.9: Diagrams indicating the assessment of the wear volumes: (a) surface obtained by profilometry of a worn cylindrical specimen (coloured surface) and the fitted reference surface (black mesh); (b) assessment of transfer material transferred, V^+ (■), and material lost, V^- (■), with respect to the reference surface.

In order to estimate the wear volume, a reference (unworn) surface must be determined. In the case of the flat specimen, the reference surface was defined as the best fit plane to all points outside of the wear scar. However, definition of the reference surface is more difficult for the cylindrical specimen. When conducting the profilometry, it was ensured that the first and last profiles were always entirely outside of the worn area. A polynomial fit was then taken for these two profiles and an estimate of the unworn surface was generated by interpolating between these two fitted profiles—illustrated by the mesh in Figure 4.9a. Any material build-up above the reference plane (for either the flat or cylindrical specimen) is considered to be transferred material or debris, and is defined by a positive volume (V^+); any loss of material from below the reference plane is defined as a negative volume (V^-) (Figure 4.9b). The overall wear volume (V^w) is then defined as follows:

$$V^+ = V^+_{cylinder} + V^+_{flat} \tag{4.1a}$$

$$V^- = V^-_{cylinder} + V^-_{flat} \tag{4.1b}$$

$$V^w = V^+ + V^- \tag{4.1c}$$

The surface height measured by the profilometry (z_m) is a discretized representation of the true surface $z = f(x,y)$. A wear volume is calculated by numerically integrating (using the trapezium rule) the residual surface, z_r, which is the difference between the unworn and worn surfaces ($z_r = z_0 - z_m$). The previously defined wear volumes are then calculated as

$$V^+ = \iint_A z_r \, dx dy \quad \text{for } z_r > 0 \tag{4.2a}$$

$$V^- = \iint_A z_r \, dx dy \quad \text{for } z_r < 0 \tag{4.2b}$$

$$V^w = \iint_A z_r \, dx dy \quad \text{for all } z_r \tag{4.2c}$$

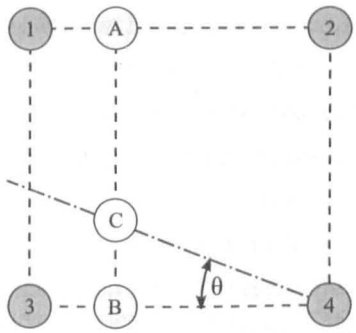

Figure 4.10: Diagram indicating bilinear interpolation used to rotate the profilometry data by an angle θ; points 1–4 are original data points, point A is found by interpolating 1–2, point B is found by interpolating 3–4 and the final point C is found by interpolating A–B.

The software supplied with the profilometer was unable to provide the required functionality, particularly the form removal for the cylindrical specimen. As a consequence, custom software (written by the author in Matlab™) was used to process all of the profilometry data. The software provides a GUI tool to enable the user to interactively define the wear scar and limit the volume integral to that region. These limits are also used to centre the wear scar for later graphical presentation.

Since the wear scars are of a predominantly 2D nature, they may be represented by a single, average, profile. In order to collapse the 3D data set into a 2D profile, the scar must be orientated parallel to the axis along which the data is averaged. Since the profilometer defined no accurate axis, a rotation function is included in the software written for the project. This function used bilinear interpolation (Figure 4.10) to allow the user to rotate the data set so that the wear scar is parallel to the axis.

After running the custom software, a new results file is produced containing the calculated values of V^+, V^-, V^w, the maximum height and depth found on the surface and the 2D profile of the wear scar.

4.4.2 Microscopy

Initial assessment of the worn specimens was conducted using a binocular optical microscope. Specimens which showed interesting features (identified by either the profilometry or optical examination) were sectioned and examined by SEM.

The specimens were sectioned using a Struers Accutom-5 precision cut-off machine fitted with an alumina abrasive wheel[‡]. To aid the subsequent location of shallow wear scars under the the microscope, a small hacksaw cut was made either side of the wear scar.

Sectioned specimens were mounted in conductive black phenolic resin according to the manufacturers instructions. After mounting, the specimens were manually ground using silicon-carbide grinding paper (initially a P240 grit, and then progressing through to a P1200 grit), then polished to a mirror finish using diamond impregnated

[‡]a rotational speed of 3000 rpm and a feed speed of $0.03\,\mathrm{mm\,s^{-1}}$ was used

pads (first to 6 µm and finally to 1 µm). To better reveal the microstructure, and aid differentiation between debris and substrate material, the sectioned specimens were etched using 2 % Nital for approximately 15 to 20 s.

A Philips XL30 scanning electron microscope, fitted with a Lanthanum Hexaboride (LaB_6) filament, was used for SEM. The microscope was typically operated with an accelerating voltage of 20 kV and a working distance of 10 mm. Images were taken using both secondary electron (SE) and back scattered electron (BSE) imaging techniques; BSE imaging is particularly useful since it shows contrast proportional to the average atomic number of the materials being imaged; hence, it allows the oxide debris formed in fretting to be readily distinguished from the metallic substrate.

4.4.3 Energy dispersive X-ray spectroscopy

Where necessary, more quantitative chemical characterisation of features observed in the SEM was achieved with energy dispersive X-ray spectroscopy (EDX) analysis. An EDAX™CDU LEAP detector was used, with a 10 kV beam accelerating voltage.

4.5 Data acquisition and post-processing

After a fretting test run (of 10^5 cycles), the rig will produce a data file of approximately 500 MB. This file contains all of the data relevant to the test as well as meta-data describing the test parameters. The majority of the data in the file is the tangential force, displacement and cycle-count channels; these are sampled at 4 kHz, resulting in 200×10^6 data points per channel, and 200 readings per cycle (at 20 Hz). For immediate visualisation and initial data processing, a program called DIAdem, from NI, was used; DIAdem is designed for handling large datasets and is capable of managing in excess of 65×10^3 channels with over 2×10^6 values per channel (actually 2^{16} and 2^{31} respectively). A number of parameters are derived from the raw data; these are outlined in Sections 4.5.1 to 4.5.4. Once calculated, the derived parameters were written to disk along with the raw data so that they could be easily, and quickly, loaded for plotting and analysis.

4.5.1 Sliding amplitude

The sliding amplitude, δ^*, is always less than the applied displacement amplitude, Δ^*, due to elastic deflection of the structures (mainly the specimens) between the points where the relative displacement is measured (see Figure 2.10, Page 15).

The sliding amplitude can be assessed by measuring the fretting loop aperture i.e., the difference between the displacement at the beginning and end of a cycle, when the tangential force, Q, is zero. The two positions in a cycle where $Q = 0$ can be distinguished from each other, as one is associated with a positive-negative zero crossing and the other with a negative-positive zero crossing. In order to locate these

positions, a new force channel (vector) $\mathbf{Q_{n+1}}$ is created from the original force vector, $\mathbf{Q}$, by deleting the first element in $\mathbf{Q}$. A logical array, $\mathbf{L}$, containing logical-true at the index immediately before negative-positive zero crossings, and logical-false in all other positions, is found by evaluating Equation (4.3) in an element-wise manner.

$$\mathbf{L}^{-} = (\mathbf{Q} \leq 0) \wedge (\mathbf{Q_{n+1}} > 0) \tag{4.3}$$

$\mathbf{L}^{-}$ can then be used as a *mask* to identify the corresponding value of Δ at the zero crossings, resulting in a new vector, $\mathbf{C}^{-}$. By suitably modifying the inequalities in Equation (4.3), a corresponding vector, $\mathbf{C}^{+}$, of the values of Δ at the positive-negative zero crossings can be found. A vector, $\mathbf{D}$, containing elements corresponding to $2\delta^*$ (twice the sliding amplitude) for every cycle can then be calculated as:

$$\mathbf{D} = \mathbf{C}^{+} - \mathbf{C}^{-} \tag{4.4}$$

The total *slid* distance, L, for a test of n cycles can subsequently be calculated by summing the elements in $\mathbf{D}$:

$$L = 2\sum_{i=1}^{n} \mathbf{D}_n \tag{4.5}$$

4.5.2 Dissipated energy

The dissipated energy per cycle, E_d, (visualised by the area enclosed by the fretting loop) is calculated as:

$$E_d = \int Q \, \mathrm{d}\Delta \tag{4.6}$$

It is actually calculated by finding the cumulative dissipated energy as a new time-series channel and using the cycle-count channel to find the cumulative dissipated energy at the start and end of each cycle; the dissipated energy of a cycle is then the difference between those values.

4.5.3 Coefficient of friction

The COF may be naïvely calculated as the ratio of the maximum tangential force (Q^*), seen in any cycle, to the applied normal load i.e., $\mu = Q^*/P$. This is representative if the fretting contact is freely sliding and the loop appears as a parallelogram with the upper and lower sides parallel to the displacement axis (Figure 2.10, Page 15). However, experimentally acquired loops often appear more diamond-like in shape i.e., the tangential force is observed to increase during the sliding stroke. Alternatively, sudden force peaks may be observed toward the end of the sliding stroke (Figure 6.2, Page 136). Respectively, these effects are attributed to plasticity [170, 171] and the build up of material at the extreme edges of the wear scar [172].

As a consequence of this behaviour, the non-dimensional tangential force ratio (Q^*/P) is no longer an effective estimate of the COF. To account for this, Fouvry et al.

[172] proposed an estimate for the COF (μ_e) based on the dissipated energy per cycle, which is less sensitive to such behaviour (Equation (4.7)). Throughout the remainder of this work, μ_e is used as the definition of the COF.

$$\mu_e = \frac{E_d}{4P\delta^*} \tag{4.7}$$

As the data is acquired continuously for the test, it is possible to calculate $\delta*$ and E_d for every cycle (Sections 4.5.1 and 4.5.2); since P is constant for a test, then μ_e can similarly be calculated for every test cycle.

4.5.4 Wear rate

In fretting, wear is typically quoted directly as a volume of material lost (e.g., in mm^3); alternately, a dimensional form of Archard's wear constant [173, 174] is given in terms of the volume of material lost per unit normal load and per unit slid distance (e.g., a specific wear rate in $mm^3\,N^{-1}\,m^{-1}$). Quoting a dimensional value makes sense since it is generally accepted that under fretting, the wear coefficient is dependent on the sliding regime (see Section 2.3.3, Page 16).

Mohrbacher et al. [175] found that, during the fretting of a TiN coated contact, the fretting wear volume was a linear function of the dissipated frictional energy i.e., derived a wear rate in units of $mm^3\,J^{-1}$. Using this approach, a linear relationship between the wear volume and dissipated energy has been found under a wide range of test conditions and for a variety of materials, particularly by Fourvy et al. [99, 108, 176, 177].

If the two methods are compared, it can be seen that they are, in fact, equivalent—accordingly, it is not surprising that wear rates for both methods have the same units ($mm^3\,J^{-1} \equiv mm^3\,N^{-1}\,m^{-1}$). If the Archard wear equation is considered (Equation (4.8)), it states that the wear volume, Q, is proportional to WL where W is the normal load and L is the slid distance.

$$Q = \frac{KWL}{H} \tag{4.8}$$

Other variables are K, which is the dimensionless wear constant and H, the hardness of the softer of the contacting surfaces. Therefore for a given material pair, the equation may be restated as:

$$Q = AWL \tag{4.9}$$

where A is a new constant, incorporating K and H; A may also be assumed to include the COF, μ, such that the equation could be written as:

$$Q = B\mu WL \tag{4.10}$$

where B is a new constant. If L is taken to be the actual slid distance rather than the applied displacement (see Section 4.5.1), then μWL is the frictional work done at the

contact, E_d.

The difference between the approaches is in what is measured and assumed: using the dissipated energy approach, the *actual* tangential force is measured as a function of cycles, as is the *actual* sliding distance (both implicit by the use of the dissipated energy) and it is not assumed that the COF is constant; in contrast, the traditional Archard approach *does* assume a constant (or at least only material dependent) COF.

Chapter 5

Fretting at Ambient Temperature

5.1 Introduction

The work in this chapter considers the ambient temperature fretting wear of SCMV and SCMVN, both in heterogeneous and homogeneous material combinations. A range of normal loads and displacement amplitudes were evaluated in order to explore both the frictional and fretting wear behaviour of the materials. The choice of materials and combinations is representative of practice in the aerospace industry where nitriding is commonly employed to improve the wear performance of components such as spline couplings [153]. Traditionally, as a result of limitations of the nitriding processes employed (Section 2.7.4, Page 35), the female half of a splined coupling is not nitrided (many engine types run with this setup). Accordingly, tests were firstly undertaken with homogeneous pairings of SCMV and SCMVN to understand the fretting behaviour of the two material types in such contacts, and then subsequently with heterogeneous combinations—a contact condition more representative of many operational splined couplings running in aeroengines today.

In the relatively large body of fretting literature, the behaviour of various steels is well represented; contrastingly, there is a notable absence concerning the fretting wear of nitrided steels—in fact, the author is only aware of two papers directly considering this topic [178, 179]. Both of these investigations utilised a nitrided specimen fretted against an untreated steel, making it difficult to isolate the impact of nitriding; moreover, they considered only a limited set of experimental conditions.

Ramesh and Gnanamoorthy [178] compared the fretting wear of a liquid nitrided EN24 steel (713 HV) with a hardened and tempered EN24 steel (372 HV), both being worn against a hardened and tempered EN31 (698 HV) counterface. A crossed cylinder ($\varnothing$ 10 mm) geometry was used with a fixed displacement amplitude of 60 µm, a normal load in the range 2.4 to 29.4 N and a test duration of 100×10^3 cycles. The results showed that the increased hardness produced by the heat treatment had no significant effect on the fretting wear. However, nitriding was found to reduce the specific wear rate by approximately 30 % under gross-sliding fretting conditions: the

improvement was attributed to the ϵ–$Fe_{2-3}N$ compound layer. Conversely, when a higher normal load was applied (resulting in a partial slip condition), nitriding resulted in an approximately 25 % increase in the wear rate; however, since the sliding was not fully developed, the wear rates were in general small. Although not directly measured, it is apparent from their results that the COF was lower for the fretting pair with the nitrided steel, since the transition to partial slip occurred at a higher normal load (19.6 N compared with 9.8 N).

Luo et al. [179] considered the effect of plasma nitriding on a medium carbon (0.5 wt. %) steel flat against a hard steel ball (745 HV) in a rotational fretting mode. They used a normal load of 20 N, a displacement amplitude from 0.125 to 1° and a short test length of 1×10^3 cycles. The hardness of the base steel was 365 HV and after nitriding was 511 HV; the compound layer was identified to be primarily ϵ–$Fe_{2-3}N$ and γ'–Fe_4N. Their results indicated that nitriding reduced the initial COF but had little effect on the steady state value, both reaching approximately 0.76. From the limited profilometry data presented, it appears that there was less adhesion and material transfer but a greater wear volume when the specimen was nitrided. The authors of the paper concluded that nitriding was beneficial, but from their results, it is not clear how they reached this conclusion. They attributed the apparently lower COF to the properties of the compound layer providing easier shear and reducing adhesion.

In the wider literature, nitriding has been found to significantly improve the sliding wear behaviour of steels. For example, Kato et al. [146] conducted tests under a wide range of loads and sliding speeds to characterise the dry sliding wear of a nitrided steel pin against an untreated steel disc. In all cases, the wear rate of the steel pin was significantly reduced by nitriding, varying from two to four orders of magnitude less, depending on the test conditions. Additionally, nitriding increased the mild–severe transition load, and when operating under severe wear conditions, reduced the aggressiveness of the wear.

In similar tests on a stainless steel, Sun and Bell [147] found the sliding wear to be reduced by more than a factor of 200 by nitriding and severe wear was eliminated under the conditions studied. Despite the reduction in wear, they found the COF to be higher for the nitrided specimens: approximately 0.75 compared with 0.6 for the plain specimens. Moreover, the evolution of the COF was significantly modified: the nitrided specimens exhibited an increase in COF up to approximately 0.9 following 200 m of sliding, and then a gradual decline throughout the test (up to 800 m); in contrast, the untreated specimens reached a steady state value of COF following 100 m of sliding.

In both studies, the compound layer was not thought to be influential on the wear process and was found to be quickly removed in the initial stages. The observed reduction in wear was attributed to the properties of the diffusion zone where the increased hardness and changed surface chemistry reduced plastic deformation and eliminated severe adhesive wear [146, 147]. However, in complementary work, Kato

et al. [144] did find that the presence of a thin and dense ϵ–Fe_3N compound layer could reduce the initial wear rate.

One of the primary effects of the nitriding process is to increase the surface hardness (in this work, it was ≈ 1000 HV after nitriding, see Section 4.1.1 , Page 64). Increasing the surface hardness is generally found to reduce wear since increasing the hardness reduces the real contact area [180] and wear, as shown by Archard [173], is found to be proportional to to the real contact area.

Kayaba and Iwabuchi [90] investigated the influence of hardness on the fretting wear of a medium carbon (0.6 wt. %) steel plate against a high carbon (0.86 wt. %) bearing steel ball. A fixed load of 34.3 N and peak-to-peak displacement amplitudes of 45 µm and 260 µm were used, at a fixed frequency of 16.6 Hz with a test duration of 100×10^3 cycles. The specimens were heat treated to a range of different hardnesses: 221 to 850 HV for the flat specimens and 246 to 800 HV for the balls. Sets of experiments were conducted with both equal and unequal hardness pairs. The conclusions drawn from the similar hardness pairs (at both amplitudes) was that fretting wear is not inversely proportional to hardness. At the higher amplitude, there was a discontinuity in the wear volume as a function of hardness and a simple relationship was not clear. However, over the full range of hardness values considered (covering an increase in hardness of more than 250 %), there was a marginal effect: examination of the data finds that the observed wear volume at 850 HV was a few percent higher than that for the 235 HV pair. In the case of the lower displacement amplitude tests, the wear of the hardest couple compared to the softest was ≈ 10 % lower; again, there was no clear relationship found between hardness and resultant wear volume.

A similar lack of a significant effect or apparent relationship was found for the mixed hardness tests. However, in a number of cases, the harder specimen was found to wear more than the softer specimen. During the tests, Kayaba and Iwabuchi [90] observed the production of both a compacted black oxide and a loose red oxide—electron diffraction identified both oxides as α-Fe_2O_3. The formation of the black oxide was concluded to be critical to the ensuing wear: in the cases where the softer specimen wore more, the behaviour was attributed to the formation of the black oxide compact on the soft specimen, which abraded the harder specimen; in the absence of the black oxide, the wear was found to be directly dependent on hardness; finally the discontinuity in the wear response observed at 260 µm displacement amplitude was attributed to the change from production of red to black oxide.

Later work by Ramesh and Gnanamoorthy [181] also considered the effect of hardness on fretting. They fretted a high carbon (1 wt. %) steel (EN31) hardened to 698 HV against a medium carbon (0.4 wt. %) steel (EN24) hardened to 207, 375 and 640 HV. The tests were conducted with a crossed cylinder (⌀10 mm) arrangement with a fixed (60 µm) applied displacement amplitude, at normal loads from 2.4 to 29.4 N and a fixed 5 Hz frequency for 100×10^3 cycles; as a consequence of the load range, the tests spanned both the partial slip and gross sliding regimes. However, under all

Table 5.1: Summary of ambient temperature test conditions for homogeneous and heterogeneous specimen pairs.

Normal Load (P) / N	250, 450 and 650
Displacement amplitude (Δ^*) / μm	10[a], 25, 50 and 100
Duration (N) / cycles	100×10^3
Frequency (f) / Hz	20

[a] homogeneous pairs only

loads there was no appreciable effect of material hardness on the fretting wear of the specimens. Unfortunately, no breakdown of the relative wear of the two specimens was provided, nor was there much qualitative examination of the wear scars; consequently, it is not possible to establish if abrasive oxide compacts, similar to those observed by Kayaba and Iwabuchi [90], were formed.

5.2 Experimental procedure

The materials, test procedure and subsequent data analysis were as described in Chapter 4 (Page 63). Fretting tests were conducted at combinations of four different displacement amplitudes, ranging from 10 to 100 μm, and three normal loads, ranging from 250 to 650 N; in all cases a constant frequency of 20 Hz and fixed duration of 100×10^3 cycles were used. All experiments were conducted under normal laboratory conditions in an uncontrolled air atmosphere: the mean temperature for all tests was 22 °C (σ = 1.7 °C) and the mean relative humidity was 34 % (σ = 9.5 %). The full range of tests conditions is summarised in Table 5.1.

5.3 Results: homogeneous specimen pairs

5.3.1 SCMV-SCMV specimen pairs

Coefficient of friction and sliding regime

Figures 5.1 to 5.3 show the instantaneous COF as a function of fretting cycles, grouped by applied displacement amplitude, Figure 5.4 shows the steady state COF (mean average of the last 95×10^3 cycles) as a function of normal load for the same loading conditions and Figures 5.5 to 5.7 show-mid test ($N = 50 \times 10^3$) fretting loops, similarly, at the same loading conditions. By considering these three data sets, it is apparent that the tests conducted at 10 μm displacement amplitude were not in what is typically described the *gross sliding* regime. Figure 5.4 shows that, at each normal load increment, increasing the applied displacement amplitude from 10 μm to 25 μm results in an approximate increase of 0.17 in the *apparent* COF while further increases have no discernible effect. This indicates that at 10 μm displacement amplitude (at all loads considered), the contact is not experiencing fully developed sliding at the interface;

clearly the quoted figures are not then the "COF", but simply the applied tractional force normalised by the normal load. Qualitatively, the loops in Figures 5.5 to 5.7 at 10 μm displacement amplitude are similar to those of Vingsbo and Söderberg [20] associated with the stick-slip sliding regime. It can additionally be seen that at 250 N normal load and 10 μm displacement amplitude, the loop shape is more comparable to the fully developed sliding case at 25 μm displacement amplitude (Figure 5.5) than is the case with 450 N and 650 N normal loads (Figure 5.6 and Figure 5.7 respectively), indicating that the transition may be very close to that point. However, examination of the wear scars (e.g., Figure 5.15a) indicated that there is certainly damage and oxide—indicated by the dark regions in the BSE SEM image—across the full width of the scar with no evidence of a central *stick* region. At the highest normal load considered (650 N), the instantaneous COF for 10 μm displacement amplitude displays a large number of spikes—very short time periods where the apparent COF is very high. These are also related to the fact that the contact is not fully sliding, resulting in a zero (or near zero) sliding distance and consequently a "divide by zero" in the COF calculation (see Section 4.5.3, Page 73).

Considering the instantaneous COF, for the specimens with an applied displacement amplitude greater than 10 μm (Figures 5.2 and 5.3), it can be seen that initially the COF is low but rises rapidly over the course of a few thousand cycles, as the surface films on the specimens are dispersed [56]. After approximately 5×10^3 cycles, it may be considered that a quasi steady-state value is reached, during which the COF is in general stable over a period of tens of thousands of cycles. For the tests at 50 μm displacement amplitude, there is a slightly more notable peak in the COF in the initial 10×10^3 cycles. As the normal load is increased, the peak is progressively reduced and it takes a greater number of cycles to reach it. At the highest normal load and displacement amplitude combination ($P = 650$ N, $\Delta^* = 50$ μm), the COF shows a greater degree of instability with reductions of approximately 0.06 over a period of $\approx 1 \times 10^3$ cycles.

For all displacement amplitudes (including 10 μm), the COF is in general lower over the course of the test for a test at a higher normal load than one at a lower normal load (Figures 5.1 to 5.3). By considering the average steady-state COF (Figure 5.4) and applying a linear fit to the data (where $\Delta^* > 10$ μm), the COF (μ) can be found as a function of the normal load (P, in N) to be:

$$\mu = 0.82 - 1.64 \times 10^{-4} P \tag{5.1}$$

Similar reductions in the COF with increasing normal load have been observed in the literature for fretting contacts; in these cases it has been attributed to the interfacial shear stress being a function of contact pressure [153, 182].

Discounting the tests where fully developed sliding of the contact had not been established ($\Delta^* = 10$ μm), it can be seen that the characteristic fretting loops share a

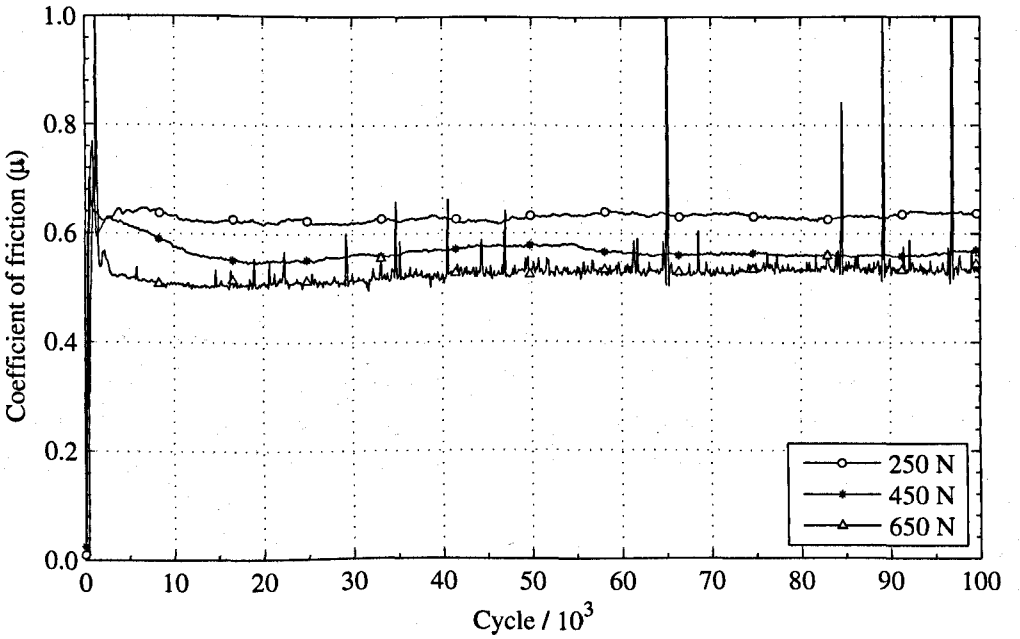

Figure 5.1: Instantaneous coefficient of friction for SCMV specimen pairs with P = 250, 450 and 650 N and Δ^* = 10 μm.

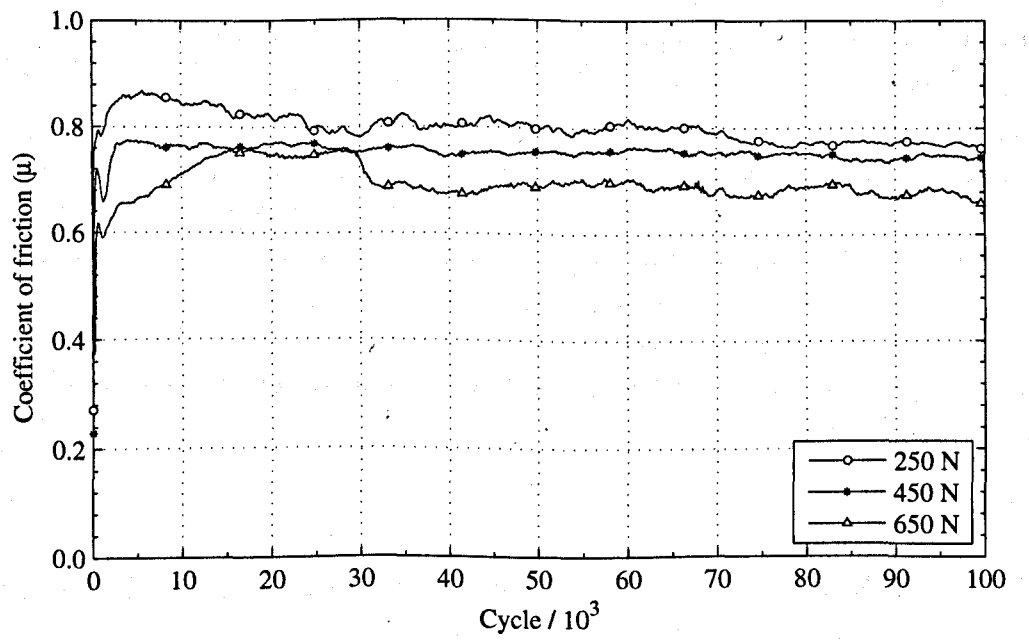

Figure 5.2: Instantaneous coefficient of friction for SCMV specimen pairs with P = 250, 450 and 650 N and Δ^* = 25 μm.

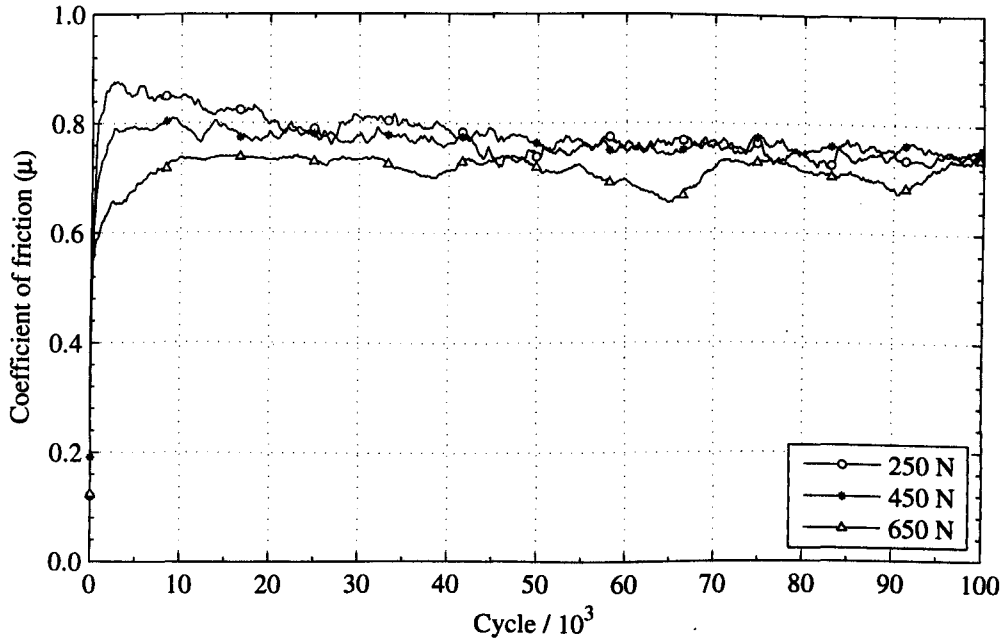

Figure 5.3: Instantaneous coefficient of friction for SCMV specimen pairs with P = 250, 450 and 650 N and Δ^* = 50 μm.

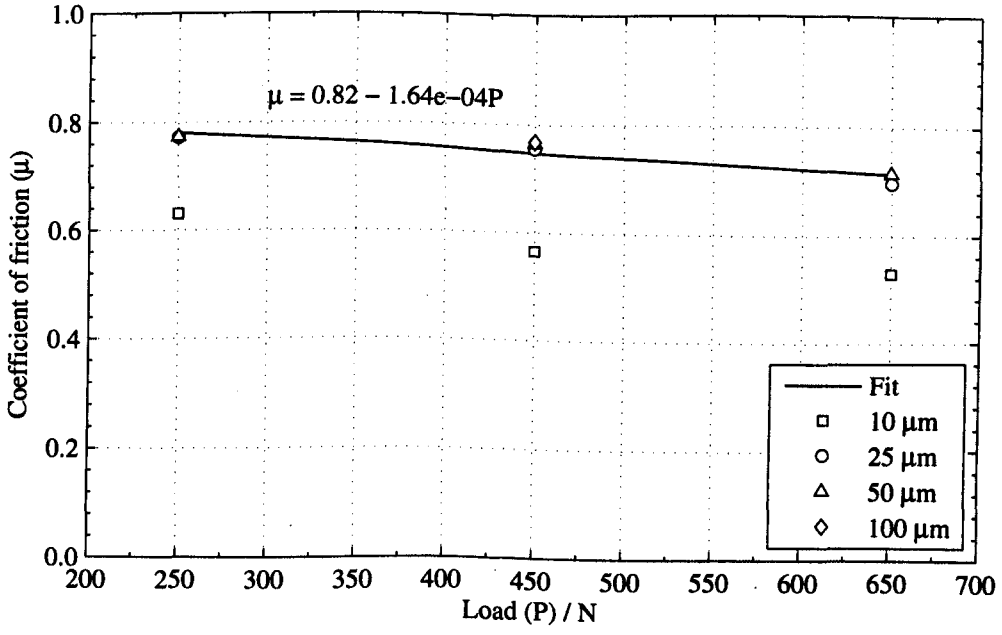

Figure 5.4: Steady state COF (mean average of the last 95 × 10^3 cycles), for SCMV specimen pairs, as a function of normal load for a range of applied displacement amplitudes.

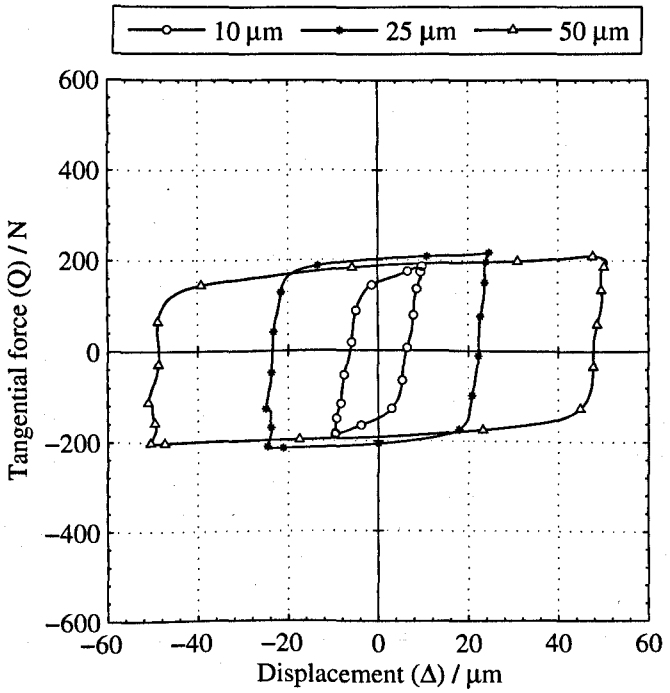

Figure 5.5: Mid test (cycle 50×10^3) force-displacement loops, from SCMV fretting tests with $P = 250\,\text{N}$ and $\Delta^* = 10$, 25 and 50 μm.

number of common features (Figures 5.5 to 5.7). The general shape is of a parallelogram: the near vertical sides correspond to the period of the cycle when the specimen is stuck and the approximately horizontal upper and lower sides correspond to the sliding period of the cycle. The gradient of the stuck portions of the cycle correspond to the *rig stiffness* i.e., the combined contact, bulk specimen and fixture stiffness (a least squares fit shows this to be $57.3 \times 10^3\,\text{kN m}^{-1}$). The upper and lower sides, corresponding to the sliding period of the cycle, may be expected to be horizontal with a constant value of $Q = \mu P$. However, examination of Figures 5.5 to 5.7 indicates that the tangential force in general increases throughout the sliding periods of the cycle, reaching a maximum at the end of the stroke—consequently indicating that the Coulomb COF is increasing as a function of δ. Explanations for this type of behaviour typically cite ongoing plasticity and the geometry of the wear scar [54, 171, 183]. Indeed, at the extreme, interlocking features (the result of material transfer) can result in ploughing in the contact which may cause sudden force peaks at the end of the stroke (Figure 6.2, Page 136).

Profilometry and wear analysis

Figures 5.8 to 5.10 show the average worn profiles for both the flat and cylindrical specimens, grouped by displacement amplitude. The profiles for the cylindrical specimens are plotted as the deviation from the unworn surface to enable the wear to be

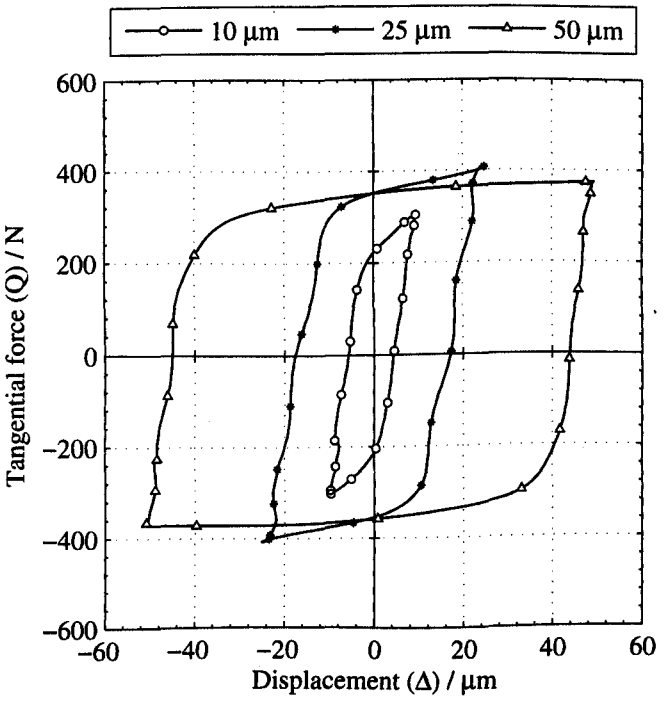

Figure 5.6: Mid test (cycle 50×10^3) force-displacement loops, from SCMV fretting tests with $P = 450$N and $\Delta^* = 10$, 25 and 50 μm.

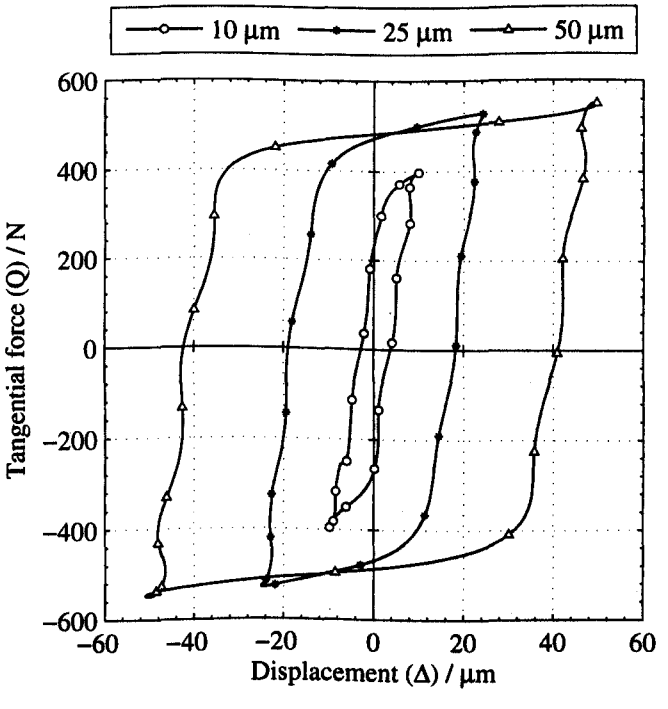

Figure 5.7: Mid test (cycle 50×10^3) force-displacement loops, from SCMV fretting tests with $P = 650$N and $\Delta^* = 10$, 25 and 50 μm.

differentiated from the underlying cylindrical profile (for more details see Section 4.4.1, Page 69).

Figure 5.8 shows the profiles for specimens with a displacement amplitude of 10 μm and normal loads of 250 to 650 N: it can be seen that while there is surface damage at all normal loads, there is no apparent increase in the scar depth, nor change in shape with increasing normal load. Moreover, there is no evidence of a central *stick* region, supporting the conclusions drawn from the SEM (Figure 5.31a) that, although not fully sliding, damage occurred over the width of the scar.

In all cases where there was fully developed sliding (Figures 5.9 and 5.10), the scars on the flat specimens show a characteristic "U" shape—examination of the 3D profilometry shows that this is 2D in nature i.e., consistent over the full width of the scar; there is no evidence of any localised pitting or material transfer. However, while the cylindrical profiles appear to also show a "U" shaped scar profile, this is a result of plotting the deviation from the unworn surface (which is curved with a 6 mm radius). Consequently, the cylindrical specimens actually tend toward a flattened *punch* type profile. Increasing the normal load resulted in a monotonic increase in the depth and width of the scar, on both the flat and cylindrical specimens: for example, at $P = 250$ N, $\Delta^* = 25$ μm, the depth of the scar was approximately 7 and 5 μm for the flat and cylindrical specimen respectively; increasing the normal load to $P = 650$ N resulted in the respective depths increasing to approximately 14 and 10 μm. Similarly, increasing the applied displacement to $\Delta^* = 50$ μm (and maintaining the normal load at $P = 250$ N) resulted in the depths increasing to 17.5 and 13 μm. In all these cases, a general trend is observed where the depth of the wear on the cylindrical specimen is consistently deeper than on the flat specimen.

The distribution of wear between the specimens is quantified in Figure 5.11 which shows the normalised wear of the flat specimen (normalised against the total wear of the flat and cylindrical specimens) against the *loading parameter*, defined as $P\Delta^*$ and, assuming an Archard type wear law, would be expected to be proportional to the wear volume i.e., it is an estimate of the severity of the loading conditions. From Figure 5.11, it can be seen that the total wear is evenly distributed between the flat and cylindrical specimens, with relatively little scatter: the mean wear of the flat specimen (as a fraction of the total wear of the couple) is 0.47 with a standard deviation of 0.05.

Figure 5.12 plots the total wear volume as a function of the measured dissipated energy during a test (see Section 4.5.4, Page 74). This is plotted for all combinations of load and applied displacement amplitudes where tests were conducted. It can be seen that, as may be expected, there is a linear relationship between the wear volume and dissipated energy [177]. Using simple linear regression (where $R^2 = 0.98$ is found), the wear volume (V^w, in mm^3) is found as a function of the dissipated energy (E_d, in kJ) to be

$$V^w = 7.69 \times 10^{-2} E_d - 8.47 \times 10^{-2} \tag{5.2}$$

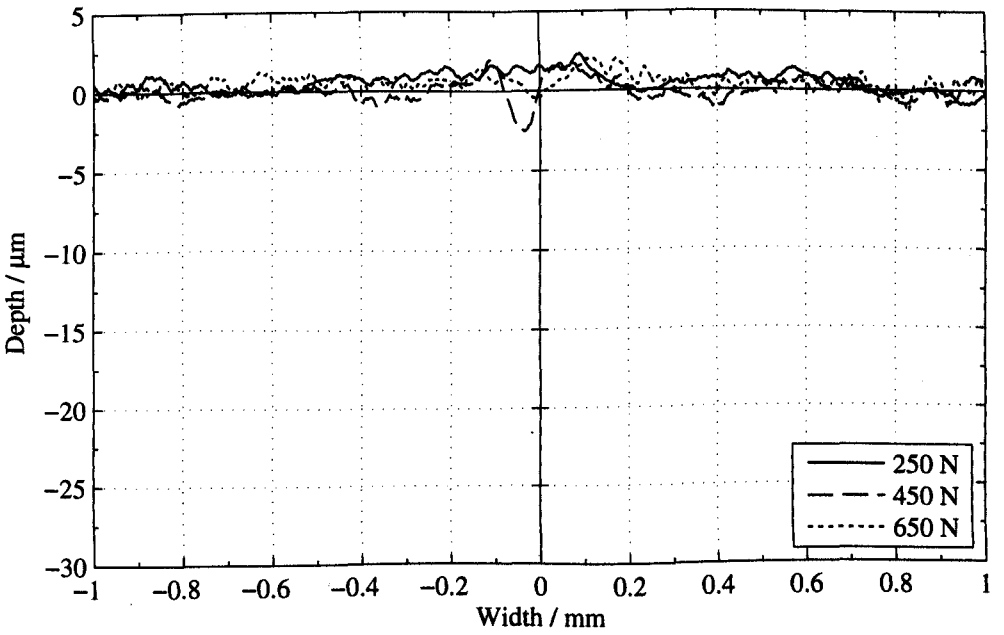

(a)

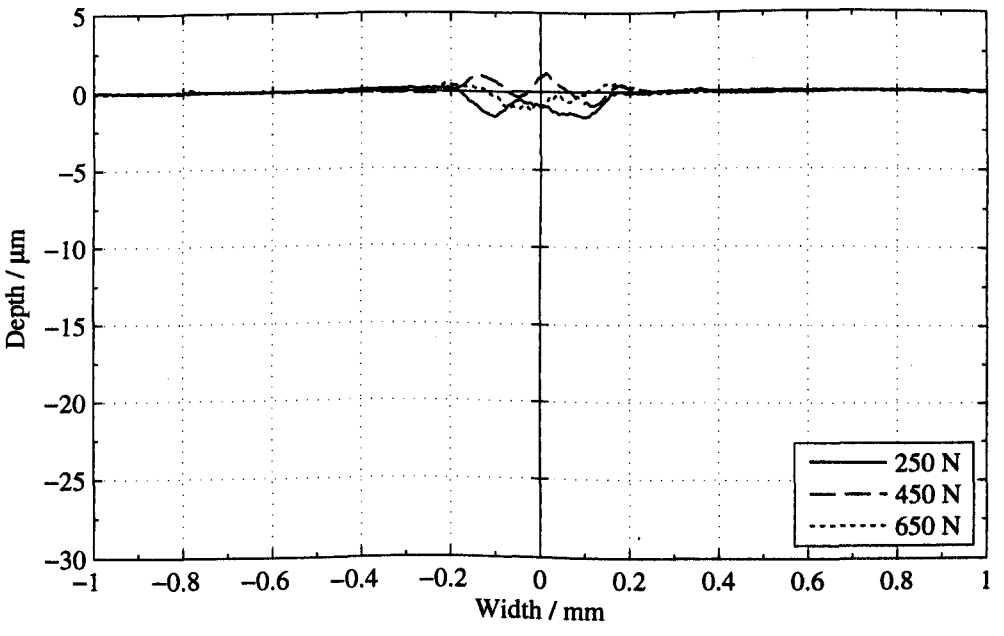

(b)

Figure 5.8: Average profiles of the: (a) cylindrical specimen and (b) flat specimen; from SCMV specimen pairs, following 100×10^3 fretting cycles with P = 250, 450 and 650 N and Δ^* = 10 µm.

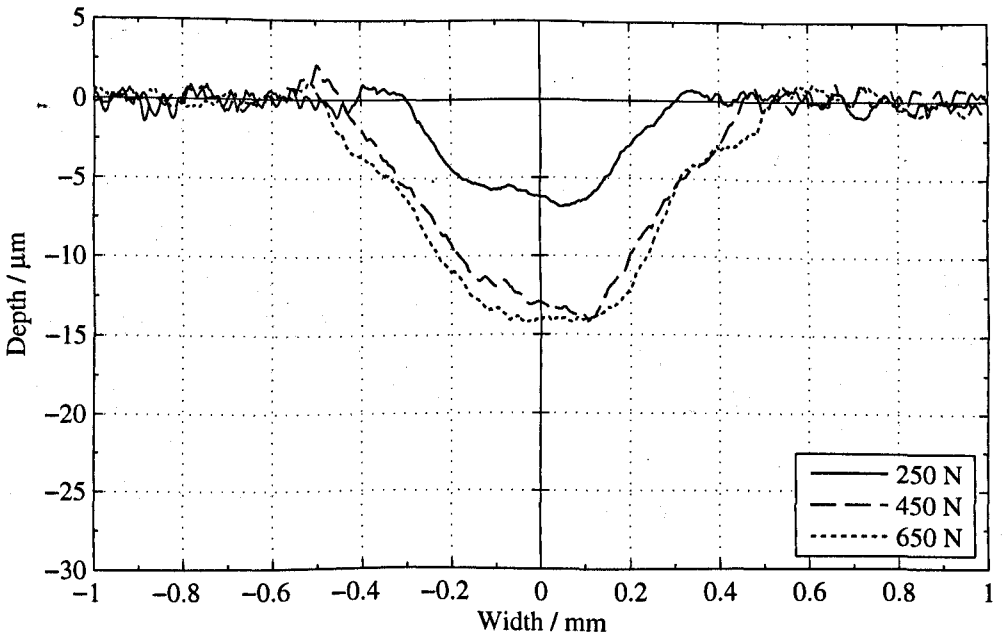

(a)

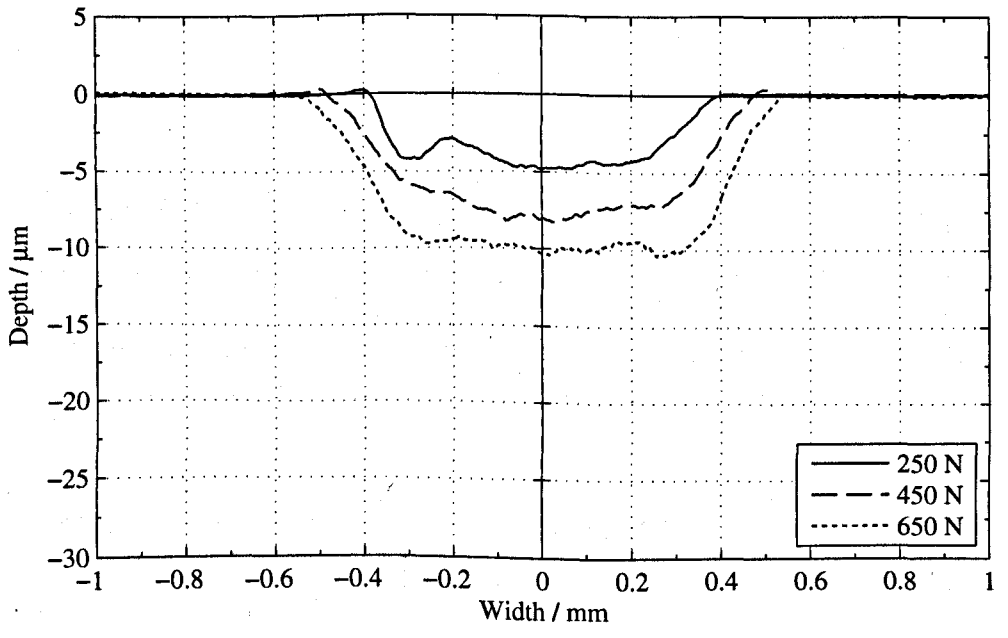

(b)

Figure 5.9: Average profiles of the: (a) cylindrical specimen and (b) flat specimen; from SCMV specimen pairs, following 100×10^3 fretting cycles with P = 250, 450 and 650 N and Δ^* = 25 µm.

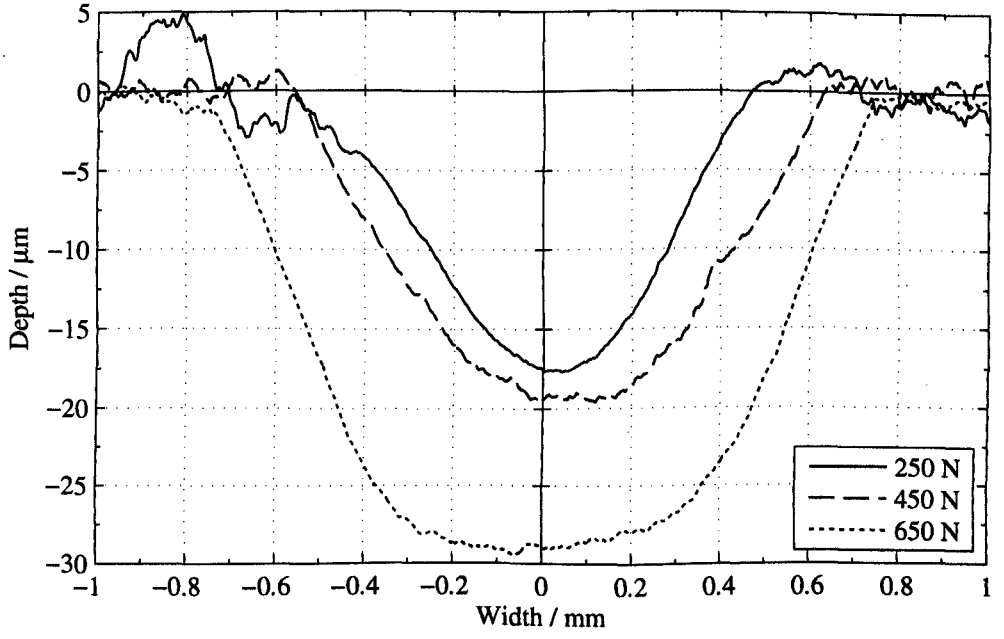

(a)

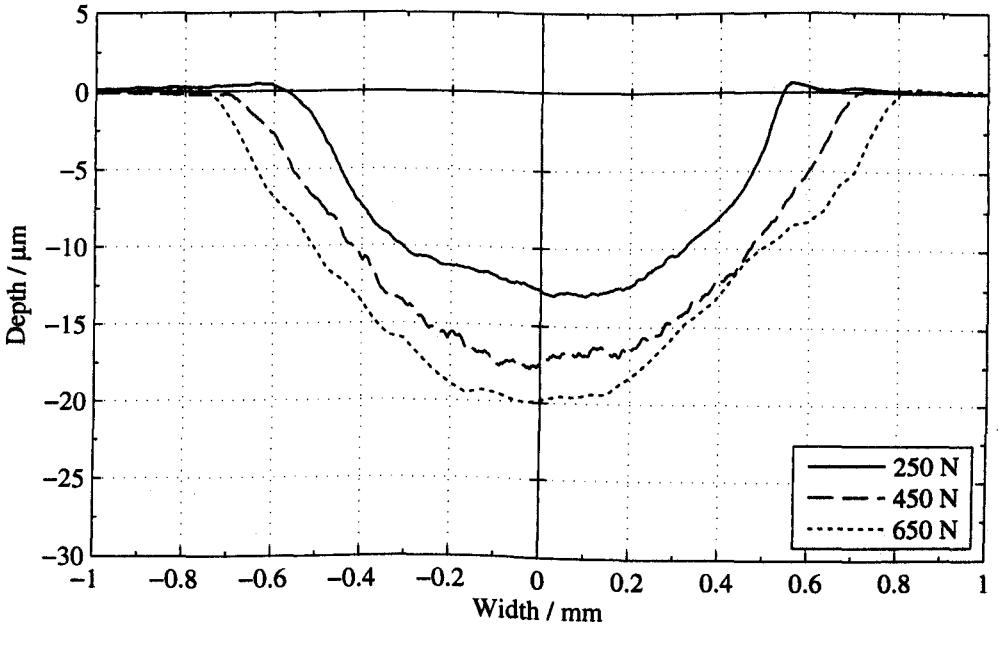

(b)

Figure 5.10: Average profiles of the: (a) cylindrical specimen and (b) flat specimen; from SCMV specimen pairs, following 100×10^3 fretting cycles with P = 250, 450 and 650 N and Δ^* = 50 µm.

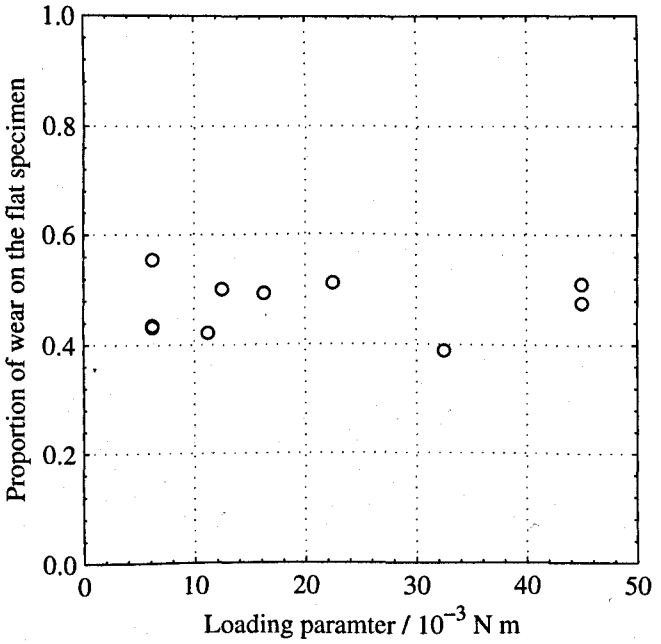

Figure 5.11: Wear (in terms of volume) of the flat specimen, normalised against the total wear of the flat and cylindrical specimen, as a function of the loading parameter for SCMV specimen pairs.

allowing the energy wear coefficient to be identified as $k_e = 7.69 \times 10^{-2}\,\mathrm{mm^3\,kJ^{-1}}$. The small positive intercept with the E_d axis is termed the threshold energy ($E_{th} = 1.10\,\mathrm{kJ}$)—in metals this is related to the minimum energy density required to form the TTS and hence initiate wear [74].

Microscopy and topographic observation of the scar

In order to assess the wear products observed on the specimen surfaces, EDX and XRD analyses were conducted. EDX spectra were taken in regions of the wear scar assumed to be oxide debris (areas of lower brightness in the BSE micrographs), regions of exposed metal within the wear scar (areas of higher brightness in the BSE micrographs) and outside of the wear scar where no damage had occurred. Since EDX analysis has limited accuracy when assessing lighter elements such as carbon and oxygen, the results are tabulated such that broad comparisons can be drawn (Table 5.2). Comparing the spectra taken from outside the wear scar (C) and the region assumed to be exposed metal within (B) it can be seen that they show very similar elemental composition with low levels of oxygen (0.9 and 2.1 wt. % respectively) and high levels of iron (90.4 and 89.1 wt. % respectively). In contrast the elemental composition of the wear debris (A) shows a much higher proportion of oxygen (31.6 wt. %) and a lower proportion of iron (59.7 wt. %) while the proportions of the remaining significant elemental constituents are relatively unchanged.

Structural analysis of the oxide debris is provided by XRD analysis: spectra from a

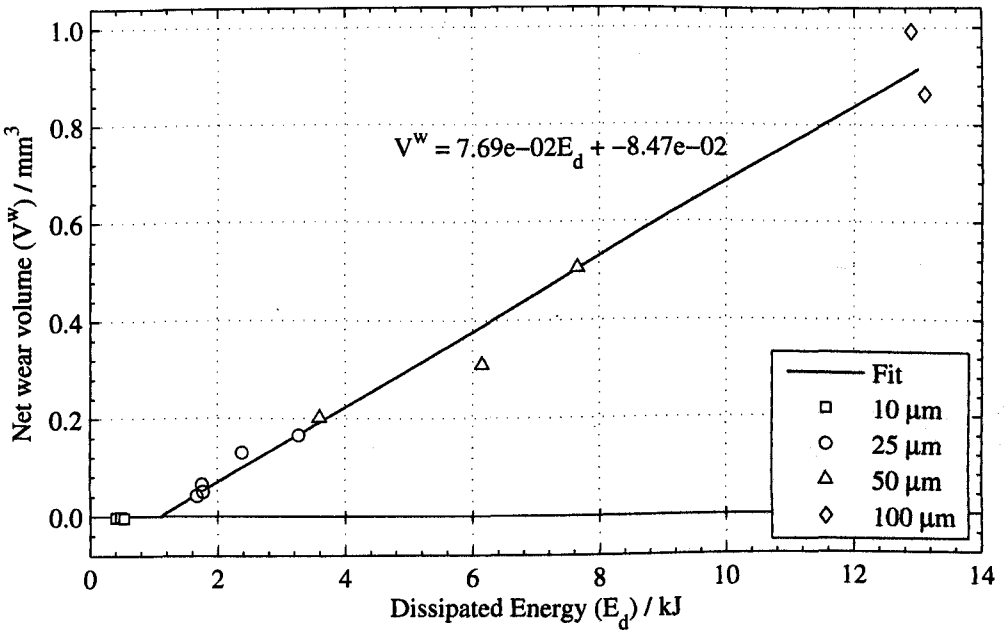

Figure 5.12: Wear volume as a function of dissipated energy for SCMV specimen pairs; for combinations of P = 250, 450 and 650 N and Δ^* = 10, 25, 50 and 100 μm.

Table 5.2: Data from EDX spectra from the surface of a flat SCMV specimen from a homogeneous pair taken in three locations: (A) area of wear debris; (B) metallic region in the wear scar; (C) region outside of the worn area.

	Composition at location / wt. %		
Element	A	B	C
C	5.1	3.2	3.9
O	31.6	2.1	0.9
V	0.2	0.3	0.2
Cr	2.4	3.5	3.1
Fe	59.7	89.1	90.4
Mo	0.6	1.4	0.9

worn and unworn specimen are plotted in Figure 5.13 with the characteristic peaks highlighted. The small peaks (labelled (F)), unique to the worn specimen, are identified as haematite (Fe_2O_3); the peaks are small since the area exposed to the x-ray beam (ranging from approximately 6 to 20 mm as the incidence angle was varied) is large compared to the wear scar width.

Figures 5.14 and 5.15, present top-view SEM microscopy providing an overview of the oxide bed development with varying load and displacement amplitude parameters: Figure 5.14 shows the effect of increasing normal load (P = 250 to 650 N) at a fixed displacement amplitude (Δ^* = 25 μm) and Figure 5.15 shows specimens following fretting under a common normal load of 450 N, with displacement amplitudes of 10 and 50 μm. In both cases, low magnification images are given in the left hand column

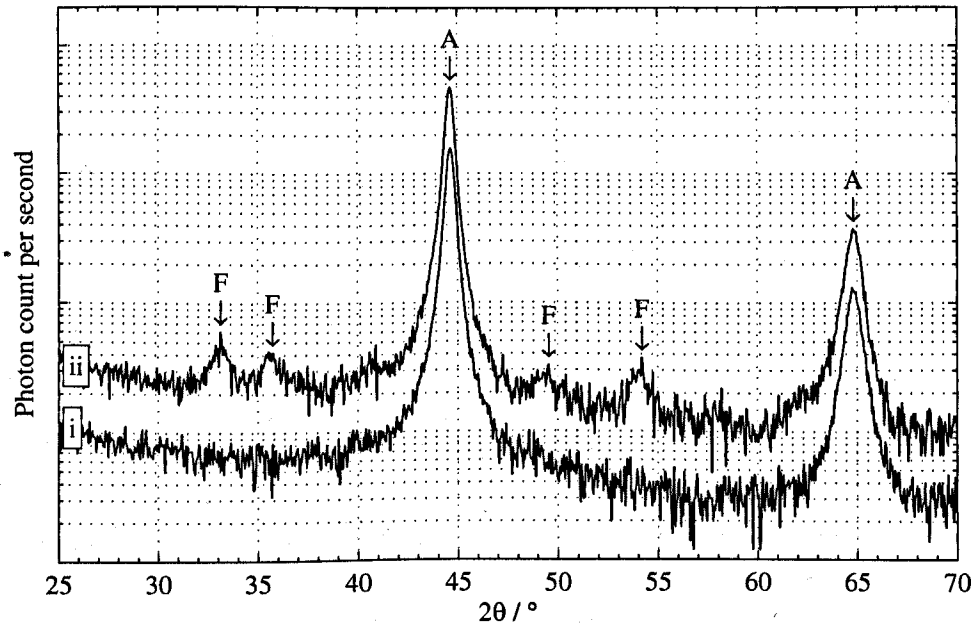

Figure 5.13: XRD spectra of a flat SCMV specimen in the (i) unworn and (ii) worn states; Peaks corresponding to the following compounds are highlighted: (A) Fe, (F) Fe_2O_3.

and higher magnifications images in the right hand column. Images are presented only of the flat specimen, as the profilometry and examination of the cylindrical specimens found very similar behaviour and features.

Considering Figure 5.14, all of the scars show significant oxide coverage (indicated by the low brightness regions). As the load is increased, the debris bed appears to become thicker and regions where the bed is breaking up become more noticeable (d, f). The degree of coverage of the scar by oxide is higher at 450 and 650 N (c, e) than at 250 N (a), although further changes on increasing the normal load from 450 N to 650 N (c, e) are less apparent.

Figure 5.15, in conjunction with Figures 5.14c and 5.14d, allows the effect of varying the displacment amplitude to be assessed. From Figures 5.15a and 5.15b, it can be clearly seen that there are regions of adhered oxide over the full width of the scar with no evidence of a central *stick* region even at 10 μm displacement amplitude. Increasing the applied displacement amplitude to 25 μm (Figures 5.14c and 5.14d) resulted in a significant increase in oxide coverage and thickness with regions of breakdown becoming apparent—much of the change may be associated with the contact transitioning to a fully gross sliding regime. On increasing the displacement amplitude further to 50 μm (Figures 5.15c and 5.15d), large coherent areas of oxide beds are still apparent although the degree of coverage is reduced compared to the 25 μm case.

Figure 5.16 provides BSE SEM micrographs of a cross section through a specimen following 100×10^3 fretting cycles with 450 N normal load and a displacement amplitude of 25 μm. There is no evidence of extensive plastic deformation of the surface, but there

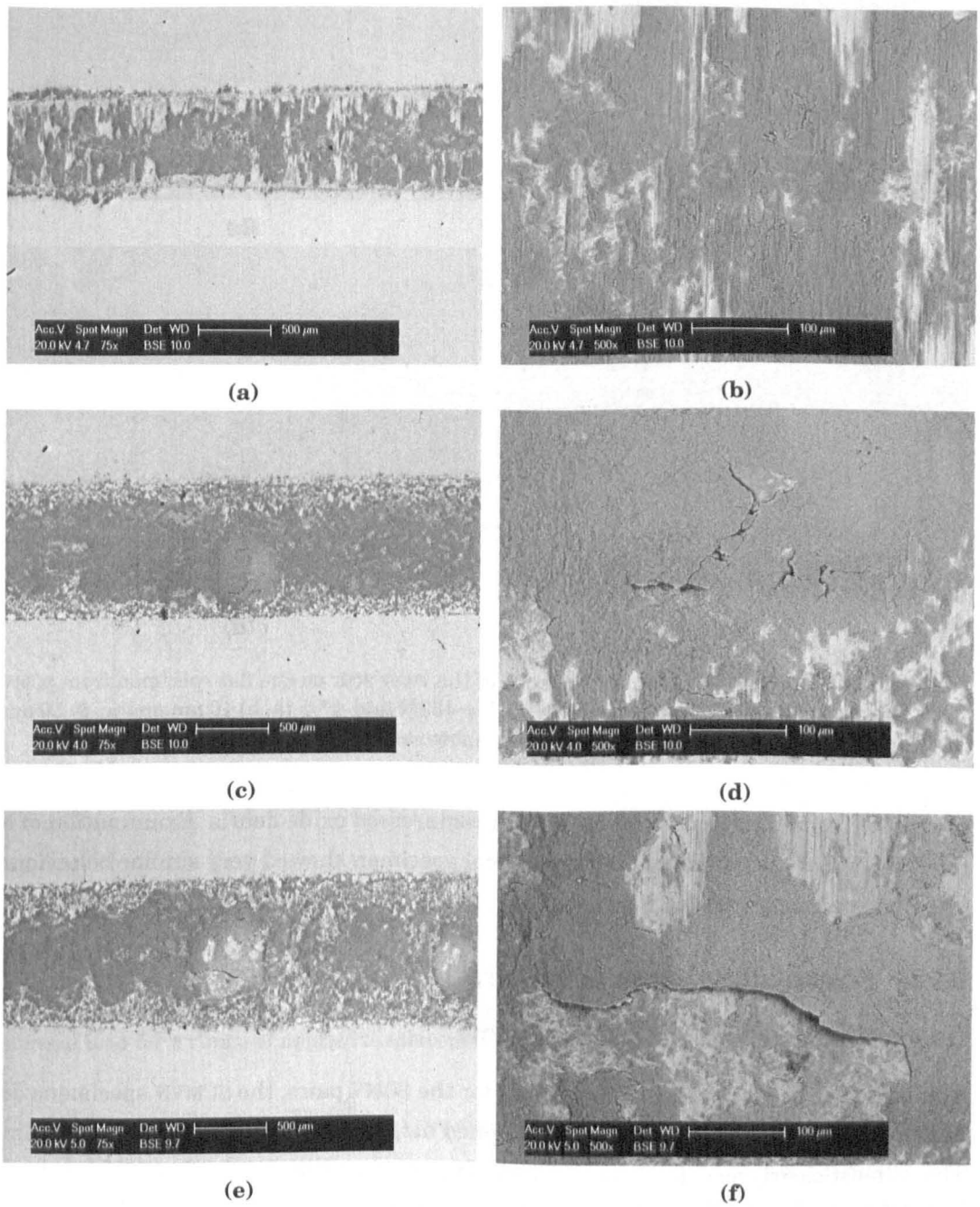

Figure 5.14: Top view, BSE SEM micrographs of the wear scar on the flat specimen from SCMV pairs, following 100×10^3 fretting cycles with $\Delta^* = 25\,\mu m$ and P = (a, b) 250 N, (c, d) 450 N and (e, f) 650 N.

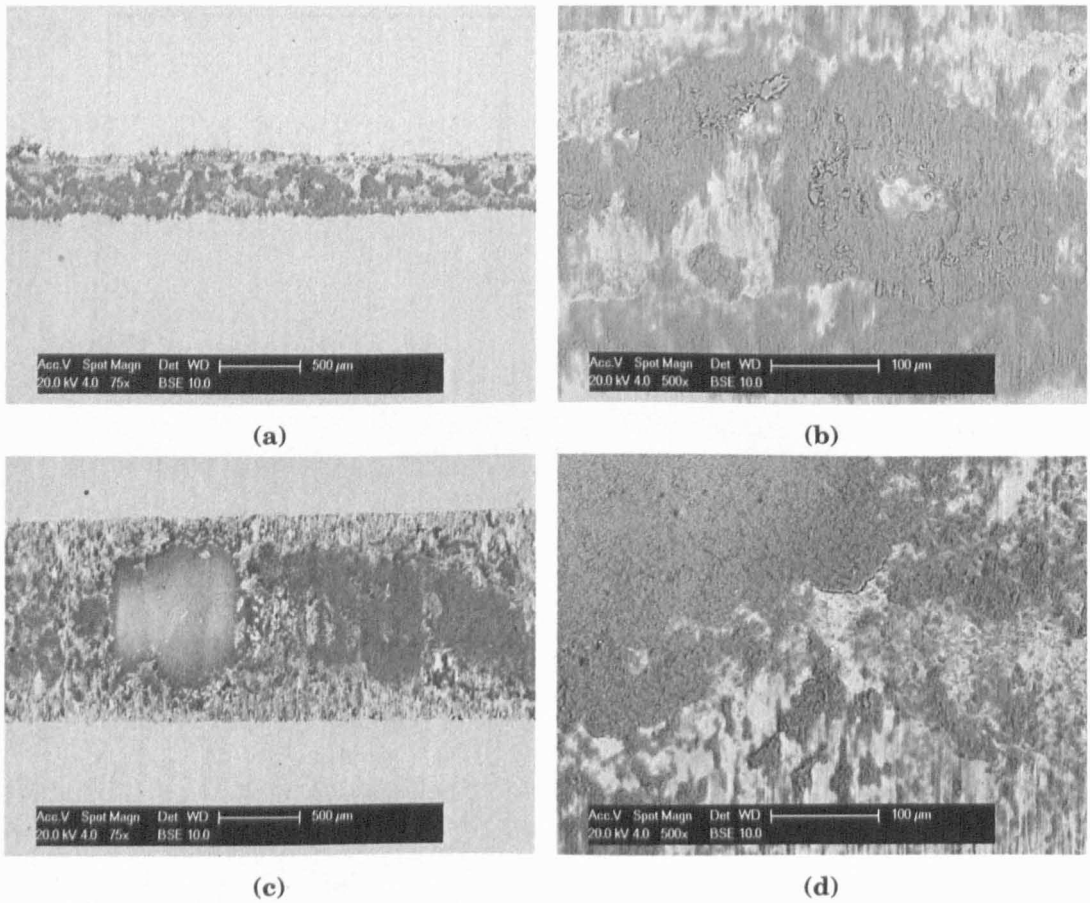

Figure 5.15: Top view, BSE SEM micrographs of the wear scar on the flat specimen from SCMV pairs, following 100×10^3 fretting cycles with $P = 450\,\text{N}$ and $\Delta^* =$ (a, b) 10 μm and (c, d) 50 μm (note, for comparison $P = 450\,\text{N}$, $\Delta^* = 25\,\mu\text{m}$ is shown as Figure 5.14c and Figure 5.14d).

is visible roughening and inlets filled with compressed oxide debris. Examination of a cross section of the corresponding cylindrical specimen showed very similar behaviour and hence is not presented here.

5.3.2 SCMVN-SCMVN specimen pairs

Coefficient of friction and sliding regime

Similar to the frictional results for results for the SCMV pairs, the SCMVN specimens do not show fully developed sliding at an applied displacement amplitude of $\Delta^* = 10\,\mu\text{m}$. This is most clearly seen in Figure 5.17 which plots the average quasi steady state COF as a function of load. From this, it can be seen that the observed "COF" is consistently lower (by ≈ 0.17) at 10 μm than at higher slip amplitudes. Using the same methodology as for the SCMV specimens, the COF as a function of normal load is found to be

$$\mu = 0.92 - 3.55 \times 10^{-4} P \tag{5.3}$$

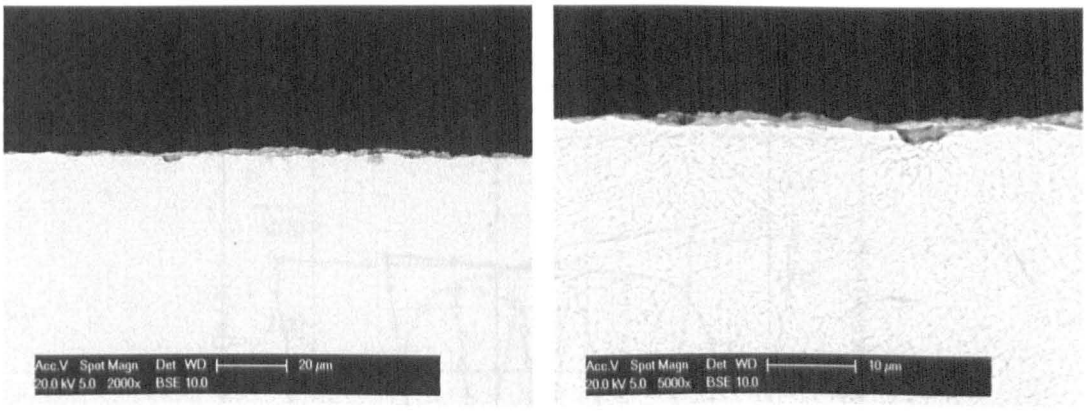

(a) (b)

Figure 5.16: BSE SEM micrographs of a cross section of the flat specimen of an SCMV pair, following 100×10^3 fretting cycles with $P = 450\,\text{N}$ and $\Delta^* = 25\,\mu\text{m}$ at (a) intermediate magnification and (b) high magnification.

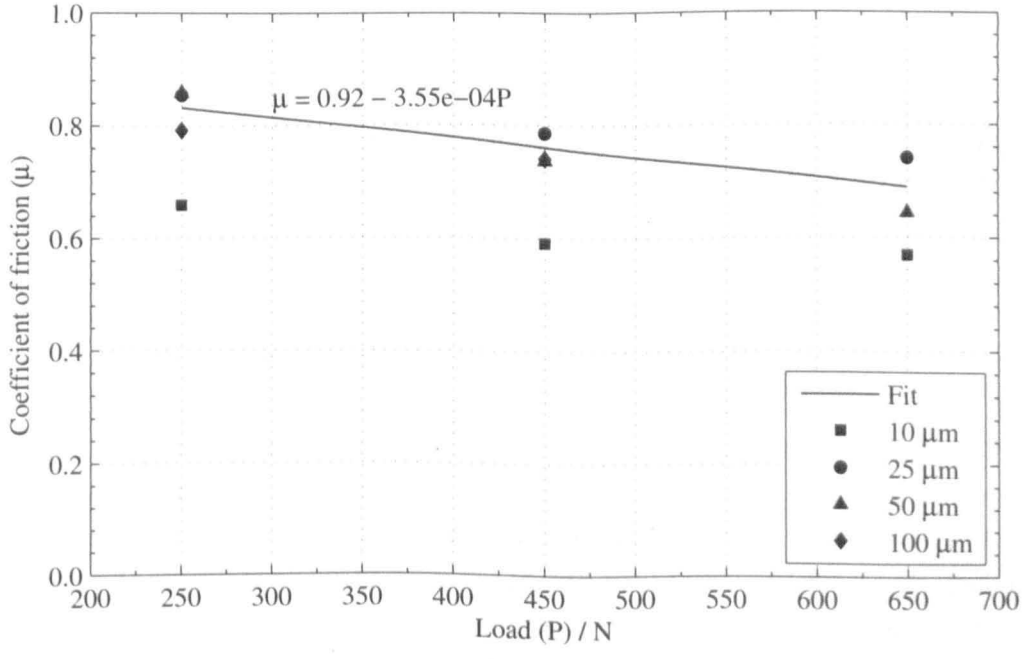

Figure 5.17: Mean average steady state COF, for SCMVN specimen pairs, as a function of normal load for a range of applied displacement amplitudes.

Comparing this to the relationship previously found for the SCMV specimens (Equation (5.1)), the COF for SCMVN is higher at lower loads but reduces more strongly with increasing load, and consequently has a lower COF than for the SCMV specimens at normal loads greater than 524 N.

The characteristic fretting loops (Figures 5.18 to 5.20) show similar behaviour to that for the SCMV specimens. The stiffness during the stick period of the cycle is found to be the same as for SCMV ($57.3 \times 10^3\,\text{kN m}^{-1}$), indicating that any differences between the specimen material types associated with the actual contact stiffness is negligible. Qualitatively, the loops at 10 μm displacement amplitude are more similar

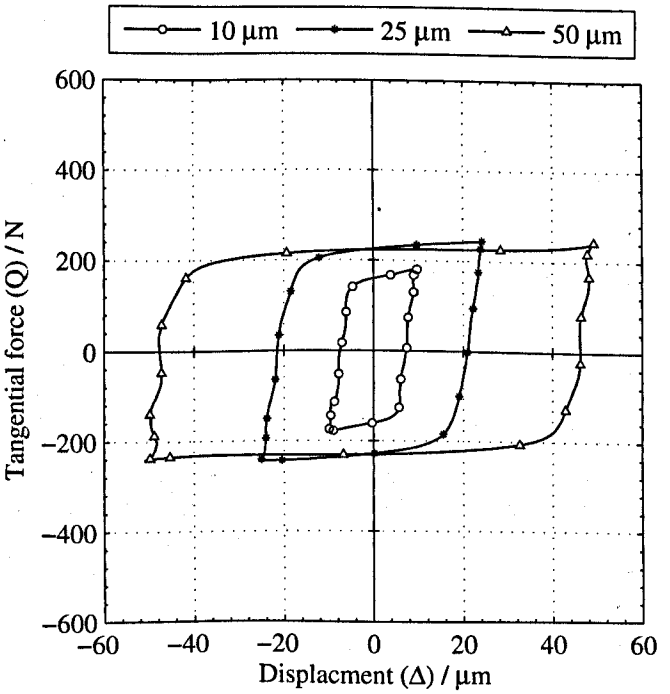

Figure 5.18: Mid test (cycle 50×10^3) force-displacement loops, from SCMVN fretting tests with $P = 250\,\text{N}$ and $\Delta^* = 10$, 25 and 50 μm.

to a sliding loop for the SCMVN specimens than for the SCMV specimens i.e., they are more rectangular in shape with a more horizontal upper and lower sides; this may be a result of the less ductile white layer undergoing brittle fracture rather than plastic flow.

Considering Figures 5.21 to 5.23, which show the instantaneous COF for homogeneous SCMVN pairs, the behaviour is in general comparable with that observed for the SCMV specimens. However, at a displacement amplitude of 50 μm (Figure 5.23), particularly at 650 N normal load, there was a greater instability in the COF with variations in the order of 0.1 over a period of tens of thousands of cycles. In contrast, the behaviour at 10 μm is very different to that seen for the SCMV pairs: at all normal loads considered, the COF rises rapidly to a peak and then drops rapidly to a quasi steady state lower value (as previously discussed, since the contact is not fully sliding these values are the normalised tangential force and not actually the COF). As the normal load is increased, the initial peak is lower and the steady state value is reached faster. For example, at a normal load of 250 N, the maximum value of ≈ 0.92 is reached by ≈ 3000 cycles and the steady state value of ≈ 0.64 is reached by 25×10^3 cycles. In comparison, on increasing the normal load to 450 N, the initial peak is reduced to 0.8 and the steady state value of ≈ 0.6 is reached after only 15×10^3 cycles.

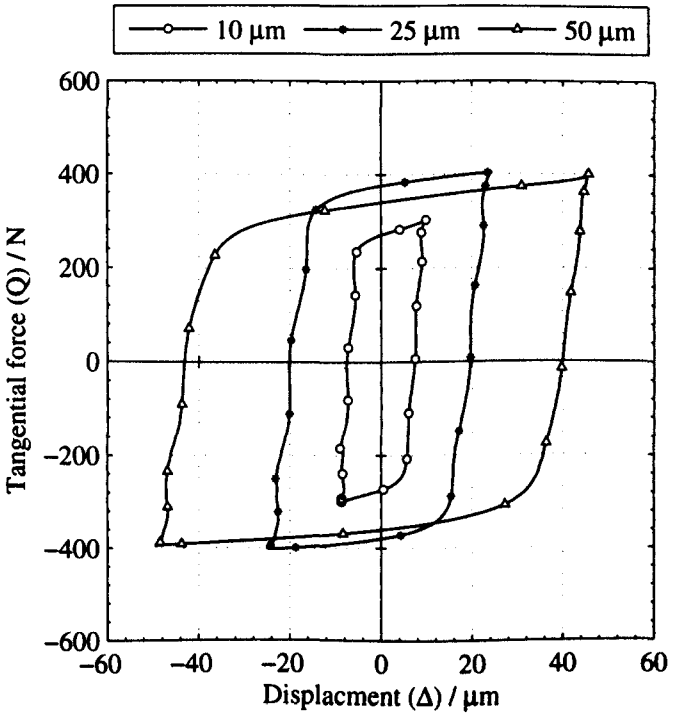

Figure 5.19: Mid test (cycle 50×10^3) force-displacement loops, from SCMVN fretting tests with $P = 450$N and $\Delta^* = 10$, 25 and 50 μm.

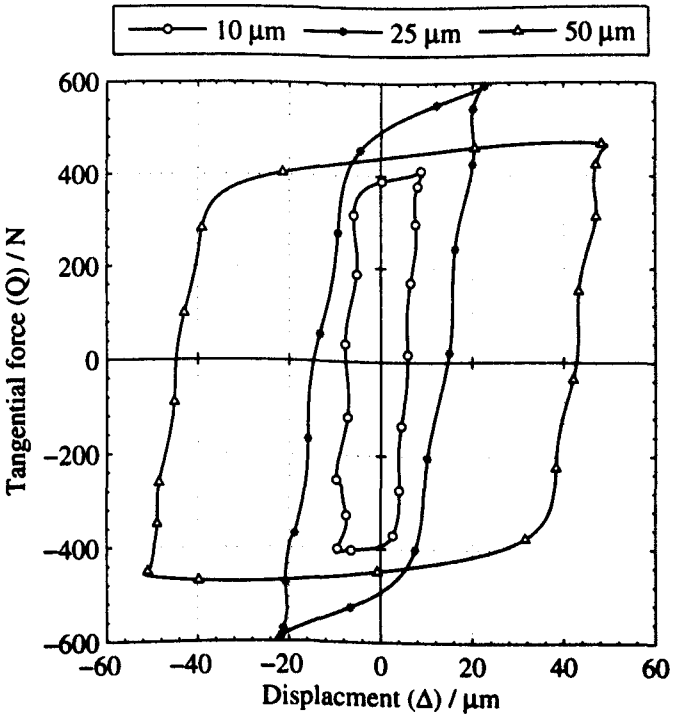

Figure 5.20: Mid test (cycle 50×10^3) force-displacement loops, from SCMVN fretting tests with $P = 650$N and $\Delta^* = 10$, 25 and 50 μm.

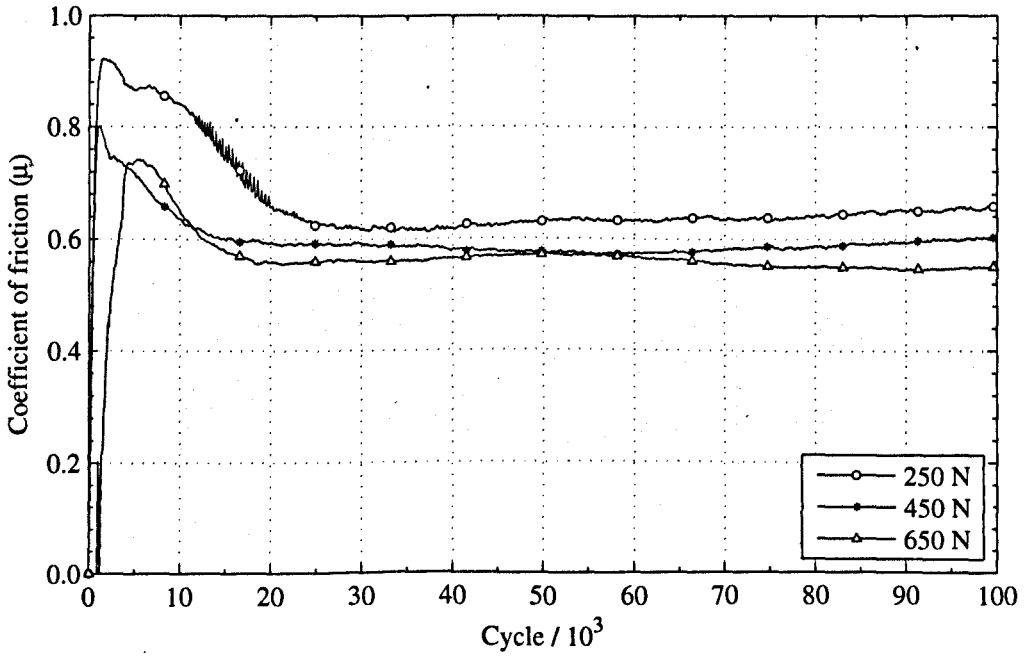

Figure 5.21: Instantaneous coefficient of friction for SCMVN specimen pairs with P = 250, 450 and 650 N and Δ^* = 10 μm.

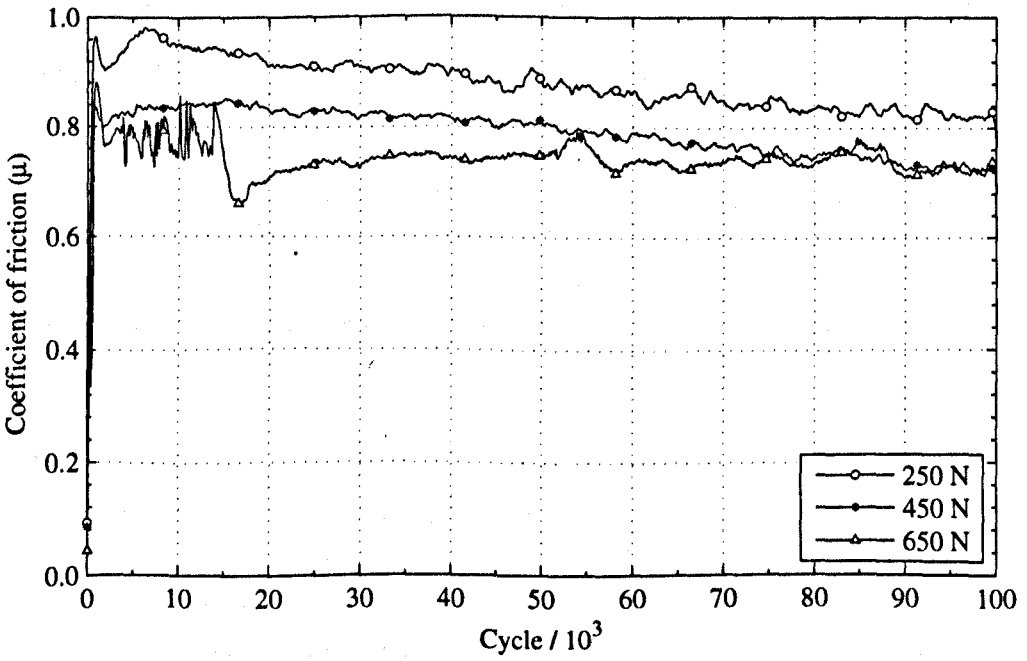

Figure 5.22: Instantaneous coefficient of friction for SCMVN specimen pairs with P = 250, 450 and 650 N and Δ^* = 25 μm.

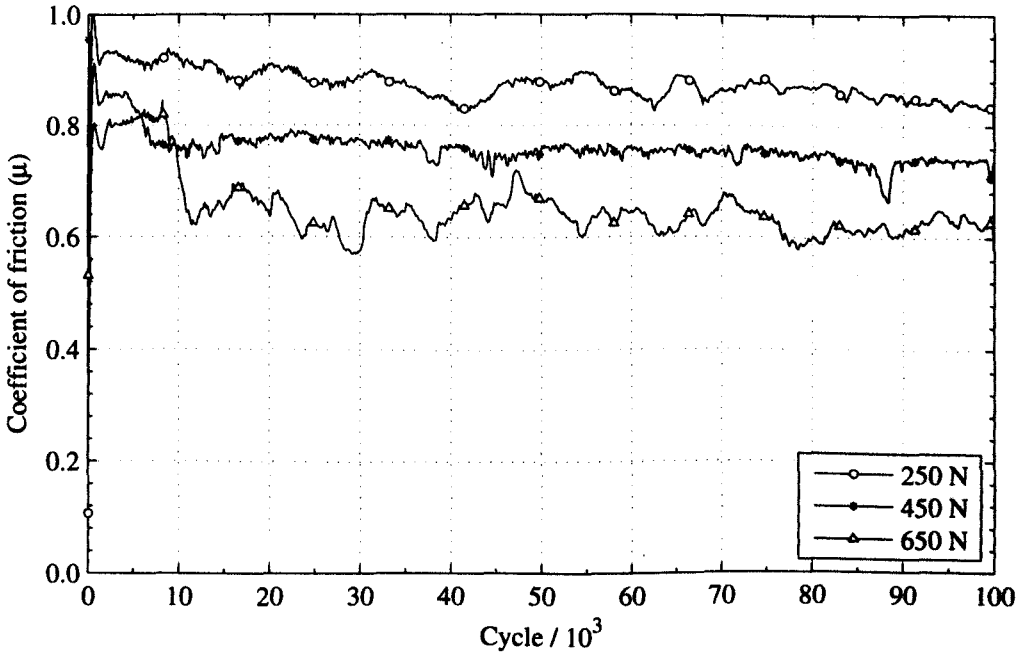

Figure 5.23: Instantaneous coefficient of friction for SCMVN specimen pairs with P = 250, 450 and 650 N and Δ^* = 50 μm.

Profilometry and wear analysis

Figures 5.24 to 5.26 show the averaged profiles for the SCMVN specimens, grouped by stroke. When the applied displacement amplitude was 10 μm (Figure 5.24), the damage to the surface was small: on the cylindrical specimen (at 250 N normal load), the region of the scar is only marginally smoother; however, on the flat specimen, there is a notable shallow scar, of approximately 3 μm depth and 0.4 mm width. As the load was increased to 450 and 650 N, there was no significant change in scale or nature of the damage. The behaviour is in contrast to that of the SCMV specimens under similar conditions which showed surface roughening rather than distinct material removal.

Figure 5.25 shows the averaged profiles for normal loads from 250 to 650 N with a 25 μm displacement amplitude: at all of the loads considered, there was bulk material removal with characteristic "U" shaped scars on the flat specimen; the wear scars are of a similar width (≈ 0.9 mm) on the flat and cylindrical specimens. As the load was increased from 250 to 450 N and finally to 650 N, the wear scar depth on the cylindrical specimen increased from approximately 8.7 μm to 11 μm and 16.5 μm respectively. At the same time, the wear scars on the corresponding flat specimens did not appreciably change in depth (remaining between 7 and 10 μm). Since the WL is approximately 10 μm deep, then the wear remained, in general, confined to that region on the flat specimens.

Figure 5.26 shows the averaged profiles for tests conducted at 50 μm applied displacement amplitude and 250 to 650 N normal loads. At all loads, the scars on the cylindrical specimen indicated bulk material removal (i.e., a "U" shape relative

to the unworn surface): at 250 N normal load, the depth was approximately 16 μm; on increasing the normal load to 450 and 650 μm, the depth of the scar increased to 36 and 50 μm respectively. Consequently, in all cases, the wear fully penetrated the WL. In contrast, the corresponding scars on the flat specimen showed a different evolution: at 250 N, the scar was roughly "U" shaped and approximately 13 μm deep; on increasing the normal load to 450 N, the depth reduced to ≈ 6 μm and had become more like a flat trough in character; as the load was increased further to 650 N, the scar became "W" shaped with the centre showing a small positive height of ≈ 2 μm.

Figure 5.27 plots the normalised wear of the flat specimen against the loading parameter in the same manner as for the SCMV specimens (Figure 5.27). It can be seen that there is significant scatter in the wear distribution at lower values of the loading parameter while at higher values, the wear is predominantly of the cylindrical specimen (as indicated by the average profiles). Overall, it appears that there is a correlation between the severity of the wear condition and an increasing bias toward wear of the cylindrical specimen. The wear distribution has also been examined as a function of normal load and displacement amplitude independently but no further correlations were found.

Figure 5.28 shows the total wear volume as a function of the actual measured dissipated energy; in the same manner as for the SCMV pairs, points are plotted for all test conditions considered. Simple linear regression (where $R^2 = 0.98$ is found) indicates that the relationship between the wear volume (V^w in mm^3) and the dissipated energy (E_d, in kJ) is

$$V^w = 6.78 \times 10^{-2} E_d - 6.21 \times 10^{-2} \tag{5.4}$$

giving the energy wear coefficient and the threshold energy respectively as $k_e = 6.78 \times 10^{-2}\,mm^3\,kJ^{-1}$ and $E_{th} = 0.92\,kJ$. Compared to the values for the SCMV specimens, the energy threshold is 16 % lower and the energy wear coefficient is 12 % less. Consequently, the nitrided specimens would be expected to wear less than the plain specimens at all dissipated energies below 2.5 kJ.

Microscopy and topographic observation of the scar

EDX analysis Table 5.3 was conducted on three areas of a flat SCMVN specimen following fretting: (A) in a region of wear debris (low brightness region in the BSE SEM micrographs); (B) from a metallic region within the wear scar; (C) from outside the wear scar. On comparison of the spectra from the unworn region (C) and the exposed metallic region inside the scar (B), it was found that the proportion of nitrogen drops from 10.7 to 4.1 wt. % while the proportion of iron increased from 73.7 to 85.1 wt. %—the changes being attributed to dispersal of the WL which is mainly iron nitrides (Section 4.1, Page 63). The spectrum taken in the region of wear debris (A) showed the lowest level of nitrogen (1.3 wt. %) and a high level of oxygen (37.6 wt. %) with an intermediate level of iron present (53.5 wt. %) compared to the other regions.

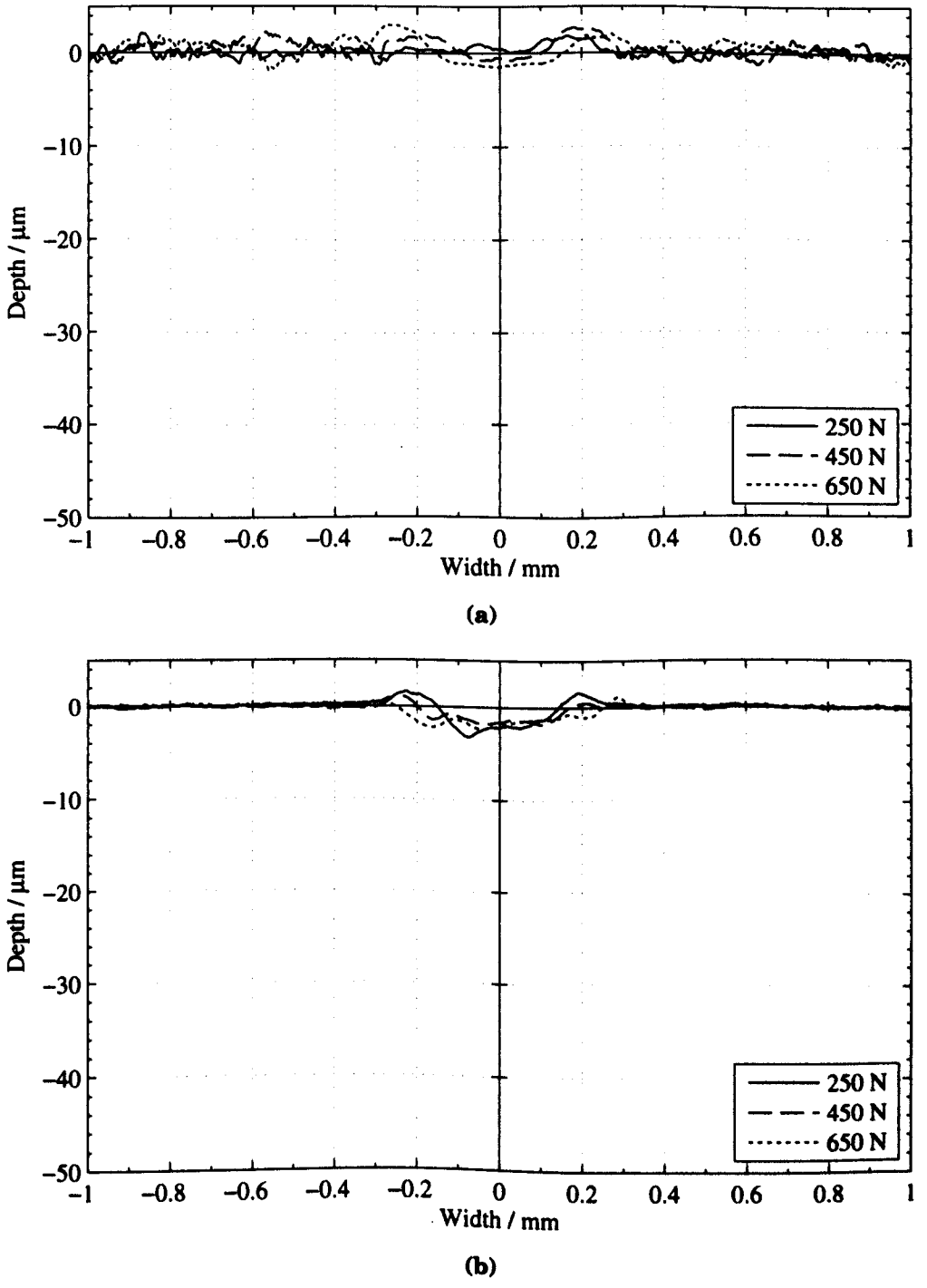

Figure 5.24: Average profiles of the: (a) cylindrical specimens and (b) flat specimens; from SCMVN specimen pairs, following 100×10^3 fretting cycles with P = 250, 450 and 650 N and Δ^* = 10 µm.

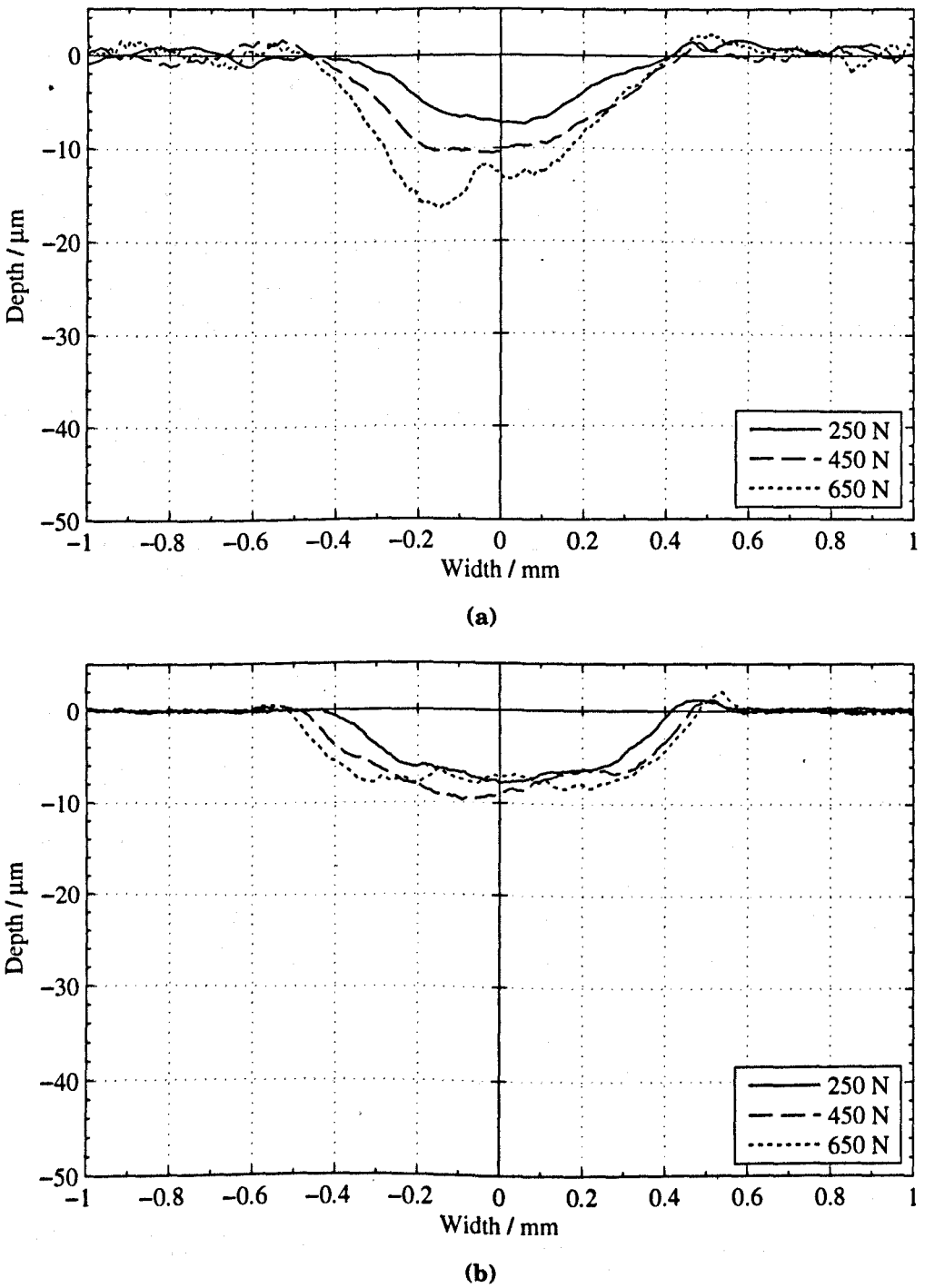

Figure 5.25: Average profiles of the: (a) cylindrical specimens and (b) flat specimens; from SCMVN specimen pairs, following 100×10^3 fretting cycles with P = 250, 450 and 650 N and Δ^* = 25 µm.

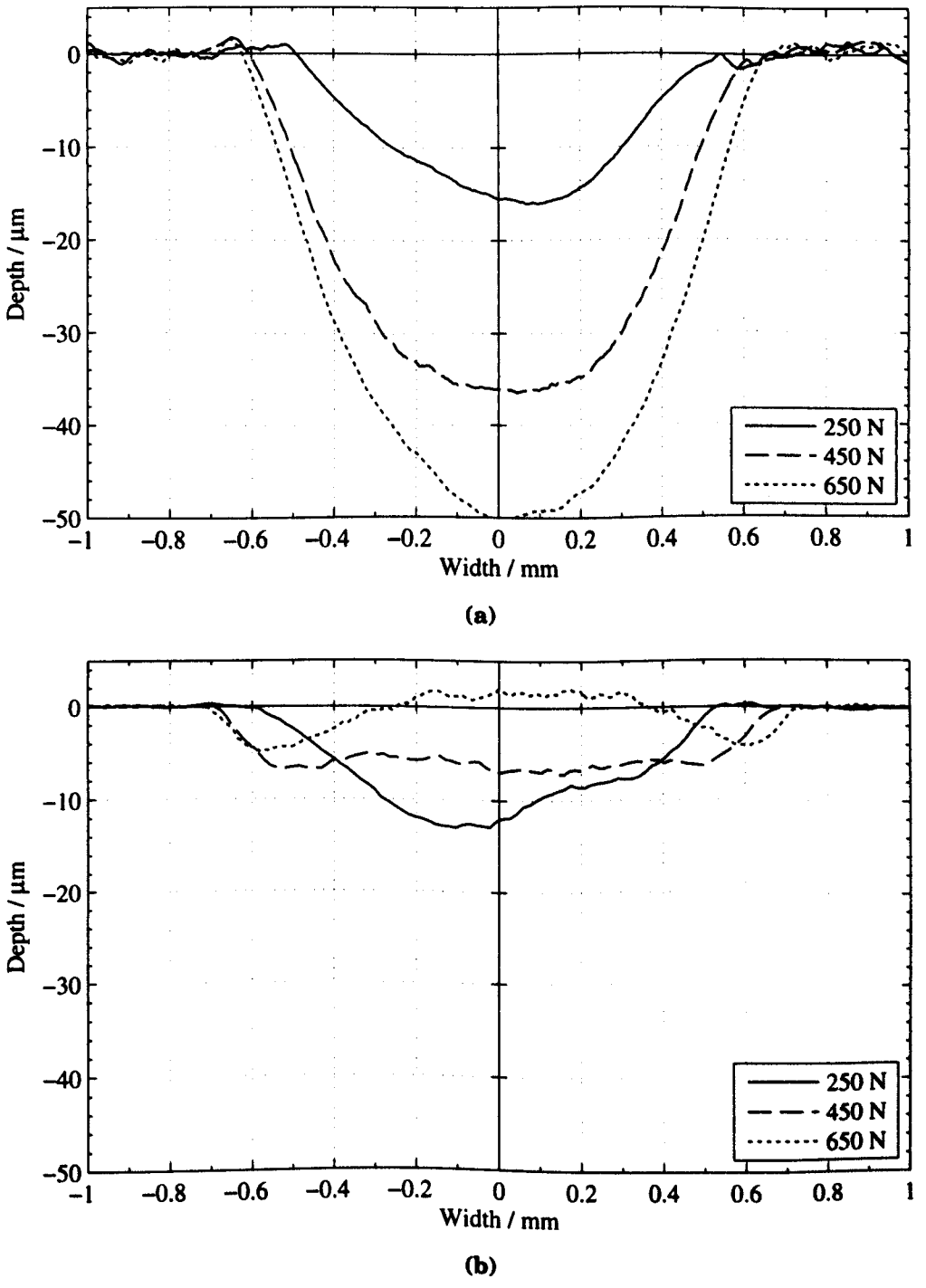

Figure 5.26: Average profiles of the: (a) cylindrical specimens and (b) flat specimens; from SCMVN specimen pairs, following 100×10^3 fretting cycles with P = 250, 450 and 650 N and Δ^* = 50 µm.

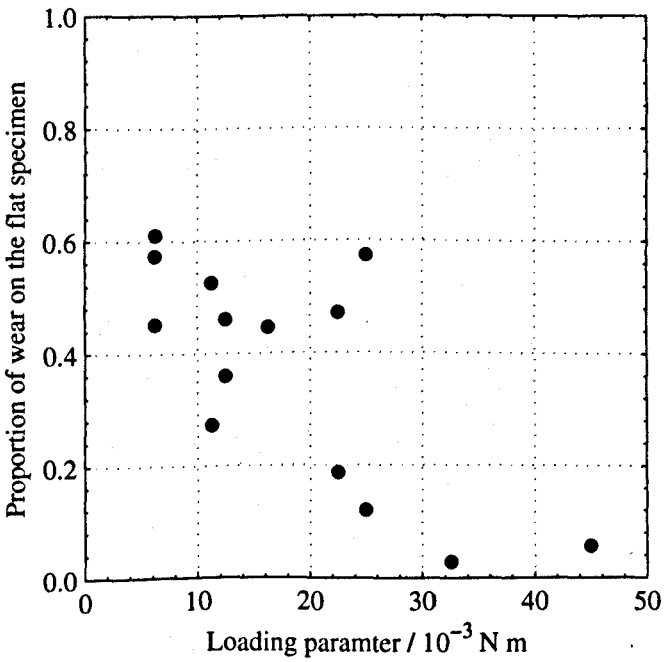

Figure 5.27: Wear of the flat specimen, normalised against the total wear of the flat and cylindrical specimen, as a function of the loading parameter for SCMVN specimen pairs.

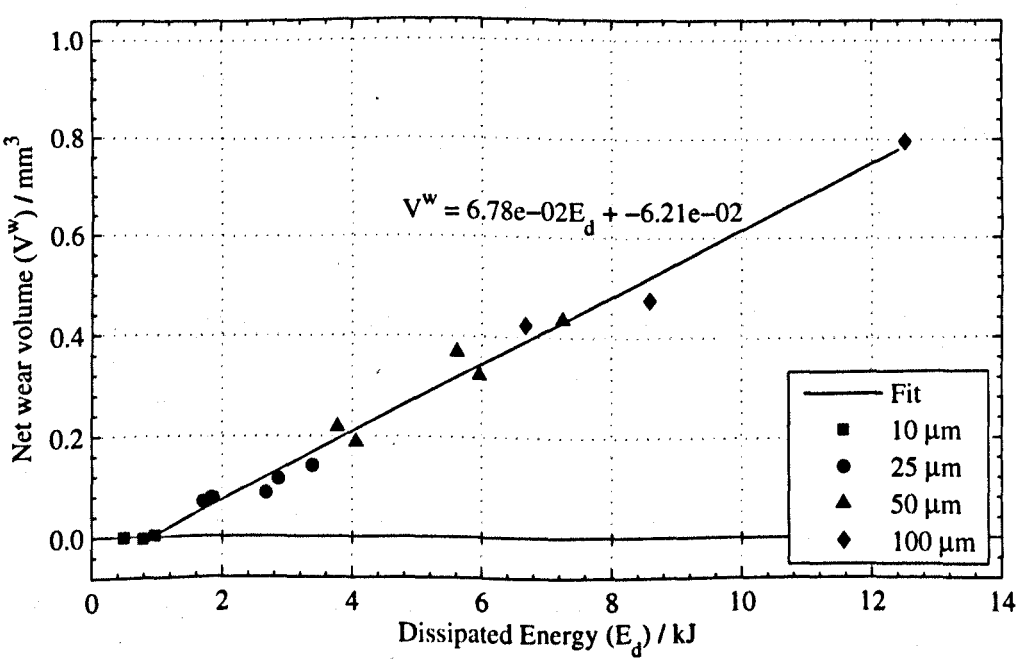

Figure 5.28: Wear volume as a function of dissipated energy for SCMVN specimen pairs; for combinations of P = 250, 450 and 650 N and Δ^* = 10, 25, 50 and 100 µm. .

Table 5.3: Data from EDX spectra from the surface of a flat SCMVN specimen from a homogeneous pair taken in three locations: (A) area of wear debris; (B) metallic region in the wear scar; (C) region outside of the worn area.

	Composition at location / wt. %		
Element	A	B	C
C	4.0	3.4	7.8
N	1.3	4.1	10.7
O	37.6	2.3	5.0
V	0.1	0.2	0.1
Cr	2.1	3.2	2.0
Fe	53.5	85.1	73.7
Mo	1.0	1.1	0.4

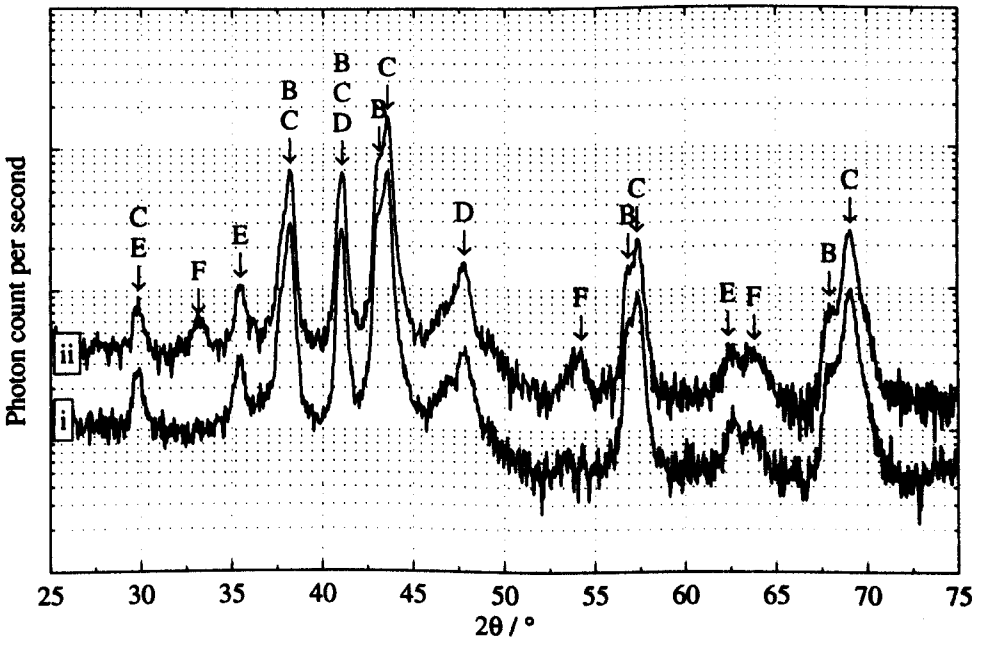

Figure 5.29: XRD spectra of a flat SCMVN specimen in the (i) unworn and (ii) worn states; peaks corresponding to the following compounds are highlighted: (B) Fe_2N, (C) Fe_3N, (D) Fe_4N, (E) Fe_3O_4, (F) Fe_2O_3.

Structural analysis of the worn and unworn surfaces was provided by XRD; unworn and worn spectra are shown overlayed in Figure 5.29. The majority of the spectral peaks are from iron nitrides which constitute the WL (Section 4.1, Page 63). However, it can be seen that haematite (Fe_2O_3) was uniquely identified in the spectra of the worn specimen (peaks labelled (F)).

Figures 5.30 and 5.31 present top view BSE SEM micrographs of SCMVN specimens following fretting under a range of normal loads (250 to 650 N) and displacement amplitudes (10 to 50 μm). In all cases, the selected specimens exhibited symmetrical wear behaviour—an instance where biased wear of one specimen occurred is examined separately in Figure 5.33.

Considering the BSE SEM images in Figure 5.30, it can be seen that all of the scars show a significant coverage of oxide debris. There appears to be more oxide coverage at the higher normal loads (Figure 5.30a compared with Figure 5.30d), although it is difficult to assess quantitatively. At 650 N normal load (Figure 5.30e), the debris bed toward the centre of the scar seems thicker and more coherent than at the lower normal loads (Figures 5.30a and 5.30c). In areas where the debris bed is breaking down (Figures 5.30d and 5.30f), it appears to be detaching in relatively large flakes (in the order of 75 μm).

Examining Figure 5.31 in conjunction with Figures 5.30c and 5.30d allows the variation in surface damage to be compared over a range of displacement amplitudes. As was observed with the homogeneous SCMV case at 10 μm displacement amplitude, the wear scar shows a significant coverage of oxide with no evidence of any change in character which could be associated with a central stick region (Figures 5.31a and 5.31b). When the displacement amplitude was increased to 25 μm (Figures 5.30c and 5.30d), there was a more complete layer of oxide which appears to be thicker, evidenced by the larger number of flakes in the process of detaching (Figure 5.30d). At 50 μm displacement amplitude (Figure 5.31c), there is again a high degree of oxide coverage, although there are relatively larger concentrated regions of exposed metal which were not apparent at the lower normal loads.

Figure 5.32 shows high magnification BSE SEM micrographs of the cross section of a flat specimen from a homogeneous SCMVN couple, following 100×10^3 fretting cycles with a 450 N normal load and 25 μm displacement amplitude: there is no evidence of any plasticity and the surface is smooth across the width of the scar. Where there is oxide debris on the surface, the boundary between the oxide and the underlying material is very abrupt. Comparing the image to the unworn case (Figure 4.4, Page 66), it is apparent that the wear has penetrated through the WL.

Figure 5.33 provides BSE SEM micrographs of a homogeneous SCMVN specimen pair (following 100×10^3 fretting cycles with $P = 450$ N and $\Delta^* = 100$ μm) where significantly higher wear of the cylindrical specimen was measured. Lower magnification images (Figures 5.33a and 5.33b) give a general overview of the flat and cylindrical specimen surfaces respectively: it is immediately apparent that the surface of the cylindrical specimen is predominantly exposed metallic material with a sparse coverage of oxide debris (Figure 5.33b). In comparison, the flat specimen is covered in a thick layer of adhered oxide (Figure 5.33a); higher magnification inspection of the oxide bed (Figure 5.33c) reveals distinctive smooth polished regions. In contrast, higher magnification imaging of the cylindrical specimen (Figure 5.33d) finds a smooth, relatively featureless, metal surface with abrasive scratch marks orientated in the direction of fretting.

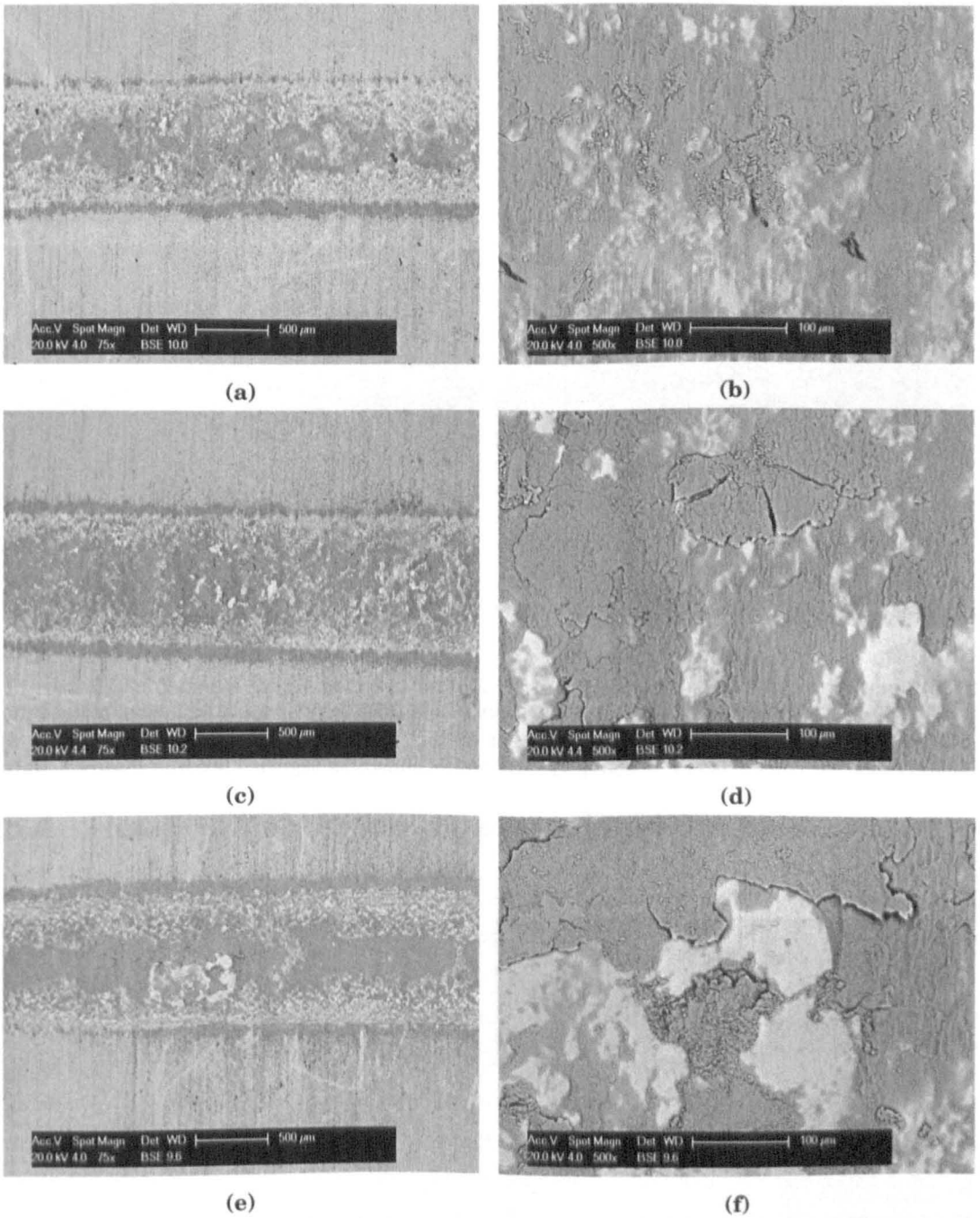

Figure 5.30: Top view, BSE SEM, micrographs of the wear scar on the flat specimen, from SCMVN pairs, following 100×10^3 fretting cycles with $\Delta^* = 25\,\mu m$ and P = (a, b) 250 N, (c, d) 450 N and (e, f) 650 N.

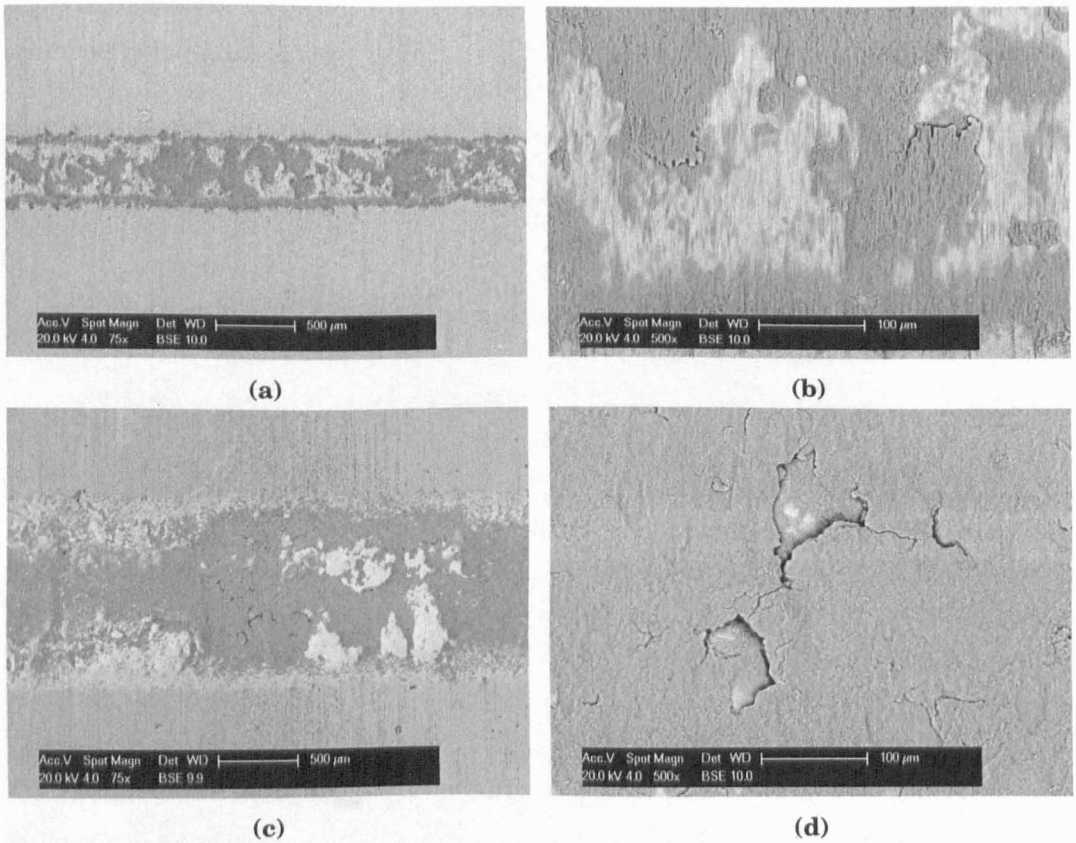

Figure 5.31: Top view, BSE SEM, micrographs of the wear scar on the flat specimen, from SCMVN pairs, following 100×10^3 fretting cycles with $P = 450\,\text{N}$ and $\Delta^* =$ (a, b) $10\,\mu\text{m}$ and (c, d) $50\,\mu\text{m}$ (note, for comparison $P = 450\,\text{N}$, $\Delta^* = 25\,\mu\text{m}$ is shown as Figure 5.30c and Figure 5.30d).

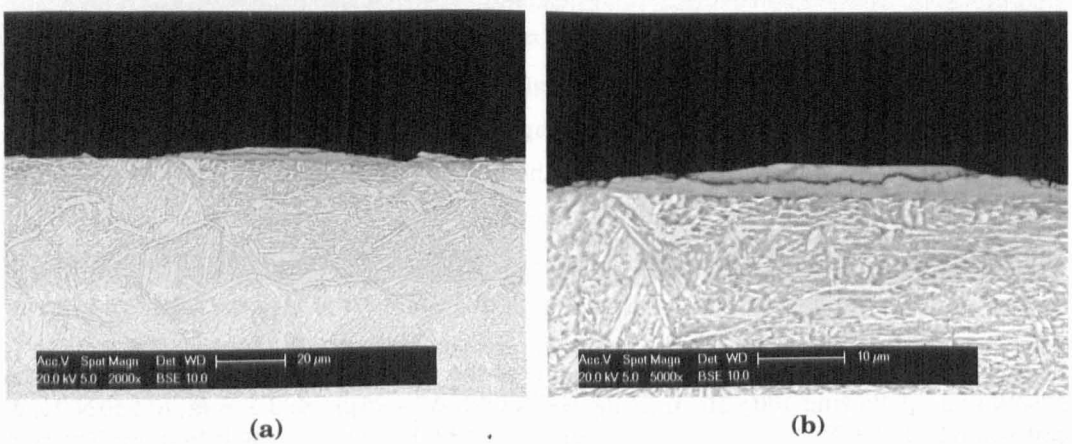

Figure 5.32: BSE SEM micrographs of a cross section of the flat specimen, of an SCMVN pair, following 100×10^3 fretting cycles with $P = 450\,\text{N}$ and $\Delta^* = 25\,\mu\text{m}$ at (a) intermediate magnification and (b) high magnification.

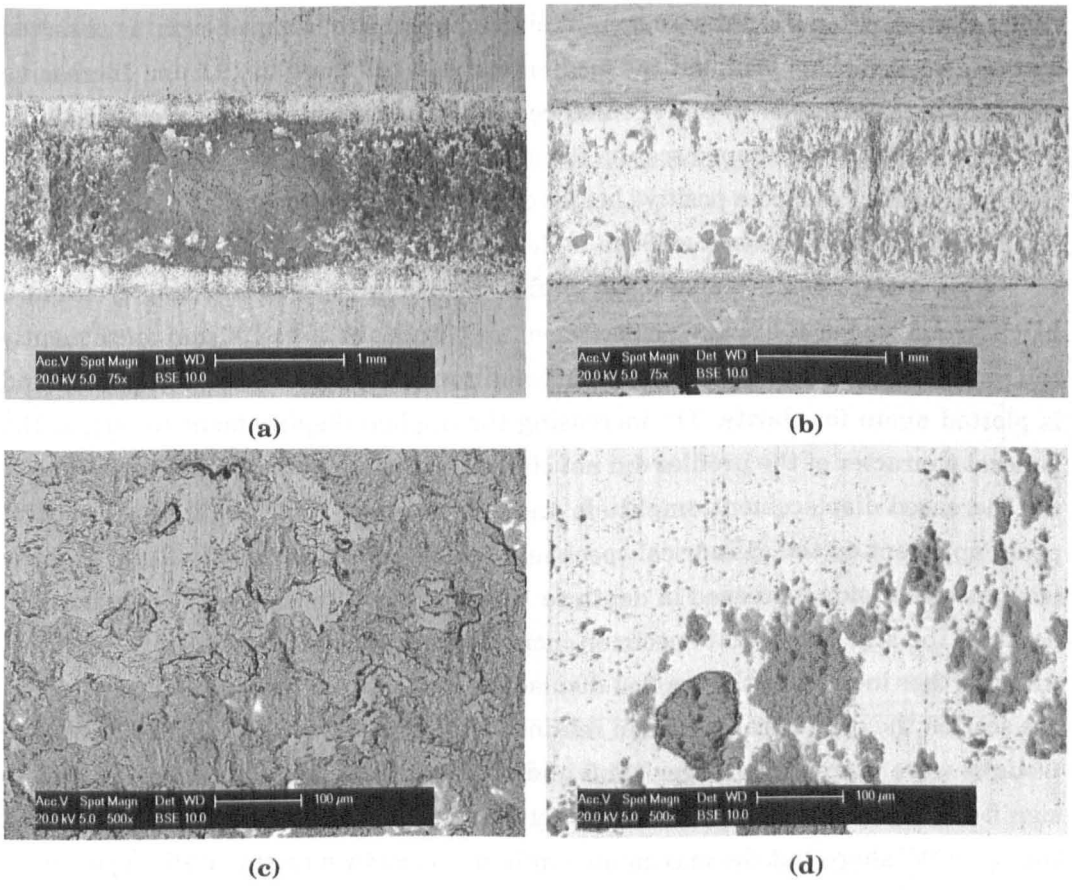

Figure 5.33: BSE SEM micrographs of an SCMVN specimen pair—(a, c) flat specimen, (b, d) cylindrical specimen—where biased wear was observed following 100×10^3 fretting cycles with $P = 450\,\text{N}$ and $\Delta^* = 100\,\mu\text{m}$.

5.4 Results: heterogeneous specimen couples

Figures 5.34 and 5.35 show the average wear scar profiles for heterogeneous specimen pairs (SCMVN flat and SCMV cylindrical specimens) as a function of load and displacement amplitude. The profiles in Figure 5.34 are following 100×10^3 fretting cycles at a fixed displacement amplitude of 25 µm and normal loads of 250 to 650 N. When the normal load was 250 N, the scar on the flat and cylindrical specimen were both "U" shaped (with respect to the unworn surfaces), indicating bulk material removal. The maximum depth of the wear scar on the cylindrical (SCMV) specimen was $\approx 8\,\mu\text{m}$ i.e., both the shape and depth were comparable to those found under the same loading conditions with a homogeneous pairings (Figure 5.9a). However, the wear scar on the flat (SCMVN) specimen had a more distinctive "V" shape and was $\approx 14\,\mu\text{m}$ deep—significantly deeper than the more "U" shaped scar ($\approx 10\,\mu\text{m}$) from the equivalent homogeneous test (Figure 5.25a). As the load was increased to 450 µm, the appearance of the cylindrical specimen's wear profile changed to a pronounced "W" shape with a significant central peak. The trough of each side of the peak was 7.5 and 7 µm deep, while the central peak was $\approx 1\,\mu\text{m}$ deep i.e., still below the original surface height. In

contrast, the scar on the flat specimen retained the same "U" shaped form, as observed with the lower normal load, but the maximum depth increased to 19.5 μm. Increasing the normal load further to 650 N enhanced the features already apparent at 450 N: the troughs of the "W" shaped scar on the cylindrical specimen were 5 and 8 μm while the central peak reached a positive height of ≈ 4 μm; concurrently the "U" shaped scar on the flat specimen reached ≈ 29 μm in depth.

Figure 5.35 presents the average profiles following 100×10^3 fretting cycles at a fixed normal load of 450 N and displacement amplitudes of 25 to 100 μm; consequently the profile for the $P = 450$ N, $\Delta^* = 25$ μm condition is the same as in Figure 5.34 and is plotted again for clarity. On increasing the applied displacement to 50 μm, the general character of the profiles did not change, although both became wider due to the increased displacement amplitude and greater wear. The height of the central peak, apparent on the cylindrical specimen, remained comparable (≈ 0 μm) and the troughs either side increased in depth to 10.5 and 9 μm. In contrast, the maximum depth of the scar on the flat specimen increased, by approximately 100 %, to 40 μm. After further increasing the applied displacement to 100 μm (the maximum studied), the scar on the cylindrical specimen retained the same "W" shaped character but the troughs were marginally larger (11.5 and 15.5 μm deep) and the central peak less significant (6 μm deep). In contrast, the counter scar on the flat specimen maintained the same "V" shape but the maximum depth increased by a further 65 % to 66 μm.

Figures 5.36 and 5.37 present the instantaneous COF over the full test period for heterogeneous specimen pairs (SCMVN flat and SCMV cylindrical specimen) under a range of load conditions. Figure 5.36 shows the instantaneous COF over a range of normal loads (250 to 650 N) at a fixed displacement amplitude (25 μm). When the normal load was 250 N, the COF showed significant instability: variations of more than 0.2 over a period of 5×10^3 cycles were apparent throughout the test. This contrsts strongly with the homogeneous cases (Figures 5.2 and 5.22) which showed comparably little variation. Increasing the normal load to 450 N saw the COF remain in general reduced compared to that at the lower normal load but the large variations over a period of thousands of cycles remained. In addition, for the first 50×10^3 cycles, there were periods during which the COF would drop rapidly by 0.2 to 0.4 over a duration of tens of cycles. At the highest normal load (650 N), the COF was in general less than at the lower normal loads; the large fluctuations over thousands of cycles remained and the higher frequency, sudden reductions, were greater in amplitude (up to 0.3) and evident up to $\approx 55 \times 10^3$ cycles.

Figure 5.37 plots the instantaneous COF for a range of displacement amplitudes (25 to 100 μm) at a fixed normal load (450 N). In general, the behaviour is very similar over the range of displacement amplitudes considered: in all cases there was an initial peak after approximately 1×10^3 cycles—0.88, 0.92 and 0.98 for $\Delta^* = 25$, 50 and 100 μm respectively—subsequently the COF decreased until the quasi steady state value (0.6 to 0.8) was reached after $\approx 15 \times 10^3$ cycles. At all of the displacement amplitudes

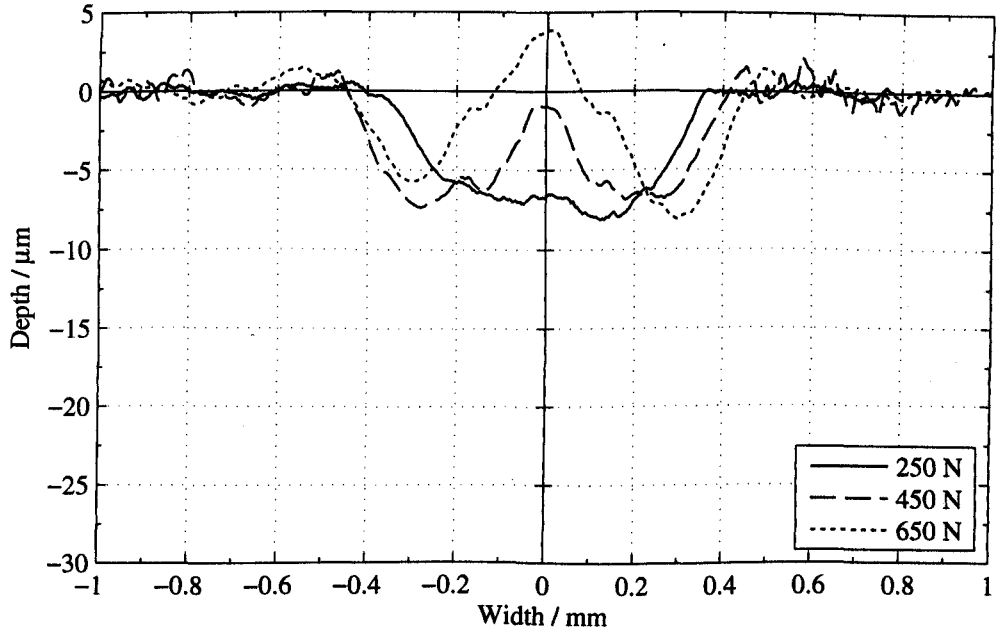

(a)

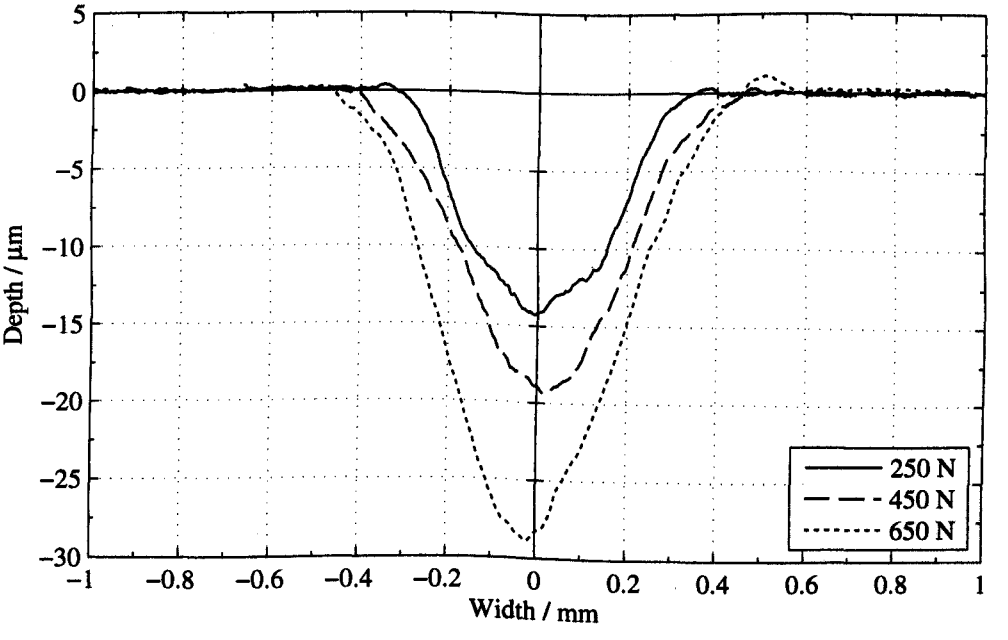

(b)

Figure 5.34: Average profiles of the: (a) cylindrical (SCMV) specimens and (b) flat (SCMVN) specimens; from heterogeneous SCMVN-SCMV pairs, following 100×10^3 fretting cycles with $P = 250$, 450 and 650 N and $\Delta^* = 25\,\mu m$.

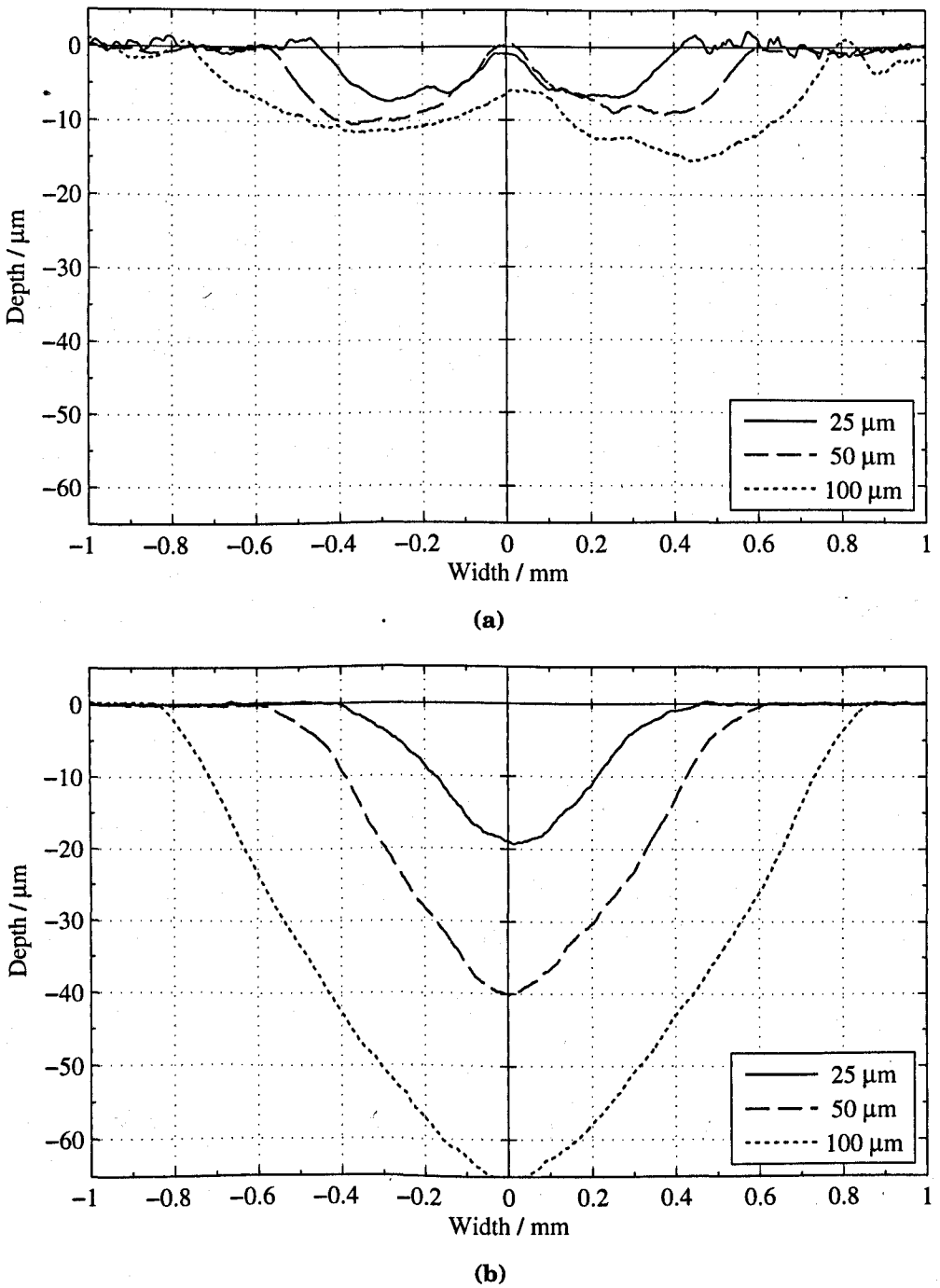

Figure 5.35: Average profiles of the: (a) cylindrical (SCMV) specimens and (b) flat (SCMVN) specimens; from heterogeneous SCMVN-SCMV pairs, following 100×10^3 fretting cycles with $P = 450\,\text{N}$ and $\Delta^* = 25$, 50 and 100 µm.

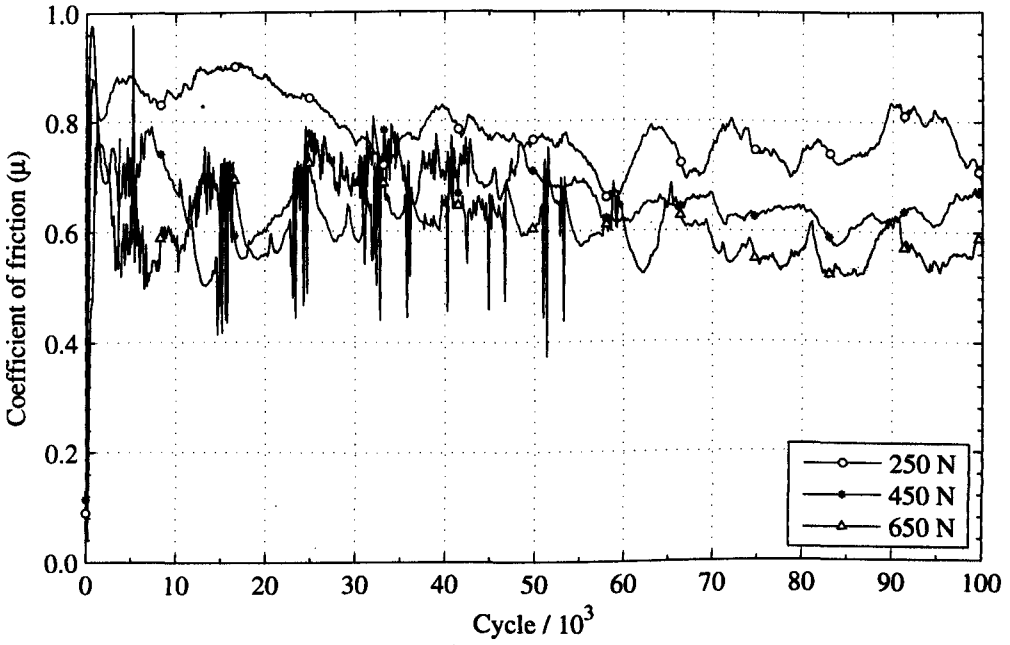

Figure 5.36: Instantaneous coefficient of friction for heterogeneous SCMVN-SCMV specimen pairs with P = 250, 450 and 650 N and Δ^* = 25 μm.

considered, the instantaneous COF displays comparable levels of instability—variations of 0.2 over a period of thousands of cycles—which does not show any appreciable correlation with changes in the displacement amplitude.

Figure 5.38 shows the average steady state COF for heterogeneous specimen pairs as a function of normal load. From the best fit line the COF (μ) as a function of the normal load (P) is found to be

$$\mu = 0.92 - 3.55 \times 10^{-4} P \tag{5.5}$$

Comparing this with the similar values found for the homogeneous cases (Equations (5.1) and (5.3)), it can be seen that the coefficient of friction is lower—over the evaluated range—for the heterogeneous combination than for either of the homogeneous combinations. Additionally, the variation with load is higher than that found for homogeneous SCMV, being more similar to the value for homogeneous SCMVN (-3.19×10^{-4} N^{-1} compared with -3.55×10^{-4} N^{-1}).

Figures 5.39 and 5.40 show the mid test characteristic fretting loops ($N = 50 \times 10^3$) for heterogeneous specimen pairs (SCMVN flat and SCMV cylindrical specimens) under a range of load conditions. Figure 5.39 shows the loop variation with normal load (P = 250 to 650 N) at a fixed displacement amplitude (Δ^* = 25 μm). The loops are characteristic of gross sliding and the positive stiffness during the sliding period is indicative of plasticity. As a consequence of the normal load increasing, the maximum and minimum tangential forces also increase. The loop plotted for a normal load of 650 N coincides with one of the periods of suddenly reduced COF seen in Figure 5.36

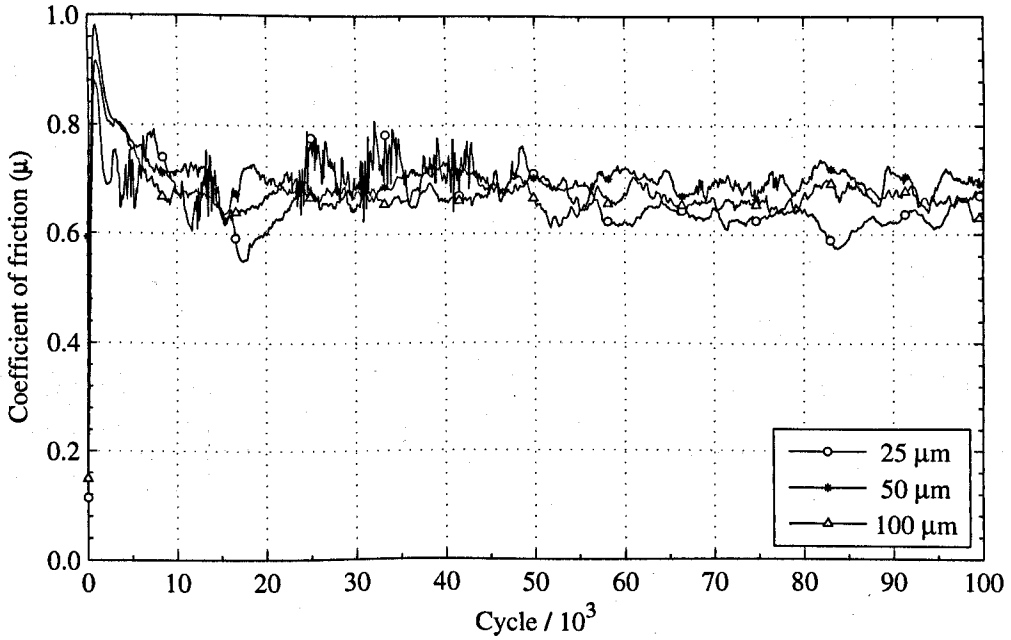

Figure 5.37: Instantaneous coefficient of friction for heterogeneous SCMVN-SCMV specimen pairs with $P = 450\,\text{N}$ $\Delta^* = 25$, 50 and 100 μm.

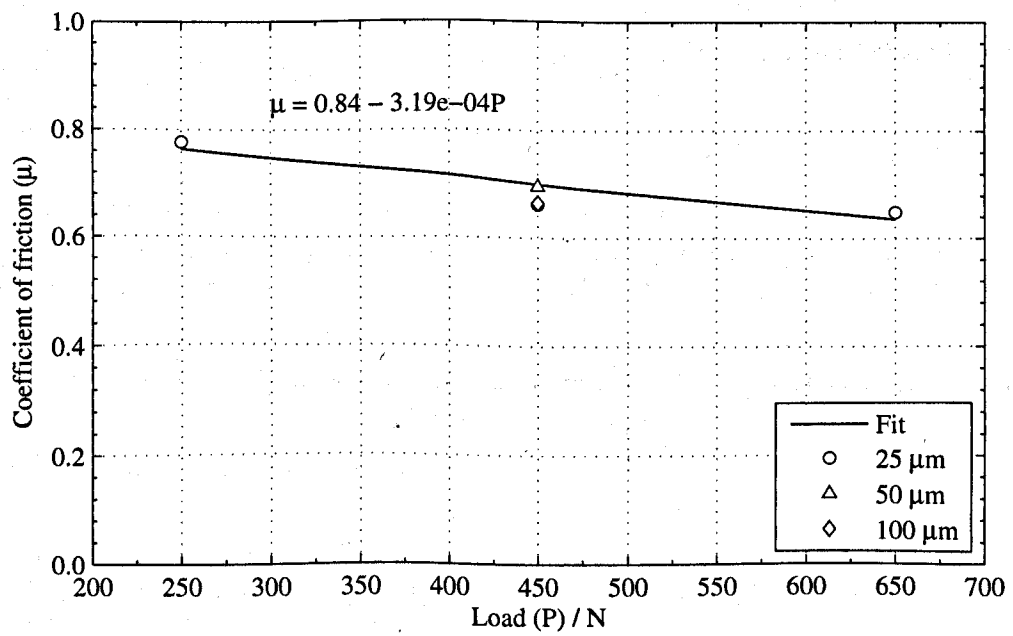

Figure 5.38: Mean average steady state COF, for heterogeneous specimen pairs, as a function of normal load for a range of applied displacement amplitudes.

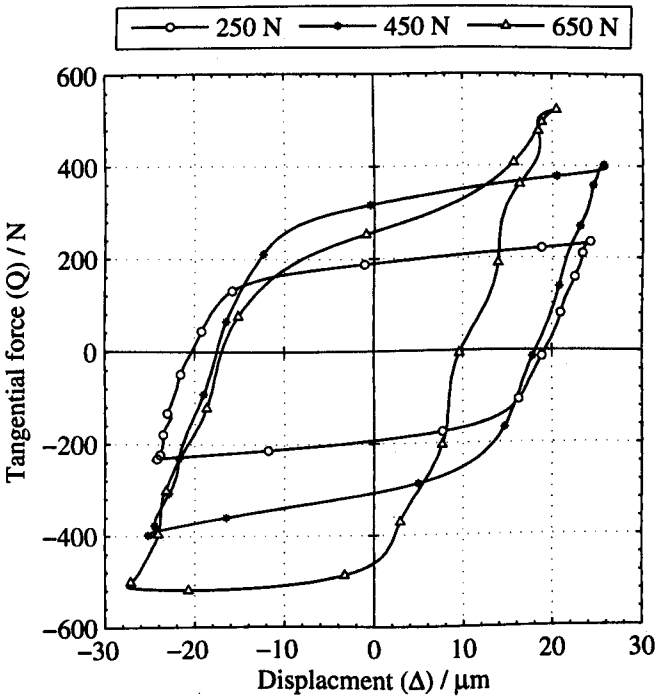

Figure 5.39: Mid test (cycle 50×10^3) force-displacement loops for heterogeneous SCMVN-SCMV fretting tests, with P = 250, 450 and 650 N and Δ^* = 25 μm.

and is representative of those observed during other, similar, periods in the COF history. As can be seen, the loop is highly asymmetrical; the upper half of the loop is truncated with a significant peak in tangential force toward the end of the stroke. The behaviour is not dissimilar to that seen when there was ploughing at the end of the displacement stroke seen at higher temperature (Figure 6.2, Page 136).

Figure 5.40 plots the characteristic loops at a fixed normal load (P = 450 N) and a range of displacement amplitudes (Δ^* = 25, 50 and 100 μm). For all the displacement amplitudes considered, the loops display a positive stiffness during the sliding period which becomes less, but is not eliminated, as the displacement amplitude is increased—indicating that there is still significant plasticity occurring in the contact.

Figure 5.41 shows the normalised wear of the SCMVN specimen (normalised by the total wear of both specimens) plotted as a function of the loading parameter (as previously described in Section 5.3.1, Page 86). It can be seen that the wear is biased toward the SCMVN specimen which is the harder of the couple; the mean normalised wear of the SCMVN specimen (as a fraction of the total wear of the couple) is found to be 0.74 with a standard deviation of 0.11. There appears to be some correlation between a higher load parameter and increased wear of the nitrided specimen. Examination of the wear data reveals that this is not the result of an independent correlation with load or displacement amplitude.

Figure 5.42 plots the total wear volume as a function of the measured dissipated energy for the heterogeneous specimen pairs for each load condition considered. Using

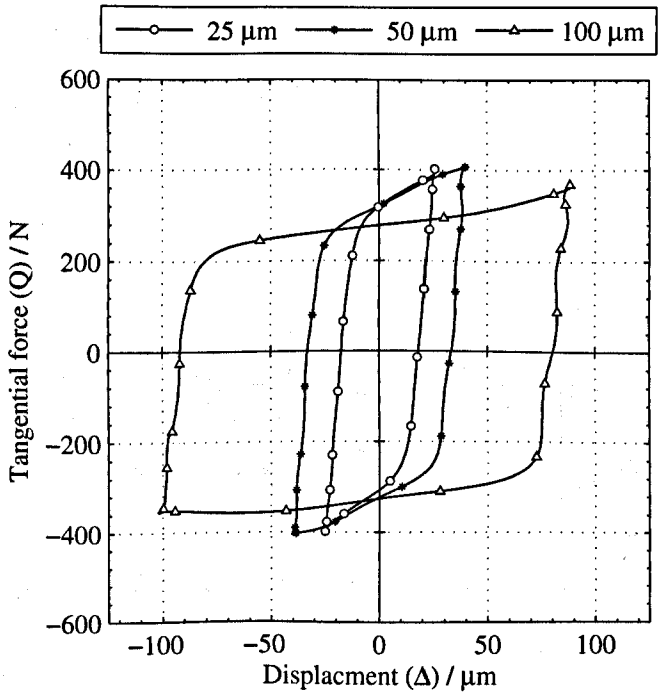

Figure 5.40: Mid test (cycle 50×10^3) force-displacement loops for heterogeneous SCMVN-SCMV fretting tests, with $P = 450\,\text{N}$ and $\Delta^* = 25$, 50 and 100 μm.

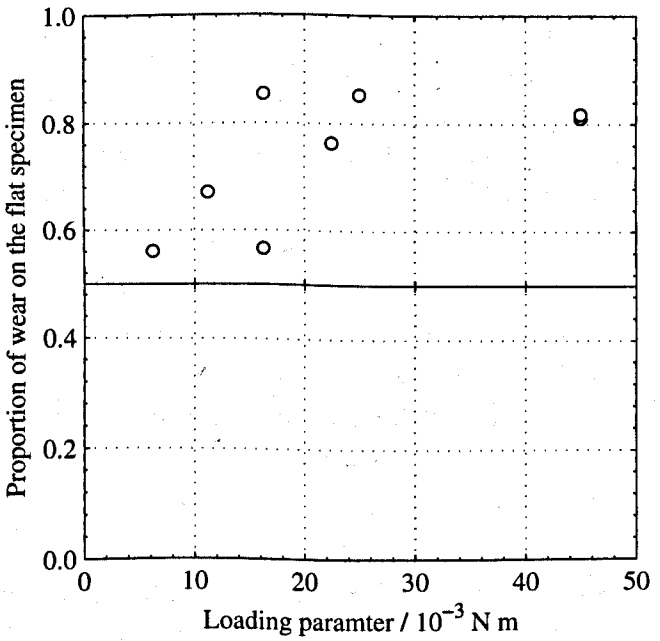

Figure 5.41: Normalised wear of the nitrided specimen (normalised against the total wear of the flat and cylindrical specimen) as a function of the loading parameter for heterogeneous specimen pairs.

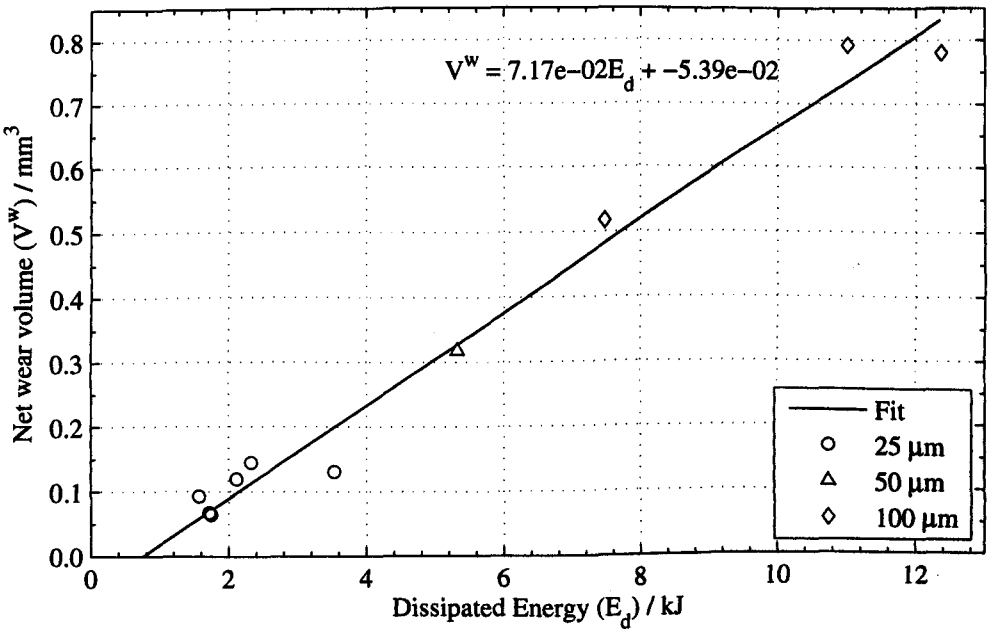

Figure 5.42: Wear volume as a function of dissipated energy for heterogeneous SCMVN-SCMV specimen pairs; for P = 250, 450 and 650 N and Δ^* = 10, 25, 50 and 100 µm.

a least squares method (the correlation coefficient was found to be $R^2 = 0.98$), the wear volume (V^w, in mm^3) was found to be linearly dependent on the dissipated energy (E_d, in kJ) such that:

$$V^w = 7.17 \times 10^{-2} E_d - 5.39 \times 10^{-2} \tag{5.6}$$

Consequently, the threshold energy and wear coefficient are found to be $E_{th} = 0.75$ kJ and $k_e = 7.17 \times 10^{-2}$ mm^3 kJ^{-1} respectively.

Figure 5.43 shows BSE SEM top-view micrographs specimens from a heterogeneous couple after 100×10^3 fretting cycles with a normal load of 450 N and an applied displacement amplitude of 25 µm; micrographs of the flat (SCMVN) specimen are shown in the left hand column while images of the cylindrical (SCMV) specimen are in the right hand column. The lower magnification images (Figures 5.43a and 5.43b) give an overview of the wear scars: both samples are generally covered in oxide debris (shown by the lower brightness regions), but there are relatively large areas of bright metal visible on the surface of the SCMVN specimen (Figure 5.43b) with no similar features apparent on the SCMV specimen (Figure 5.43a). Inspection of the higher magnification images (Figures 5.43c and 5.43e) finds the metallic areas to be smooth with scratches orientated in the direction of the fretting motion. The higher magnification images of the SCMV specimen (Figures 5.43d and 5.43f) focus on the central region of the scar—which the profilometry indicated to be raised (Figure 5.34, Page 111). This region is of noticeably higher brightness, indicating significant metallic content, while the outer regions of the scar are more completely covered in oxide; close inspection of Figure 5.43f reveals scratch marks on the large metallic feature in the centre of the

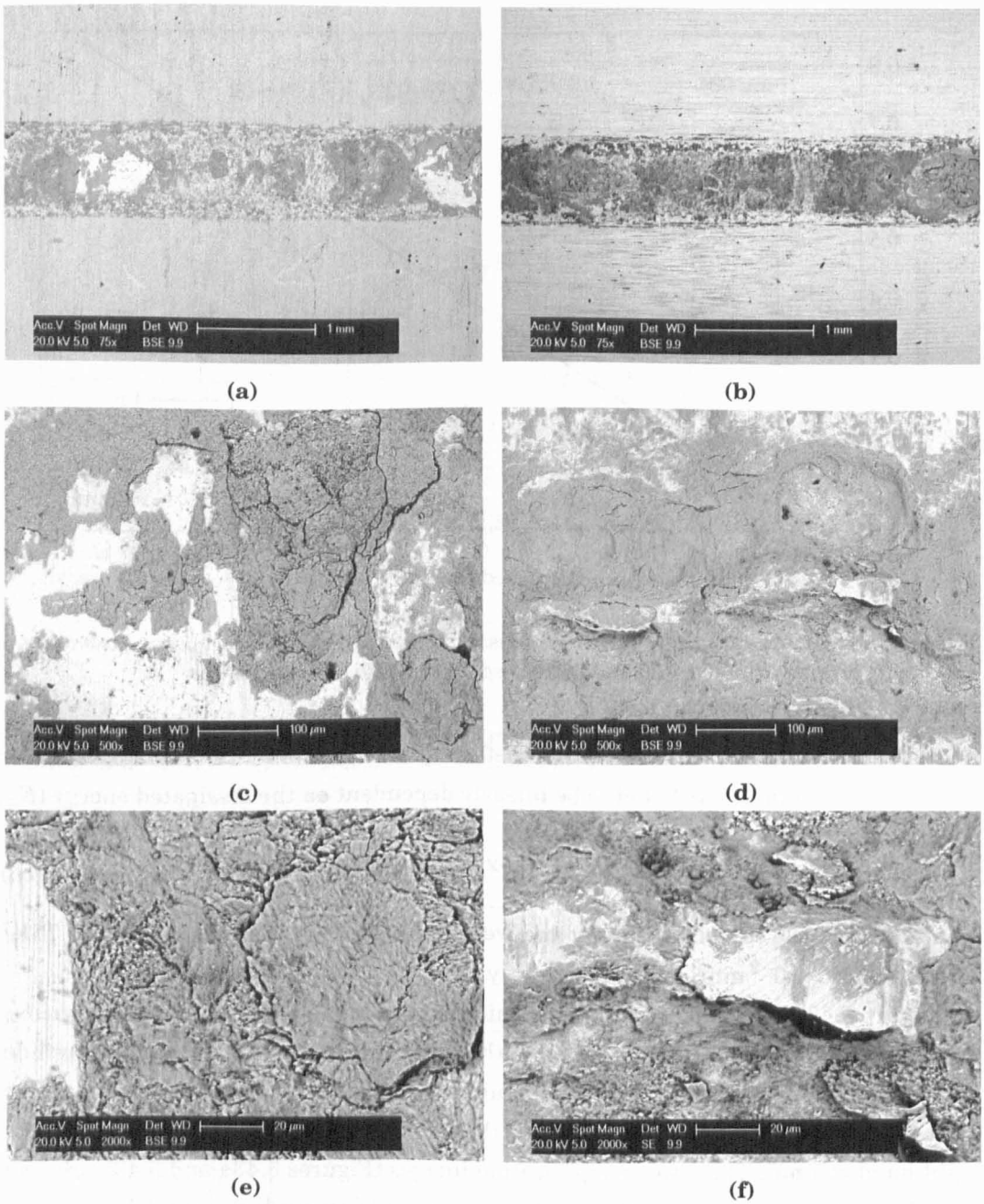

Figure 5.43: Top view, BSE SEM, micrographs of the wear scar of: (a, c, e) flat (SCMVN) specimens and (b, d, f) cylindrical (SCMV) specimens at low, medium and high magnification, from a heterogeneous specimen pair following 100×10^3 fretting cycles with $P = 450\,\text{N}$ and $\Delta^* = 25\,\mu\text{m}$.

field of view running at approximately 45° to the fretting direction, suggesting that the material has at some point become detached from the parent surface.

Figure 5.44 provides BSE SEM micrographs of cross sections of the same specimens as in Figure 5.43; as before, views of the SCMVN flat specimen are shown in the left hand column and the images of the SCMV cylindrical specimen are arranged in the right hand column. In these views, the differences between the wear morphology is

striking: the underlying metal of the nitrided specimen (Figures 5.44a, 5.44c and 5.44e) shows a very smooth surface—there is no evidence of any plasticity and there is a sharp interface between the adhered oxide debris and underlying metallic bulk. In contrast, the raised central region of the scar on the SCMV specimen (Figures 5.44b, 5.44d and 5.44f) is metallic (not transferred or adhered oxide debris) and shows very high levels of plastic flow—evident in the highly distorted grain structure. Moreover, the interface between the adhered debris and underlying metallic bulk is less well defined with notable surface roughening and small inlets filled with compacted oxide.

Figure 5.45 shows top-view BSE SEM micrographs of a heterogeneous specimen pair following 100×10^3 fretting cycles with a 450 N normal load and 100 μm applied displacement amplitude—the corresponding profilometry (Figure 5.35, Page 112) indicated that the raised central feature was less prominent than when the displacement amplitude was lower. Images of the flat (SCMVN) specimen are shown to the left and images of the cylindrical (SCMV) specimen to the right. Examination of the lower magnification images (Figures 5.45a and 5.45b) reveals similar features to those already seen in Figure 5.44 i.e., the flat SCMVN specimen (Figure 5.45a) shows significant regions of exposed metal with no adhered debris while the cylindrical SCMV specimen (Figure 5.45b) is fully covered in oxide. Figure 5.45c focusses on the central region of the flat specimen showing that while there is significant oxide, it is *patchy* and there are regions of metal clearly visible across the entire area. Figure 5.45e focusses on one of the large metallic regions visible in Figure 5.45a in which the scratch marks, resulting from abrasive damage, are evident. Figures 5.45d and 5.45f highlight a large flake of compacted oxide (approximately 230 μm × 240 μm) on the surface of the SCMV specimen. From the higher magnification image shown in Figure 5.45e, it is apparent that the surface is smooth and polished, indicating it may have been abrading the opposing surface.

Figure 5.46 provides BSE SEM micrographs of the cross sections of the specimens presented in Figure 5.45 (images of the SCMVN specimen are in the left hand column and images of the SCMV specimen are in the right hand column). As was expected from the profilometry (Figure 5.35, Page 112), there are no raised regions in either scar (Figures 5.46a and 5.46b). However, the features are very similar to those already observed in Figure 5.43: the SCMVN specimen shows no evidence of plasticity—there is no grain deformation or roughening of the surface (Figure 5.46c); where there is oxide debris adhered to the surface, there is a very abrupt interface with no mechanical "key" into the surface. In contrast, there is extensive plastic flow evident in the surface of the SCMV specimen (Figures 5.46d and 5.46f), with highly distorted grains being visible near the surface. Moreover, the high level of plastic deformation has resulted in a rough surface into which the oxide layer has become compacted. Particularly visible in Figures 5.46d and 5.46f, there is a band—approximately 16 μm deep from the surface—running across the specimen where the surface has etched more heavily; this indicates the depth of the plasticity since these regions are more chemically reactive

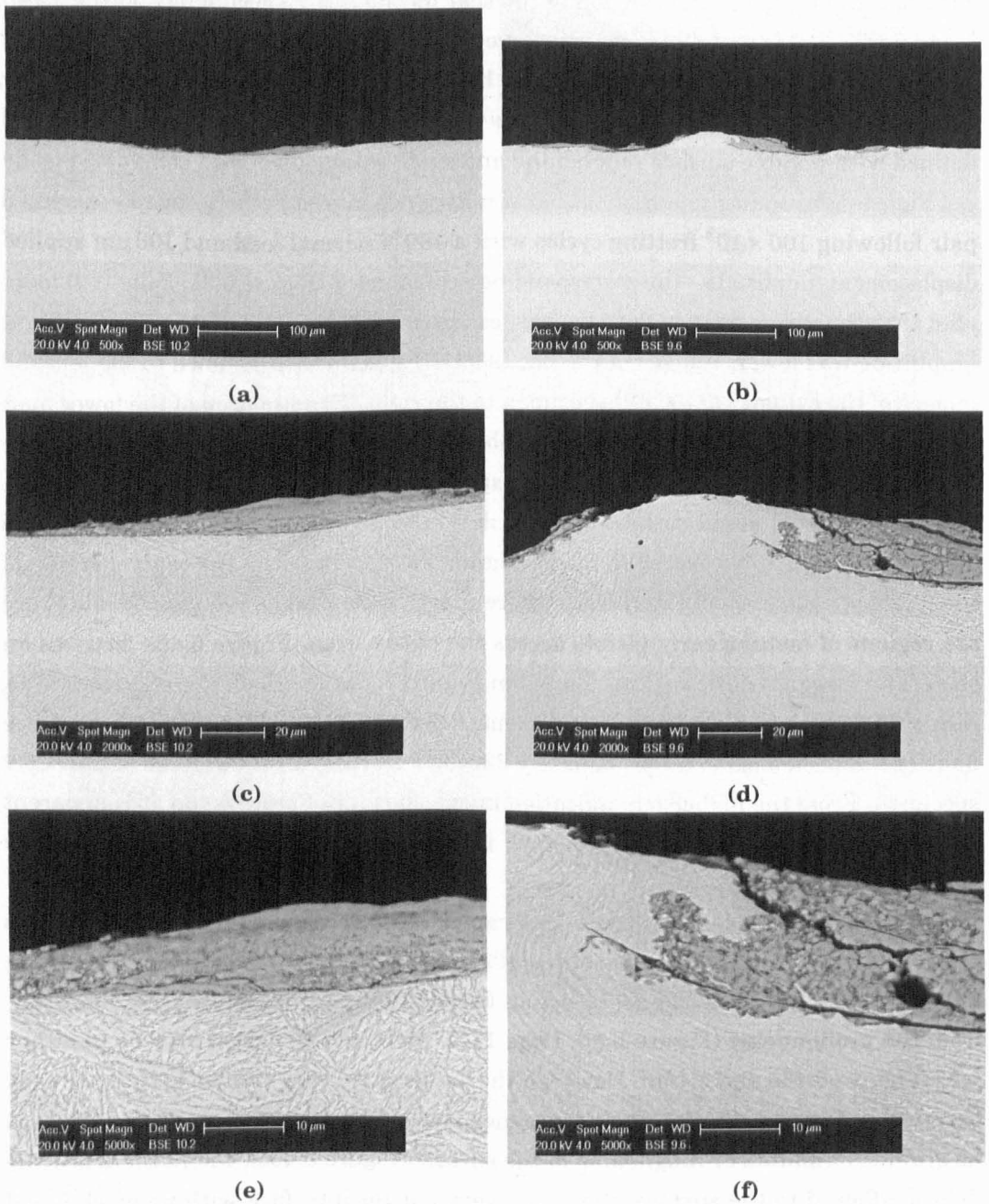

Figure 5.44: Cross section, BSE SEM, micrographs of the wear scar of the (a, c, e) flat (SCMVN) and (b, d, f) cylindrical (SCMV) specimens at low, intermediate and high magnification, from a heterogeneous specimen pair, following 100×10^3 fretting cycles with $P = 450\,\text{N}$ and $\Delta^* = 25\,\mu\text{m}$.

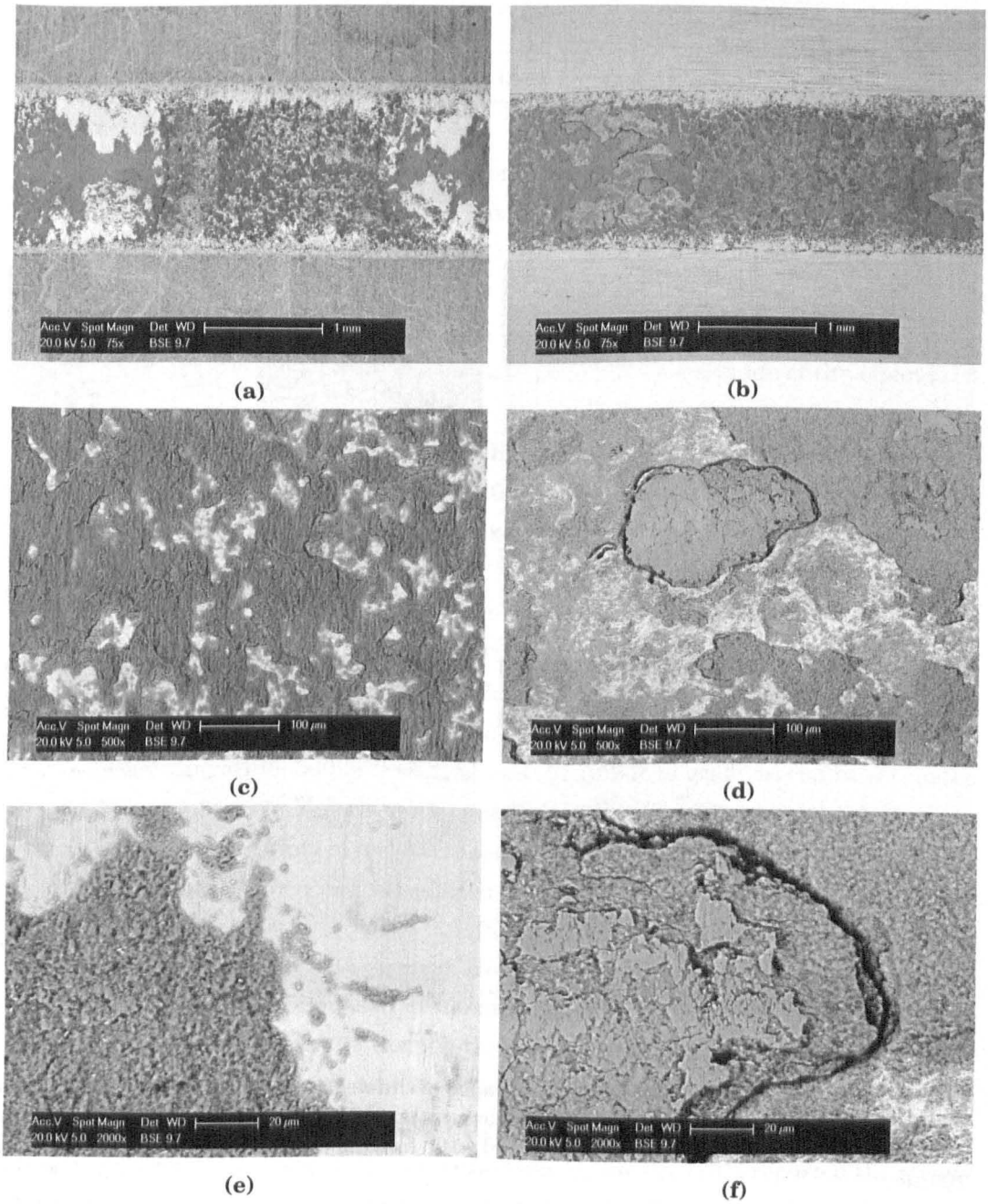

Figure 5.45: Top view, BSE SEM, micrographs of the wear scar of: (a, c, e) flat (SCMVN) specimen and (b, d, f) cylindrical (SCMV) specimen at low, intermediate and high magnification, from a heterogeneous specimen pair following 100×10^3 fretting cycles with $P = 450\,\text{N}$ and $\Delta^* = 100\,\mu\text{m}$.

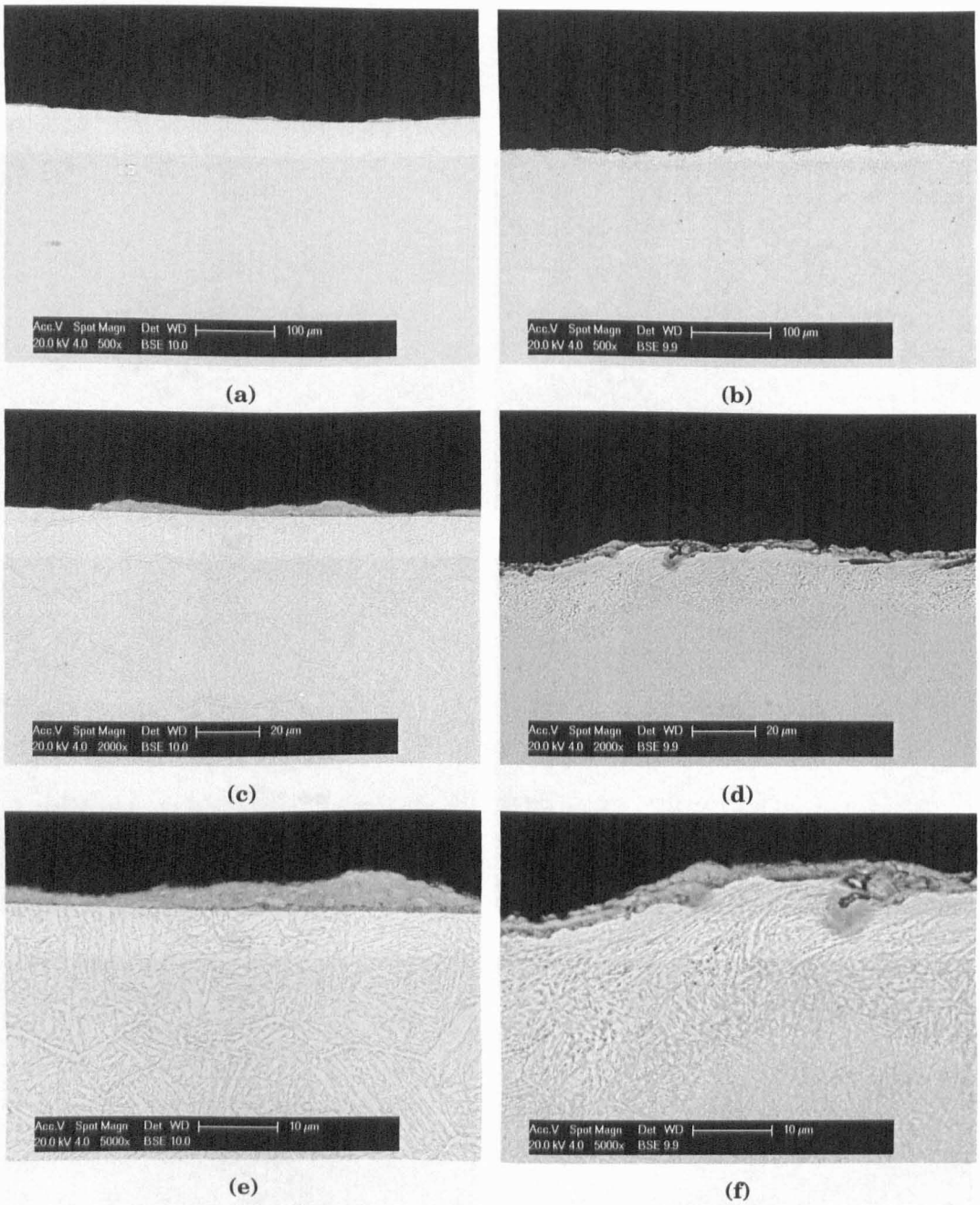

Figure 5.46: Cross section, BSE SEM, micrographs of the wear scar of the (b, d, f) flat (SCMVN) and (a, c, e) cylindrical (SCMV) specimens at low, intermediate and high magnification from a heterogeneous specimen pair, following 100×10^3 fretting cycles with $P = 450\,\text{N}$ and $\Delta^* = 100\,\mu\text{m}$.

and hence etch faster than the un-deformed bulk material [184].

5.5 Discussion

The results presented here clearly indicate that the COF is a function of normal load; the behaviour is summarised in Table 5.4 in terms of the the theoretical zero-load COF

Table 5.4: Summary of the COF parameters derived for the various material combinations

Material combination	Zero-load COF (μ_0)	COF-load gradient (β_p) / $\times 10^{-4} N^{-1}$
SCMV	0.82	-1.64
SCMVN	0.92	-3.55
SCMVN-SCMV	0.84	-3.19

(μ_0) and the COF-load gradient (β_p) for comparison. Over the load interval studied (250, 450 and 650 N), it has been found that the COF decreases linearly with increasing normal load: the rate of change was -1.6×10^{-4}, -3.6×10^{-4} and $-3.2 \times 10^{-4} N^{-1}$ for homogeneous SCMV, homogeneous SCMVN and heterogeneous SCMV-SCMVN specimen pairs respectively. An investigation of the literature reveals that this is not a unique finding, although no direct investigation seems to have been made of the effect [153, 181, 182, 185, 186].

Fouvry [182] fretted a 10 mm radius chromium steel cylinder against a flat steel plane; he considered two normal loads (200 and 1000 N) and reported that the steady state COF was lower at the higher load—examination of the data allows the COF-load gradient to be estimated as $-1.3 \times 10^{-4} N^{-1}$. Similarly, in a paper primarily on finite element modelling of fretting of wear, McColl et al. [153] published limited data on the fretting SCMV-SCMVN heterogeneous material pairs. In this work, they used a cylinder on flat geometry with a 6 mm radius cylinder (similar to the set-up used in the present work); their data indicated that the COF decreased linearly with increasing normal load (over the range 185, 500 and 1670 N) and the COF-load gradient can be estimated to have been $-1.3 \times 10^{-4} N^{-1}$. In work concerning the effect of material substrate on coating performance, Shima et al. [185] used a crossed cylinder specimen arrangement (with a 6 mm radius). However, in addition to data on the fretting of the coating, they included values for the steady state COF for a steel (SUJ2), titanium alloy (Ti6Al4V) and aluminium alloy (ASCM20) under fretting conditions with normal loads of 1.4 to 22.7 N. Although not discussed in the original work, it is apparent that at all but the lowest normal load, the COF (for the three substrate materials) decreased linearly with increasing normal load, and the COF-load gradient can be estimated to have been $9.7 \times 10^{-3} N^{-1}$. In a study considering the fretting of EN24 and EN31 steels in a crossed cylinder arrangement, Ramesh and Gnanamoorthy [181] reported the steady state COF values over a range of normal loads (2.4 to 29.4 N); their results again showed the COF to be a linear function of the normal load: the COF-load gradient is estimated from their data to have been $-9.3 \times 10^{-3} N^{-1}$. Zhang et al. [186] also considered a crossed cylinder fretting arrangement using 1 mm diameter (0.87 wt. % C) steel wires; their steady state COF data again showed a linear relationship with the normal load—in this case the COF-load gradient was estimated from their data to have been $-11.0 \times 10^{-3} N^{-1}$.

From these reports it is apparent that the steady state COF *is* in general a function of the normal load under fretting conditions. However, (as far as the author is aware) only two workers have directly discussed the phenomena and neither offered a satisfying hypothesis: Fouvry [182] suggested that if a pressure dependent term were added to the Bowden and Tabor [180] description of the interfacial shear stress, it would account for the observed behaviour; the mechanistic basis for this modification is, however, unclear. Zhang et al. [186] claimed that the the asperity contacts were elastic at low loads and resulted in an interlocking of opposing asperities (causing high friction) while at higher loads the interaction was plastic—presumably smoothing off the previously interlocking asperities. Since the reported COF values are all under steady state, where the interaction is no longer between two surfaces but is a complex three body case [87–89] (Section 2.5.3, Page 23), any plausible explanation must be based in the rheology of the debris. Closer examination of the reported data indicates a further relationship: of the cases (including the present work) which utilised a 2D line contact, the COF-load gradient was in the order of $1 \times 10^{-4}\,\mathrm{N}^{-1}$, while for the studies that considered a point contact (which all employed crossed cylinders), the values were consistently two orders of magnitude higher ($\approx 100 \times 10^{-4}\,\mathrm{N}^{-1}$). Such a contact geometry dependent effect may also be related to the third body, since a stable debris bed may more readily form within a more conforming contact [104–106].

For each of the material combinations studied in this work—above some critical energy (E_{th})—the wear volume has been found to be proportional to the dissipated energy (E_d); consequently, it makes more sense to express the wear rate in terms of:

$$V^w(x) = \begin{cases} k_e(E_d - E_{th}) & \text{for } E_d \geq E_{th} \\ 0 & \text{otherwise} \end{cases} \tag{5.7}$$

As was discussed in Section 4.5.4 (Page 74), an analysis of the wear volume as a function of the dissipated energy is equivalent to considering wear volume in terms of the Archard type work (the product of the normal load and total slid distance) i.e., if the COF is constant, then it is merely a scaling factor between the two. However, in this case it has already been demonstrated that the COF is itself a function of the normal load, so only the energy-wear analysis is considered further. The resulting values of the energy-wear constant (k_e) and threshold energy for the material combinations considered in this study are tabulated in Table 5.5. The wear coefficients established for homogeneous SCMV and SCMVN material combinations indicate that there is only a 12 % improvement in wear rate resulting from nitriding ($6.78\,\mathrm{mm^3\,kJ^{-1}}$ compared with $7.69\,\mathrm{mm^3\,kJ^{-1}}$). However, as a result of a lower threshold energy for the homogeneous SCMVN couples, they would be expected to show higher wear (than SCMV) up to a cumulative dissipated energy of 2.5 kJ. The wear rate for the SCMVN specimens remained linear over the range of loading conditions examined, with no evidence to indicate that the WL failed prematurely; indeed, microscopic evaluation of the edges

Table 5.5: Summary of the energy-wear parameters identified for the different material combinations

Material combination	Wear coefficient (k_e) / $\times 10^{-2}$mm^3 kJ^{-1}	Threshold energy (E_{th}) / kJ
SCMV	7.69	1.10
SCMVN	6.78	0.92
SCMVN-SCMV	7.17	0.75

of the wear scars showed a smooth profile across the various layers. However, the lower threshold energy may indicate that the globular surface of the WL (Figure 4.4a, Page 66) did breakdown under relatively light wear. The heterogeneous SCMVN-SCMV pairings showed an intermediate wear rate of 6.78 mm^3 kJ^{-1} but (since they exhibit the lowest threshold energy) would be expected to wear more than a homogeneous SCMVN couple under all load conditions, and more than a homogeneous SCMV couple up to a dissipated energy of ≈ 6 kJ.

Micrographic examination of the surface of the worn specimens—for both the homogeneous SCMV and SCMVN pairs—indicates, as may be expected (Section 2.5.3, Page 23), that the tribology of the contact is dominated by the formation of compressed debris beds (Figures 5.14 and 5.14). Higher magnification images show that the beds have a highly granular structure: EDX analysis indicated a high oxygen content and XRD analysis identified Fe_2O_3 as the particular oxide formed during fretting. Qualitative examination of the SEM images indicated that at higher loads, the debris bed was thicker with relatively large flakes formed i.e., it is reasonable to conclude that the beds are in a state of continuous formation and breakdown. While the surfaces of the worn SCMV and SCMVN specimens showed similar morphology, the cross-sections (Figures 5.16 and 5.32) indicated significant differences: from Figure 5.16, it is apparent that the worn surface of the SCMV is rough, with the oxide being compressed into the surface features and appearing well adhered; close examination shows small pieces of the metallic substrate becoming detached within the oxide; despite the rough surface, there is no clear evidence of plasticity (grain deformation) extending below the very surface region. In contrast, the SCMVN specimen (Figure 5.32) showed no roughening of the surface, resulting in a very clearly defined interface with an oxide debris layer which gives the impression of being less strongly adhered.

In all cases, for the SCMV specimens, the wear was evenly distributed between the flat and cylindrical specimens of a mating couple (Figure 5.11). However, the SCMVN couples showed a bias toward significantly higher wear of the cylindrical specimen at higher combinations of load and displacement. The SEM micrographs presented in Figure 5.33 indicate the mechanism by which this is occurring: the flat specimen has an almost complete coverage of compressed oxide; higher magnification images reveal the elevated areas to have a smooth, polished surface. In contrast, the worn surface of the opposing flat specimen is almost entirely metallic with a dispersed covering

of oxide with no similar compressed or polished regions. From this, it is concluded that the adhered oxide on the flat specimen is abrading the unprotected surface of the cylindrical specimen; the mechanism which causes the oxide bed to preferentially form on the flat specimen is, however, unclear.

The wear of the heterogeneous specimen pairs showed a particularly striking morphology, very different to those of the homogeneous cases. In general, the wear was found to be biased toward the harder (SCMVN) specimen (Figure 5.41) with the severity of bias increasing with the severity of loading. Profilometry indicated further morphological changes in the scar: at a constant displacement amplitude, increasing the normal load resulted in the formation of an increasingly prominent raised central feature forming a characteristically "W" shaped wear scar (Figure 5.34); however, there were no significant changes in other dimensions of the scar i.e., the troughs either side of the central peak did not change in size significantly. In contrast, the scars on the mating SCMVN specimens developed a characteristic "U" shape which increased monotonically in scale with increasing normal load. Under a constant normal load and increasing displacement amplitude, a similar "W" shaped scar was found on the SCMV specimen but the prominence of the central peak reduced as the displacement amplitude was increased (Figure 5.35); the opposing scars on the SCMVN specimens showed a similar "U" shaped wear scar as before and the overall depth and width increased monotonically with the displacement amplitude.

High magnification SEM microscopy of the heterogeneous specimen couples allow some interpretation of the features seen in the profilometry. Figures 5.43 and 5.45 provide top views of both the SCMVN flat and SCMV cylindrical specimens. In the lower magnification images, it is apparent that, while both scars are in general covered in oxide, there are regions of exposed metal on the SCMVN specimen (of which there are no corresponding areas on the SCMV specimen). In the higher magnification images, these regions show scratches, orientated in the direction of fretting, indicating that the area has suffered abrasive damage. The corresponding SCMV specimens show regions of compressed oxide debris with smooth, polished surfaces (particularly visible in Figures 5.45d and 5.45f), the features being very similar to the formations previously discussed in relation to the homogeneous SCMVN specimens where unequal wear of the flat and cylindrical bodies was found. Furthermore, this behaviour is similar to that described by Kayaba and Iwabuchi [90] when they reported wear of a harder specimen by a softer: in those instances, they found the formation of a compressed black oxide (α–Fe_2O_3) on the surface of the softer specimen which abraded the opposing (harder) surface.

Microscopic examination of the cross sections of the heterogeneous specimen pairs indicates the mechanism by which the debris beds form a protective lamina on the SCMV specimens. From the cross sections in Figures 5.44 and 5.46, it is clear that although the SCMV specimen shows less *wear* (at least in terms of volume lost) than the SCMVN specimen, it is certainly not less *damaged*. The surface of the SCMVN

specimen is almost completely smooth; there is no evidence of any plastic flow in the near surface material and the interface between any oxide debris and the underlying metal is abrupt. In contrast, the surface material of the SCMV specimen has undergone extensive plastic deformation; the surface (in comparison to the SCMVN specimen) is rough with a compacted oxide debris compressed into the small inlets and depressions. Consequently, it is suggested that the interface between the oxide debris bed and the nitrided specimen is weak and easily sheared while the bond with the SCMV specimen is enhanced by the roughness (a mechanical "key"); consequently, the oxide bed is protective of the SCMV specimens to which it is strongly attached while it abrades the harder SCMVN counterface.

The finding that the wear volume lost from a fretting contact may be expressed in terms of a linear function of the dissipated energy is not new. Mohrbacher et al. [175] first reported that the fretting wear of a TiN coating was directly proportional to the dissipated energy over a range of test durations in 1995. Subsequently, Fouvry et al. [21, 176] also investigated fretting wear in terms of dissipated energy and found that over a range of normal loads (50 to 200 N) and displacement amplitudes (25 to 200 μm), the wear volume was proportional the dissipated energy (in this case using an alumina ball fretted against both a HSS flat and a TiN coated flat). In further work, Fouvry et al. [177] found the linear relationship between the dissipated energy and fretting wear to be valid even under variable loading conditions—the displacement amplitude was varied (as a number of alternating steps) between 50 and 100 μm during a test. In addition, Fouvry et al. [177] identified a threshold energy below which wear did not occur: for a steel-alumina couple, the threshold was identified as 13 J, whereas for a TiN-alumina couple it was found to be near zero (2.3 J) (both utilising a point contact). It was proposed that the threshold energy was related to the minimum energy density required to cause recrystallization of the microstructure (known as the TTS) before the incipient formation of wear debris [74]. Furthermore, by a utilizing a finite element model, Fouvry et al. [177] showed that only 10 % of the total input energy could be accounted for by plasticity (and hence formation of the TTS) with the remainder being dissipated through abrasion, adhesion, heating etc., of the first and third bodies.

A more recent study [35]—using a 40 mm diameter Ti6Al4V cylinder on plane contact—investigated the mixed fretting regime i.e., the transition from partial slip to gross sliding (Section 2.3.2, Page 9). In this work, the displacement amplitude was varied with a constant normal load; the resulting data showed that there was a critical sliding amplitude ($\Delta^* \approx 27\,\mu m$, $\delta^* \approx 10\,\mu m$) below which there was no wear and above which, the wear was found to be proportional to the sliding amplitude; since the normal load was held constant, the wear volume as a function of dissipated energy showed the same trends and a threshold energy of 4 kJ was reported. This is clearly a significantly higher value than the tens of Joules reported for a steel-alumina point contact or the values in the order of 1 kJ reported in this work (using a ⌀6 mm cylinder on flat). Given the energy density and TTS related explanation, an increase

in threshold energy with contact size would be compatible (i.e., the threshold should be described as an energy density and not as an energy); however, it does not exclude the possibility that there is also a minimum displacement amplitude below which, while debris may be formed, there is insufficient relative motion to result in it being ejected and hence establish a steady wear phenomena; indeed, this was the conclusion of Heredia and Fouvry [35]. In the current work, the microscopy results (Figures 5.15d and 5.31d) from tests below the energy threshold clearly indicate the formation of oxide across the contact interface, and hence support the theory that, while there was sufficient energy to initiate the detachment of particles from the first bodies, there was insufficient relative displacement to eject the nascent debris from the contact and establish a continuous wear process of any significant magnitude.

The current data, and that available in the literature, indicates that there is an energy-displacement threshold above which the wear is proportional to the dissipated energy and generally the Archard work (ignoring any variation in COF with load). The presence of an offset becomes highly important when interpreting a *wear rate* for any single test; the general practice is to take a wear volume and divide it by the product of the load and slid distance to derive a specific wear rate. If the volume as function of loading parameters takes the form $V = k(P\delta)$, then an accurate estimate of k (the wear rate) can be found from a single point; however, if $V = k(P\delta) + c$, then it is impossible to estimate k from a single point. There is evidence in the literature that such an erroneous interpretation is not uncommon.

In the discussion so far, the "c" value is related to the energy threshold and as a consequence of using the dissipated energy, the slid distance is implicitly used; however, if the applied displacement amplitude (Δ^*) is used, then there is an additional elastic component, which may be significant. For example, one of the most cited papers in the fretting literature is "On fretting maps" by Vingsbo and Söderberg [20]; this work is the source of an often reproduced figure—a fretting map, compiled from contemporary published data—plotting wear rate and fatigue life as a function of displacement amplitude (Figure 2.12, Page 18). This figure indicates that the wear rate is very low (and increasing slightly with increasing displacement amplitude) in what was identified as the mixed stick and slip regime; as the displacement amplitude was increased further and the gross slip regime entered, the wear rate was found to increase rapidly with displacement amplitude until the reciprocating sliding regime was reached, where the wear rate became approximately constant (Vingsbo and Söderberg estimated this to be 300 μm).

This would appear to be in contention with the current results and the discussion up to this point. However, if some of the original sources are considered then it is immediately apparent from where the discrepancy arises; for example, Ohmae and Tsukizoe [43]—whose work was one of the primary sources used by Vingsbo and Söderberg [20] to estimate the transition to sliding wear—considered the fretting of a flat (conforming) steel contact. Their results indicated that there was very little

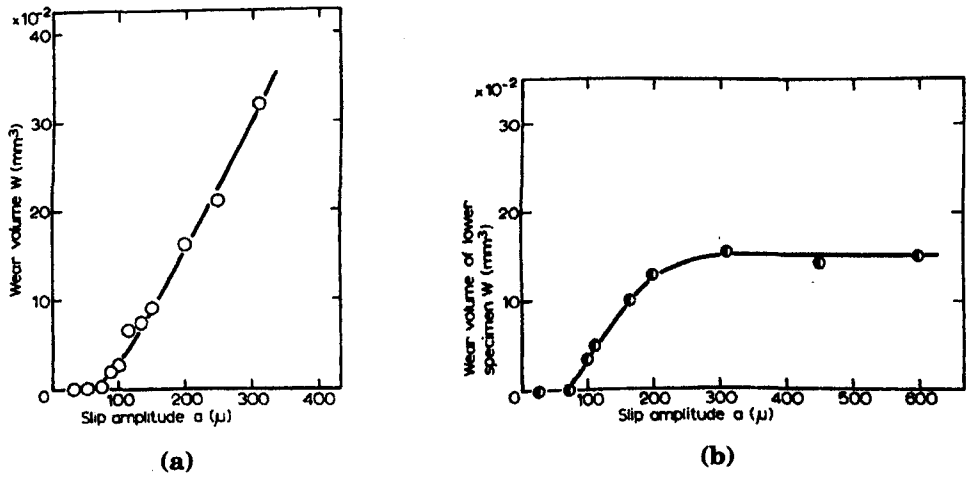

Figure 5.47: Wear volume as a function of slip amplitude: (a) after 100×10^3 cycles and (b) at a fixed sliding distance of 36 m as reported by Ohmae and Tsukizoe [43].

wear below a slip amplitude of 70 μm and then a linearly increasing volume above (Figure 5.47a). A complementary plot, showing the wear volume as a function of slip amplitude (after a constant sliding distance), is shown in Figure 5.47b—this is essentially a plot of wear rate as a function of slip amplitude as the tests were all conducted at the same load. The *apparent* asymptotic increase between 70 and 300 μm is only due to the offset in the primary data resulting in a "$1/x$" term in the wear rate. This is shown graphically in Figure 5.48 where the wear rate (when calculated without any consideration of the offset) is given by the gradient of the dotted lines (k_n), from this it is apparent that $k \rightarrow m$ (the real wear rate) as $\Delta^* \rightarrow \infty$ and hence the shape of the plot seen in Figure 5.47b. Algebraically, the wear volume, as a function of displacement amplitude, is $V^w = m\Delta^* - C$; if the wear rate is then calculated (ignoring the offset) it is found to be $k = m - C/\Delta^*$, where m is the *true* wear rate and the C/Δ^* term results in the apparent asymptotic increase in the wear rate.

It must be noted that the value of 70 μm as the transition displacement amplitude for measurable wear is high compared to that reported in more recent work. In this case, the slip amplitude quoted is actually the applied displacement, some way distant from the contact point (i.e. Δ^*), since the capacity to record fretting loops was not available; as such, the values of slip amplitude quoted should more properly be termed the distant applied displacement, and recognised as incorporating a number of elastic displacements as well as the true slip.

Another source was the work of Bill [3] who—using a steel ball on flat contact—reported the wear below 25 μm amplitude to be characterised by surface damage but not increasing with sliding distance (not dissimilar to the present work) while above, it was linear with increasing amplitude (up to a maximum reported amplitude of 75 μm) i.e., if a wear rate were to be directly calculated, it would result in the same erroneous conclusion that the wear rate increased as a continuous non-linear function of slip amplitude. Work by Toth [98] also contributed to the findings of Vingsbo and

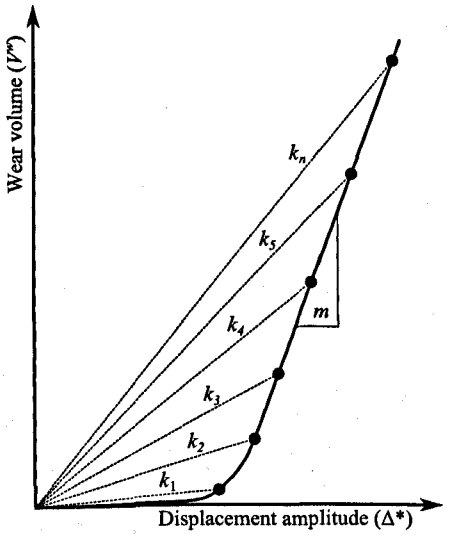

Figure 5.48: Diagram illustrating the calculation of the *apparent* wear rate k_n, represented by the gradient of the dotted lines, compared to the real wear rate m, if the effect of the offset is ignored.

Söderberg; in this work, slip amplitudes from 50 to 500 µm were considered at a range of normal loads, with the findings clearly indicating a linear relationship between wear volume and displacement amplitude under a range of normal loads. Extrapolation of the lines gives a value of ≈ 25 µm below which no wear would be observed.

In all these cases, the wear (above some threshold) was reported to be proportional to the displacement amplitude over a significant range (up to 500 µm). The threshold in these cases may be almost entirely attributed to elastic deformation of the test fixtures between the points where the displacement was measured—the technique of measuring the actual sliding amplitude (δ^*) from the fretting loops is a comparatively modern technique and requires continuous data acquisition. There is one exception to this that the author is aware of, that being an extensive early study of fretting wear by Feng and Uhlig [63] (alternative source [95]). In this work, they developed a novel fretting rig which used torsional fretting between two cylinders with the centre relieved to create a narrow contact annulus (Figure 3.4, Page 44); this arrangement allowed them to optically observe the *actual* slip at the contact (with no elastic component). It is then perhaps not surprising that they found the wear volume to be directly proportional to the slip amplitude (i.e., a constant wear rate) over a range of approximately 10 to 230 µm.

Chapter 6

Fretting at Elevated Temperature

6.1 Introduction

The behaviour of a fretting contact is known to depend critically upon the debris which is formed during the process, in particular its rate of creation and ejection from the contact, and the properties of any debris which is retained in the contact (Section 2.5.3, Page 23).

Fretting of mating components is encountered in many industrial contexts, with these contacts existing in a range of environments, including across a range of temperatures. Temperature has a strong influence on many physical systems through its influence on thermodynamics (for example, influencing which phases are favoured in a system), kinetics (for example, influencing the rate of oxidation and sintering) and material properties (for example, influencing stiffness and strength of solids). In light of this, it can be assumed that the formation of debris beds within a fretting contact depends upon many attributes which are influenced by temperature; accordingly, a body of research exists which has examined the effects of elevated temperature on the tribology of dry fretting steel contacts [95, 107, 108, 187–189].

In general terms, as the temperature is increased, the wear rate and COF are observed to decrease significantly over a relatively narrow range of temperature, commonly referred to as the transition temperature. Reductions of over an order of magnitude in the wear rate of both medium carbon and stainless steels (with associated decreases in the COF of approximately 20 to 30 %) have been observed [108, 187]. Analogous behaviour is widely reported in the literature relating to reciprocating sliding wear at elevated temperatures [190–194], indicating that similar changes in mechanisms controlling the contact tribology are not specific to fretting.

Hurricks [107, 189] (under fretting conditions) related the transition temperature to a change in oxidation from logarithmic to parabolic growth (related to the growth of a sufficiently thick protective surface oxide film) and to the growing predominance of Fe_3O_4 within the oxide film (rather than α-Fe_2O_3 which was thought to be the dominant oxide below the transition temperature). This is supported by Kayaba

and Iwabuchi [187], who similarly associated the reduction in fretting wear and COF with increasing temperature with the change in oxide from α-Fe_2O_3 to Fe_3O_4. Under sliding wear conditions, researchers have also attributed the reduction in wear and COF observed at elevated temperatures to the formation of Fe_3O_4 which is thought to adhere more strongly to the surface and act as a better solid lubricant than α-Fe_2O_3 [194, 195].

Later work has emphasized the mechanical role of the debris rather than the properties of the particular oxide or the rate at which a surface oxide film may form. Godet [87] outlined the importance of the behaviour of debris interposed between the primary wearing surfaces in terms of a *third-body-approach*. When the wearing faces of a contact are separated by a layer of debris, then the debris layer itself can protect the primary surfaces by supporting the bearing load and providing a means through which the shear displacement between the faces may be accommodated [60]. Experimentally, this approach has been substantiated by Colombie et al. [64] who performed a number of tests with oxide debris formed in situ, debris introduced artificially and open-and-shut tests where the oxide debris was periodically removed. They found that the fretting wear behaviour depended critically on the formation of a debris bed, and that identical wear behaviour was found, independent of the primary body materials, once the debris bed had formed. Iwabuchi et al. [93] conducted fretting tests which mirrored those of Colombie et al. [64], but in this case, oxide particles were artificially supplied to a fretting contact; they concluded that it is the formation of the compacted oxide film that reduces wear in such a contact, and demonstrated that if such a stable layer does not develop, then the addition of oxide particles to the contact can increase the wear rate by promoting abrasion. In similar work examining a sliding wear contact, Kato and Komai [196] again found that supplying oxide particles into the contact could either reduce or increase the wear rate depending on whether a stable debris bed formed.

The successful formation of a load-bearing debris bed is dependent on the balance between the breakdown and ejection of any existing debris bed and the consolidation of new debris into that bed. Jiang et al. [197] proposed that inter-particle adhesion forces predicted by the Johnson-Kendall-Roberts (JKR) model [198] are sufficient to explain the formation of protective debris beds from individual debris particles. They suggested that as the temperature is raised, the surface free energy of the debris particles increases, following an Arrhenius relationship (with $E_a \approx 12\,\mathrm{kJ\,mol^{-1}}$). As such, increasing the temperature results in an increase in the strength of adhesion between debris particles (and thus the stability of the layer) and will promote the incorporation of larger particles into the film and thus increase the rate of its formation.

Sintering is an activation energy dependent process and is generally classed as being significant at a temperature above approximately half of the absolute melting temperature of the material [199]. However, in a tribological contact, the sintering process is seen to be modified by the local conditions. Adachi and Kato [200] demonstrated

experimentally that tribo-sintering of alumina wear particles is possible at high test temperatures of 900 °C (a temperature much lower than normally associated with sintering of alumina), with Kato [201] and Kato and Komai [196] demonstrating sintering (in the form of neck growth) between 300 nm Fe_2O_3 particles at room temperature when these particles were supplied to a sliding interface. Additionally, it was found that the wear behaviour of these contacts was governed by the sintering rate of the supplied particles, which was related to their oxygen diffusivity and diameter. Oxides which exhibited higher rates of diffusion showed accelerated tribofilm formation and thus a more rapid transition to mild wear. In the case of Fe_2O_3, it was demonstrated that smaller particles were sintered more easily (and thus promoted the transition to mild wear) whilst larger particles did not sinter and actually increased the rate of wear of the contacts to which they were added [196, 201]. This sintering of oxide particles at ambient temperatures in tribological contacts will be accelerated both by the conditions within the contact and also by the fact that the oxide debris particles produced are themselves very small: oxide debris resulting from fretting has been reported to be less than 5 nm in diameter [62].

It has been demonstrated that even without any tribological action, the rate of sintering is highly dependent upon the particle size; in early theoretical work, Herring [202] showed that for sintering via surface diffusion, a reduction in particle size by a factor of 10 would result in a reduction in time to the same degree of sintering by a factor of 10^4. Such an increase in rate indicates that nano-particles are expected to sinter at much lower temperatures than larger particles; for example, recent work [203] on uranium dioxide demonstrated sintering of nano-particles at 500 to 600 °C, some 700 to 1000 °C below the normal sintering temperatures of bulk uranium dioxide. There is a wider body of research concerning low temperature sintering of metallic nano-particles where sintering of metals has been observed at temperatures around ambient; for example, Zhou et al. [204] investigated the sintering behaviour of a range of ultra-fine powders, and observed that sintering of iron particles (30 to 40 nm) initiated as soon as the temperature was increased above 20 °C.

At elevated temperatures (under both fretting and sliding wear conditions), workers have reported the formation of a *glaze* in the worn contact [108, 187, 192]. This is often described as a smoothly-burnished layer forming on top of a compacted oxide layer. It was originally thought that these glazes were silicon-rich due to their glassy appearance [190]; however, it is now known that they in fact consist of compacted sub-micron size oxide particles [190]. Furthermore, Stott and Wood [190] proposed that the glaze formed as a result of plastic flow of the oxide which was possible due to the small size of the asperity contact and hydrostatic loading conditions present in the tribo-film; more recent publications point to glaze formation being associated with the completion of the sintering process [192, 196].

To date, much of the research reported in the literature relating to fretting behaviour at elevated temperature has naturally focused on stainless steels. There appears

to be consistent experimental evidence that the transition in fretting wear and COF occurs at ≈ 200 °C for such steels [108, 187]. However, similar investigations involving carbon steels are less conclusive: Kayaba and Iwabuchi [187] reported the transition temperature to be 200 °C for a 0.45 wt. % C steel. However, examination of the data indicates that the wear had dropped to about one third of its room temperature value at 100 °C and was small (but still positive) at 200 °C, while becoming negative at all temperatures > 200 °C. In contrast, Hurricks [107] found a gradual decrease in the fretting wear of a mild steel (EN3B) up to 150 °C followed by a more rapid drop until 200 °C. Moreover, despite their widespread use in industrial contacts prone to fretting at elevated temperatures (such as in aero-engine spline couplings), there are no reports in the literature concerning elevated temperature fretting of high strength alloy steels: work with such steels has more generic applicability since it is known that substrate strength can significantly affect the formation and stability of the glaze layer [205], and thus the tribology of the contact. Furthermore, it has been suggested that the transition temperature is dependent on the chromium content of the steel alloy [107, 194] (associated with the fact that alloying of the oxide will affect both its rate of formation and its sintering behaviour due to differences in physical properties); many high strength steels have chromium contents between those of the mild steels and stainless steels which have been the subjects of fretting at elevated temperature reported in the literature.

In modern engineering assemblies, particularly modern gas-turbines, wearing parts utilising high strength alloy steels often experience operational temperatures spanning the range previously suggested for the fretting transition temperature. As such, it is important to understand the fretting response of such steels at elevated temperatures. The aim of the work summarised in this chapter is to characterise and understand the high temperature fretting wear behaviour of one such steel, SCMV [13] in its as heat treated and heat treated and nitrided forms.

6.2 Experimental procedure

All of the tests were conducted, and the data processed, according to the procedures outlined in Chapter 4 (Page 63). Tests were completed using both SCMV and SCMVN (in all cases arranged in a homogeneous pair configuration i.e., SCMV-SCMV and SCMVN-SCMVN) over a temperature range from 24 to 450 °C; a fixed frequency and test duration was used (20 Hz and 100×10^3 cycles respectively); a normal load of 250 N and an applied displacement amplitude of 25 μm was employed, although a limited number of SCMV-SCMV tests were carried out at higher loads; the test conditions are summarised in Table 6.1.

Elevated temperature nano-indentation testing was conducted by Micro Materials Ltd. (Wrexham, UK) in order to characterise the hardness of the test material as a function of temperature. Before indentation the specimens were lightly ground and

Table 6.1: Summary of elevated temperature test conditions for SCMV-SCMV and SCMVN-SCMVN specimen pairs.

Normal Load (P) / N	250, 450[a] and 650[a]
Applied displacement (Δ^*) / μm	25
Duration (N) / cycles	100×10^3
Frequency (f) / Hz	20
Temperature (T) / °C	24, 85, 120, 150, 300 and 450

[a] SCMV-SCMV specimen pairs only

polished to a 1 μm finish; for the SCMVN specimens this was sufficient to remove the WL and leave a suitable surface for indentation. A heated cubic boron nitride Berkovich indenter was used and the maximum indentation depth was ≈ 1.1 μm. During the indentation tests, the loading and unloading periods were 20 s, with a 30 s dwell at peak load. Thermal drift was corrected over a period of 120 s at 90 % unloading for elevated temperatures, and over a period of 60 s at ambient temperatures. Further information on the procedure and analysis can be found in the literature [86, 206].

6.3 Results

The relationship between surface hardness and temperature for both the SCMV and SCMVN specimens is shown in Figure 6.1. For the SCMV, it can be seen that there was little material softening until the region of 300 to 450 °C, whereupon the hardness began to decrease sharply. The hardness fell by ≈ 14 % on raising the temperature from room temperature to 300 °C, with the decrease reaching ≈ 30 % by 450 °C. In contrast the SCMVN displayed little change in hardness until between 150 to 300 °C, at which point the hardness decreased by ≈ 37 %. Subsequently, the SCMVN hardness mirrored that of the SCMV with the decrease reaching ≈ 52 % by 450 °C and ≈ 79 % by 500 °C—at which point the hardness is comparable to that of the SCMV (2.21 GPa cf. 1.9 GPa)

All fretting tests conducted below 300 °C exhibited classic parallelogram shaped force-displacement loops indicative of gross sliding (Figure 2.10, Page 15). However, loops from some SCMV-SCMV tests conducted at temperatures ≥ 300 °C exhibited distinctive force peaks at the extremes of the stroke, Δ^* (Figure 6.2). Such features have previously been reported during the fretting of ductile materials [170, 172], and also during high temperature fretting of a stainless steel [108]. They are believed to be caused by ploughing at the edges of the contact leading to a build-up of material in that area [172]. Subsequent interaction between the moving specimen and the built up material then results in the observed force peaks. Cross-sectioning and SEM examination (Figure 6.3) of a specimen where this behaviour was observed clearly indicates a significant build-up of highly plastically deformed metallic material at the extreme edges of the wear scar. As a consequence of this behaviour, the normalised tangential

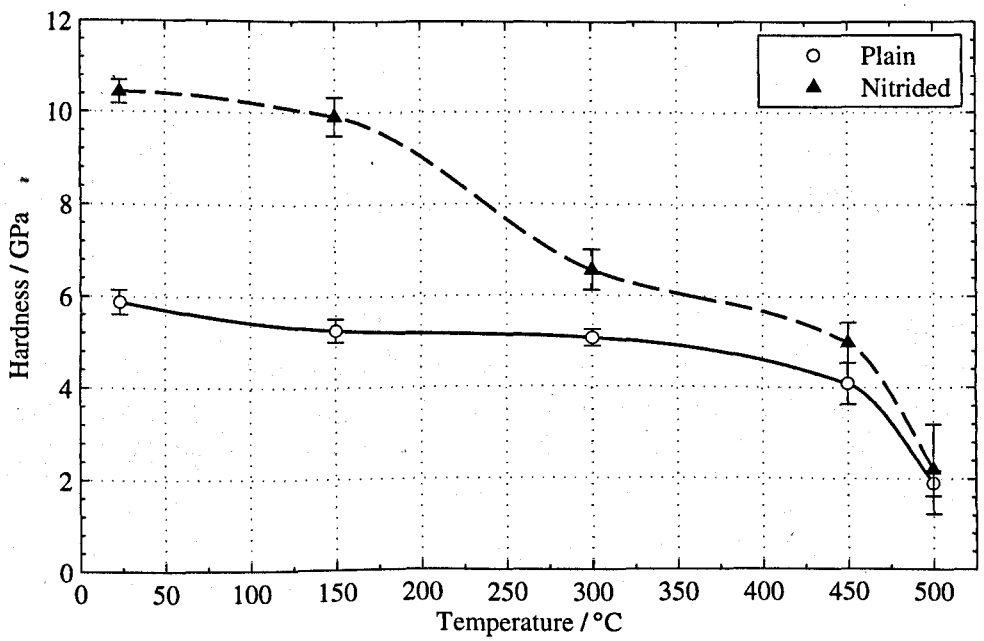

Figure 6.1: Nano-indentation surface hardness of SCMV and SCMVN as a function of temperature.

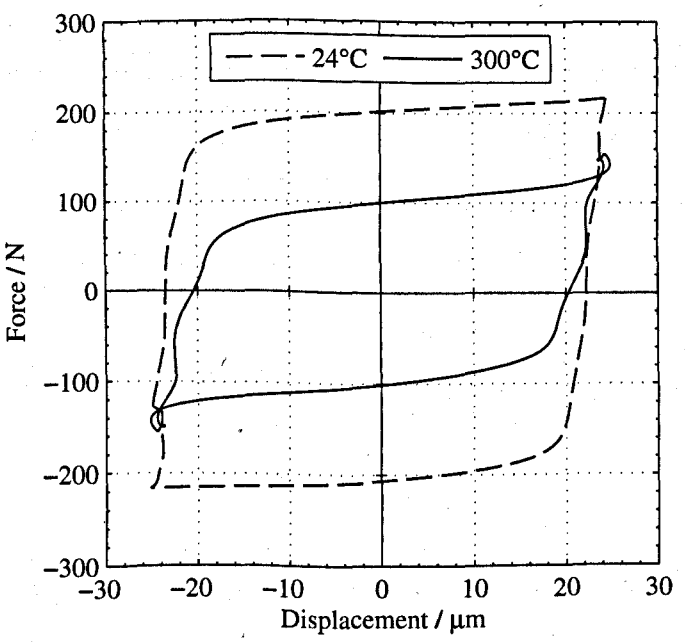

Figure 6.2: Force-displacement loops for fretting tests conducted at 24 and 300 °C (P = 250 N, Δ^* = 25 µm) at cycle number 50×10^3.

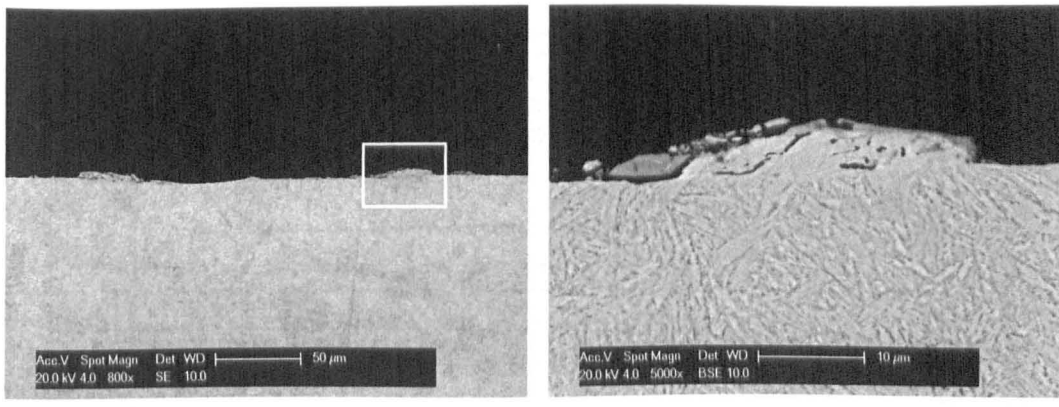

(a) (b)

Figure 6.3: SEM micrographs, showing ploughing of metallic material at the edge of the wear scar, following 100×10^3 fretting cycles ($P = 250\,\text{N}$, $\Delta^* = 25\,\mu\text{m}$) at 300 °C which showed force peaks at the extremes of the stroke: (a) low magnification image of the whole scar, (b) higher magnification image of the region highlighted in (a).

force ratio (Q^*/P) would no longer be an effective estimate of the COF. However, in this work an estimate of the COF based on the dissipated energy is used where

$$\mu_e = \frac{E_d}{4P\delta} \tag{6.1}$$

which essentially gives an averaged value of the COF over the sliding period of the cycle (Section 4.5.3, Page 73).

Figure 6.4 shows the development of the COF with time for SCMV-SCMV fretting tests conducted under each of the temperatures examined. It was observed that at 24 °C, the COF rapidly rose to a maximum of 0.86 at approximately 6×10^3 cycles, before gradually dropping to 0.8 at 24×10^3 cycles, where it may be considered to have reached a quasi-stable value. Whilst quasi-stable, the COF displayed notable variation over a period of hundreds of cycles and continued to do so throughout the test. In contrast, at 85 °C, the COF declined rapidly from an initial peak of 0.82 at 500 cycles, reaching a value of 0.68 by 20×10^3 cycles. Subsequently, the COF assumed its quasi-stable value and was contrastingly stable over a period of hundreds of cycles. As the temperature was increased further, the COF became more stable, and the minimum (quasi-stable) value was reached following a smaller number of cycles; at 150 °C, the steady value of COF was 0.62, with this value being reached in 12×10^3 cycles. At the highest temperatures studied (300 and 450 °C), there was no discernible initial peak in the COF and the steady state value was immediately attained.

Very similar behaviour was observed for the SCMVN-SCMVN specimen pairs, with increasing stability of the COF found at higher temperatures and the quasi-stable value being achieved in a lower number of cycles, as the temperature was increased (Figure 6.5). Compared to the SCMV specimens examined at 24 °C, the peak COF is higher (0.98 at 640 cycles compared to 0.82 at 500 cycles). Similarly the peak value

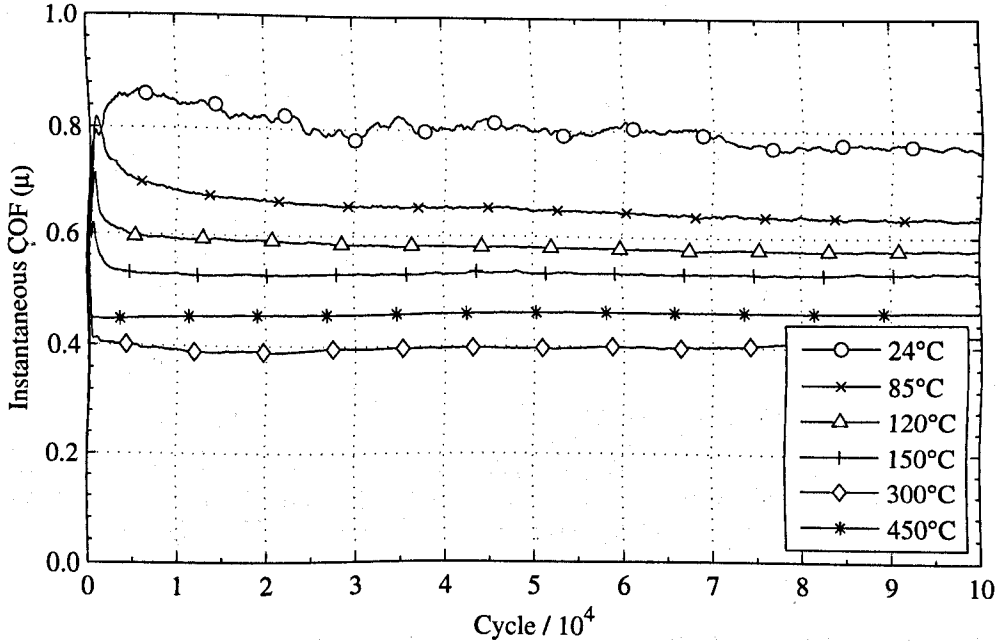

Figure 6.4: Development of the COF with cycle count during fretting as a function of temperature for SCMV-SCMV specimen pairs ($P = 250\,\text{N}$, $\Delta^* = 25\,\mu\text{m}$).

attained at 85 and 120 °C is consistently higher. Moreover, at 85 and 120 °C the drop from the initial peak to the quasi-steady state value is more significant. For example, at 85 °C, the drop between the peak COF, after a few hundred cycles, and the value at 50×10^3 cycles is $\approx 30\,\%$ whereas for the SCMV specimens it was $\approx 20\,\%$. Furthermore, the behaviour at 85 and 120 °C remains more similar to the ambient case, with small instabilities and a gradual decline in the COF over the duration of the test. However, at temperatures above 120 °C, the behaviour (as a function of cycles) is very similar to that of the SCMV specimens.

In order to quantitatively compare the dependence of the COF on temperature, the mean COF for the last 75×10^3 cycles of each test was calculated to produce a quasi-steady state COF value (Figure 6.6). Data for repeat tests are plotted, and it is apparent that differences in the COF readings between tests conducted under the same conditions were small (< 0.04). For both the SCMV and SCMVN pairs, the steady state COF drops monotonically with increasing temperature from a maximum at 24 °C to a minimum at 300 °C; as the temperature is increased further to 450 °C, there is a small increase (≈ 0.05) in the steady state COF. For both materials, the rate of change of the COF is initially rapid: for the SCMV couples, the COF dropped from 0.77 at 24 °C to 0.64 at 150 °C; however, above 150 °C the rate of change reduces significantly. At temperatures lower than 150 °C, the steady state COF for the SCMVN pairs is consistently higher than for the SCMV pairs (by ≈ 0.08); however, at 150 °C and above, while the steady state COF remains higher for SCMVN, the difference becomes negligible (< 0.02)—this agrees with the qualitative trends observed in Figure 6.4 and Figure 6.5 where the behaviour of the SCMVN COF (as a function of cycles) was found

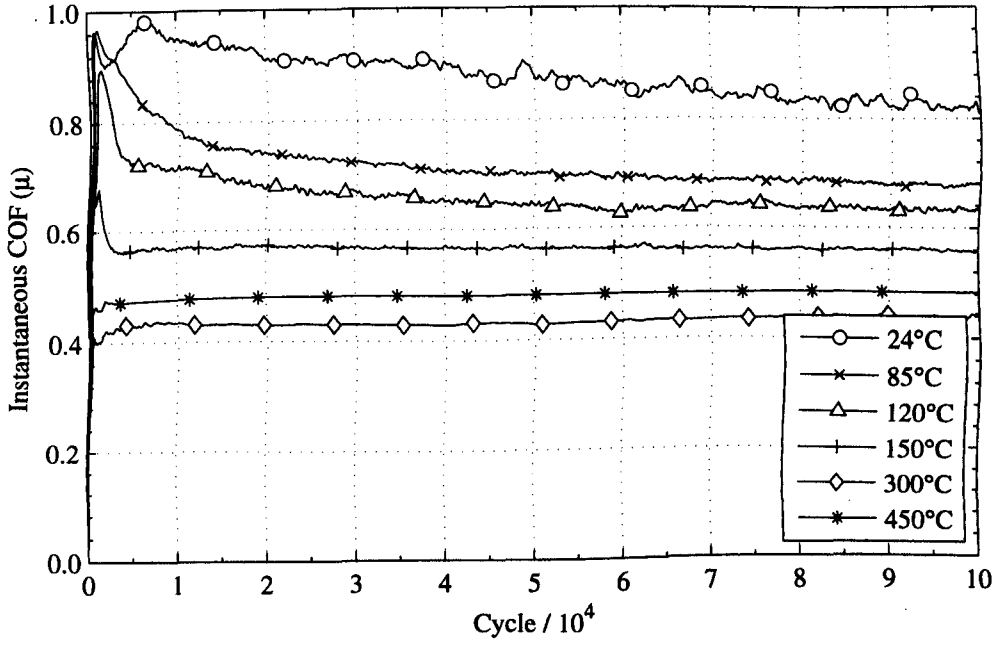

Figure 6.5: Development of the COF with cycle count during fretting as a function of temperature for SCMVN-SCMVN specimen pairs ($P = 250\,\text{N}$, $\Delta^* = 25\,\mu\text{m}$).

to become more similar to that for SCMV above 150 °C.

The relationship between temperature and net total wear volume is plotted in Figure 6.7a; it is observed (for both the SCMV and SCMVN couples) that the wear volume decreases rapidly with increasing temperature, until a critical transition temperature (TT), above which the wear response altered from one of net volume loss to net volume gain (such volume gains are small and are associated with the fact that both Fe_2O_3 and Fe_3O_4 have Pilling-Bedworth ratios greater than two [207]). For SCMV, the transition occurs in the first temperature interval (24 to 85 °C), while for SCMVN, it occurs at approximately 150 °C. Initially the wear (for SCMVN) decreases rapidly, with the rate of change reducing as the temperature is increased toward the transition temperature: on raising the temperature from ambient to 85 °C (approximately 50 % of the interval to the TT), the wear was reduced by approximately 72 %.

Figure 6.7b decomposes the net wear volume into its constituent volumes: V^- and V^+. It is apparent (for both materials) that the significant decrease in wear volume on raising the temperature to 85 °C was mainly due to a sudden, and large (> 80 %), decrease in the volume of material lost (V^-). For the SCMV specimens, this is concurrent with a smaller increase in the amount of additional material built up on the surfaces (V^+). In the case of the SCMVN specimens, where more experiments have been conducted between ambient and the transition temperature (due to the transition temperature being higher), it can be seen that the material build up (V^+) increases progressively toward the TT.

There is no evidence of significant material transfer between the two members of

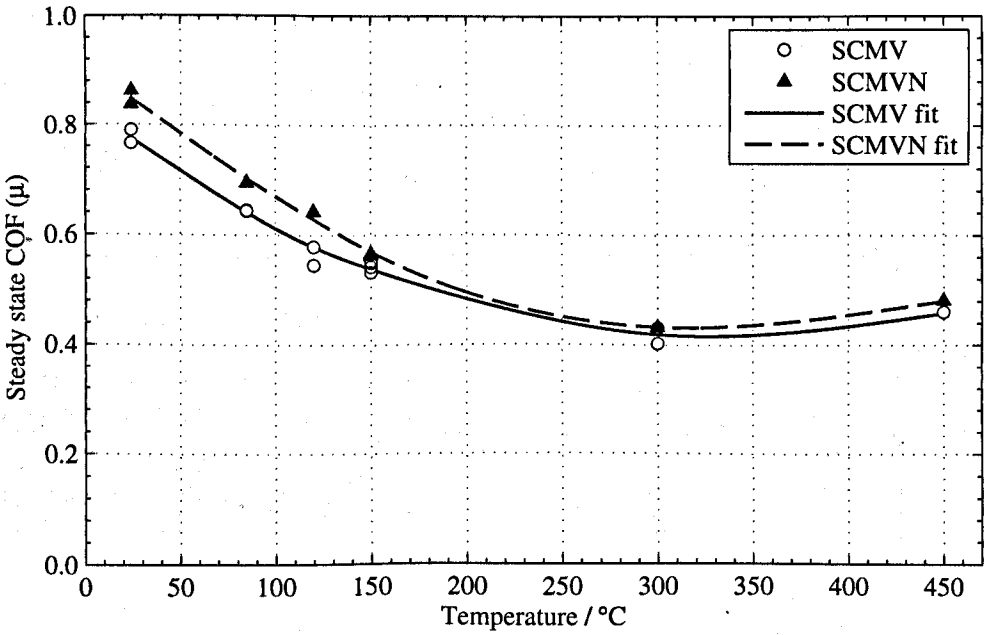

Figure 6.6: Relationship between the steady state COF and temperature for SCMV-SCMV and SCMVN-SCMVN specimen pairs with $P = 250\,\text{N}$ and $\Delta^* = 25\,\mu\text{m}$ (steady state COF represents the average of the values recorded in the fretting tests from 25×10^3 to 100×10^3 cycles).

the fretting couple having occurred; such a situation would be indicated by similarly sized volumes of material removed and material built up within the contact. As the temperature was increased above the TT, there were no further notable changes in the wear response, and the behaviour remained one of low material removal and additional material build up on the surface, resulting in small negative total wear volumes (i.e., increases in total volume). This relative insensitivity of wear volume to temperature is in contrast to the changes in the COF, which continued to drop significantly for both material types as the temperature was increased beyond its TT.

Qualitative assessment of the wear scars was made using SEM. Figure 6.8 and Figure 6.9 show a plan view SE micrograph of a flat specimen for each temperature studied, for the SCMV and SCMVN couples respectively. In both cases, at 24 °C, the debris bed exhibited a roughened appearance, with large flakes of oxide being apparent; examination using BSE imaging (Figure 6.10a) indicates that the compacted oxide debris (regions of lower contrast) only partially covered the wear scar, with relatively large areas of metal remaining exposed. In contrast, at 85 °C, the compacted oxide debris exhibited almost total coverage of the scar (Figure 6.10b) and was much smoother in appearance, although there were still areas where delamination and breakdown of the oxide had occurred (Figure 6.8b). The reduced roughness and decreased production of oxide flakes is most pronounced for the SCMVN-SCMVN specimens (Figure 6.9b). For both materials, as the temperature was increased further, the surface of the compacted oxide formed appears progressively smoother. At temperatures beyond the TT, the surface appears glassy and burnished and may be described as

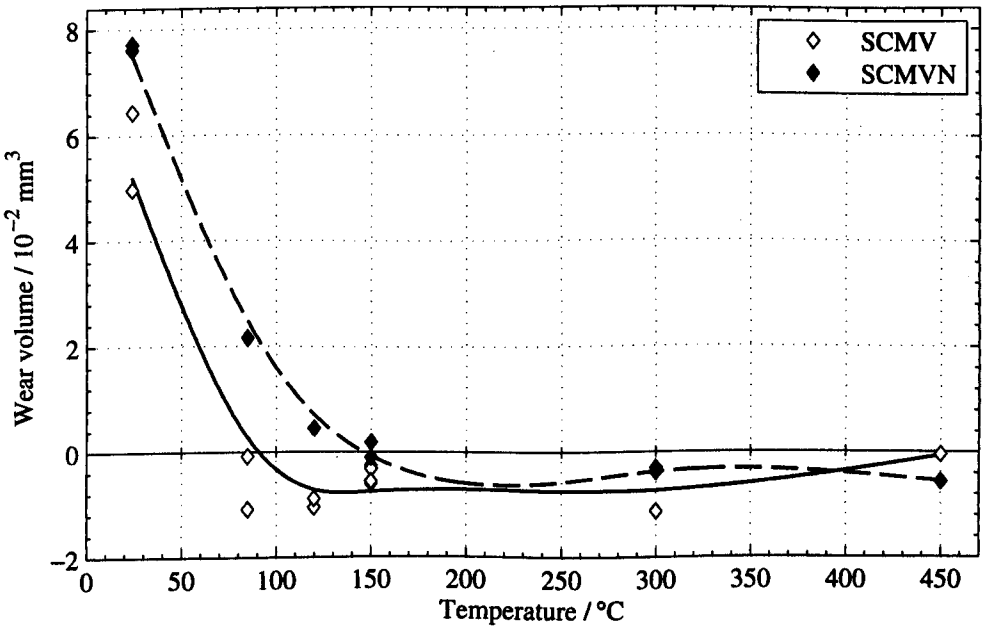

(a)

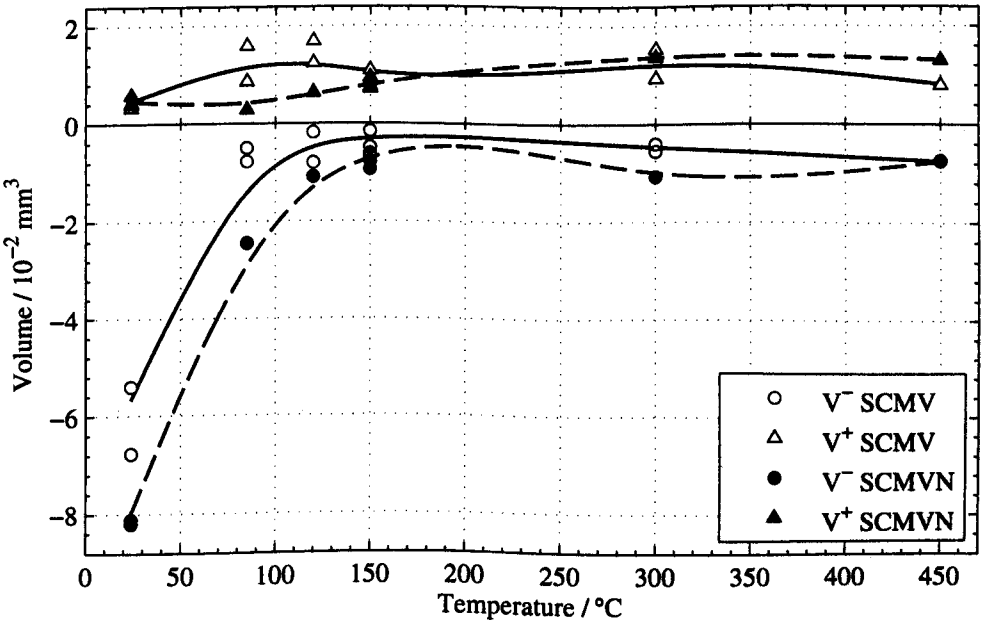

(b)

Figure 6.7: Relationship between wear and temperature of fretting for SCMV and SCMVN specimen pairs: (a) net wear volume, (b) constituent material build-up (V^+) and removal (V^-) volumes; after 100×10^3 fretting cycles with $P = 250\,\text{N}$, $\Delta^* = 25\,\mu\text{m}$.

a *glaze-layer*; at 300 and 450 °C, the evolution of the glaze was complete, with large islands of smooth polished oxide on the surface of oxide debris. Figure 6.11 shows higher magnification detail of some of these smooth glazes at 300 and 450 °C on the SCMV specimens; Figure 6.12a finds corresponding behaviour for the nitrided material. Figure 6.12b shows detail of local transfer of the glaze occurring between the SCMVN flat and cylindrical specimen at 300 °C. A cross section through the glaze layer formed on a SCMV specimen (Figure 6.13) indicates that the glaze was composed of finely divided oxide debris which had been compacted to form the bed.

As the temperature of fretting was increased above ambient, not only are changes in the nature of coverage of the oxide debris beds found, but it is also observed that the width of the wear scar (and hence contact area) decreased. It can be seen that the width dropped rapidly with increasing temperature up to the TT and subsequently more progressively with further increases in temperature. While this is predominantly concurrent with the reduction in the material removal rate, seen up to the TT, notable reductions in the scar width continue with subsequent increases in the temperature (where there is no further reduction in the material removed)—this effect is quantified in Figure 6.14: for SCMV, the scar width reduces by 0.35 mm (from 0.63 to 0.28 mm) on raising the temperature by 61 °C (from ambient to 85 °C, the TT); raising the temperature a further 215 °C (to 300 °C) results in an additional reduction of 0.17 mm in the width of the wear scar. Similarly, the SCMVN scar width reduced by 48 % when the temperature was raised by 126 °C (from ambient to 150 °C, the TT); further increasing the temperature by 300 °C (to 450 °C) increased the reduction to 73 %. At the lower temperatures (before the glaze is formed), there is a notable difference between the widths of the wear scars for SCMV and SCMVN: at 24 °C, the scar width for the SCMVN is 0.84 mm compared to 0.63 mm for the SCMV; however, at 300 and 450 °C (once the glaze has fully formed for both materials), the difference in width has reduced to ≈ 0.04 mm.

In order to evaluate the endurance of the glaze layer structures observed in the SEM (Figure 6.8), a test was run with a variable temperature. The temperature was initially set at 300 °C and the test was allowed to proceed normally for 50×10^3 cycles, at which point, the test was automatically stopped, and the rig was left to cool with the specimens in place. When the rig had cooled to ambient temperature, the test was restarted and continued for a further 50×10^3 cycles. The resulting COF as a function of cycles is shown in Figure 6.15. It can be seen that the initial behaviour (dashed line) is in close agreement with that previously observed from tests at 300 °C (Figure 6.4). On resumption of the test at 24 °C (solid line), it can be seen that the COF climbs rapidly to a maximum of ≈ 0.95 in a period of 3400 cycles from the test restarting. By the end of the test, the COF had stabilised at a similar steady-state value to those previously observed for tests conducted at ambient temperatures. On completion of the test, a large amount of characteristic red-oxide was observed—similar to tests run at ambient temperature rather than those run at or above 85 °C (which showed greatly

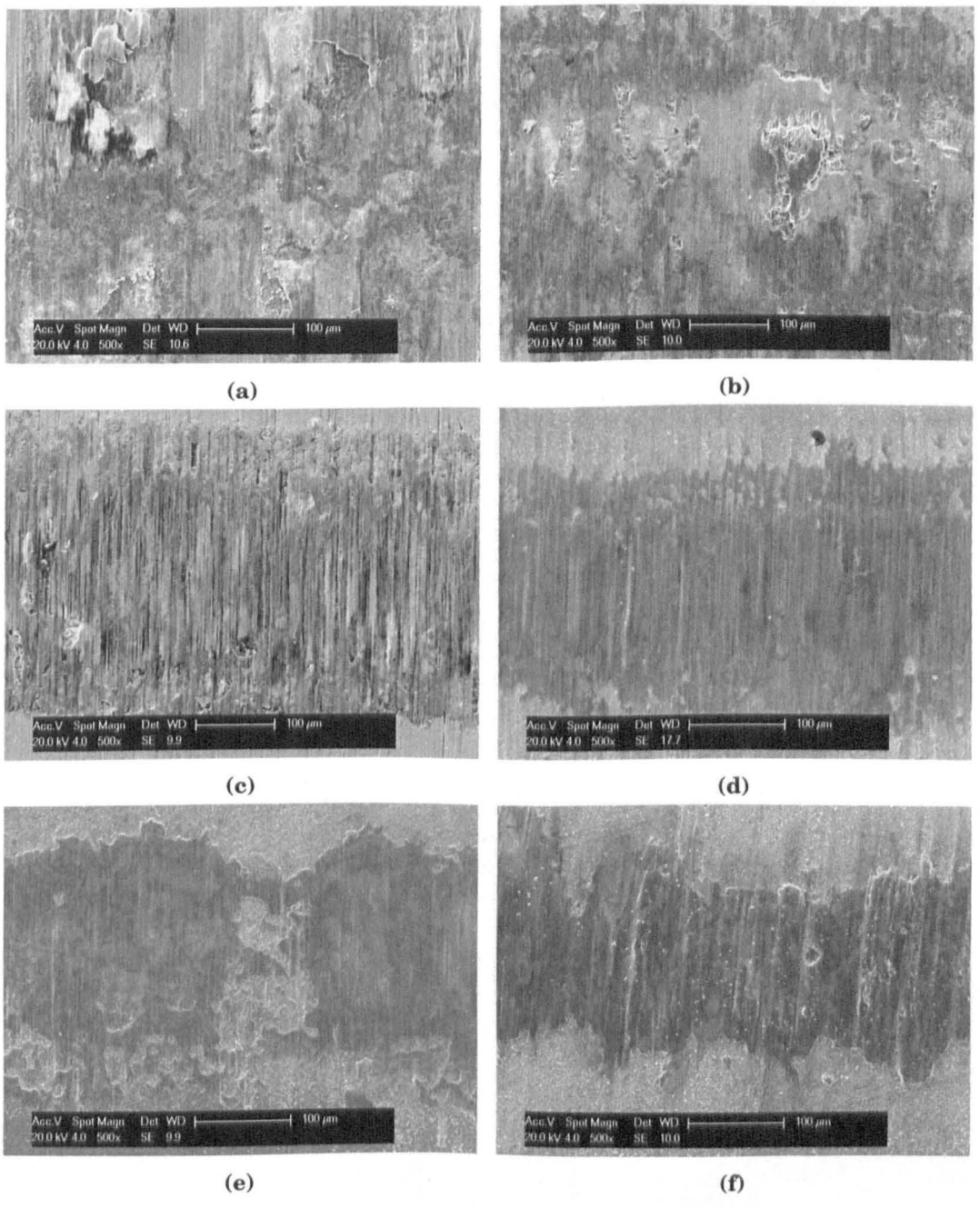

Figure 6.8: SE SEM plan-view micrographs of wear scars on the flat specimen following 100×10^3 fretting cycles with $P = 250\,\text{N}$, $\Delta^* = 25\,\mu\text{m}$, at a range of temperatures for SCMV–SCMV pairs: (a) 24 °C, (b) 85 °C, (c) 120 °C, (d) 150 °C, (e) 300 °C, (f) 450 °C.

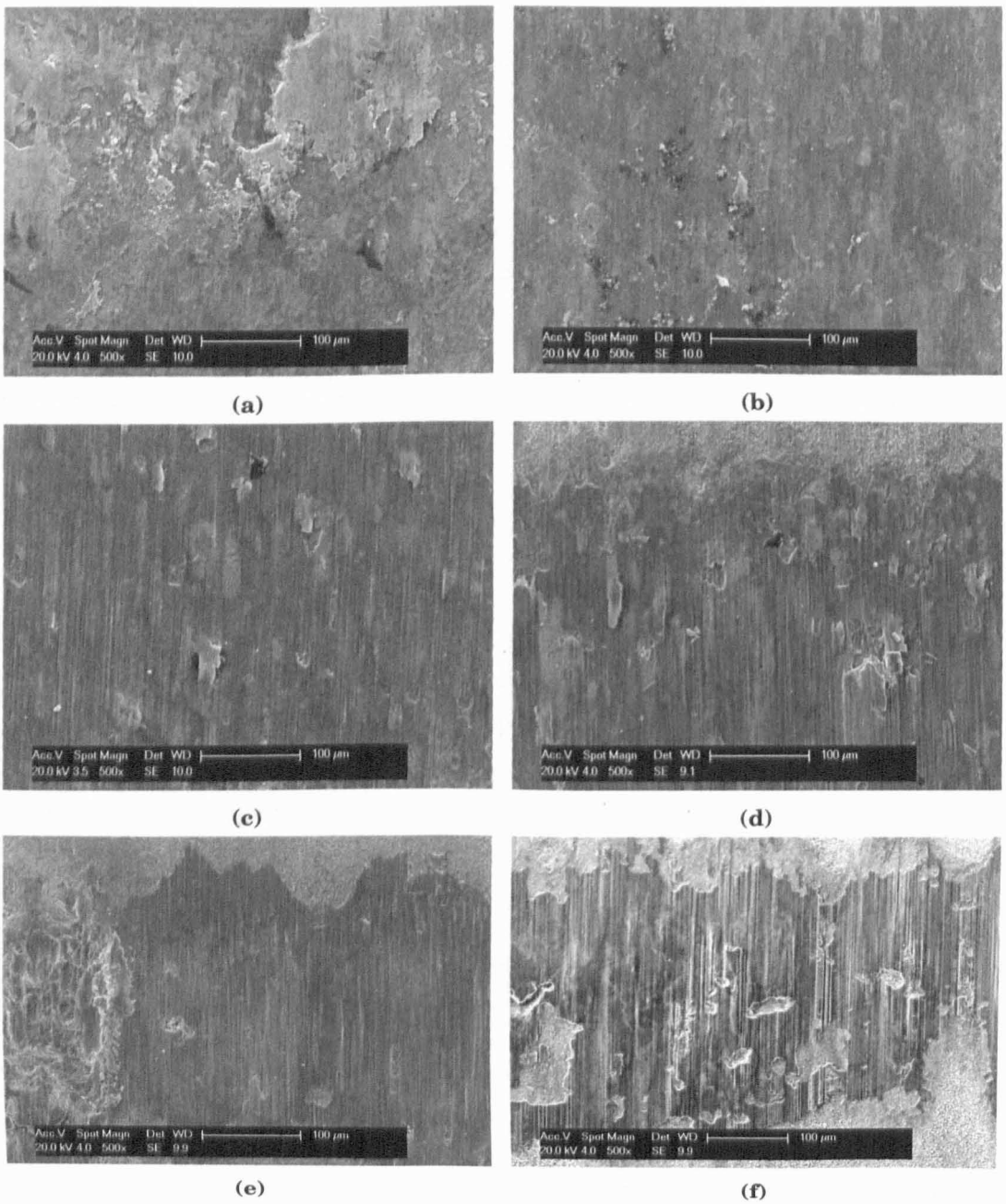

Figure 6.9: SE SEM plan-view micrographs of wear scars on the flat specimen following 100×10^3 fretting cycles with $P = 250\,\text{N}$, $\Delta^* = 25\,\mu\text{m}$ at a range of temperatures for SCMVN-SCMVN pairs: (a) 24 °C, (b) 85 °C, (c) 120 °C, (d) 150 °C, (e) 300 °C, (f) 450 °C.

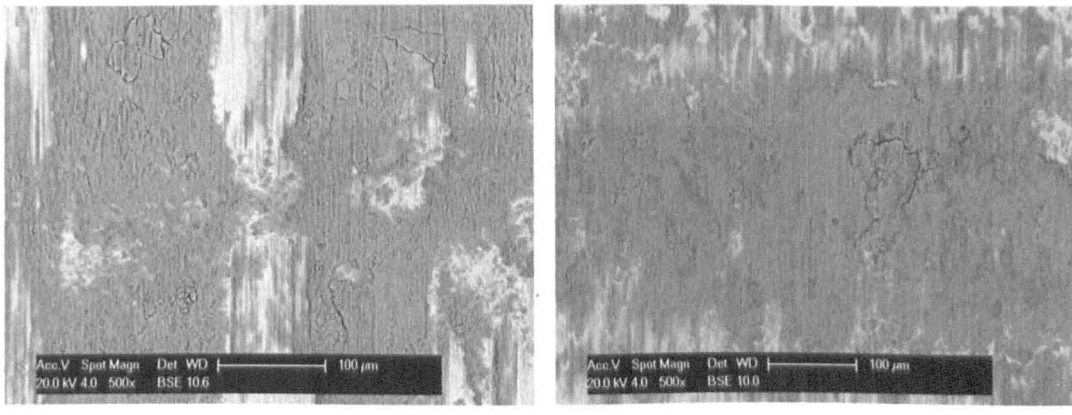

(a) (b)

Figure 6.10: BSE SEM plan-view micrographs of the wear scar on the flat specimen, from a SCMV–SCMV pair, following 100×10^3 fretting cycles with $P = 250\,\text{N}$, $\Delta^* = 25\,\mu\text{m}$ at: (a) 24 °C, (b) 85 °C.

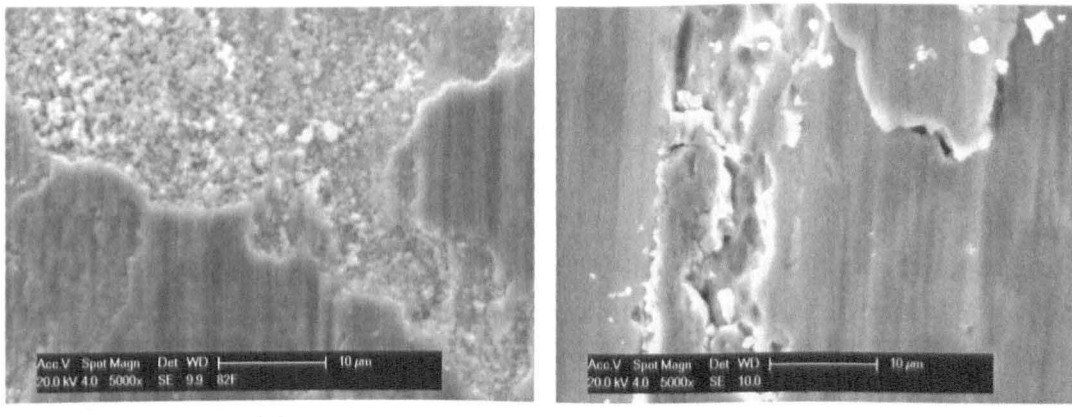

(a) (b)

Figure 6.11: SE SEM micrographs of significant *glaze* formation on the surface of oxide beds on the flat specimen, from a SCMV–SCMV specimen pair, following 100×10^3 fretting cycles with $P = 250\,\text{N}$, $\Delta^* = 25\,\mu\text{m}$ at: (a) 300 °C, (b) 450 °C.

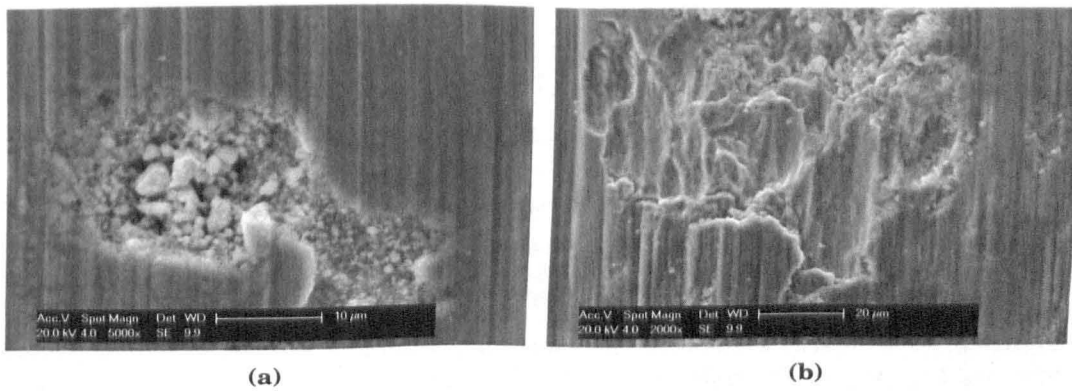

(a) (b)

Figure 6.12: High magnification SE SEM micrographs showing: (a) sintering and (b) glaze layer transfer occurring on a SCMVN-SCMVN specimen pair after a 100×10^3 fretting cycles with $P = 250\,\text{N}$, $\Delta^* = 25\,\mu\text{m}$ at 300 °C.

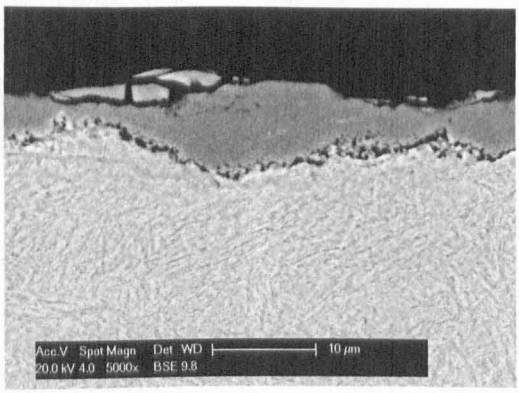

Figure 6.13: BSE SEM micrograph cross-section through the surface glaze formed on a flat specimen, from a SCMV–SCMV couple, following 100×10^3 fretting cycles with $P = 250\,\text{N}$, $\Delta^* = 25\,\mu\text{m}$ at 450 °C.

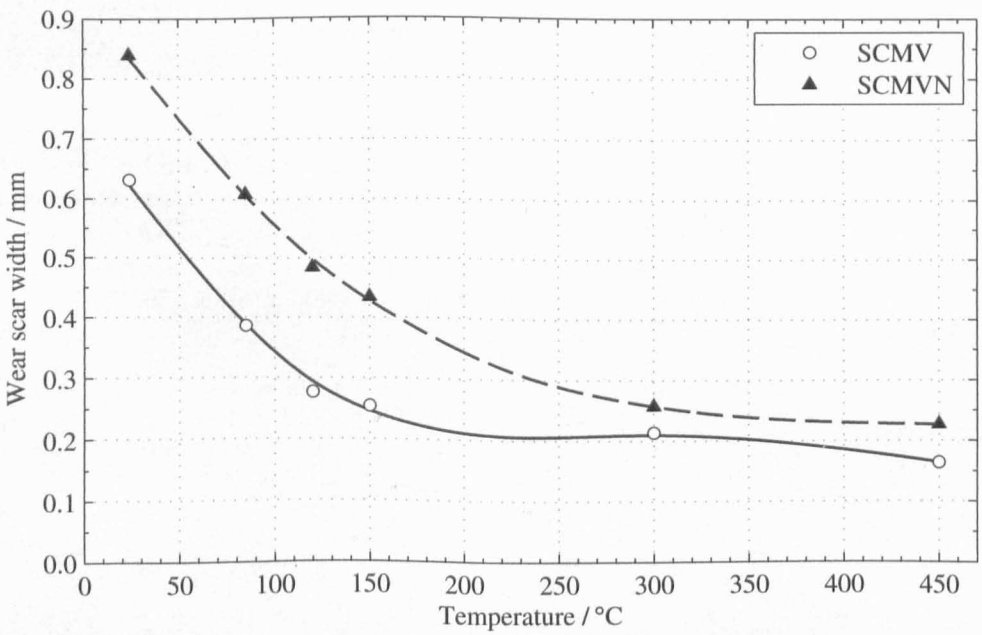

Figure 6.14: Wear scar width as a function of temperature for SCMV-SCMV specimen pairs following 100×10^3 fretting cycles ($P = 250\,\text{N}$, $\Delta^* = 25\,\mu\text{m}$).

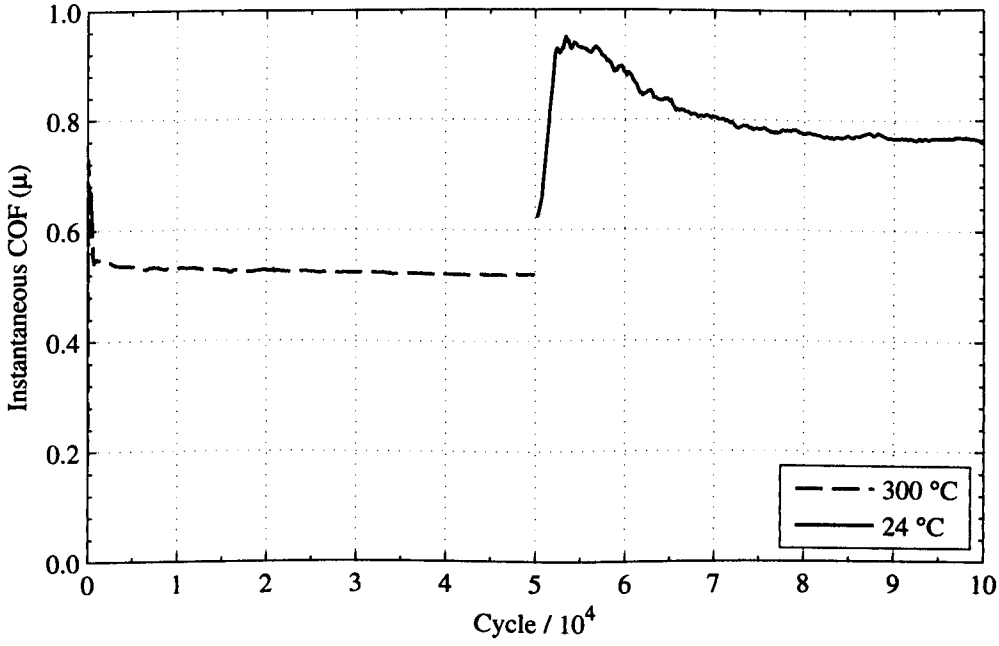

Figure 6.15: Coefficient of friction as a function of cycles for a test run at 300 °C for 50×10^3 cycles and then at 24 °C for a further 50×10^3 cycles ($P = 250$ N, $\Delta^* = 25\,\mu$m).

reduced production of oxide debris).

A limited number of tests, using SCMV-SCMV pairs, were completed using a normal load of 450 and 650 N. On increasing the normal load, a small decrease in the COF was observed: from 0.40 to 0.39 on increasing the load from 250 to 650 N resulting in a gradient of $\approx 2.5 \times 10^{-4}\,\text{N}^{-1}$ (Figure 6.16)—these changes are smaller than those encountered under ambient conditions (Table 5.4, Page 123) but nonetheless a reduction in the COF with increasing normal load is apparent. However, more significant changes were observed in the wear and transferred material volumes (Figure 6.17): it is seen in Figure 6.17a that increasing the normal load to 450 N resulted in a reduction in net wear volume from -0.76×10^{-2} to $-1.77 \times 10^{-2}\,\text{mm}^3$; increasing the normal load further to 650 N resulted in only a small additional reduction to $-1.79 \times 10^{-2}\,\text{mm}^3$. However, Figure 6.17b indicates that the relatively small total volume changes were the result of a more significant significant increase in the volume of adhered material (V^+) and a simultaneous (but smaller) increase in the amount of material lost from the contact (V^-): on increasing the normal load from 250 to 650 N, the volume of adhered material (V^+) increased by $2.03 \times 10^{-2}\,\text{mm}^3$ (from 1.23×10^{-2} to $3.26 \times 10^{-2}\,\text{mm}^3$) while the volume of material lost (V^-) increased by $0.99 \times 10^{-2}\,\text{mm}^3$ (from 0.48×10^{-2} to $1.47 \times 10^{-2}\,\text{mm}^3$); both exhibit a quasi-linear relationship. Examination of the profilometry (Figure 6.18) indicates that the scar on the flat specimen is "U" shaped with regions of adhered material either on either side, while the scar on the cylindrical specimen shows a central area of adhered material; as the load is increased, the features remain consistent in form but grow in scale.

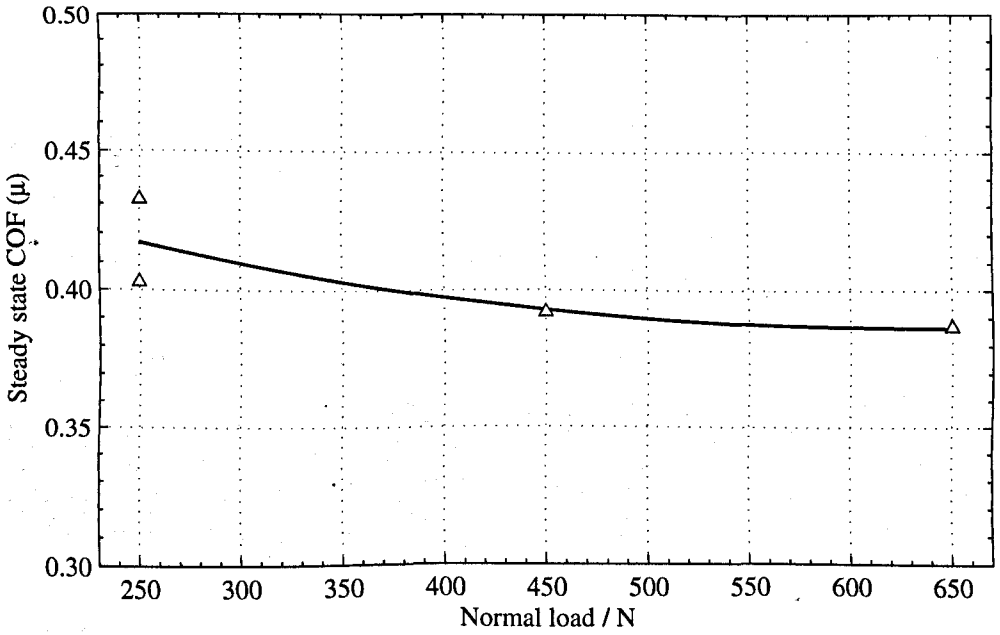

Figure 6.16: Steady state COF as a function of load ($\Delta^* = 25\,\mu m$) at 300 °C for SCMV-SCMV specimen pairs (steady state COF represents the average of the values recorded in the fretting tests from 25×10^3 to 100×10^3 cycles).

XRD analysis was conducted for SCMV and SCMVN specimens in the following conditions: unworn, unworn and thermally exposed (at 300 °C) and following fretting at 300 °C. The diffraction angle, 2θ, was scanned between 20° and 70°, using a step size of 0.05° and a counting time of 4 s per step. The beam width was 3 mm; due to the change in incidence angle, the length of the sample exposed ranged from 6 to 20 mm—much larger than the fretting scar—and thus it is expected that the peaks from the fretted oxide will be only a small fraction of the peaks associated with the un-fretted material surrounding it—consequently, the XRD spectra are plotted on a logarithmic scale.

Figure 6.19 is a composite of the three spectra for an SCMV specimen—labelled i to iii for the unworn, thermally exposed and thermally exposed and fretted cases respectively. Comparing the unworn and unworn-thermally exposed cases (Figure 6.19 i and ii), it is apparent that the thermal exposure resulted in the formation of trace amounts Fe_2O_3 (peaks labelled *F*). Following fretting at elevated temperature (Figure 6.19 iii), it is apparent that there is an increased amount of Fe_2O_3; the peak, labelled *G*, indicates the unique formation of $FeMoO_4$ under fretting conditions at elevated temperature.

Spectra from similar conditions (and using the same labelling convention) for SCMVN are presented in Figure 6.20. In general, the results mirror those of SCMV: thermal exposure results in the formation of Fe_2O_3 and fretting at elevated temperature increases the amount of Fe_2O_3 observed; in contrast to the SCMV specimens, there do not appear to be uniquely formed compounds as the result of elevated temperature

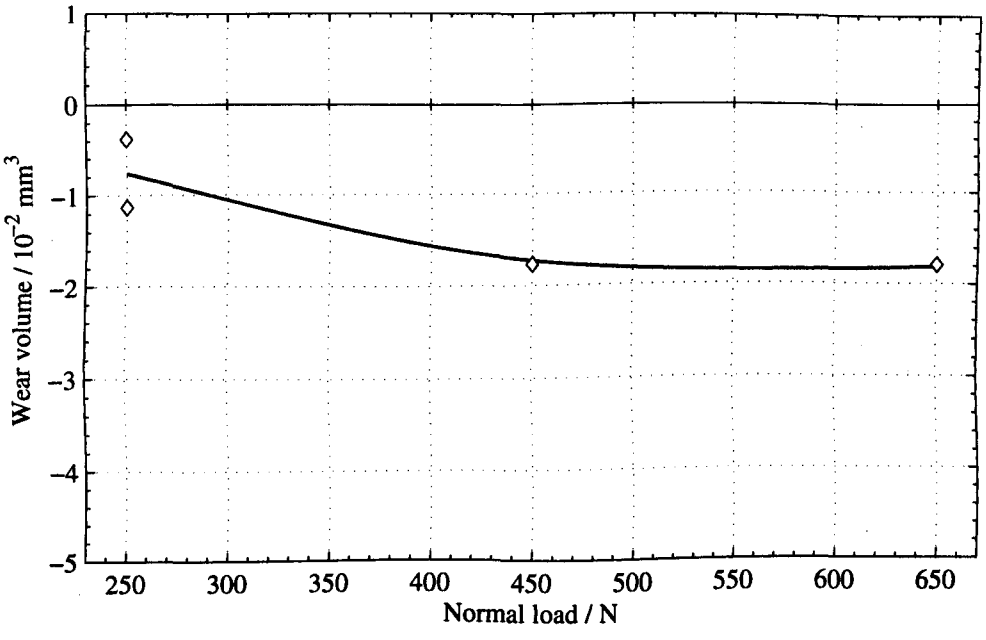

(a)

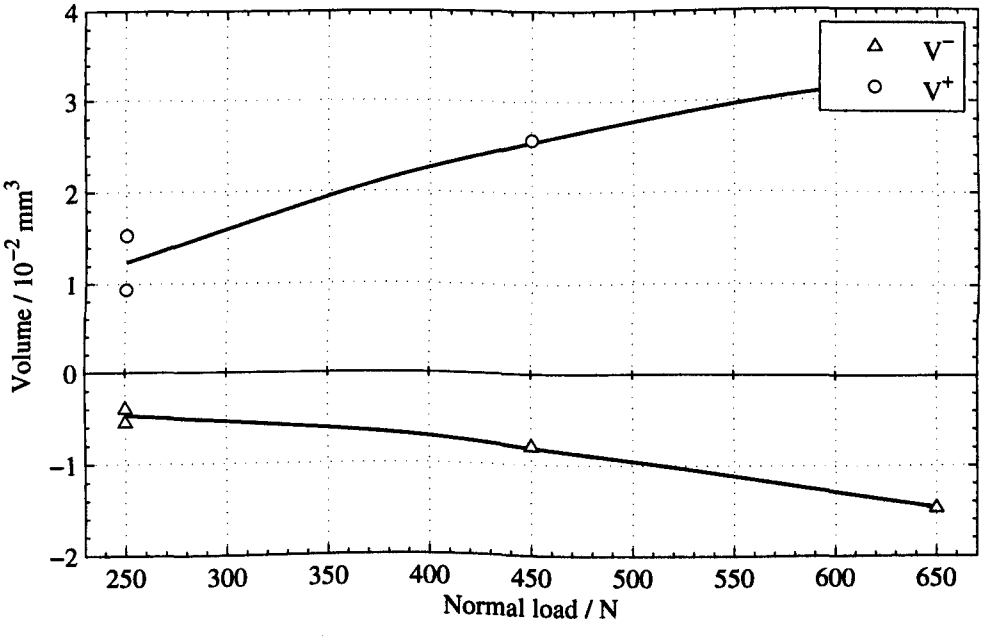

(b)

Figure 6.17: Relationship between wear and normal load for SCMV–SCMV specimen pairs at 300 °C following 100×10^3 fretting cycles ($\Delta^* = 25\,\mu$m): (a) net wear volume, (b) constituent material build-up and removal volumes.

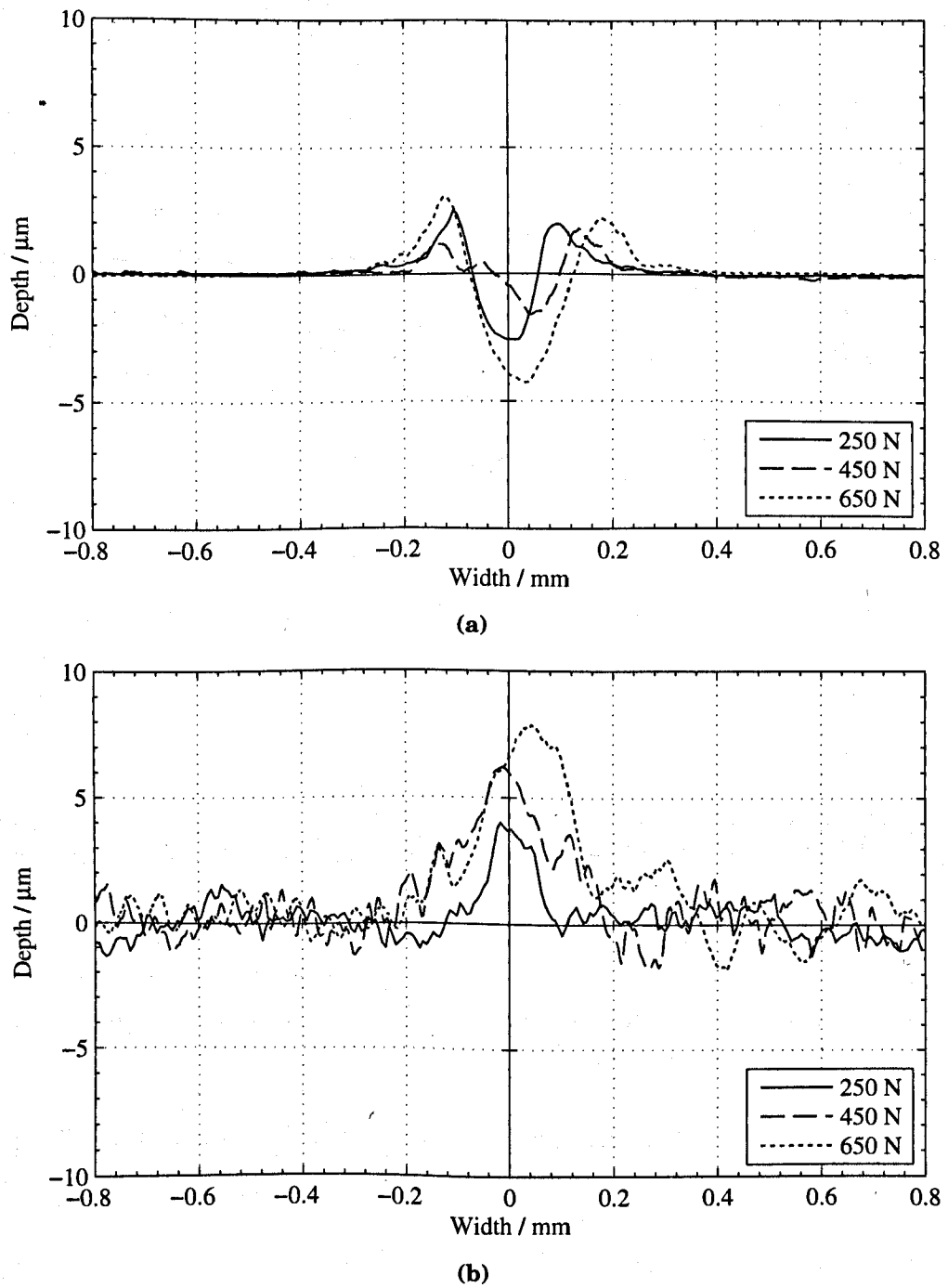

Figure 6.18: Average wear scar profiles for SCMV-SCMV specimen pairs after 100×10^3 fretting cycles at 300 °C with P = 250, 450 and 650 N and Δ^* = 25 µm: (a) flat specimens, (b) cylindrical specimens.

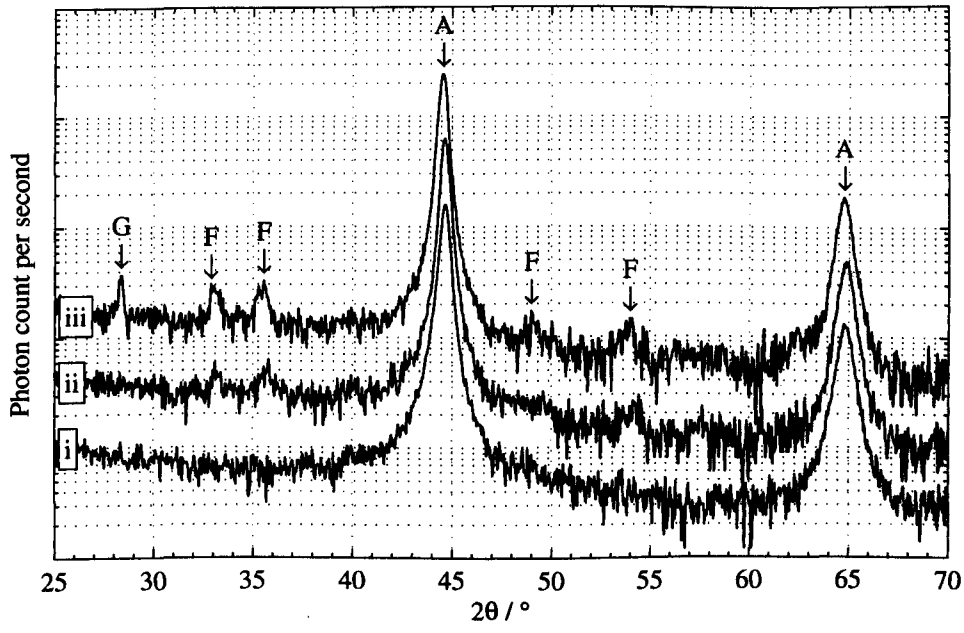

Figure 6.19: XRD spectra of a flat SCMV specimen in the states: (i) unworn, (ii) unworn and thermally exposed (at 300 °C) and (iii) following 100×10^3 fretting cycles at 300 °C. Peaks corresponding to the following compounds are highlighted: (A) Fe, (F) Fe_2O_3, (G) $FeMoO_4$.

fretting wear.

Vickers hardness (HV20) readinges were taken of the surface hardness (for both flat and cylindrical of SCMV specimens) to assess if any tempering of the material occurred during an elevated temperature test. Calculations show that this is not expected and the experimental results similarly support the conclusion that no tempering occurred during the test (Figure 6.21).

6.4 Discussion

It is clear that a significant modification of the wear behaviour of SCMV and SCMVN occurred at some critical transition temperature (TT): for SCMV this was found in the temperature interval between 24 °C and 85 °C, while for SCMVN the transition was found to occur at ≈ 150 °C. For all temperatures between room temperature and the TT, bulk material removal was observed; in contrast, above the TT there was *negative* wear i.e., the volume of material built up on the surfaces was greater than the volume of material removed. This behaviour was not amplified by further increasing the temperature, and the wear volume remained approximately constant (and small). While the transition temperature for SCMV is in agreement with the value that Kayaba and Iwabuchi [187] reported for a 0.45 wt. % C steel fretting at a much higher amplitude of 150 µm, the behaviour at the transition appears to show a different evolution. Kayaba and Iwabuchi [187] observed the wear rate of the steel to initially drop rapidly between 80 to 100 °C and then more progressively until

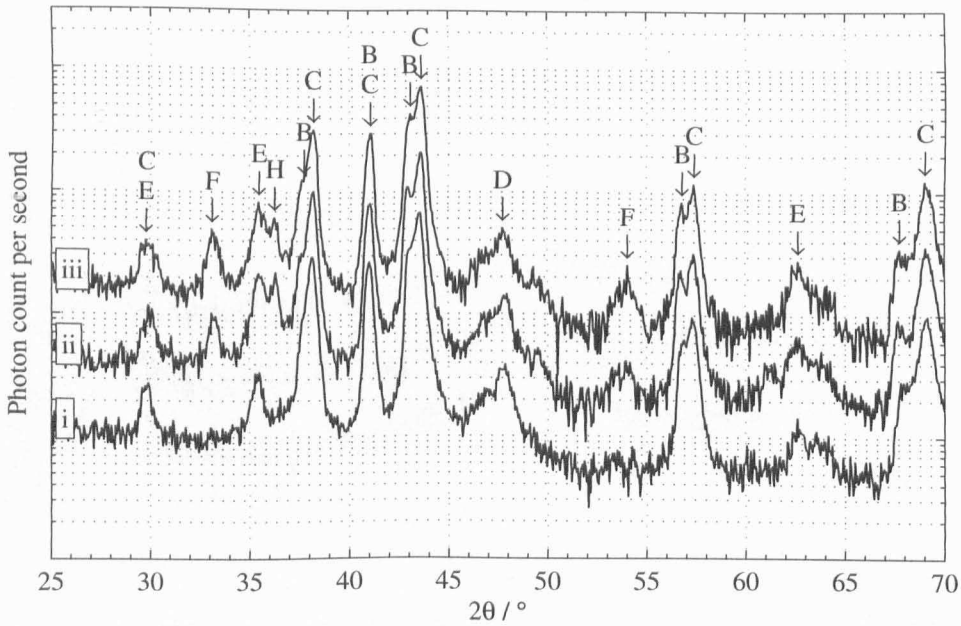

Figure 6.20: XRD spectra of a flat SCMVN specimen in the states: (i) unworn, (ii) unworn and thermally exposed (300 °C) and (iii) following 100×10^3 fretting cycles at 300 °C. Peaks corresponding to the following compounds are highlighted: (B) Fe_2N, (C) Fe_3N, (D) Fe_4N, (E) Fe_3O_4, (F) Fe_2O_3, (H) FeN.

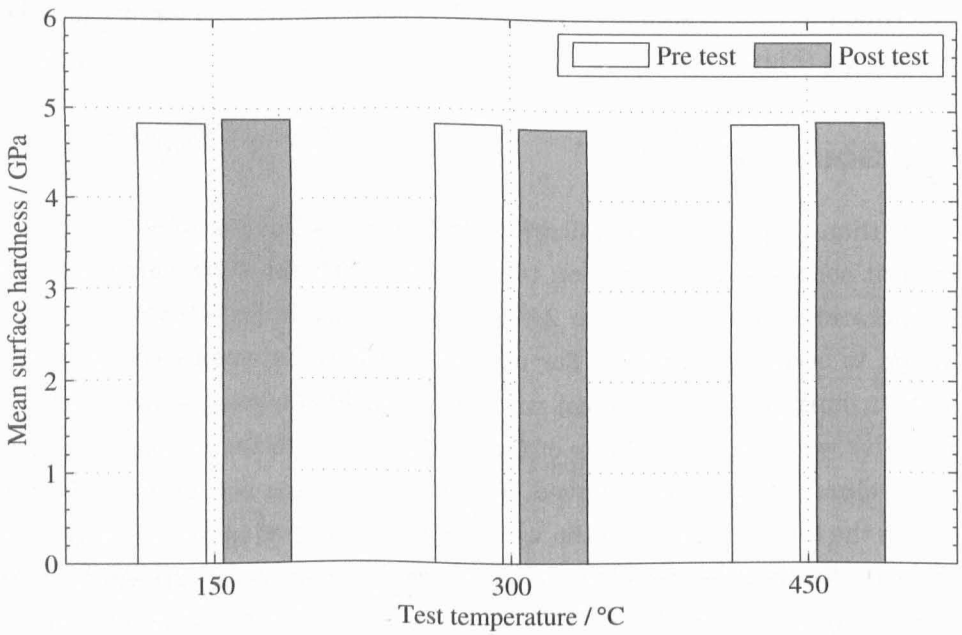

Figure 6.21: Mean surface hardness for SCMV specimens pre (□) and post (▨) elevated temperature tests.

200 °C, whereupon the wear became negative. At this temperature, the initiation of significant adhesive transfer of the oxide layer was found to occur. In the current work, negative wear was similarly observed at all temperatures examined above the TT, but no evidence of significant material transfer was found. SEM examination of the scars (Figures 6.11a, 6.12a and 6.13) indicates that the formation of the debris bed resulted from accumulation and retention of finely divided oxide debris within the contact. Particular examination of the SEM micrographs for the SCMVN specimens indicates that there were small areas of oxide transfer (Figure 6.12b); however, the profilometry results (Figure 6.7b) indicate that there was no initiation of any significant adhesive transfer which, if it were occurring, would be indicated by an increase in the V^+ and V^- volumes (although not necessarily by any change in the overall wear volume). Additional tests for SCMV indicated that net material transfer, from the flat to cylindrical specimen, may be initiated by increasing the normal load (Figures 6.17 and 6.18).

Observation of the SEM micrographs (Figures 6.8 and 6.9) indicates that as the wear rates fell with increasing temperature, there was an associated change in the appearance of the debris bed formed within the contact. Following fretting below the TT, the debris bed was rough in appearance with large areas in the process of delamination and breakdown; in addition, significant areas of exposed metal were visible across the wear scar. In contrast, as the temperature was elevated, the surface of the wear scar appeared smoother and the oxide exhibited more complete coverage of the scar—whilst there were still areas of the debris bed undergoing breakdown, those areas were less prevalent. This trend continued with increasing temperature: above the TT, the debris bed surface was generally very smooth and burnished—consistent with the typical description of a *glaze-layer* (Figures 6.8d and 6.9e). High magnification examination (in cross section and surface views) of the smooth areas shows them forming on the surface of fine granular oxide beds (Figures 6.11a and 6.12a).

Whilst the glaze-layer formation may be observed qualitatively in the SEM micrographs, plotting the width of the wear scar (Figure 6.14) provides some form of quantitative analysis. It can be seen that the width of the wear scar drops rapidly up to the region of the TT and more progressively at higher temperatures, until becoming approximately constant at the highest temperatures. The initial drop in width (up to the TT) can be mainly attributed to a reduction in wear volume. However, at temperatures above the TT, the wear volume remained approximately constant while the width of the wear scar continued to decrease, indicating that the load bearing capacity of the established tribo-film was greater at higher temperatures. For example, considering the SCMV specimens, it can be seen that the width of the wear scar dropped by 40 % between 24 °C and 85 °C (the TT)—this is mainly attributed to the reduction in wear; as the temperature was increased further to 150 °C (when the wear volume remained approximately constant), the reduction in width of the wear scar still increased by a further 20 %. At the highest temperature studied (450 °C), the scar widths

are comparable to the minimum expected width e.g., for SCMV the scar width was 160 μm, not dissimilar to the minimum expected width of ≈ 133 μm (resulting from an initial Hertzian contact width of ≈ 83 μm and an applied displacement amplitude of 25 μm). Similar observations can be made for the COF: for both materials, it decreased monotonically between 24 °C and 300 °C, but with no commensurate change in the wear rate.

Testing to explore the resilience of the glaze-layer formed at high temperatures found it to disperse almost immediately when fretting was resumed at ambient temperature (Figure 6.15). Subsequent optical examination of the scar showed it to be similar in appearance to tests conducted entirely at ambient temperature with dispersed areas of compressed oxide and visible metal; this is in accord with work conducted by Rybiak et al. [108] on the fretting of a stainless steel under variable temperature conditions.

Considering the quantitative data for both materials (SCMV and SCMVN), it is apparent that there was a notable difference between their fretting wear response at lower temperatures; however, this difference was eliminated when wear occured above their respective TTs. For example, the steady-state COF is consistently higher (≈ 0.08) for SCMVN pairs compared to SCMV pairs up to 150 °C; similarly the wear scar width of the SCMVN pairs is 0.2 mm wider than the SCMV pairs below 300 °C, whilst above this temperature, they are of comparable values. A similar trend is also observed in the wear volume data: below 150 °C, the wear of the SCMVN pairs is found to be consistantly higher than that of the SCMV pairs, while above 150 °C, the wear volumes are similar for both material pair types. Moreover, in all cases, the change in the observed variable as a function of temperature occurs at a similar rate for both SCMV and SCMVN pairs; these changes appear commensurate with the initiation and progressive formation of an oxide glaze-layer.

As outlined in the introduction, changes in temperature will affect the formation and properties of the oxide bed primarily through changes to the rate of oxidation or changes to the way that individual debris particles are either formed into a load-bearing bed (through changes both to the adhesion forces between particles and changes in the kinetics of sintering) or ejected from the contact. Additionally, the bulk steel properties may be sufficiently changed at elevated temperatures to influence the wear process, or affect the formation of a stable load-bearing bed. Whilst all of these will clearly influence the tribology of the contact, it is important to understand which is the primary cause of the changes observed.

Figure 6.1 indicates that increases in temperature above ambient have a relatively small effect (less than ≈ 14 %) on the hardness of SCMV until temperatures greater than 300 °C, a temperature significantly higher than the 24 to 85 °C temperature interval over which the wear rate was observed to fall rapidly. In contrast, the hardness of SCMVN is found to be relatively constant until 150 to 300 °C where it drops by ≈ 34 %; nonetheless, there are no coincident sudden changes in wear response. As such, it may be concluded that changes in the mechanical properties of the substrate are not

the cause of the transition in wear. However, both material types show a similar marked material softening above 300 °C which does coincide with a slight increase in the steady state COF at 450 °C (Figure 6.6). Furthermore, hardness testing before and after elevated temperature tests indicates that there is no time dependant tempering of the materials occurring (Figure 6.21).

Hurricks [107, 189] suggested that increases in temperature above ambient affected the tribology of fretting contacts primarily through a change in oxidation kinetics. The change in oxidation rate for iron from logarithmic to parabolic behaviour is known to occur at approximately 200 °C [208], which is significantly higher than the temperature of the transition in wear behaviour observed in the current tests with SCMV pairs (85 °C). As such, it seems unlikely that the specimen surface oxide film can spontaneously grow to a critical thickness at these lower temperatures. Additionally, if the transition were due to a change in the oxide from α-Fe_2O_3 to Fe_3O_4, (the latter being thought to act as a better solid lubricant), then it would be anticipated that the trends observed in the measured COF as a function of temperature would mirror the changes in the wear rate; this is not observed, with the wear rate changing little between 85 °C and 300 °C, whereas the COF continued to decline over the same temperature range. In fretting experiments on stainless steel over a range of temperatures, Rybiak et al. [108] concluded that the transition in wear behaviour was due to the tribo-sintering process demonstrated by Kato and Komai [196] and Kato [201]. In the current experiments, this also seems the most likely explanation for the significant reduction in the rate of wear between 24 °C and 85 °C for SCMV and at approximately 150 °C for SCMVN. The sudden drop in wear at these temperatures occurred simultaneously with a significant reduction in the amount of ejected oxide debris and a noticeable change in character of the wear scars (Figures 6.8 and 6.9). There seems to be a critical temperature at which the adhesion between the oxide debris particles becomes sufficient to inhibit their independent removal from the contact and thus results in the formation of a stable load bearing tribofilm; as a result, the wear rate reduces dramatically. Likewise, increasing the coverage of the oxide debris bed within the contact reduces the number of interactions between metallic-asperities resulting in a reduction in COF. As the temperature is raised, the JKR adhesive forces [198] will be stronger between individual debris particles (reducing their tendency for ejection from the contact), and the rate of sintering will increase (meaning that a stable debris bed is formed), both resulting in a more rapid development of the protective bed. This is reflected in the time evolution of the COF in individual tests (Figures 6.4 and 6.5), where the steady state was seen to be attained more quickly at higher temperatures. As the sintering became more complete, so the load capacity of the debris bed increased, resulting in a reduction in wear scar width with temperature (Figure 6.14). The monotonic decrease in COF with increasing temperature in the range 24 to 300 °C is commensurate with the increasingly glaze-like appearance of the worn surface (Figures 6.8 and 6.9).

Chapter 7

Conclusions

The first objective of this work was to design and build a new fretting wear apparatus and put in place the test methodology and data processing routines necessary to quantitatively evaluate the wear behaviour of materials under test. The results presented in this work verify the successful completion of that objective. Moreover, other workers have been able to use the facility to produce high quality data [209].

The fretting wear performance of SCMV and SCMVN in heterogeneous and homogeneous combinations was assessed under a range of normal loads and applied displacement amplitudes. It was found that the COF for each contact types was not a constant, but instead was a linear function of the normal load (reducing with increasing load); this was found to be in accord with a number of published data sets, although no detailed explanation of this effect is presented in the literature. As a consequence of a non-constant COF, the wear behaviour has been described in terms of dissipated energy (E_d). It was found that the wear (over the range of test conditions evaluated) could be adequately described by a relationship of the form:

$$V^w(x) = \begin{cases} k_e(E_d - E_{th}) & \text{for } E_d \geq E_{th} \\ 0 & \text{otherwise} \end{cases}$$

where k_e is the wear rate and E_{th} is a critical dissipated energy below which no wear will be initiated. Due to the significance of the offset (associated with E_{th}), it is not possible to categorically classify one material as superior to another under all conditions. However, in terms of the wear rate of homogeneous pairings, nitriding was found to offer a 12 % reduction in wear rate compared to the as heat treated SCMV but the threshold energy concurrently decreased from 1.1 to 0.92 kJ (for the specimen geometry employed). No evidence was found to indicate that the WL on the surface of the nitrided steel had any significant effect on the ensuing wear. When heterogeneous combinations of the materials—representative of arrangements found in aerospace transmission assemblies—were evaluated, the wear rate was intermediate between the values for homogeneous material combinations, although the energy threshold

was lower than that observed for either of the self-mated combinations (0.75 kJ for the specimen geometry employed).

The wear mechanisms for the self-mated material combinations resulted (in general) in bulk, uniform material removal from both surfaces; however, in some cases a protective oxide debris bed was found to form on one nitrided specimen from the pair which abraded the other specimen. When heterogeneous material combinations were evaluated, the wear response was found to differ greatly: despite being significantly harder than the SCMV, the SCMVN specimen was found to wear more (in terms of volume lost) although the SCMV specimen suffered significant plastic damage of the surface. It was concluded that the oxide debris became embedded and consequently strongly adhered to the softer material and abraded the harder counterface.

From the fretting wear testing conducted over a range of temperatures (24 to 450 °C) for homogeneous SCMV and SCMVN material combinations, a number of conclusions can be drawn. For both materials, there was a significant reduction in wear above some critical TT: for SCMV this was between 24 and 85 °C and for SCMVN it was at ≈ 150 °C. The reduction in wear is due to the retention of oxide debris within the wearing contact leading to the formation of a stable load-bearing bed and eventually a *glaze-layer*; the results support the view that this is due to a tribo-sintering process as described by Kato and Komai [196]. For both material types, the coefficient of friction was found to decrease rapidly with temperature, the effect being commensurate with the progressive formation of the glaze-layer. Although the glaze-layer was stable at temperature, it was not found to show any endurance if the temperature was reduced and fretting recommenced. Mechanistically, the results agreed well with those found by Rybiak et al. [108] for a stainless steel; however, the temperature of transition between the high wear regime and the low wear regime occurred at a much lower temperature, particularly for the as heat treated SCMV.

Chapter 8

Future Work

Under a range of normal loads and displacement amplitudes, the fretting wear rates and coefficients of friction—for a set of material combinations—have been shown to be simple linear functions of the loading parameters. As has been discussed, the wear rate has not generally been considered to be constant with displacement amplitude under fretting conditions; indeed, the point at which the wear rate becomes constant (as a function of displacement amplitude) has historically been used as the characteristic to differentiate fretting wear from sliding wear. As a result, there is opportunity for a piece of work, investigating a large range of displacement amplitudes (e.g. 10 to 1000 μm), to define the relationship between fretting and reciprocating sliding. Consequently, it could be concluded that fretting is predominantly differentiated from sliding wear only by its adventitious nature and higher frequencies at which it can occur due to characteristically small displacement amplitudes.

The current work used a fixed test duration of 100×10^3 cycles, since this is believed to adequately capture the steady state behaviour of the contact. However, in the context of the design life of an aeroengine, where displacements may be driven by once-per-revolution vibrations (at frequencies commonly in excess of 3000 rpm) with a single transatlantic flight accruing more than 10^6 cycles, this is not a particularly high fraction. Accordingly, investigation of frequency effects and verification of the long duration fretting behaviour would enhance the general engineering applicability of the data. Additionally, much of the fretting literature—particularly the more modern literature—utilises a non-conforming contact (often a ball or cylinder, of relatively small radius, on flat configuration). However, it could be argued that the majority of engineering contacts are either fully conforming or very nearly so. Accordingly, relating the behaviour of a conforming contact to a non-conforming contact should be a high priority; indeed, recent work, in which the author was involved, indicates that different wear mechanisms may be active in the fretting of conforming contacts than occur in non-conforming cases [209].

At even slightly elevated temperatures, the tribology of the contact was found to be dominated by the formation of a glaze-layer but tests showed this layer to disperse

almost instantly at ambient temperatures. Inevitably, an aeroengine will experience such a temperature cycle at startup and shutdown; with some modifications to the test rig to enable higher cooling rates (and hence practical test durations), the wear rate of SCMV under such conditions could be evaluated.

Bibliography

[1] R. B. Waterhouse, Fretting Corrosion, volume 10 of *International series of monographs on materials science and technology*, Permagon Press, 1972.

[2] P. L. Hurricks, Mechanism of fretting—a review, Wear 15 (1970) 389–408.

[3] R. C. Bill, Fretting wear and fretting fatigue—how are they related?, Journal of Lubrication Technology 105 (1983) 230–238.

[4] H. H. Uhlig, Mechanism of fretting corrosion, Journal of Applied Mechanics – Transactions of the ASME 21 (1954) 401–407.

[5] J. M. Dobromirski, Variables of fretting process: are there 50 of them?, in: M. Helmi Attia, R. B. Waterhouse (Eds.), Standardization of Fretting Fatigue Test Methods and Equipment, volume 1159 of *ASTM Special Technical Publication*, ASTM, 1992, pp. 60–69.

[6] I. McColl, R. Waterhouse, S. Harris, M. Tsujikawa, Lubricated fretting wear of a high-strength eutectoid steel rope wire, Wear 185 (1995) 203 –212.

[7] W. Wallace, D. W. Hoeppner, P. V. Kandachar, AGARD Corrosion Handbook. Volume 1. Aircraft Corrosion: Causes and Case Histories, Technical Report, AGARD, 1985.

[8] M. Helmi Attia, Fretting fatigue and wear damage of structural components in nuclear power stations—fitness for service and life management perspective, Tribology International 39 (2006) 1294–1304.

[9] R. B. Waterhouse, Occurrence of fretting in practice and its simulation in the laboratory, in: S. R. Brown (Ed.), Materials evaluation under fretting conditions, volume 780 of *ASTM Special Technical Publication*, ASTM, 1982, pp. 3–16.

[10] S. B. Leen, T. R. Hyde, E. J. Williams, A. A. Becker, I. R. McColl, T. H. Hyde, J. W. Taylor, Development of a representative test specimen for frictional contact in spline joint couplings, The Journal of Strain Analysis for Engineering Design 35 (2000) 23.

[11] S. B. Leen, I. J. Richardson, I. R. McColl, E. J. Williams, T. R. Hyde, Macroscopic fretting variables in a splined coupling under combined torque and axial load, Journal of Strain Analysis for Engineering Design 36 (2001) 481–497.

[12] C. H. H. Ratsimba, I. R. McColl, E. J. Williams, S. B. Leen, H. P. Soh, Measurement, analysis and prediction of fretting wear damage in a representative aeroengine spline coupling, Wear 257 (2004) 1193–1206.

[13] T. Ford, Mainshafts for the trent, Aircraft Engineering and Aerospace Technology 69 (1997) 555–560.

[14] S. B. Leen, I. R. McColl, E. J. Willams, Fatigue life prediction for a barrelled spline coupling under torque overload, Proceedings of the Institution of Mechanical Engineers, Part G: Journal of Aerospace Engineering 217 (2003) 123–142.

[15] J. Ding, The modelling of fretting wear, Ph.D. thesis, The University of Nottingham, 2003.

[16] J. Ding, W. S. Sum, R. Sabesan, S. B. Leen, I. R. McColl, E. J. Williams, Fretting fatigue predictions in a complex coupling, International Journal of Fatigue 29 (2007) 1229–1244.

[17] E. M. Eden, W. N. Rose, F. L. Cunningham, The endurance of metals: experiments on rotating beams at University College, London, Proceedings of the Institution of Mechanical Engineers 81 (1911) 829–880.

[18] G. A. Tomlinson, The rusting of steel surfaces in contact, Proceedings of the Royal Society A 115 (1927) 472–483.

[19] D. Godfrey, Investigation of fretting corrosion by microscopic observation, Technical Note TN–2039, NACA, 1950.

[20] O. Vingsbo, S. Söderberg, On fretting maps, Wear 126 (1988) 131–147.

[21] S. Fouvry, L. Vincent, P. Kapsa, Quantification of fretting damage, Wear 200 (1996) 186–205.

[22] J. E. Shigley, C. R. Mischke, R. G. Budynas, Mechanical Engineering Design, seventh edition, McGraw-Hill, 2003.

[23] D. C. H. Yang, S. Tong, On the profile design of transmission splines and keys, Mechanism and Machine Theory 42 (2007) 82–87.

[24] D. W. Dudley, How to design involute splines, Product Engineering 28 (1957) 75–80.

[25] A. Deutschman, W. Michels, C. Wilson, Machine Design: Theory and Practice, Macmillan, New York, 1975.

[26] Rolls-Royce, The jet engine, Rolls-Royce Technical Publications, 5 ed., Rolls-Royce Technical Publications, 2005.

[27] H. Hertz, On the contact of rigid elastic solids and on hardness, Ch 6: Assorted Papers (1882).

[28] R. D. Mindlin, Compliance of elastic bodies in contact, Journal of Applied Mechanics – Transactions of the ASME 16 (1949) 259–268.

[29] R. D. Mindlin, H. Deresiewicz, Elastic spheres in contact under varying oblique forces, Journal of Applied Mechanics – Transactions of the ASME 20 (1953) 327–344.

[30] K. L. Johnson, Contact Mechanics, Cambridge University Press, 1985.

[31] K. L. Johnson, Surface interaction between elastically loaded bodies under tangential forces, Proceedings of the Royal Society of London. Series A. Mathematical and Physical Sciences 230 (1955) 531–548.

[32] Z. R. Zhou, S. Fayeulle, L. Vincent, Cracking behaviour of various aluminium alloys during fretting wear, Wear 155 (1992) 317–330.

[33] Z. R. Zhou, L. Vincent, Mixed fretting regime, Wear 181 (1995) 531–536.

[34] C. H. Hager, Jr., J. Sanders, S. Sharma, Characterization of mixed and gross slip fretting wear regimes in Ti6Al4V interfaces at room temperature, Wear 257 (2004) 167–180.

[35] S. Heredia, S. Fouvry, Introduction of a new sliding regime criterion to quantify partial, mixed and gross slip fretting regimes: Correlation with wear and cracking processes, Wear 269 (2010) 515–524.

[36] Z. R. Zhou, K. Nakazawa, M. H. Zhu, N. Maruyama, P. Kapsa, L. Vincent, Progress in fretting maps, Tribology International 39 (2006) 1068–1073.

[37] S. C. Lim, Recent developments in wear-mechanism maps, Tribology International 31 (1998) 87–97.

[38] O. Vingsbo, M. Ödfalk, N. Shen, Fretting maps and fretting behavior of some F.C.C. metal alloys, Wear 138 (1990) 153–167.

[39] Z. R. Zhou, L. Vincent, Effect of external loading on wear maps of aluminium alloys, Wear 162 (1993) 619–623.

[40] O. Vingsbo, J. Schön, Gross slip criteria in fretting, Wear 162 (1993) 347–356.

[41] S. Fouvry, P. Kapsa, L. Vincent, Analysis of sliding behaviour for fretting loadings: determination of transition criteria, Wear 185 (1995) 35–46.

[42] J. Warburton, The fretting of mild steel in air, Wear 131 (1989) 365–386.

[43] N. Ohmae, T. Tsukizoe, The effect of slip amplitude on fretting, Wear 27 (1974) 281–294.

[44] G. X. Chen, Z. R. Zhou, Study on transition between fretting and reciprocating sliding wear, Wear 250 (2001) 665–672.

[45] J. S. Halliday, W. Hirst, The fretting corrosion of mild steel, Proceedings of the Royal Society of London Series A – Mathematical and Physical Sciences 236 (1956) 411–425.

[46] X. Zhang, C. Zhang, C. Zhu, Slip amplitude effects and microstructural characteristics of surface layers in fretting wear of carbon steel, Wear 134 (1989) 297–309.

[47] M. Varenberg, I. Etsion, G. Halperin, Slip index: a new unified approach to fretting, Tribology Letters 17 (2004) 569–573.

[48] M. Varenberg, I. Etsion, E. Altus, Theoretical substantiation of the slip index approach to fretting, Tribology Letters 19 (2005) 263–264.

[49] R. B. Waterhouse (Ed.), Fretting Fatigue, Applied Science Publishers Ltd., 1981.

[50] O. Jin, S. Mall, Effects of slip on fretting behavior: experiments and analyses, Wear 256 (2004) 671–684.

[51] J. Ding, S. B. Leen, I. R. McColl, The effect of slip regime on fretting wear-induced stress evolution, International Journal of Fatigue 26 (2004) 521–531.

[52] J. J. Madge, S. B. Leen, I. R. McColl, P. H. Shipway, Contact-evolution based prediction of fretting fatigue life: Effect of slip amplitude, Wear 262 (2007) 1159–1170.

[53] R. B. Waterhouse, Fretting wear, in: P. J. Blau (Ed.), ASM Handbook Volume 18: Friction, Lubrication, and Wear, volume 18 of *ASM Handbook*, ASM International, 1992.

[54] D. Aldham, J. Warburton, R. E. Pendlebury, The unlubricated fretting wear of mild steel in air, Wear 106 (1985) 177–201.

[55] I. M. Feng, B. G. Rightmire, An experimental study of fretting, Proceedings of the Institution of Mechanical Engineers 170 (1956) 1055–1064.

[56] E. Rabinowicz, Friction and Wear of Materials, Wiley, 1965.

[57] R. E. Pendlebury, Unlubricated fretting wear of mild steel surfaces in air at room temperature: II electrical contact resistance measurements and the effect on wear of intermittent loading, Wear 118 (1987) 341–364.

[58] D. Godfrey, J. M. Bailey, Coefficient of friction and damage to contact area during the early stages of fretting I: Glass, copper, or steel against copper, Technical Note TN–3011, NACA, 1953.

[59] J. M. Bailey, D. Godfrey, Coefficient of friction and damage to contact area during the early stages of fretting II: steel, iron, iron oxide, and glass combinations, Technical Note TN–3144, NACA, 1954.

[60] Y. Berthier, L. Vincent, M. Godet, Velocity accommodation in fretting, Wear 125 (1988) 25–38.

[61] J. F. Andrew, P. D. Donovan, J. Stringer, Fretting corrosion products of aluminium alloys, British Corrosion Journal 3 (1968) 85–87.

[62] R. C. Bill, Review of the factors that influence fretting wear, in: S. R. Brown (Ed.), Materials Evaluation Under Fretting Conditions, volume 780 of *ASTM Special Technical Publication*, ASTM, 1982, pp. 165–182.

[63] I. M. Feng, H. H. Uhlig, Fretting corrosion of mild steel in air and in nitrogen, Journal of Applied Mechanics – Transactions of the ASME 21 (1954) 395–400.

[64] C. Colombie, Y. Berthier, A. Floquet, L. Vincent, M. Godet, Fretting—load carrying capacity of wear debris, Journal of Tribology 106 (1984) 194–201.

[65] R. B. Waterhouse, D. E. Taylor, Fretting debris and delamination theory of wear, Wear 29 (1974) 337–344.

[66] R. E. Pendlebury, Unlubricated fretting wear of mild steel surfaces in air at room temperature. Part III. the conversion of (artificial) metallic wear particles to oxide, in: D. Dowson, C. M. Taylor, M. Godet, D. Berthe (Eds.), Interface Dynamics Proceedings of the 14th Leeds-Lyon Symposium on Tribology, volume 12 of *Tribology Series*, Elsevier, 1988, pp. 99–103.

[67] T. F. J. Quinn, Oxidational wear, Wear 18 (1971) 413–419.

[68] I. F. Stowers, E. Rabinowicz, The mechanism of fretting wear, Journal of Lubrication Technology 95 (1973) 65–70.

[69] N. P. Suh, Delamination theory of wear, Wear 25 (1973) 111–124.

[70] N. P. Suh, Overview of delamination theory of wear, Wear 44 (1977) 1–16.

[71] E. S. Sproles, D. J. Duquette, Mechanism of material removal in fretting, Wear 49 (1978) 339–352.

[72] S. Fayeulle, P. Blanchard, L. Vincent, Fretting behavior of titanium alloys, Tribology Transactions 36 (1993) 267–275.

[73] P. Blanchard, C. Colombie, V. Pellerin, S. Fayeulle, L. Vincent, Material effects in fretting wear – application to iron, titanium, and aluminium-alloys, Metallurgical transactions. A, Physical metallurgy and materials science 22 (1991) 1535–1544.

[74] E. Sauger, S. Fouvry, L. Ponsonnet, P. Kapsa, J. M. Martin, L. Vincent, Tribologically transformed structure in fretting, Wear 245 (2000) 39–52.

[75] E. Sauger, L. Ponsonnet, J. M. Martin, L. Vincent, Study of the tribologically transformed structure created during fretting tests, Tribology International 33 (2000) 743–750.

[76] Z. R. Zhou, E. Sauger, J. J. Liu, L. Vincent, Nucleation and early growth of tribologically transformed structure (TTS) induced by fretting, Wear 212 (1997) 50–58.

[77] R. B. Waterhouse, Influence of local temperature increases on the fretting corrosion of mild steel, Journal of the Iron and Steel Institute 197 (1961) 301–305.

[78] M. Kalin, J. Vizintin, A tentative explanation for the tribochemical effects in fretting wear, Wear 250 (2001) 681–689.

[79] M. Kalin, J. Vizintin, High temperature phase transformations under fretting conditions, Wear 249 (2001) 172–181.

[80] E. S. Sproles, D. J. Duquette, Interface temperature-measurements in fretting of a medium carbon-steel, Wear 47 (1978) 387–396.

[81] B. L. Weik, M. J. Furey, B. Vick, Surface temperatures generated with ceramic materials in oscillating fretting contact, Journal of Tribology 116 (1994) 260–267.

[82] F. E. Kennedy, Single pass rub phenomena – analysis and experiment, Journal of Lubrication Technology 104 (1982) 582–588.

[83] F. Vodopivec, J. Viźntin, B. Suśtarśić, Effect of fretting amplitude on microstructure of 1C-1.5Cr steel, Materials Science and Technology 12 (1996) 355–361.

[84] M. Kalin, Influence of flash temperatures on the tribological behaviour in low-speed sliding: a review, Materials Science and Engineering: A 374 (2004) 390–397.

[85] M. Kalin, J. Viźintin, Comparison of different theoretical models for flash temperature calculation under fretting conditions, Tribology International 34 (2001) 831–839.

[86] N. M. Everitt, J. Ding, G. Bandak, P. H. Shipway, S. B. Leen, E. J. Williams, Characterisation of fretting-induced wear debris for Ti-6Al-4V, Wear 267 (2009) 283–291.

[87] M. Godet, The third-body approach: A mechanical view of wear, Wear 100 (1984) 437–452.

[88] M. Godet, Third-bodies in tribology, Wear 136 (1990) 29–45.

[89] Y. Berthier, M. Godet, M. Brendle, Velocity accommodation in friction, Tribology Transactions 32 (1989) 490–496.

[90] T. Kayaba, A. Iwabuchi, Effect of the hardness of hardened steels and the action of oxides on fretting wear, Wear 66 (1981) 27–41.

[91] A. Iwabuchi, The role of oxide particles in the fretting wear of mild-steel, Wear 151 (1991) 301–311.

[92] M. Varenberg, G. Halperin, I. Etsion, Different aspects of the role of wear debris in fretting wear, Wear 252 (2002) 902–910.

[93] A. Iwabuchi, K. Hori, H. Kubosawa, The effect of oxide particles supplied at the interface before sliding on the severe-mild wear transition, Wear 128 (1988) 123–137.

[94] A. Iwabuchi, H. Kubosawa, K. Hori, The dependence of the transition from severe to mild wear on load and surface roughness when the oxide particles are supplied before sliding, Wear 139 (1990) 319–333.

[95] H. H. Uhlig, I. M. Feng, W. D. Tierney, A. McClellan, A fundamental investigation of fretting corrosion, Technical Note TN–3029, NACA, 1953.

[96] G. A. Tomlinson, P. L. Thorpe, H. J. Gough, An investigation of the fretting corrosion of closely fitting surfaces, Proceedings of the Institution of Mechanical Engineers 141 (1939) 223–248.

[97] W. E. Campbell, The current status of fretting corrosion, in: Symposium on Fretting Corrosion, volume 144 of *ASTM Special Technical Publication*, ASTM, 1953, pp. 3–23.

[98] L. Toth, The investigation of the steady stage of steel fretting, Wear 20 (1972) 277–286.

[99] C. Mary, S. Fouvry, J. Martin, B. Bonnet, Pressure and temperature effects on fretting wear damage of a Cu-Ni-In plasma coating versus Ti17 titanium alloy contact, Wear 272 (2011) 18–37.

[100] Y. Berthier, C. Colombie, L. Vincent, M. Godet, Fretting wear mechanisms and their effects on fretting fatigue, Journal of Tribology 110 (1988) 517–524.

[101] S. Söderberg, U. Bryggman, T. McCullough, Frequency-effects in fretting wear, Wear 110 (1986) 19–34.

[102] S. Söderberg, T. Colvin, K. Salama, O. Vingsbo, Ultrasonic fretting wear of a plain carbon-steel, Journal of Engineering Materials and Technology – Transactions of the ASME 108 (1986) 153–158.

[103] U. Bryggman, S. Söderberg, Contact conditions in fretting, Wear 110 (1986) 1–17.

[104] M. Kuno, R. B. Waterhouse, The effect of oscillatory direction on fretting wear under crossed cylinder contact conditions, in: K. Holmberg, I. Nieminen (Eds.), EUROTRIB 89 Helsinki: June 12, 1989, Espoo, Finland, volume 3, 1989.

[105] S. Fouvry, C. Paulin, S. Deyber, Impact of contact size and complex gross-partial slip conditions on Ti-6Al-4V/Ti-6Al-4V fretting wear, Tribology International 42 (2009) 461–474.

[106] R. Merhej, S. Fouvry, Contact size effect on fretting wear behaviour: Application to an AISI 52100/AISI 52100 interface, Lubrication Science 21 (2009) 83–102.

[107] P. L. Hurricks, Fretting wear of mild-steel from room-temperature to 200 °C, Wear 19 (1972) 207–229.

[108] R. Rybiak, S. Fouvry, B. Bonnet, Fretting wear of stainless steels under variable temperature conditions: Introduction of a 'composite' wear law, Wear 268 (2010) 413–423.

[109] R. C. Bill, Fretting wear of iron, nickel, and titanium under varied environmental conditions., Technical Memorandum TM–78972, NASA, 1978.

[110] H. Goto, D. H. Buckley, Effect of humidity on fretting wear of several pure metals, Technical Paper TP–2403, NASA, 1984.

[111] H. Mohrbacher, B. Blanpain, J. P. Celis, J. R. Roos, The influence of humidity on the fretting behaviour of PVD TiN coatings, Wear 180 (1995) 43–52.

[112] Z. B. Cai, M. H. Zhu, J. F. Zheng, X. S. Jin, Z. R. Zhou, Torsional fretting behaviors of LZ50 steel in air and nitrogen, Tribology International 42 (2009) 1676–1683.

[113] D. W. Hoeppner, Fretting fatigue case studies of engineering components, Tribology International 39 (2006) 1271–1276.

[114] D. W. Hoeppner, Fretting fatigue considerations in holistic structural integrity based design processes (HOLSIP)—a continuing evolution, Tribology International 44 (2011) 1364–1370.

[115] I. M. Hutchings, Tribology: Friction and Wear of Engineering Materials, Edward Arnold, 1992.

[116] R. Bayer, Engineering Design For Wear, Dekker Mechanical Engineering Series, Marcel Dekker, 2004.

[117] Y. Fu, J. Wei, A. W. Batchelor, Some considerations on the mitigation of fretting damage by the application of surface-modification technologies, Journal of Materials Processing Technology 99 (2000) 231–245.

[118] S. C. Gordelier, T. C. Chivers, A literature review of palliatives for fretting fatigue, Wear 56 (1979) 177–190.

[119] D. Hoeppner, F. Gates, Fretting fatigue considerations in engineering design, Wear 70 (1981) 155–164.

[120] Z. Zhou, L. Vincent, Lubrication in fretting—a review, Wear 225–229 (1999) 962–967.

[121] A. Neyman, The influence of oil properties on the fretting wear of mild steel, Wear 152 (1992) 171–181.

[122] M. Shima, H. Suetake, I. McColl, R. Waterhouse, M. Takeuchi, On the behaviour of an oil lubricated fretting contact, Wear 210 (1997) 304–310.

[123] Z. Zhou, P. Kapsa, L. Vincent, Grease lubrication in fretting, Journal of Tribology - Transactions of the ASME 120 (1998) 737–743.

[124] J. Sato, M. Shima, T. Sugawara, A. Tahara, Effect of lubricants on fretting wear of steel, Wear 125 (1988) 83–95.

[125] M. Grahn, A. Naveira-Suarez, R. Pasaribu, Effect of ZDDP on friction in fretting contacts, Wear 273 (2011) 70–74.

[126] J. Xu, Z. Zhou, C. Zhang, M. Zhu, J. Luo, An investigation of fretting wear behaviors of bonded solid lubricant coatings, Journal of Materials Processing Technology 182 (2007) 146–151.

[127] M. Zhu, Z. Zhou, An investigation of molybdenum disulfide bonded solid lubricant coatings in fretting conditions, Surface and Coatings Technology 141 (2001) 240–245.

[128] A. L. Mohd Tobi, P. Shipway, S. Leen, Gross slip fretting wear performance of a layered thin W-DLC coating: Damage mechanisms and life modelling, Wear 271 (2011) 1572–1584.

[129] P. J. Golden, A. Hutson, V. Sundaram, J. H. Arps, Effect of surface treatments on fretting fatigue of Ti-6Al-4V, International Journal of Fatigue 29 (2007) 1302–1310.

[130] M. Kalin, J. Vižintin, The tribological performance of DLC coatings under oil-lubricated fretting conditions, Tribology International 39 (2006) 1060–1067.

[131] B. Blanpain, H. Mohrbacher, E. Liu, J. P. Celis, J. R. Roos, Hard coatings under vibrational contact conditions, Surface and Coatings Technology 74 (1995) 953–958.

[132] E. Meletis, A. Erdemir, G. Fenske, Tribological characteristics of DLC films and duplex plasma nitriding/DLC coating treatments, Surface and Coatings Technology 73 (1995) 39–45.

[133] B. Blanpain, J. P. Celis, J. R. Roos, J. Ebberink, J. Smeets, A comparative-study of the fretting wear of hard carbon coatings, Thin Solid Films 223 (1993) 65–71.

[134] S. A. Namjoshi, V. K. Jain, S. Mall, Effects of shot-peening on fretting-fatigue behavior of Ti-6Al-4V, Journal of Engineering Materials and Technology 124 (2002) 222–228.

[135] N. R. Naidu, S. S. Raman, Effect of shot blasting on plain fatigue and fretting fatigue behaviour of Al-Mg-Si alloy AA6061, International Journal of Fatigue 27 (2005) 323–331.

[136] V. Fridrici, S. Fouvry, P. Kapsa, Effect of shot peening on the fretting wear of Ti-6Al-4V, Wear 250 (2001) 642–649.

[137] K. Kubiak, S. Fouvry, A. Marechal, A practical methodology to select fretting palliatives: Application to shot peening, hard chromium and WC-Co coatings, Wear 259 (2005) 367–376.

[138] D. Pye, Practical Nitriding and Ferritic Nitrocarburizing, ASM International, 2003.

[139] W. Kowaks, W. Russell, An introduction to ion nitriding; what is it? Why is it used? Where is it used?, in: T. Spalivins (Ed.), Proceedings Int Conf Ion Nitriding, Cleveland, OH, USA, 1986, pp. 9–17.

[140] B. Edenhofer, Physical and metallurgical aspects of ionitriding, Heat Treatment of Metals 1 (1974) 59–67.

[141] A. Alsaran, A. Çelik, Structural characterization of ion-nitrided AISI 5140 low-alloy steel, Materials Characterization 47 (2001) 207–213.

[142] Y. Sun, T. Bell, Plasma surface engineering of low alloy steel, Materials Science and Engineering: A 140 (1991) 419–434.

[143] M. Berg, C. Budtz-Jørgensen, H. Reitz, K. Schweitz, J. Chevallier, P. Kringhøj, J. Bøttiger, On plasma nitriding of steels, Surface and Coatings Technology 124 (2000) 25–31.

[144] H. Kato, T. S. Eyre, B. Ralph, Sliding wear characteristics of nitrided steels, Surface Engineering 10 (1994) 65–74.

[145] A. Alsaran, M. Karakan, A. Çelik, The investigation of mechanical properties of ion-nitrided AISI 5140 low-alloy steel, Materials Characterization 48 (2002) 323–327.

[146] H. Kato, T. S. Eyre, B. Ralph, Wear mechanism map of nitrided steel, Acta Metallurgica et Materialia 42 (1994) 1703–1713.

[147] Y. Sun, T. Bell, Sliding wear characteristics of low temperature plasma nitrided 316 austenitic stainless steel, Wear 218 (1998) 34–42.

[148] M. M. Hamdy, M. P. Overs, R. B. Waterhouse, A new high-temperature fretting wear test rig, Journal of Physics E-Scientific Instruments 14 (1981) 889–894.

[149] H. Mohrbacher, J. P. Celis, J. R. Roos, Laboratory testing of displacement and load induced fretting, Tribology International 28 (1995) 269–278.

[150] E. Marui, H. Endo, N. Hasegawa, H. Mizuno, Prototype fretting-wear testing machine and some experimental results, Wear 214 (1998) 221–230.

[151] R. Ramesh, R. Gnanamoorthy, Development of a fretting wear test rig and preliminary studies for understanding the fretting wear properties of steels, Materials & Design 27 (2006) 141–146.

[152] J. S. Halliday, The measurement of frictional forces at vibrating contacts, Journal of Scientific Instruments 33 (1956) 213.

[153] I. R. McColl, J. Ding, S. B. Leen, Finite element simulation and experimental validation of fretting wear, Wear 256 (2004) 1114–1127.

[154] A. L. Mohd Tobi, J. Ding, S. R. Pearson, S. B. Leen, P. H. Shipway, The effect of gross sliding fretting wear on stress distributions in thin w-dlc coating systems, Tribology International 43 (2010) 1917–1932.

[155] K. G. Budinski, Evaluation of fretting corrosion by means of a new device for the control of oscillation amplitude, in: S. R. Brown (Ed.), Materials Evaluation Under Fretting Conditions, volume 780 of *ASTM Special Technical Publication*, ASTM, 1982, pp. 49–67.

[156] M. Antler, Fretting of electrical contacts, in: S. R. Brown (Ed.), Materials Evaluation Under Fretting Conditions, volume 780 of *ASTM Special Technical Publication*, ASTM, 1982, pp. 68–85.

[157] P. Kennedy, M. B. Peterson, L. Stallings, An evaluation of fretting at small slip amplitudes, in: Materials Evaluation Under Fretting Conditions, ASTM, 1982, pp. 30–48.

[158] D. Kusner, C. Poon, D. Hoeppener, A new machine for studying surface damage due to wear and fretting, in: S. R. Brown (Ed.), Materials Evaluation Under Fretting Conditions, volume 780 of *ASTM Special Technical Publication*, ASTM, 1982, pp. 17–29.

[159] M. G. El-Sherbiny, F. B. Salem, Fretting-resistant ion-plated coatings, in: S. R. Brown (Ed.), Materials Evaluation Under Fretting Conditions, volume 780 of *ASTM Special Technical Publication*, ASTM, 1982, pp. 125–137.

[160] R. Smallwood, B. R. Pearson, P. A. Brook, The influence of dissolved oxygen in seawater on the fretting corrosion of roping steel, Wear 125 (1988) 97–106.

[161] O. Vingsbo, J. Schön, Giant-magnetostrictive vibrator system for fretting testing at low amplituides, Wear 162 (1993) 1129–1138.

[162] D. A. Hills, D. Nowell, J. J. O'Connor, On the mechanics of fretting fatigue, Wear 125 (1988) 129–146.

[163] M. H. Zhu, Z. R. Zhou, On the mechanisms of various fretting wear modes, Tribology International 44 (2011) 1378–1388.

[164] A. L. Mohd Tobi, J. Ding, G. Bandak, S. B. Leen, P. H. Shipway, A study on the interaction between fretting wear and cyclic plasticity for Ti-6Al-4V, Wear 267 (2009) 270–282.

[165] P. J. Lotz, D. Greenspan, R. Godwin, P. Taylor, Discovery channel telescope software development overview, in: Society of Photo-Optical Instrumentation Engineers (SPIE) Conference Series, 2010.

[166] M. C. Ashe, G. Schumacher, SOAR telescope control system: a rapid prototype and development in LabVIEW, in: Society of Photo-Optical Instrumentation Engineers (SPIE) Conference Series, 2000.

[167] M. Poinot, Five good reasons to use the hierarchical data format, Computing in Science Engineering 12 (2010) 84–90.

[168] National Instruments, The NI TDMS file format, `http://www.ni.com/white-paper/3727/en`, 2013. Accessed: 12/03/2013.

[169] J. Conway, S. Watts, A Software Engineering Approach to LabVIEW, National Instruments Virtual Instrumentation Series, Prentice Hall, 2003.

[170] T. Dick, C. Paulin, G. Cailletaud, S. Fouvry, Experimental and numerical analysis of local and global plastic behaviour in fretting wear, Tribology International 39 (2006) 1036–1044.

[171] M. Cheikh, S. Quilici, G. Cailletaud, Presentation of KI-COF, a phenomenological model of variable friction in fretting contact, Wear 262 (2007) 914–924.

[172] S. Fouvry, P. Duó, P. Perruchaut, A quantitative approach of Ti-6Al-4V fretting damage: friction, wear and crack nucleation, Wear 257 (2004) 916–929.

[173] J. F. Archard, Contact and rubbing of flat surfaces, Journal of Applied Physics 24 (1953) 981–988.

[174] J. F. Archard, W. Hirst, The wear of metals under unlubricated conditions, Proceedings of the Royal Society of London. Series A. Mathematical and Physical Sciences 236 (1956) 397–410.

[175] H. Mohrbacher, B. Blanpain, J. P. Celis, J. R. Roos, L. Stals, M. Van Stappen, Oxidational wear of tin coatings on tool steel and nitrided tool steel in unlubricated fretting, Wear 188 (1995) 130–137.

[176] S. Fouvry, P. Kapsa, H. Zahouani, L. Vincent, Wear analysis in fretting of hard coatings through a dissipated energy concept, Wear 203-204 (1997) 393–403.

[177] S. Fouvry, T. Liskiewicz, P. Kapsa, S. Hannel, E. Sauger, An energy description of wear mechanisms and its applications to oscillating sliding contacts, Wear 255 (2003) 287–298.

[178] R. Ramesh, R. Gnanamoorthy, Fretting wear behavior of liquid nitrided structural steel, EN24 and bearing steel, EN31, Journal of Materials Processing Technology 171 (2006) 61–67.

[179] J. Luo, Y. D. Wang, C. Song, J. L. Mo, M. H. Zhu, Rotational fretting wear of ion nitrided medium carbon steel, in: Z. Jiang, C. Zhang (Eds.), Manufacturing Science and Engineering, pts 1–5, 2010.

[180] F. P. Bowden, D. Tabor, The friction and lubrication of solids, International series of monographs on physics, Oxford: Clarendon Press, Oxford, England, 1964.

[181] R. Ramesh, R. Gnanamoorthy, Effect of hardness on fretting wear behaviour of structural steel, EN24, against bearing steel, EN31, Materials & Design 28 (2007) 1447–1452.

[182] S. Fouvry, Shakedown analysis and fretting wear response under gross slip condition, Wear 251 (2001) 1320–1331.

[183] D. Mulvihill, M. Kartal, A. Olver, D. Nowell, D. Hills, Investigation of non-Coulomb friction behaviour in reciprocating sliding, Wear 271 (2011) 802–816.

[184] R. Kuppuswamy, Aluminium Alloys, Theory and Applications, InTech, 2011.

[185] M. Shima, J. Okado, I. R. McColl, R. B. Waterhouse, T. Hasegawa, M. Kasaya, The influence of substrate material and hardness on the fretting behaviour of TiN , Wear 225 (1999) 38–45.

[186] D. Zhang, S. Ge, Y. Qiang, Research on the fatigue and fracture behavior due to the fretting wear of steel wire in hoisting rope, Wear 255 (2003) 1233–1237.

[187] T. Kayaba, A. Iwabuchi, The fretting wear of 0.45 % C steel and austenitic stainless steel from 20 to 650 °C in air, Wear 74 (1981) 229–245.

[188] D. E. Taylor, F. B. Hardisty, R. B. Waterhouse, A. Y. Nehru, The fretting wear of an austenitic stainless steel in air and in carbon dioxide at elevated temperatures, Wear 56 (1979) 9–18.

[189] P. L. Hurricks, Fretting wear of mild-steel from 200 °C to 500 °C, Wear 30 (1974) 189–212.

[190] F. H. Stott, G. C. Wood, The influence of oxides on the friction and wear of alloys, Tribology International 11 (1978) 211–218.

[191] F. H. Stott, J. Glascott, G. C. Wood, The sliding wear of commercial Fe–12%Cr alloys at high temperature, Wear 101 (1985) 311–324.

[192] F. H. Stott, High-temperature sliding wear of metals, Tribology International 35 (2002) 489–495.

[193] J. Glascott, G. C. Wood, F. H. Stott, The influence of experimental variables on the development and maintenance of wear-protective oxides during sliding of high-temperature iron-base alloys, Proceedings of the Institution of Mechanical Engineers, Part C: Journal of Mechanical Engineering Science 199 (1985) 35–41.

[194] W. T. Clark, C. Pritchard, J. W. Midgley, Mild wear of unlubricated hard steels in air and carbon dioxide, Proceedings of The Institution of Mechanical Engineers 182 (1967) 97–105.

[195] R. T. Foley, M. B. Peterson, C. Zapf, Frictional characteristics of cobalt, nickel, and iron as influenced by their surface oxide films, ASLE Transactions 6 (1963) 29–39.

[196] H. Kato, K. Komai, Tribofilm formation and mild wear by tribo-sintering of nanometer-sized oxide particles on rubbing steel surfaces, Wear 262 (2007) 36–41.

[197] J. Jiang, F. H. Stott, M. M. Stack, The role of triboparticulates in dry sliding wear, Tribology International 31 (1998) 245–256.

[198] K. L. Johnson, K. Kendall, A. D. Roberts, Surface energy and the contact of elastic solids, Proceedings of the Royal Society of London. A. Mathematical and Physical Sciences 324 (1971) 301–313.

[199] R. M. German, Sintering theory and pratice, A Wiley-Interscience publication, John Wiley & Sons, 1996.

[200] K. Adachi, K. Kato, Formation of smooth wear surfaces on alumina ceramics by embedding and tribo-sintering of fine wear particles, Wear 245 (2000) 84–91.

[201] H. Kato, Effects of supply of fine oxide particles onto rubbing steel surfaces on severe–mild wear transition and oxide film formation, Tribology International 41 (2008) 735–742.

[202] C. Herring, Effect of change of scale on sintering phenomena, Journal of Applied Physics 21 (1950) 301–303.

[203] T. M. Nenoff, B. W. Jacobs, D. B. Robinson, P. P. Provencio, J. Huang, S. Ferreira, D. J. Hanson, Synthesis and low temperature in situ sintering of uranium oxide nanoparticles, Chemistry of Materials 23 (2011) 5185–5190.

[204] Y. H. Zhou, M. Harmelin, J. Bigot, Sintering behaviour of ultra-fine Fe, Ni and Fe-25wt%Ni powders, Scripta Metallurgica 23 (1989) 1391–1396.

[205] R. B. Waterhouse, Fretting at high temperatures, Tribology International 14 (1981) 203–207.

[206] N. M. Everitt, M. I. Davies, J. F. Smith, High temperature nanoindentation - the importance of isothermal contact, Philosophical Magazine 91 (2011) 1221–1244.

[207] N. Birks, G. Meier, Introduction to High Temperature Oxidation of Metals, Chemistry Series, Edward Arnold, 1983.

[208] W. H. J. Vernon, E. A. Calnan, C. J. B. Clews, T. J. Nurse, The oxidation of iron around 200 °C, Proceedings of the Royal Society of London. Series A. Mathematical and Physical Sciences 216 (1953) 375–397.

[209] A. R. Warmuth, S. R. Pearson, P. H. Shipway, W. Sun, The effect of contact geometry on fretting wear rates and mechanisms for a high strength steel, Wear 301 (2013) 491–500.

Appendix A

Detailed Drawings

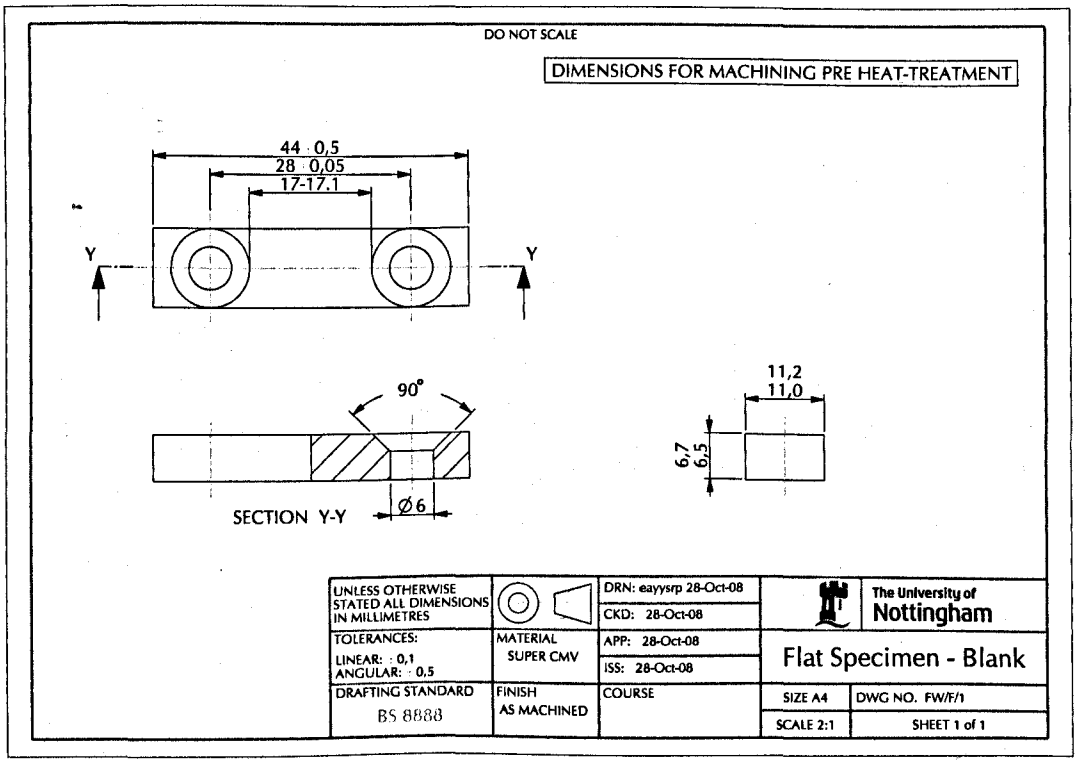

(a) Flat specimen

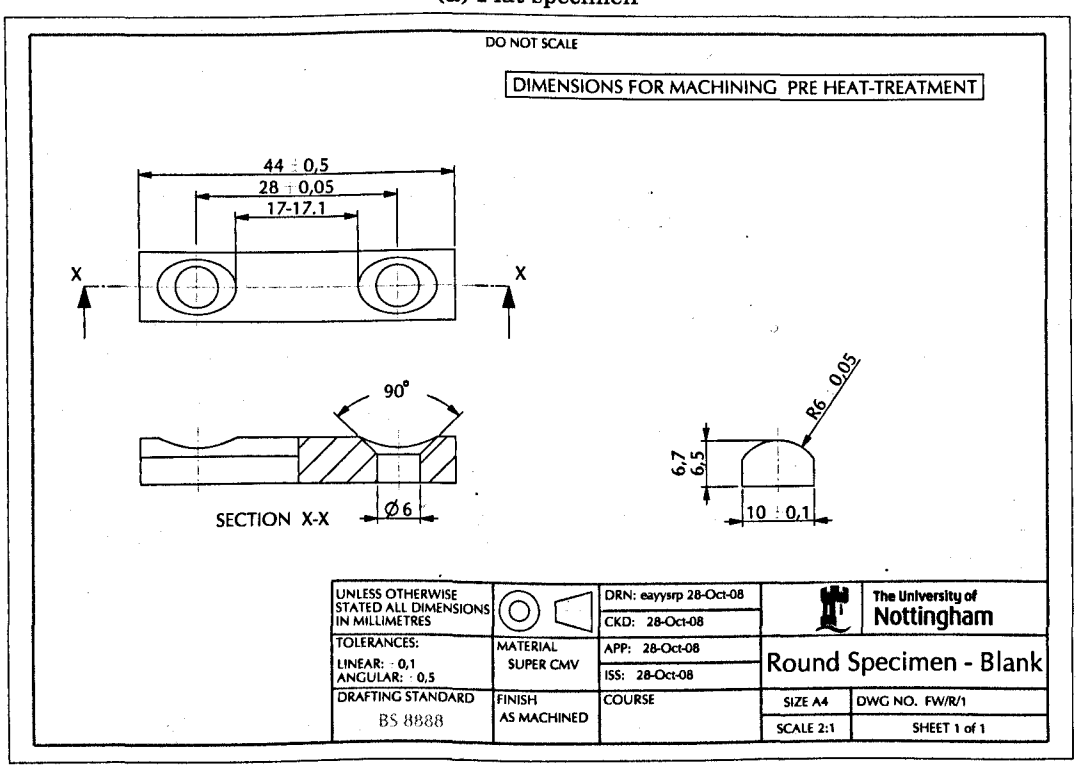

(b) Cylindrical specimen

Figure A.1: Detail manufacturing drawings for the fretting specimen "blanks" prior to heat treatment and grinding.

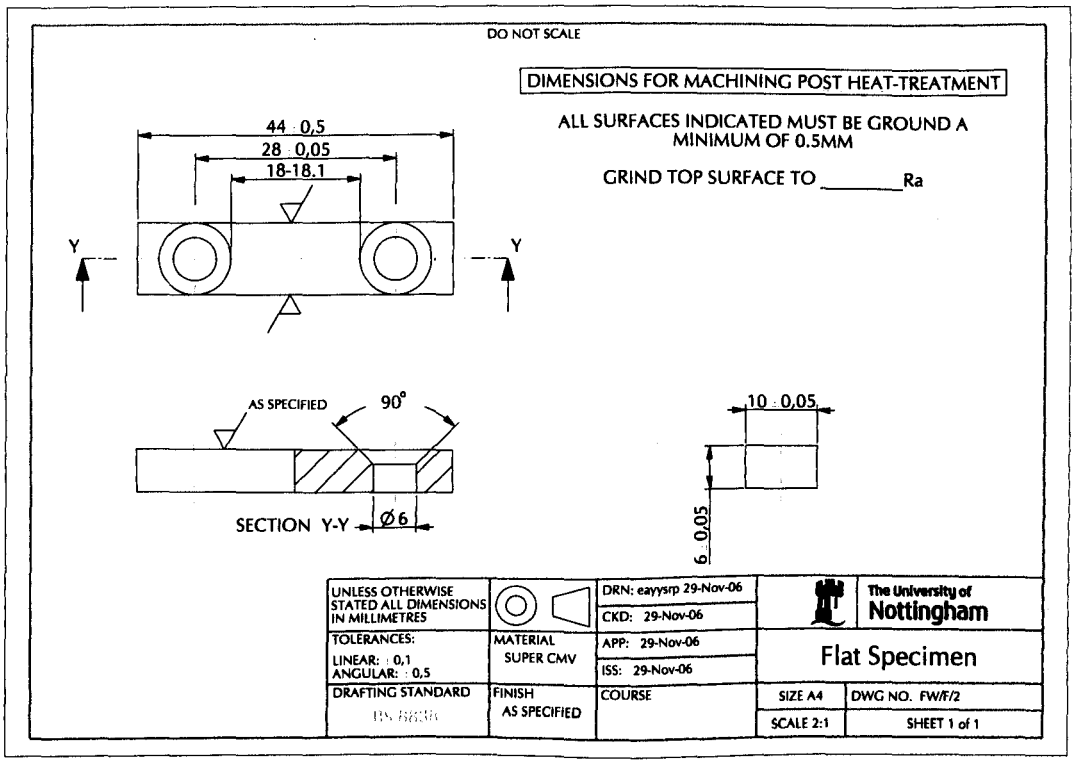

(a) Flat specimen

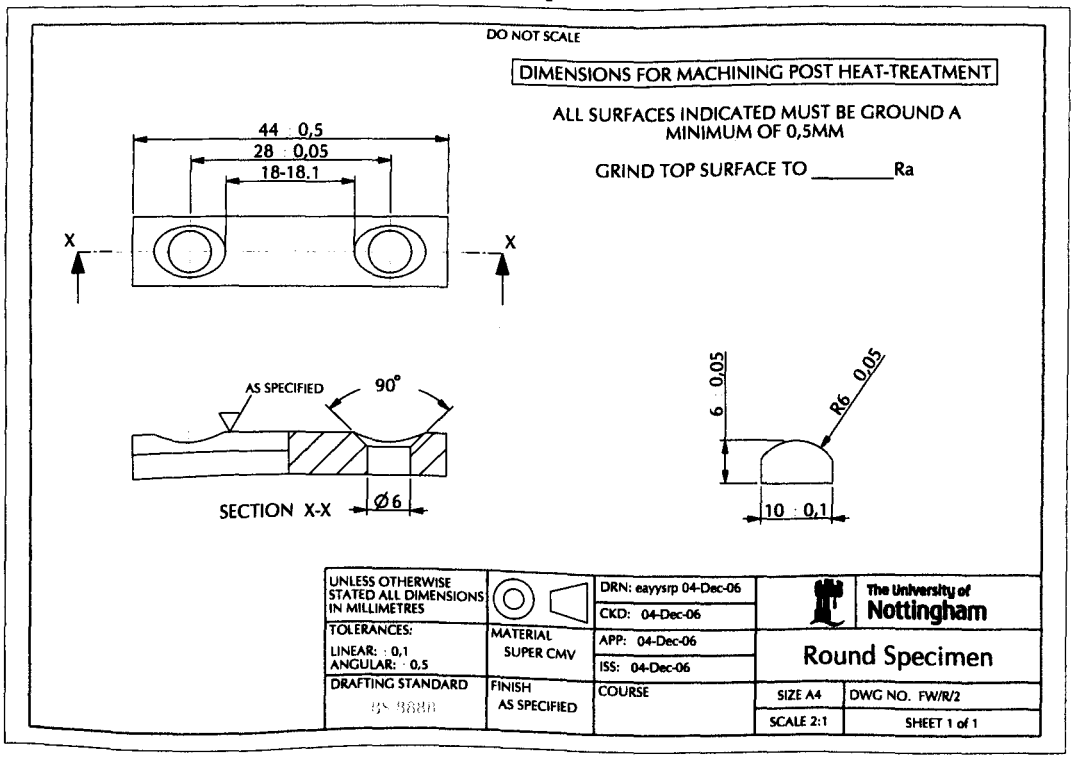

(b) Cylindrical specimen

Figure A.2: Detail manufacturing drawings for final machining of the fretting specimens.